

**Studies of Natural Convection in  
Enclosures Using the Finite Volume  
Method**

**Huafu Yao**

A dissertation submitted to the Faculty of Graduate Studies in  
partial fulfilment of the requirements for the degree of

**Doctor of Philosophy**

Centre for Research in Earth and Space Science

**York University  
North York, Ontario, Canada**

**January 1999**



National Library  
of Canada

Acquisitions and  
Bibliographic Services  
  
395 Wellington Street  
Ottawa ON K1A 0N4  
Canada

Bibliothèque nationale  
du Canada

Acquisitions et  
services bibliographiques  
  
395, rue Wellington  
Ottawa ON K1A 0N4  
Canada

Your file Votre référence

Our file Notre référence

The author has granted a non-exclusive licence allowing the National Library of Canada to reproduce, loan, distribute or sell copies of this thesis in microform, paper or electronic formats.

The author retains ownership of the copyright in this thesis. Neither the thesis nor substantial extracts from it may be printed or otherwise reproduced without the author's permission.

L'auteur a accordé une licence non exclusive permettant à la Bibliothèque nationale du Canada de reproduire, prêter, distribuer ou vendre des copies de cette thèse sous la forme de microfiche/film, de reproduction sur papier ou sur format électronique.

L'auteur conserve la propriété du droit d'auteur qui protège cette thèse. Ni la thèse ni des extraits substantiels de celle-ci ne doivent être imprimés ou autrement reproduits sans son autorisation.

0-612-42781-1

Canadä

**Studies of Natural Convection in Enclosures  
Using the Finite Volume Method**

by      **Huafu Yao**

a dissertation submitted to the Faculty of Graduate Studies of  
York University in partial fulfillment of the requirements for the  
degree of

**DOCTOR OF PHILOSOPHY**

**© (1997)**

Permission has been granted to the LIBRARY OF YORK  
UNIVERSITY to lend or sell copies of this dissertation, to the  
NATIONAL LIBRARY OF CANADA to microfilm this dissertation  
and to lend or sell copies of the film, and to UNIVERSITY  
MICROFILMS to publish an abstract of this dissertation.

The author reserves other publication rights, and neither the  
dissertation nor extensive extracts from it may be printed or  
otherwise reproduced without the author's written permission.

## **Abstract**

Natural convection is a physical phenomenon which often occurs in natural processes such as in the atmosphere, lakes, oceans, the Earth's mantle and core as well as in engineering areas such as solar collectors, double window systems and electronic device cooling. Natural convection in enclosures has been an active research topic in recent years due to its importance in fundamental studies and applications.

Several projects concerning the natural convection problem in enclosures using numerical and experimental methods are reported in this dissertation. In the first project a numerical method is applied to the classical Rayleigh-Bénard problem defined as convection caused by heating a fluid from below. Second, natural convection in a rectangular enclosure with a partly heated bottom and one cooled sidewall is studied numerically. Third, natural convection in a rectangular enclosure with sidewalls heated and cooled is investigated by a numerical method. Fourth, a numerical investigation on natural convection in a parallelogrammic enclosure with vertically opposite walls heated and cooled and two inclined walls is carried out. Fifth, numerical and experimental methods are used to study the natural convection in a parallelogrammic enclosure with two inclined walls heated and cooled and two

horizontal walls.

The numerical method used in the research is the finite volume method which was chosen because of its advantageous physical way to obtain a discretization and the geometric flexibility in the choice of a grid. All enclosures are modelled as two-dimensional. Non-orthogonal, staggered grids have been employed to discretize the computational domain. The numerical procedures have been formulated and written in a Fortran computer program that is applied to all the above problems. Experiments for the last project have been conducted using Digital Particle Image Velocimetry in the flow field visualization. The velocity fields obtained experimentally are compared with those found numerically.

Results for velocity and temperature fields are presented, compared with early work and discussed. The results presented are for a wide range of Rayleigh and Prandtl numbers. Several heat transfer features for the different cases have been revealed such as the heat transfer rate associated with flow patterns in Rayleigh-Bénard convection and inclination angle in natural convection in a parallelogrammic enclosure. The flexibility of the finite volume method is demonstrated through these study cases. Flow structures in natural convection have been revealed in the forms of boundary layers, stagnation regions and reverse flows with two and three rolls flow patterns. Future research works are recommended.

## **Acknowledgments**

I would specially like to thank my supervisor Professor Keith Aldridge for offering me the opportunity to carry out the research. His guidance, suggestions and encouragement have been very significant to me in completing the current research. His friendly help in the period of my study will always remain in my memory.

I would also specially like to thank Professor Gary Jarvis, Professor Gary Klaassen for many helpful discussions and suggestions during my study.

I would like to thank Professor Jafar Arkani-Hamed, Professor James G. Laframboise, Professor Peter A. Taylor, Professor Qiuming Cheng for taking time to review and comment on my thesis.

I am grateful to the financial support partly from NSERC through grants to Professor Keith Aldridge.

I would also like to express my appreciation to Patrice Meunier, Dr. S. Joshi, Ming Xiao, Karen Cunningham, the staff of CRESS.

# Contents

<b>1</b>	<b>Introduction</b>	<b>1</b>
1.1	Literature Survey .....	1
1.1.1	Natural Convection in an Enclosure .....	2
1.1.2	Rayleigh-Bénard Convection .....	11
1.2	Present Study .....	17
<b>2</b>	<b>Basic Theory of Natural Convection</b>	<b>22</b>
2.1	Introduction .....	22
2.2	Governing Differential Equations .....	25
2.3	Boussinesq Approximation in Natural Convection .....	27
2.4	Nondimensionalization .....	28
2.5	Mathematical Formulation for Two-Dimensional Enclosure Natural Convection Flow .....	30
2.5.1	Governing Equations for Natural Convection in Parallelogrammic and Rectangular Enclosures .....	30
2.5.2	Dimensionless Parameters and Nondimensionalization ..	32
2.5.3	Physical Models for the Five study cases and Boundary Conditions .....	34
2.5.4	Average Heat Transfer Coefficient .....	40
<b>3</b>	<b>Numerical Method - Finite Volume Method</b>	<b>41</b>
3.1	The General Differential Equation .....	41

<b>3.2 Discretization Equation .....</b>	<b>43</b>
<b>3.3 Calculation of the Flow Field .....</b>	<b>52</b>
<b>3.3.1 Discretization of the Momentum Equations .....</b>	<b>55</b>
<b>3.3.2 The Pressure-Correction Equation .....</b>	<b>59</b>
<b>3.3.3 Algorithm .....</b>	<b>64</b>
<b>3.3.3.1 Steps of Operations .....</b>	<b>64</b>
<b>3.3.3.2 Boundary Conditions for the Pressure- Correction Equation .....</b>	<b>65</b>
<b>3.3.3.3 The Relative Nature of Pressure .....</b>	<b>66</b>
<b>3.4 Solver for the Algebraic Equations .....</b>	<b>66</b>
<b>4 Experimental Instrumentation and Setup .....</b>	<b>67</b>
<b>4.1 Techniques of DPIV .....</b>	<b>67</b>
<b>4.2 Experimental Setup .....</b>	<b>72</b>
<b>5 Results and Discussions .....</b>	<b>78</b>
<b>5.1 Scale Analysis .....</b>	<b>79</b>
<b>5.2 Rayleigh-Bénard Convection .....</b>	<b>89</b>
<b>5.3 Natural Convection in Rectangular Enclosures Partly Heated from the Bottom and Cooled along a Side Wall .....</b>	<b>111</b>
<b>5.4 Results for Natural Convection in a Rectangular Enclosure .....</b>	<b>125</b>
<b>5.5 Natural Convection in a Parallelogrammic Enclosure with Two Vertical Walls and Two Inclined Walls .....</b>	<b>136</b>
<b>5.6 Natural Convection in a Parallelogrammic Enclosure with Two</b>	

Horizontal Walls and Two Inclined Walls .....	161
5.6.1 Numerical Results for Prandtl Number of 0.71 .....	162
5.6.2 Results for High Prandtl Numbers .....	182
5.6.3 Comparison of Numerical and Experimental Results for Velocity .....	190
<b>6 Summary and Conclusions</b>	<b>209</b>
<b>Appendix</b>	<b>220</b>
<b>References</b>	<b>224</b>

# List of Figures

2.1	Schematic of the physical model for Rayleigh-Bénard thermal convection in a rectangular domain .....	35
2.2	Schematic of the physical model for natural convection in rectangular enclosure subjected to partly heating bottom and cooling right sidewall .....	36
2.3	Schematic of the physical model for natural convection in rectangular enclosure subjected to partly heating and cooling different sidewalls .....	37
2.4	Schematic of the physical model for natural convection in a parallelogrammic enclosure with two vertical sidewalls heated and cooled .....	38
2.5	Schematic of the physical model for natural convection in a parallelogrammic enclosure with two inclined sidewalls heated and cooled .....	39
3.1	Schematic of a parallelogrammic control volume .....	45
4.1	Flow chart of the DPIV system .....	71
4.2	Schematic of the parallelogrammic enclosure and dimensions .....	74
5.1	Velocity vectors for Rayleigh-Bénard convection for $\text{Ra}=4000$ , $\text{Pr}=6.8$ .....	93
5.2	Velocity vectors for Rayleigh-Bénard convection for $\text{Ra}=5000$ , $\text{Pr}=6.8$ .....	93

5.3	Velocity vectors for Rayleigh-Bénard convection for $\text{Ra}=6000$ , $\text{Pr}=6.8$ .....	94
5.4	Velocity vectors for Rayleigh-Bénard convection for $\text{Ra}=8000$ , $\text{Pr}=6.8$ .....	94
5.5	Velocity vectors for Rayleigh-Bénard convection for $\text{Ra}=10000$ , $\text{Pr}=6.8$ .....	95
5.6	Velocity vectors for Rayleigh-Bénard convection for $\text{Ra}=12000$ , $\text{Pr}=6.8$ .....	95
5.7	Velocity vectors for Rayleigh-Bénard convection for $\text{Ra}=15000$ , $\text{Pr}=6.8$ .....	96
5.8	Velocity vectors for Rayleigh-Bénard convection for $\text{Ra}=20000$ , $\text{Pr}=6.8$ .....	96
5.9	Isotherms for Rayleigh-Bénard convection for $\text{Ra}=4000$ , $\text{Pr}=6.8$ .....	97
5.10	Isotherms for Rayleigh-Bénard convection for $\text{Ra}=5000$ , $\text{Pr}=6.8$ .....	97
5.11	Isotherms for Rayleigh-Bénard convection for $\text{Ra}=6000$ , $\text{Pr}=6.8$ .....	98
5.12	Isotherms for Rayleigh-Bénard convection for $\text{Ra}=8000$ , $\text{Pr}=6.8$ .....	98
5.13	Isotherms for Rayleigh-Bénard convection for $\text{Ra}=10000$ , $\text{Pr}=6.8$ .....	99
5.14	Isotherms for Rayleigh-Bénard convection for $\text{Ra}=12000$ , $\text{Pr}=6.8$ .....	99
5.15	Isotherms for Rayleigh-Bénard convection for $\text{Ra}=15000$ , $\text{Pr}=6.8$ .....	100
5.16	Isotherms in Rayleigh-Bénard convection for $\text{Ra}=20000$ , $\text{Pr}=6.8$ .....	100
5.17	Velocity vectors for Rayleigh-Bénard convection for $\text{Ra}=50000$ , $\text{Pr}=6.8$ , zero initial condition .....	106
5.18	Isotherms in Rayleigh-Bénard convection for $\text{Ra}=50000$ , $\text{Pr}=6.8$ zero initial condition .....	106

5.19	Velocity vectors for Rayleigh-Bénard convection for $\text{Ra}=50000$ , $\text{Pr}=6.8, K=1$	107
5.20	Velocity vectors for Rayleigh-Bénard convection for $\text{Ra}=50000$ , $\text{Pr}=6.8, K=2$	107
5.21	Velocity vectors for Rayleigh-Bénard convection for $\text{Ra}=50000$ , $\text{Pr}=6.8, K=3$	108
5.22	Velocity vectors for Rayleigh-Bénard convection for $\text{Ra}=50000$ , $\text{Pr}=6.8, K=4$	108
5.23	Velocity vectors for Rayleigh-Bénard convection for $\text{Ra}=50000$ , $\text{Pr}=6.8, K=5$	109
5.24	Velocity vectors for Rayleigh-Bénard convection for $\text{Ra}=50000$ , $\text{Pr}=6.8, K=6$	109
5.25	Temperature contours for natural convection in a rectangular enclosure with partly heated bottom and cooled right sidewall for heating section of 0.3, $\text{Ra}=10^4, 10^5, 10^6$	115
5.26	Temperature contours for natural convection in a rectangular enclosure with partly heated bottom and cooled right sidewall for heating section of 0.5, $\text{Ra}=10^4, 10^5, 10^6$	116
5.27	Temperature contours for natural convection in a rectangular enclosure with partly heated bottom and cooled right sidewall for heating section of 0.7, $\text{Ra}=10^4, 10^5, 10^6$	117
5.28	Comparison of temperature contours for natural convection in a rectangular enclosure with partly heated bottom and cooled right sidewall between current and November and Nansteel's study for $\text{Ra}=10^6$ and heating section of 0.5	117

5.29	Velocity vector fields for natural convection in a rectangular enclosure with partly heat bottom and cooled right sidewall for heating section of 0.3 , $Ra=10^4, 10^5, 10^6$ .....	120
5.30	Velocity vector fields for natural convection in a rectangular enclosure with partly heated bottom and cooled right sidewall for heating section of 0.5 , $Ra=10^4, 10^5, 10^6$ .....	121
5.31	Velocity vector fields for natural convection in a rectangular enclosure with partly heat bottom and cooled right sidewall for heating section of 0.7 , $Ra=10^4, 10^5, 10^6$ .....	122
5.32	Nusselt number versus heating section for $Ra=10^4, 10^5, 10^6$ for natural convection in a rectangular enclosure with partly heat bottom and cooled right sidewall .....	124
5.33	Velocity vector fields for natural convection in a rectangular enclosure with heating and cooling different sidewalls for $Ra=10^4, 10^5, 10^6$ , streamtraces for $10^6$ , $Pr=0.71$ .....	128
5.34	Isotherms for natural convection in a rectangular enclosure with heating and cooling different sidewalls for $Ra=10^4, 10^5, 10^6$ , $Pr=0.71$ .....	129
5.35	Horizontal velocity U at $X=0.4875, Y=0.6375$ , for $Ra= 10^6$ , $Pr=0.71$ versus dimensionless time .....	133
5.36	Horizontal velocity U at $X=0.4875, Y=0.7625$ , for $Ra= 10^6$ , $Pr=0.71$ versus dimensionless time .....	134
5.37	Horizontal velocity U at $X=0.4875, Y=0.8875$ , for $Ra= 10^6$ , $Pr=0.71$ versus dimensionless time .....	135
5.38	Velocity vectors for natural convection in a parallelogrammic	

enclosure with heating and cooling two vertical walls for $IA=15^\circ$ , $Pr=0.71$ and $Ra=10^4, 10^5, 10^6$ .....	138
5.39 Isotherms for natural convection in a parallelogrammic enclosure with heating and cooling two vertical walls for $IA=15^\circ$ , $Pr=0.71$ , $Ra=10^4, 10^5, 10^6$ .....	139
5.40 Velocity vectors in central region of the enclosure for natural convection in a parallelogrammic enclosure with heating and cooling two vertical walls for $IA=15^\circ$ , $Pr=0.71$ , $Ra=10^4, 10^5, 10^6$ .....	141
5.41 Velocity vectors for natural convection in a parallelogrammic enclosure with heating and cooling two vertical walls for $IA=30^\circ$ , $Pr=0.71$ , $Ra=10^4, 10^5, 10^6$ .....	143
5.42 Isotherms for natural convection in a parallelogrammic enclosure with heating and cooling two vertical walls for $IA=30^\circ$ , $Pr=0.71$ , $Ra=10^4, 10^5, 10^6$ .....	144
5.43 Velocity vectors for natural convection in a parallelogrammic enclosure with heating and cooling two vertical walls for $IA=45^\circ$ , $Pr=0.71$ , $Ra=10^4, 10^5, 10^6$ .....	146
5.44 Isotherms for natural convection in a parallelogrammic enclosure with heating and cooling two vertical walls for $IA=45^\circ$ , $Pr=0.71$ , $Ra=10^4, 10^5, 10^6$ .....	147
5.45 Velocity vectors for natural convection in a parallelogrammic enclosure with heating and cooling two vertical walls for $IA=60^\circ$ , $Pr=0.71$ , $Ra=10^4, 10^5, 10^6$ .....	148
5.46 Isotherms for natural convection in a parallelogrammic enclosure	

with heating and cooling two vertical walls for $\text{IA}=60^\circ$ , $\text{Pr}=0.71$ ,	
$\text{Ra}=10^4, 10^5, 10^6$ .....	149
5.47 Velocity vectors in the upper right corner for $\text{IA}=60^\circ$ ,	
$\text{Pr}=0.71$ , $\text{Ra}=10^4$ .....	153
5.48 Velocity vectors at interfaces in the upper right corner	
for $\text{IA}=60^\circ$ , $\text{Pr}=0.71$ , $\text{Ra}=10^4$ .....	154
5.49 Velocity vectors in the upper right corner for $\text{IA}=60^\circ$ ,	
$\text{Pr}=0.71$ , $\text{Ra}=10^4$ .....	156
5.50 The ratio of average kinetic energy versus $\log(\text{grid})$ .....	157
5.51 Nusselt numbers versus $\text{IA}$ and $\text{Ra}$ for $\text{Pr}=0.71$ .....	160
5.52 Velocity vectors for natural convection in a parallelogrammic	
enclosure with two horizontal walls for $\text{IA}=15^\circ$ , $\text{Pr}=0.71$ ,	
$\text{Ra}=10^4, 10^5, 10^6$ .....	163
5.53 Isotherms for natural convection in a parallelogrammic	
enclosure with two horizontal walls for $\text{IA}=15^\circ$ , $\text{Pr}=0.71$ ,	
$\text{Ra}=10^4, 10^5, 10^6$ .....	164
5.54 Streamtrace and stream function for natural convection in	
a parallelogrammic enclosure with two horizontal walls	
for $\text{IA}=15^\circ$ , $\text{Pr}=0.71$ , $\text{Ra}=10^6$ .....	166
5.55 Vertical velocity at $Y=0.4709$ for natural convection in	
a parallelogrammic enclosure with two horizontal walls	
for $\text{IA}=15^\circ$ , $\text{Pr}=0.71$ , $\text{Ra}=10^4, 10^5, 10^6$ .....	169
5.56 Temperature at $Y=0.4709$ for natural convection in	
a parallelogrammic enclosure with two horizontal walls	
for $\text{IA}=15^\circ$ , $\text{Pr}=0.71$ , $\text{Ra}=10^4, 10^5, 10^6$ .....	170

5.57	Velocity vectors for natural convection in a parallelogrammic enclosure with two horizontal walls for IA=30°, Pr=0.71, Ra=10 <sup>4</sup> , 10 <sup>5</sup> , 10 <sup>6</sup> .....	173
5.58	Isotherms for natural convection in a parallelogrammic enclosure with two horizontal walls for IA=30°, Pr=0.71, Ra=10 <sup>4</sup> , 10 <sup>5</sup> , 10 <sup>6</sup> .....	174
5.59	Velocity vectors for natural convection in a parallelogrammic enclosure with two horizontal walls for IA=45°, Pr=0.71, Ra=10 <sup>4</sup> , 10 <sup>5</sup> , 10 <sup>6</sup> .....	175
5.60	Isotherms for natural convection in a parallelogrammic enclosure with two horizontal walls for IA=45°, Pr=0.71, Ra=10 <sup>4</sup> , 10 <sup>5</sup> , 10 <sup>6</sup> .....	176
5.61	Velocity vectors for natural convection in a parallelogrammic enclosure with two horizontal walls for IA=60°, Pr=0.71, Ra=10 <sup>4</sup> , 10 <sup>5</sup> , 10 <sup>6</sup> .....	178
5.62	Isotherms for natural convection in a parallelogrammic enclosure with two horizontal walls for IA=60°, Pr=0.71, Ra=10 <sup>4</sup> , 10 <sup>5</sup> , 10 <sup>6</sup> .....	179
5.63	Isotherms for natural convection in a parallelogrammic enclosure with heating and cooling two inclined sidewalls for IA=45 ° Pr=6.8, Ra=10 <sup>4</sup> , 10 <sup>5</sup> , 10 <sup>6</sup> .....	185
5.64	Isotherms for natural convection in a parallelogrammic enclosure with heating and cooling two inclined sidewalls for IA=45 ° Pr=20, Ra=10 <sup>4</sup> , 10 <sup>5</sup> , 10 <sup>6</sup> .....	186
5.65	Isotherms for natural convection in a parallelogrammic enclosure with	

heating and cooling two inclined sidewalls for $\text{IA}=45^\circ \text{ Pr}=100$ , $\text{Ra}=10^4, 10^5, 10^6$ .....	187
5.66 Isotherms for natural convection in a parallelogrammic enclosure with heating and cooling two inclined sidewalls for $\text{IA}=45^\circ \text{ Pr}=1000$ , $\text{Ra}=10^4, 10^5, 10^6$ .....	188
5.67 Velocity vectors for $\text{Ra}=10^6, \text{Pr}=6.58, 20, 100, 1000$ .....	189
5.68 Vertical velocity profiles near central line along Y for different grids and $\text{Ra}=2.55*10^6, \text{Pr}=6.58$ .....	192
5.69 Vertical velocity profiles near central line along Y for different grids and $\text{Ra}=2.92*10^7, \text{Pr}=6.58$ .....	193
5.70 Comparison of vertical velocity component profiles between numerical and experimental results near central line along Y direction for natural convection in a parallelogrammic enclosure with heating and cooling two inclined sidewalls for $\text{Ra}=2.92*10^7$ , $\text{Pr}=6.58$ .....	195
5.71 Comparison of vertical velocity component profiles between numerical and experimental results near central line along Y direction for natural convection in a parallelogrammic enclosure with heating and cooling two inclined sidewalls for $\text{Ra}=2.55*10^6$ , $\text{Pr}=6.58$ .....	196
5.72 Comparison of vertical velocity component profiles between numerical and experimental results near central line along Y direction for natural convection in a parallelogrammic enclosure with heating and cooling two inclined sidewalls for $\text{Ra}=3.2*10^5$ , $\text{Pr}=3300$ .....	197

5.73	Comparison of vertical velocity component profiles between numerical and experimental results near central line along Y direction for natural convection in a parallelogrammic enclosure with heating and cooling two inclined sidewalls for $Ra=4.3*10^4$ , $Pr=3300$ .....	198
5.74	Velocity fields from experimental and numerical results for natural convection in a parallelogrammic enclosure with heating and cooling two inclined sidewalls for $Ra=2.92*10^7$ , $Pr=6.58$ .....	202
5.75	Velocity fields from experimental and numerical results for natural convection in a parallelogrammic enclosure with heating and cooling two inclined sidewalls for $Ra=2.55*10^6$ , $Pr=6.58$ .....	203
5.76	Velocity fields from experimental and numerical results for natural convection in a parallelogrammic enclosure with heating and cooling two inclined sidewalls for $Ra=3.2*10^5$ , $Pr=3300$ .....	204
5.77	Velocity fields from experimental and numerical results for natural convection in a parallelogrammic enclosure with heating and cooling two inclined sidewalls for $Ra=4.3*10^4$ , $Pr=3300$ .....	205

# List of Tables

5.1	Comparison of Nusselt numbers for Rayleigh-Bénard convection . . . . .	101
5.2	Nusselt numbers in the steady state for different initial conditions for Rayleigh-Bénard convection . . . . .	110
5.3	Maximum vertical velocities and their locations for different heating sections and Rayleigh numbers . . . . .	119
5.4	Comparison of Nusselt numbers for natural convection in a rectangular enclosure between current and De Vahl Davis's . . . . .	131
5.5	Nusselt numbers for natural convection in a rectangular enclosure from Hortmann et al. . . . .	131
5.6	Ratio of boundary layer thickness between numerical and scaling . . . . .	172
5.7	Nusselt numbers for natural convection in a parallelogrammic enclosure with two inclined sidewalls heated and cooled for different Rayleigh numbers and inclination angles . . . . .	181
5.8	Nusselt numbers for natural convection in a parallelogrammic enclosure with two inclined sidewalls heated and cooled for different Prandtl number and Rayleigh number for inclination angle of 45°	184

# **Chapter 1**

## **Introduction**

### **1.1 Literature Survey**

We begin by reviewing the development of studies on natural heat convection. Fundamental to this discussion are two important dimensionless parameters: these are Prandtl number and Rayleigh number which are defined as

$$Pr = \frac{\mu}{\kappa\rho} \quad \text{and} \quad Ra = \frac{g\alpha\rho\Delta T d^3}{\kappa\mu}$$

where  $g$  is the acceleration due to gravity,  $d$  and  $\Delta T$  are the representative length and temperature difference, and  $\mu$ ,  $\kappa$ ,  $\alpha$ , and  $\rho$  are the dynamic viscosity, thermal diffusivity, coefficient of thermal expansion, and density, respectively. The Prandtl number is the ratio of the momentum diffusivity to the thermal diffusivity. The Rayleigh number is a parameter representative of the strength of the buoyancy force.

### **1.1.1 Natural Convection in an Enclosure**

In the following text, we review the past work and recent developments of studies on natural convection in enclosures. The references listed here provide broad information directly relevant to the current study and are a guide for future research work by the method described in the current study.

Natural convection arises because of a density variation due to the presence of a temperature gradient, caused by heat or mass transfer processes, in a body force field, such as gravitation. Interest in natural convection arises from a multiplicity of applications in the atmosphere, lakes, oceans, the Earth's mantle and core, and in many areas of engineering applications such as solar collectors, double window systems and electronic device cooling. Natural convection flows in enclosures have been a heavily studied research topic in recent years and significant advances have been made recently in understanding of the physical processes involved. With the development of numerical methods, many of the problems of natural convection in an enclosure could be analysed. Some general reviews of research on natural convection in enclosures have been given by Ostrach (1972), Catton (1978), Ostrach (1982) and Ostrach (1988).

## **Natural Convection in a Rectangular Enclosure**

Armfield and Patterson (1991) conducted direct simulation of unsteady natural convective flow in a square enclosure with constant temperature boundary conditions on sidewalls using an implicit, second-order, time-accurate, finite volume scheme. Their results predict the occurrence of an internal wave (seiche) on the enclosure scale, the presence of waves in the vertical thermal boundary layer that travel from the walls into horizontal intrusions formed on the horizontal boundaries, and a region of strong divergence at the upstream end of the intrusions. Kazmierczak and Chinoda (1992) conducted research on buoyancy driven flow in an enclosure with time periodic boundary conditions and obtained the transient periodic solutions in time. The effects of an oscillating surface temperature on fluid flow and heat transfer through the enclosure were illustrated by their analysis of their results. Ivey (1984) studied transient natural convection in an enclosure experimentally. In his laboratory experiments, the existence of regular enclosure scale internal waves suggested by previous numerical work by Patterson and Imberger (1980) was not found.

Patterson and Imberger (1980) solved the problem of transient natural

convection in a rectangular cavity. Their results indicate that flow under side wall heating changes from conduction dominated to convection dominated for Rayleigh number beyond the value of 1 and approaches a critical Rayleigh number  $Ra_c = \max(\text{Pr}^2, A^{-1/2})$  where  $A$  is the aspect ratio of the cavity. Lage and Bejan (1993) conducted a numerical and theoretical investigation of natural convection in a two-dimensional square enclosure with one side cold and isothermal, and the other side heated with pulsating heat flux. The numerical experiments cover the Prandtl number range 0.01-7, and the Rayleigh number range  $10^3$  to  $10^9$ . They also predicted the critical period for natural convection resonance which means inducing maximum fluctuations in an enclosed porous medium saturated with fluid. Their prediction was based on a theoretical argument by Nield and Bejan (1992), and from such an argument the critical frequencies determined numerically can be anticipated. Markatos and Pericleous (1984) presented a computational method to study the buoyancy-driven laminar and turbulent flow and heat transfer in a square cavity with differentially heated side walls. In their study, the Rayleigh numbers were taken as ranging from  $10^3$  to  $10^{16}$ . A two-equation model of turbulence was used for Rayleigh numbers greater than  $10^6$ . The results for Rayleigh numbers up to  $10^6$  were compared with the benchmark numerical solution of de Vahl Davis (1983). The qualitative agreement of the plots of stream function, temperature and velocity maps with those

of the benchmark solution is very good. Quantitative comparison is provided by the Nusselt numbers and the maximum velocity values. The agreement is better than 1.5% over whole Ra range.

Hyun and Lee (1989) obtained numerical solutions for transient natural convection in a square cavity with different sidewall temperatures. Some oscillatory behaviour at a period comparable to that of an internal gravity wave occurs when  $\text{Pr} \geq 1$  and  $\text{Ra} \geq \text{Pr}^4$ . Transient natural convection in a cube-shaped cavity was investigated experimentally and numerically by Hiller et al. (1993). They showed the experimental and calculated vertical velocity profiles at the centre line. Comparison between experimental and numerical vertical velocity graphically estimates the difference to be less than 5%. The experiments were performed at a Rayleigh number of  $1.66 \times 10^5$  and a Prandtl number of 1109 for aqueous solution of glycerin. The onset of convection in a cube cavity was observed visually. Nicolette et al. (1985) conducted a numerical and experimental investigation into two-dimensional transient natural convection of single phase fluid inside a completely filled square enclosure with one vertical wall cooled and other three walls insulated. The numerical simulation of air and water over the range of  $10^5 < \text{Gr} (\text{Gr} = \text{Ra}/\text{Pr}) < 10^7$  was done using a fully transient semi-implicit upwind differencing scheme with a

global pressure correction. They employed a Mach-Zehnder interferometer to obtain transient temperature fields experimentally and found the difference of the results for temperature between experimentally measured and numerically predicted at less than 5%.

Lage and Bejan (1991) investigated the phenomenon of natural convection in a square enclosure numerically for Prandtl number range 0.01-10 and the Rayleigh number range  $10^2$ - $10^{11}$ . Their focus was on the detection of inertia-sustained fluctuations due to strong inertia effect in the flow field with low Prandtl number. They found that the fluctuation at the highest Rayleigh number decreases dramatically as the Prandtl number decreases. De Vahl Davis and Jones (1983) conducted a comparative study on natural convection in a square cavity to confirm the accuracy of the bench mark solution obtained by applying a extrapolation process in the finite element method. De Vahl Davis (1983) further reported the study on natural convection of air in a square cavity and provided a bench mark numerical solution. Second-order, central difference approximations were used to obtain the solutions for  $10^3 \leq Ra \leq 10^6$  with mesh refinement and extrapolation. Chen and Ko (1991) presented a numerical study for natural convection in a two-dimensional, partially divided, rectangular enclosure. They found the effect of the conductivity of

the partition plate on the heat transfer rate to be so small that it could be neglected. Correlation of the average Nusselt number in terms of a modified Rayleigh number and the opening ratio was obtained and discussed. They found that Nusselt number increases with increasing Rayleigh number and opening ratio. Lin and Nansteel (1987) studied natural convection in a differentially heated square enclosure containing water near its density maximum. In their study, the Rayleigh number in the range  $10^3 \leq Ra \leq 10^6$  and surface temperature range  $0^\circ C$  to  $20^\circ C$  were chosen. November and Nansteel (1987) studied analytically and numerically the steady natural convection in a water-filled enclosure with partial heating of the lower isothermal surface and cooling on vertical wall. They obtained asymptotic expressions for the stream function, temperature and heat transfer. Numerical results also were obtained for  $0 \leq Ra \leq 10^6$ . Kim and Viskanta (1985) considered the effect of wall heat conduction for natural convection in a rectangular enclosure formed by finite conductance walls of different void fractions both numerically and experimentally. Agreement to within 5% was reported between the measured and predicted temperature. They found that wall heat conduction reduces the average temperature difference across the cavity, partially stabilizes the flow and decreases natural convection heat transfer.

Using the Galerkin method, Catton et al. (1974) obtained the solutions to the stationary two-dimensional equations of motion governing natural convection flow of a large Prandtl number, Boussinesq fluid contained in a differentially heated, inclined, rectangular slot. Tabarrok and Lin (1977) carried out a finite element analysis of natural convection, giving several examples with varying aspect ratios and Rayleigh numbers from this finite element model. Morrison and Tran (1978) investigated the natural convection in a rectangular cavity for aspect ratio of 5 by laser-Doppler anemometry. Yin et al. (1978) experimentally investigated natural convection in an air layer contained in an enclosure and presented the Nusselt-Grashof correlations. Stevens(1982) considered a stream function-vorticity finite element solution of two-dimensional natural convection. Steady state solutions of the natural convection were obtained. Ozoe et al. (1974) performed numerical and experimental studies on two-dimensional natural convection in an inclined rectangular channel heated on one side and cooled on the other side. Han (1979) developed a computational method to solve nonlinear elliptic equations for natural convection in an enclosure. The finite difference method was used to obtain the results.

Ozoe et al. (1975) made experimental measurements for natural convection

in an inclined rectangular channel at various aspect ratios and angles. Rates of heat transfer were affected by the inclination and aspect ratio. Ozoe et al. (1977) solved the governing equations numerically for natural convection in a long, inclined rectangular channel. Flow patterns were presented. Mouri et al. (1985) modelled the natural convection in water in rectangular channels by the finite-difference method. Computed values compared favourably with previous experimental work. May (1991) numerically solved the two-dimensional natural convection problem in an inclined square enclosure containing heat sources. Two different numerical schemes were applied; the first was Alternating-Direction Implicit (ADI) technique where vorticity and stream function are used, and the second was a hybrid method using primitive variables. Inclination angles from the horizontal of 0, 15, 30 and 45 deg and  $\text{Ra}$   $10^4$  to  $1.5 \times 10^5$  were taken as parameters. Karayannidis and Tarasuk (1988) studied the natural convection inside an inclined rectangular cavity with different thermal boundary conditions at the top plate using a Mach-Zehnder interferometer. The correlation of the local heat transfer rate with varied cavity aspect ratio, Rayleigh number and angle of inclination was presented. They found that for  $\text{Ra} \leq 3 \times 10^4$  the different thermal boundary conditions with constant temperature and varied temperature along the top plate didn't affect the heat transfer rate from the cavity.

## **Natural Convection in Other Geometrical Enclosures**

For natural convection in other geometrical enclosures, a few publications have been reported. Maekawa and Tanasawa (1982) studied the natural convection in a parallelogrammic enclosure with two vertical walls using water and silicon oil. The heat transfer coefficient and flow patterns were presented. Chung and Trefethen (1982) examined natural convection in a vertical stack of inclined parallelogrammic cavities. An explicit finite difference scheme for two-dimensional flow was formulated and the stream function and vorticity equations were solved. Nusselt numbers were computed for several geometries, Prandtl number, Grashof numbers, and conductances between cavities. Seki et al. (1983) described the experimental measurements for natural convective heat transfer across a parallelogrammic enclosure with various tilt angles of upper and lower walls. The experiments covered a range of Rayleigh numbers between  $3.4 \times 10^4$  and  $8.6 \times 10^7$ , and Prandtl numbers between 0.7 and 480. A correlation was found for the Nusselt number as a function of tilt angle, Prandtl number and Rayleigh number.

Yang et al. (1988) developed a control-volume-based finite-difference formulation to study buoyant flow with non-orthogonal curvilinear co-ordinates in

parallelepiped enclosures. The results for Nusselt numbers for different inclination angles agreed with existing experimental data to within 2% . Yuncu and Yamac (1991) reported a study of natural convective heat transfer in an air-filled parallelogrammic cavity. Governing equations for the stream function and vorticity were formulated as finite difference equations and solved. The Nusselt numbers, which represent the average heat transfer coefficients, were presented. They compared their theoretical results with experimental results on average heat transfer coefficients and found that average deviations between the numerical results and experimental results were in the range 7% to 23%.

### **1.1.2 Rayleigh-Bénard Convection**

Rayleigh-Bénard Convection refers to convection caused by heating from below. It is named Rayleigh-Bénard Convection due to the first experimental and systematic work performed by Bénard (1900) and the first theoretical approach made by Rayleigh (1916). Rayleigh-Bénard Convection is an important convective heat transfer phenomenon which occurs in many physical processes and as such is a fundamental instability problem. The linear theories of the instability problem have been discussed extensively by Chandrasekhar (1960). Koschmieder (1993) describes

the recent research on the problems of Rayleigh-Bénard convection. Linear theory describing the onset of instability is practically complete while nonlinear problems have been at the forefront of research during the past three decades. Impressive progress has been made in the theoretical and experimental investigation of the nonlinear problems.

In a paper with widely illustrated with experimental results Bergé and Dubois (1984) presented a physicist's approach to Rayleigh-Bénard convection. They examined spatial organization of the natural structures and studied the problem. They also presented the basis of the mechanism of the instability with physical reasons for the existence of a critical threshold. The dynamics of the convective pattern were discussed. Busse (1985) reviewed the studies on transition to turbulence in Rayleigh-Bénard Convection. Busse (1989) summarized the fundamentals of thermal convection for high Prandtl number.

Foster (1969) made a theoretical analysis of two-dimensional, finite-amplitude, thermal convection of a fluid which has an infinite Prandtl number. A vertical velocity disturbance is expanded in a double Fourier series which satisfies the horizontal and lateral boundary conditions. The resulting coupled sets of

nonlinear differential equations were solved numerically. It was found that for a defined Rayleigh number, the number and size of the convection cells that form depend upon the aspect ratio and initial conditions. The steady-state solutions are not unique but rather depend on the initial conditions and the numerical procedures. Moore and Weiss (1973) studied two-dimensional Rayleigh-Bénard Convection in a series of numerical experiments. Convection in water , with  $\text{Pr}=6.8$ , was systematically investigated. They solved the governing equations for vorticity and stream function by finite difference methods. Two different modes of nonlinear behaviour were distinguished. Busse and Clever (1981) presented an approximate solution for two-dimensional convection in the limit of low Prandtl number. Their results indicated that inertial convection which is due to the dominant role of inertial force becomes possible when the Rayleigh number exceeds a critical value of about  $7 \times 10^3$ . Beyond this value the velocity and temperature fields become independent of Prandtl number except in thin boundary layers. Clever and Busse (1981) obtained steady solutions for two-dimensional thermal convection in a layer heated from below at low Prandtl number. Their studies were conducted for Prandtl numbers in the range 0.001 to 0.71 and Rayleigh numbers between 1708 and 20000 in the case of rigid boundaries. Some characteristics of the convective heat transport as a function of Prandtl number in a certain range of Rayleigh numbers have been

revealed. Mitrovica and Jarvis (1987) presented a numerical study of Bénard convection between rigid horizontal boundaries. Their numerical steady solutions were obtained for a range of Rayleigh number between 5125.5 and 512550 , and infinite Prandtl number. Hansen et al. (1992) studied heat and mass transport in two-dimensional, infinite Prandtl number, incompressible thermal convection for a range of Rayleigh numbers between  $10^6$  and  $10^8$  , and two different aspect-ratio boxes between 1.8 and 10. They employed a two-dimensional finite element method in solving the time-dependent convection equations. Numerical results were presented and discussed. Kuo et al. (1992) used a finite difference method to simulate the two-dimensional Bénard convection numerically. Effects of initial conditions, end-wall boundary conditions, Rayleigh number, Prandtl number, and aspect ratio on the development of the convection process and steady solution were all investigated.

Two-dimensional Bénard convection between free bounding surfaces for various Rayleigh and Prandtl numbers was studied by Veronis (1966). The variables were expanded in a series consisting of the eigenfunctions of the stability problem and the system was truncated to take into account a limited number of terms. The amplitudes of the eigenfunctions were evaluated by numerical integration of the resulting nonlinear equations. A steady state, with the single large cell motion was

achieved for every case. Results for Nusselt number were presented for a range of Prandtl number varying between 0.01 and 100. Plows (1968) reported numerical results for two-dimensional steady laminar Bénard convection. To calculate the Nusselt number for Rayleigh numbers between 2,000 and 22,000 and for Prandtl numbers of 0.5, 1, 2, 6, and 200, an iterative numerical technique with explicit, centred-difference scheme was used. Whitehead and Parsons (1978) reported observations of Rayleigh-Bénard convection in a fluid with a Prandtl number of 8,600 and Rayleigh number between 50,000 and 760,000. They observed bimodal convection with controlled initial conditions and oscillating convection with random initial conditions. Their observations demonstrated the existence of different possible solutions at a given Rayleigh number. Kvernvold (1979) performed a numerical analysis of Rayleigh-Bénard convection with one free and one rigid boundary. The stationary two-dimensional solutions were found and their dependence on the Rayleigh number, the wave number and the Prandtl number was discussed. Chapman and Proctor (1980) studied nonlinear Rayleigh-Bénard convection between poorly conducting boundaries using an expansion technique to investigate the problem. Nonlinear analysis revealed that eventually the solution will always exhibit the largest wavelength available to it, in contradiction to the predictions of linear theory alone. Grötzsch (1982) performed direct numerical simulation of Bénard

convection in a plane channel filled with air using the finite difference method. Grötzsch (1983) further reported discussion on the spatial resolution requirements for direct numerical simulation of Rayleigh-Bénard convection.

Goldhirsch et al. (1989) investigated the problems of dynamical onset of convection, textural transitions and chaotic dynamics in a two-dimensional, rectangular Rayleigh-Bénard system using well-resolved, pseudo-spectral simulations. All boundary conditions were taken to be no-slip. Flow patterns and textural transitions were observed. Travis et al. (1990) reported a benchmark comparison of numerical methods for infinite Prandtl number, two-dimensional thermal convection. Seven different numerical methods were applied to the problem. They evaluated the performance of each method for steady state convection and time-dependent convection and the results for temperature and velocity were presented. Four benchmark problems were chosen, progressing from a simple steady-state case to one in which the convection is intrinsically time-dependent. The Rayleigh numbers for all the benchmark problems were between  $3 \times 10^4$  and  $1.3 \times 10^5$ . Comparison of the performance of each method was based on differences between the high resolution standard and the low resolution results from a particular method. The standard residuals for the four cases were less than 2% for temperature and 0.5%

for velocity.

## 1.2 Present Study

As revealed in the previous reviews studies on natural convection and especially on the Rayleigh-Bénard problem were mostly conducted using the finite difference method, the finite element method and the spectral method as numerical tools. All these methods were deduced and developed based on mathematical analysis. The appearance and development of the finite volume method lead to a relatively new numerical tool for the research on thermal convection problems. The highly physical method used to obtain a discretization is an important feature of the finite volume method. The geometric flexibility in the choice of the grid and the flexibility in defining the discrete flow variables make the finite volume method extremely popular in engineering applications. It has been said that the finite volume method is a natural one for a first computational fluid dynamics (CFD) exposition (Burmeister 1993) since it tries to combine the best from the finite element method, i.e. the geometric flexibility, with the best of the finite difference method, i.e. the flexibility in defining the discrete values of dependent variables and their associated fluxes (Dick 1996). As further commented by Dick (1996), the finite volume method

has only advantages over the finite element method and the finite difference method and thus one could ask why all of CFD is not based on the finite volume method.

There are, however, some short comings of the finite volume method. The finite volume method has difficulties in the definition of derivatives. Since the computational grid is not necessarily orthogonal and equally spaced, a definition of a derivative based on a Taylor-expansion is impossible. Also, there is no mechanism like a weak formulation, as in the finite element method, to convert higher order derivatives into lower ones. Therefore, the finite volume method is best suited for flow problems in primitive variables. In consideration of the advantages of the finite volume method, we adapt the use of this numerical technique, formulate and develop the procedures and computer programs to perform numerical simulations on several natural convection problems.

In the present study, five projects are presented: In the first project, the finite volume method is applied to Rayleigh-Bénard convection. From the foregoing, we realize that previous investigations on this problem mostly were based on other methods and the stability analysis was based on theoretical work. Taking advantage of the relative new numerical method, finite volume method, we can perform a

comparison study, investigate the stability by numerical analysis, and even conduct transient analysis of such a process which has rarely been examined in detail in early studies. Such investigation is helpful to further understand this problem. Second, natural convection in a rectangular enclosure with a partly heated bottom and one cooled sidewall is studied numerically. For this project, we can perform a comparison with previous work using a different methodology and provide presentation of flow patterns and isotherms in detailed manner. Third, natural convection in a rectangular enclosure with heating and cooling sidewalls is investigated by the finite volume method. For this project, we can gain more understanding of the transient flow structures of this kind of convection. Fourth, the finite volume method is introduced for natural convection in a parallelogrammic enclosure with two vertical walls heated and cooled and two inclined walls insulated. Fifth, the finite volume method and experimental method are used to investigate the natural convection in a parallelogrammic enclosure with two horizontal and two inclined walls. Through these new investigations of the last two projects, we can understand the physical nature of natural convection in such enclosures, find performance limits for the finite volume method and obtain important information for designing devices involving heat transfer process.

In these studies the finite volume method which has been gaining recognition and popularity recently in the computational fluid dynamics community and included in most newly published computational fluid dynamics books by Fletcher (1988), Wendt (1996) and Kröner (1997) as a numerical tool, has been chosen to solve the unsteady and nonlinear natural convection problem. All these problems are modelled as two-dimensional numerical simulations. The parallelogrammic enclosures take two orientations. One is that the parallelogrammic enclosure has two vertical walls and other two inclined, in the case of one vertical side wall heated, another side wall cooled and two other inclined walls insulated. Two is that the parallelogrammic enclosure has two horizontal parallel walls and two inclined. This parallelogrammic enclosure is heated on one inclined side wall, cooled on the opposite inclined side wall and the other two horizontal walls insulated. The computational domain is discretized with non-orthogonal grids so that no transformation is needed. The governing equations of mass, momentum and energy transport for unsteady state are discretized for every grid to obtain nonlinear algebraic equations. The algebraic equations are solved using a line-by-line, Gauss-Seidel iterative method. The Prandtl number is varied from 0.7 to 3300 and Rayleigh number is varied from  $10^4$  to  $10^6$  for different cases. The effects of Prandtl and Rayleigh numbers on heat transfer and flow patterns are elucidated and discussed.

Digital Particle Image Velocimetry (DPIV) was employed to observe the flow patterns for natural convection in a parallelogrammic enclosure with two horizontal and two inclined walls. The experimental instrumentation for flow visualization of natural convection in a parallelogrammic enclosure consists of a laser system, CCD camera, SONY monitor, and a 486 PC with image processing program from Dantec. The experimental enclosure is 25 cm long, with 5 cm x 5 cm cross section. The two side walls which are heated and cooled are made of aluminum, while the other four sides are made of plexiglass. The velocity vectors of the field were obtained and the velocity near the centre line was compared with that obtained numerically. The structure of the flow field for the whole enclosure cross section, obtained directly from the DPIV observations, is also compared with the results obtained from the finite volume method.

## **Chapter 2**

### **Basic Theory of Natural Convection**

#### **2.1 Introduction**

Thermal convection is the term applied to the heat transfer mechanism which occurs in a fluid by the mixing of one portion of the fluid with another portion due to buoyancy driven gross movements of the mass of fluid. The actual process of internal energy transfer from one fluid particle or molecule to another is still one of conduction, but the internal energy may be transported from one point in space to another by the displacement of the fluid itself. The convective heat transfer mode includes two basic mechanisms. "If the motion of the fluid arises from an external mechanical means(e.g., a fan, a blower, the wind, pump, etc. ), in which case, the process is called forced convection. If the fluid motion is caused by density differences which are created by the temperature differences existing in the fluid

mass, the process is termed natural convection or free convection." (Jaluria 1980)

The other examples of natural convection include buoyant flows due to heat emission to the atmosphere from air conditioning, heating rooms and cooling storage.

"The main difference between natural and forced convection lies in the nature of the fluid flow generation. In forced convection, the externally imposed flow is generally known, whereas in natural convection it results from an interaction of the density difference with the gravitational ( or some other body force) field, and is therefore invariably linked with and dependent on the temperature and concentration fields. Thus the motion that arises is not known at the onset and has to be determined from a consideration of the heat and mass transfer processes coupled with fluid flow mechanisms. Also, in practice, velocities in natural convection are usually much smaller than those in forced convection."(Jaluria 1980)

"The above difference between natural and forced convection makes the analysis of, as well as experimentation on, processes involving natural convection much more complicated than those involving forced convection. Therefore special techniques and methods have been devised to study the former process with a view to providing information on the flow and on the heat and mass transfer rates." (

Jaluria 1980)

“Buoyancy is of considerable importance in the environment where differences between land, or sea and air temperatures can arise due to complicated flow patterns and in enclosures such as ventilated and heated rooms or reactor configurations.” (Burmeister, 1993) The calculation of these flows in which the effect of buoyancy force becomes significant is complex. In this study, several simplified physical assumptions are made to state the governing equations. Energy exchange by thermal radiation, viscous dissipation effects and work performed by pressure forces have been neglected (Burmeister, 1993). For the mathematical formulation here, thermal conductivity and all physical properties such as the coefficient of thermal expansion and viscosity, have been taken to be constant. As described below in section 2.3, the density has been taken as constant except in the buoyancy term in the vertical component of the momentum equation, following the Boussinesq approximation. As described in section 2.5, fluid flow is assumed to be incompressible, laminar, two-dimensional and unsteady.

## 2.2 Governing Differential Equations

A convective heat transfer process is governed by the basic conservation principles of mass, momentum and energy. These equations will be only stated since their derivations can be found in any standard heat transfer textbook. For Newtonian fluids, assuming Stokes's hypothesis of a relationship between the original two (constant) coefficients of viscosity, these equations in general may be written as (Pedlosky, 1987)

$$\frac{D\rho}{Dt} = -\rho \nabla \cdot \mathbf{u} \quad (2.1)$$

$$\rho \frac{D\mathbf{u}}{Dt} = \mathbf{F} - \nabla p + \mu \nabla^2 \mathbf{u} + \frac{\mu}{3} \nabla (\nabla \cdot \mathbf{u}) \quad (2.2)$$

$$\rho c_p \frac{DT}{Dt} = \nabla \cdot (k \nabla T) + q_v + \alpha T \frac{Dp}{Dt} + \mu \Phi \quad (2.3)$$

where

$$\frac{D}{Dt} = \frac{\partial}{\partial t} + \mathbf{u} \cdot \nabla \quad (2.4)$$

is the substantial derivative. Here we define  $\mathbf{u}$  as the velocity vector,  $T$  the local temperature,  $\mathbf{F}$  the body force per unit volume,  $p$  the pressure,  $t$  the time,  $\rho$  the fluid density,  $\mu$  the dynamic viscosity,  $c_p$  the specific heat at constant pressure,  $k$  the thermal conductivity,  $\alpha$  the coefficient of thermal expansion of the fluid,  $\Phi$  the viscous dissipation and  $q_v$  the rate of energy generation per unit volume.

In natural convection flows, the body force is the only buoyancy force due to a difference in density caused by temperature variation. For a gravitational field, the body force  $\mathbf{F} = \rho \mathbf{g}$ , where  $\mathbf{g}$  is the gravitational acceleration. The flow is initiated by variation of  $\rho$ . The temperature field is linked with the flow, and all the above equations are coupled through the variation of the density  $\rho$ . Therefore, these equations must be solved simultaneously to give the distributions of the physical variables velocity, pressure and temperature, in space and time. In the analysis of the flow, some simplifying assumptions and approximations are generally made in natural convection to overcome the complexity as discussed in section 2.3.

In the momentum equation, the local pressure  $p$  may be broken down into two terms: one,  $p_0$ , due to the hydrostatic pressure, and the other,  $p_d$ , due to the motion of the fluid. The former, coupled with the body force acting on the fluid, constitutes

the driving mechanism for the flow. Thus,  $p=p_0+p_d$ , and if  $\rho_\infty$  is the density in the ambient medium, we write

$$\mathbf{F} - \nabla p = (\rho \mathbf{g} - \nabla p_0) - \nabla p_d = (\rho \mathbf{g} - \rho_\infty \mathbf{g}) - \nabla p_d = (\rho - \rho_\infty) \mathbf{g} - \nabla p_d \quad (2.5)$$

Therefore, the resulting momentum equation is written as follows:

$$\rho \frac{D\mathbf{u}}{Dt} = (\rho_\infty - \rho) \mathbf{g} - \nabla p_d + \mu \nabla^2 \mathbf{u} + \frac{\mu}{3} \nabla(\nabla \cdot \mathbf{u}) \quad (2.6)$$

## 2.3 Boussinesq Approximation in Natural Convection

The governing equations for natural convective flow are coupled partial differential equations, and are of considerable complexity. In order to simplify these equations, the Boussinesq approximations are introduced here. The origin of the simplification is due to the smallness of the coefficient of volume expansion, so in general the variations in the density are small and can be ignored such as the one for the continuity equation. But the variability of density in the buoyancy term of the equation of motion cannot be ignored. This is because the acceleration resulting

from body force can be quite large, and sometimes much larger than the acceleration due to the inertial force in the equation of motion. Accordingly, we may treat density as a constant in all terms in the equation of motion except the one in the body force. This is the Boussinesq approximation which includes two aspects. First, the density variation in the continuity equation is neglected so that the continuity equation becomes  $\nabla \cdot \mathbf{u} = 0$ . Second, the density difference, which causes the flow, is approximated as a pure temperature effect. In fact, the density difference is estimated as

$$\rho_{\infty} - \rho = \rho \alpha (T - T_{\infty}) \quad (2.7)$$

where  $T_{\infty}$  is the ambient temperature.

## 2.4 Nondimensionalization

In natural convection transport processes, nondimensionalization is important for simplifying the governing equations and for guiding experiments that are to be carried out. In the nondimensionalization process, a series of normalizing factors or scales must be introduced. For a natural convection problem in an enclosure, these scales may include a characteristic length, characteristic velocity, characteristic

temperature, characteristic temperature difference, characteristic time and characteristic pressure. While the choice of these characteristic quantities is arbitrary, the physical implication of a given choice and its effect on the resulting nondimensional equations are not well appreciated and understood, as pointed out by Ostrach (1982). "The major difficulty lies in the fact that the phenomena for natural convection in an enclosure are multiply-scaled phenomena with different scales operating in different regimes of the flow, and also possibly at different times. If exact solutions were obtainable, then any nondimensionalization would be suitable. Unfortunately, no such exact solutions exist, even for the two-dimensional enclosure problems, and only approximate solutions can be attempted. If such attempts do not take into account the different scales involved, significant physics may be lost (Ostrach 1982)." The difficulty can be illustrated by considering the great variety of characteristic velocities that can be used for the two-dimensional enclosure problem as mentioned by Ostrach (1982). In general, the governing equations may be nondimensionlized by employing the following dimensionless variables:

$$V' = \frac{u}{v_c}, \quad P = \frac{p}{\rho v_c^2}, \quad \theta = \frac{T - T_\infty}{T_w - T_\infty}, \quad \tau = \frac{t}{t_c} \quad (2.8)$$

where  $v_c$  is a characteristic velocity scale,  $t_c$  a characteristic time scale, and  $V'$ ,  $P$ ,  $\theta$ ,

$\tau$  the dimensionless velocity, pressure, temperature and time. Here , we require only that the general characteristic quantities are in the same dimensions as physical quantities. When we choose these actual characteristic quantities, we will discuss our choice.

## **2.5 Mathematical Formulation for Natural Convection Flow in a Two-Dimensional Enclosure**

In this section, the governing equations for two-dimensional natural convection and associated dimensionless parameters are given. The physical models for cases and their boundary conditions in the present study are stated, and average heat transfer coefficient represented by Nusselt number is defined.

### **2.5.1 Governing Equations for Natural Convection in Parallelogrammic and Rectangular Enclosures**

The governing dimensional equations in a Cartesian coordinate system for

two-dimensional, incompressible Boussinesq fluid in laminar motion with constant properties, no heat generation and no viscous heating can be written as :

Continuity:

$$\frac{\partial u}{\partial x} + \frac{\partial v}{\partial y} = 0 \quad (2.9)$$

Momentum:

$$\rho \frac{\partial u}{\partial t} + \rho u \frac{\partial u}{\partial x} + \rho v \frac{\partial u}{\partial y} = - \frac{\partial p}{\partial x} + \mu \left( \frac{\partial^2 u}{\partial x^2} + \frac{\partial^2 u}{\partial y^2} \right) \quad (2.10)$$

$$\rho \frac{\partial v}{\partial t} + \rho u \frac{\partial v}{\partial x} + \rho v \frac{\partial v}{\partial y} = - \frac{\partial p}{\partial y} + \rho g \alpha (T - T_0) + \mu \left( \frac{\partial^2 v}{\partial x^2} + \frac{\partial^2 v}{\partial y^2} \right) \quad (2.11)$$

Energy:

$$\frac{\partial T}{\partial t} + u \frac{\partial T}{\partial x} + v \frac{\partial T}{\partial y} = \kappa \left( \frac{\partial^2 T}{\partial x^2} + \frac{\partial^2 T}{\partial y^2} \right) \quad (2.12)$$

where  $x$  and  $y$  are the Cartesian coordinates,  $u$  and  $v$  are velocity components in the  $x$  and  $y$  directions,  $p$  the pressure due to the motion of the fluid,  $T$  the temperature,  $T_0$  the mean temperature, and  $\mu$ ,  $\alpha$ ,  $\rho$ ,  $\kappa$  the dynamic viscosity, coefficient of thermal expansion, density, and thermal diffusivity of the fluid respectively.

### 2.5.2 Dimensionless Parameters and Nondimensionalization

We have mentioned earlier that the choice of the characteristic quantities appears somewhat arbitrary. The following characteristic quantities are chosen, however, as a result of the preference by most previous studies which already demonstrated these as a proper choice with physical meaning. For example, the dimensionless time is Fourier number characterizing the transient conduction problem. The option of these characteristic quantities guarantees that a numerical solution obtained will be quicker and more economical and no large error could be generated by improper choice. We know that a numerical error can lead to a numerical solution which does not represent the real physics. Accordingly, we introduce the dimensionless variables for coordinates, velocity, temperature, time and pressure as following:

$$X = \frac{x}{L}, \quad Y = \frac{y}{L}, \quad U = \frac{uL}{\kappa}, \quad V = \frac{vL}{\kappa}, \quad T_0 = \frac{T_h + T_c}{2}, \quad \theta = \frac{T - T_0}{T_h - T_c}, \quad \tau = \frac{\kappa t}{L^2}, \quad P = \frac{\rho L^2}{\rho \kappa^2} \quad (2.13)$$

where L the characteristic length,  $T_h$ ,  $T_c$  the temperature of heating and cooling side respectively.

Substituting the dimensionless variables into the dimensional equations , we obtain the nondimensionl system equations

$$\frac{\partial U}{\partial X} + \frac{\partial V}{\partial Y} = 0 \quad (2.14)$$

$$\frac{\partial U}{\partial \tau} + U \frac{\partial U}{\partial X} + V \frac{\partial U}{\partial Y} = - \frac{\partial P}{\partial X} + Pr \left( \frac{\partial^2 U}{\partial X^2} + \frac{\partial^2 U}{\partial Y^2} \right) \quad (2.15)$$

$$\frac{\partial V}{\partial \tau} + U \frac{\partial V}{\partial X} + V \frac{\partial V}{\partial Y} = - \frac{\partial P}{\partial Y} + Ra \cdot Pr \theta + Pr \left( \frac{\partial^2 V}{\partial X^2} + \frac{\partial^2 V}{\partial Y^2} \right) \quad (2.16)$$

$$\frac{\partial \theta}{\partial \tau} + U \frac{\partial \theta}{\partial X} + V \frac{\partial \theta}{\partial Y} = \left( \frac{\partial^2 \theta}{\partial X^2} + \frac{\partial^2 \theta}{\partial Y^2} \right) \quad (2.17)$$

where dimensionless parameters  $\text{Pr}$  the Prandtl number,  $\text{Ra}$  the Rayleigh number are defined as

$$\text{Pr} = \frac{\mu}{\rho \kappa}, \quad \text{Ra} = \frac{g \rho \alpha (T_h - T_c) L^3}{\mu \kappa} \quad (2.18)$$

### **2.5.3 Physical Models for the Five Study Cases and Boundary Conditions**

From the literature survey, we note that there exists a large amount research work on natural convection in a rectangular enclosure using the finite difference and the finite element methods as well as the finite volume method. Moreover studies on natural convection in other geometric enclosures by the finite volume method have appeared in a relatively small amount research work.

The five cases considered here are:

1. Rayleigh-Bernard thermal convection in a rectangular domain which has a bottom

wall heated and upper wall cooled, and two side vertical walls with symmetric boundary condition as shown in Fig. 2.1.

Let  $n$  be a scalar of the outward unit normal vector at boundaries. The boundary conditions are

$$\begin{aligned}
 u=0, v=0, & \quad \text{on horizontal top and bottom walls} \\
 u=0, \frac{\partial v}{\partial n}=0 & \quad \text{on the vertical sides} \\
 T=T_h \text{ and } T=T_c & \quad \text{on the bottom and the top walls} \\
 \frac{\partial T}{\partial n}=0 & \quad \text{on the left and right side walls;} 
 \end{aligned} \tag{2.19}$$

$$u=0, v=0, T=T_c$$

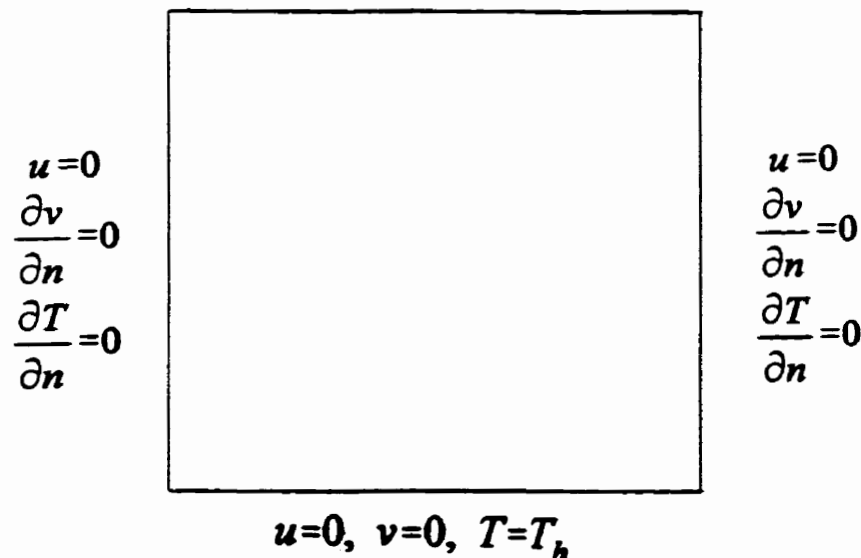


Figure 2.1 Schematic of the physical model for Rayleigh-Bérnard thermal convection in a rectangular domain.

2. Natural convection in a rectangular enclosure which has the bottom wall partly heated and one sidewall cooled, and upper and other sidewall insulated as shown in Fig. 2.2

The boundary conditions are :

$$\begin{aligned}
 u=0, v=0, & \quad \text{on all walls} \\
 T=T_h & \quad \text{on the bottom wall partly} \\
 T=T_c & \quad \text{on the right sidewall} \\
 \frac{\partial T}{\partial n}=0 & \quad \text{on the left and upper walls}
 \end{aligned} \tag{2.20}$$

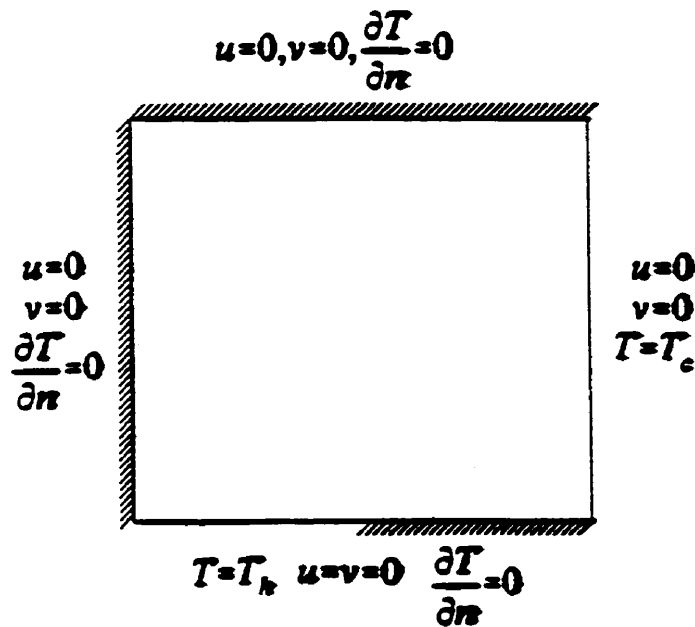


Figure 2.2 Schematic of the physical model for natural convection in a rectangular enclosure subject to a partly heated bottom and cooled right sidewall.

3. Natural convection in a rectangular enclosure with two vertical sidewalls heated and cooled and two horizontal walls insulated as shown in Fig. 2.3

The boundary conditions are:

$$\begin{aligned}
 u=0, v=0, & \quad \text{on all walls} \\
 T=T_h & \quad \text{on the vertical left wall} \\
 T=T_c & \quad \text{on the vertical right wall} \\
 \frac{\partial T}{\partial n}=0 & \quad \text{on the bottom and upper walls}
 \end{aligned} \tag{2.21}$$

$$u=0, v=0, \frac{\partial T}{\partial n}=0$$

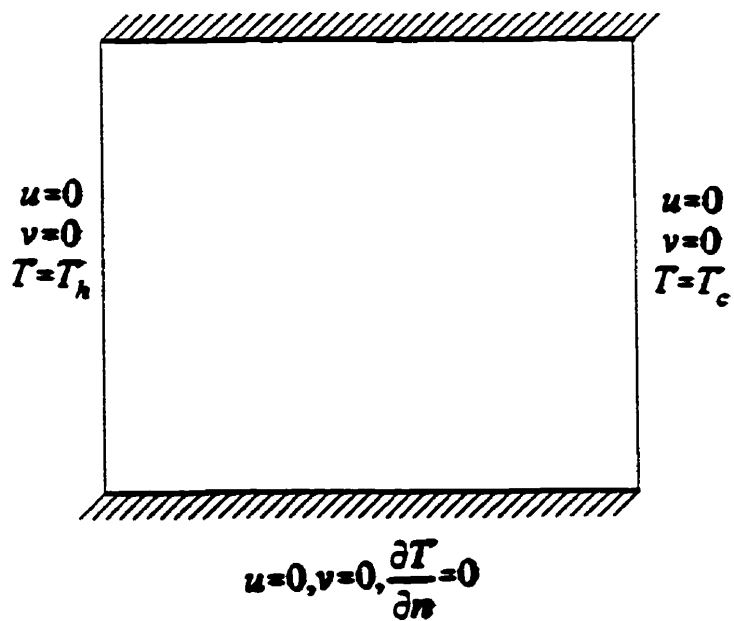


Figure 2.3 Schematic of the physical model for natural convection in a rectangular enclosure subject to heated and cooled different sidewalls.

4. Natural convection in a parallelogrammic enclosure which has two vertical walls heated and cooled and two inclined walls adiabatic as shown in Fig. 2.4

The boundary conditions are :

$$\begin{aligned}
 u=0, v=0, & \quad \text{on all walls of the enclosure} \\
 T=T_h & \quad \text{on the vertical left wall} \\
 T=T_c & \quad \text{on the vertical right wall} \\
 \frac{\partial T}{\partial n}=0 & \quad \text{on the bottom and upper inclined walls}
 \end{aligned} \tag{2.22}$$

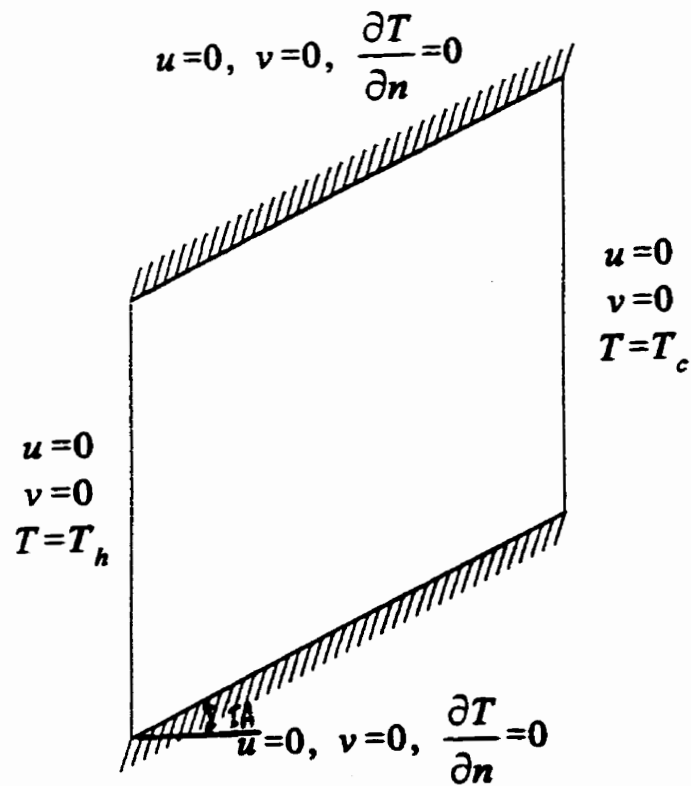


Figure 2.4 Schematic of the physical model for natural convection in a parallelogrammic enclosure with two vertical sidewalls heated and cooled.

5. Natural convection in a parallelogrammic enclosure which has two horizontal walls adiabatic and two inclined side walls heated and cooled as shown in Fig. 2.5.

The boundary conditions are :

$$\begin{aligned}
 u=0, v=0, & \quad \text{on all walls of the enclosure} \\
 T=T_h & \quad \text{on the inclined left wall} \\
 T=T_c & \quad \text{on the inclined right wall} \\
 \frac{\partial T}{\partial n}=0 & \quad \text{on the bottom and upper horizontal walls}
 \end{aligned} \tag{2.23}$$

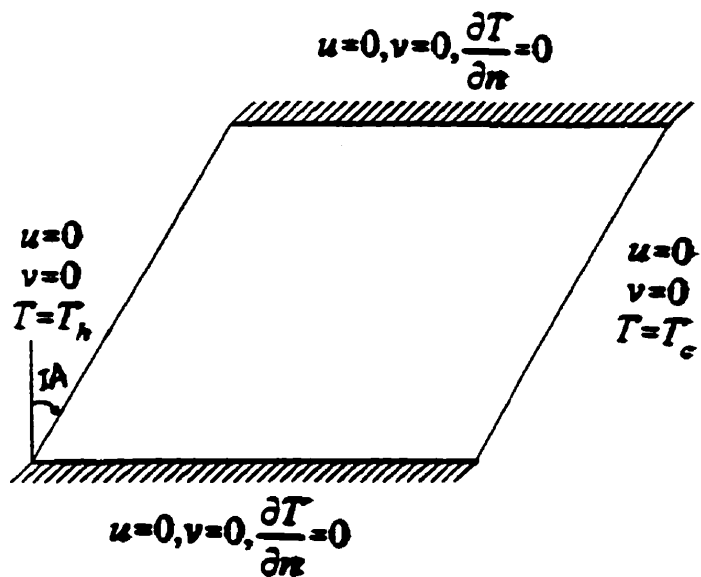


Figure 2.5 Schematic of the physical model for natural convection in a parallelogrammic enclosure with two inclined sidewalls heated and cooled.

## 2.5.4 Average Heat Transfer Coefficient

The Nusselt number is defined as

$$Nu = \frac{hL}{k} \quad (2.24)$$

where  $h$  is a heat transfer coefficient which is defined by  $h=q''/(T_h-T_c)$  through Newton's law of cooling,  $k$  is the thermal conductivity,  $L$  is the characteristic dimension of the surface. The heat flux is defined as

$$q'' = -k \frac{\partial T}{\partial n} = h(T_h - T_c) \quad (2.25)$$

and the average Nusselt number over a length  $L$  can be written  $Nu_a = 1/L \int L Nu dx$

$$Nu_a = \frac{1}{L} \int_0^L \frac{q'' x}{k(T_h - T_c)} dx \quad (2.26)$$

The Nusselt number can be also written as the form with nondimensional variables

$$Nu_a = \int_0^1 \frac{\partial \theta}{\partial n} dl \quad (2.27)$$

## **Chapter 3**

### **Numerical Method - Finite Volume Method**

In this chapter, the finite volume method will be described in detail and the procedures for mathematical formulations will be presented. Since the method was originally developed by Patankar (1980), some procedures in developing the formulation of this method are described using Patankar's wording for the purpose of completeness. The main features of the finite volume method are the satisfaction of conservation principles in a control volume and over the whole domain, and a clear physical interpretation of the discretized governing equations. The closeness of the physical principles to the final mathematical forms needed for numerical calculation makes the finite volume method a natural one for a computational heat and mass transfer treatment.

#### **3.1 The General Differential Equation**

If a dependent variable is denoted by  $\phi$ , the general differential equation is

$$\frac{\partial}{\partial t}(\rho\phi) + \nabla \cdot (\rho\mathbf{u}\phi) = \nabla \cdot (\Gamma \nabla \phi) + S^* \quad (3.1)$$

where  $\Gamma$  is the diffusion coefficient , and  $S^*$  is the source term. The quantities  $\Gamma$  and  $S^*$  are specific to a particular meaning of  $\phi$ .

This general differential equation consists of the unsteady term, the convection term, the diffusion term, and the source term. The dependent variable  $\phi$  can represent for the mass fraction of a chemical species, the enthalpy , the temperature, a velocity component, the turbulent kinetic energy, or the turbulent length scale. Therefore, the diffusion coefficient  $\Gamma$  and the source term  $S^*$  have a specific meaning for every variable.

Some diffusion fluxes can not be represented by the gradient of the relevant variable but the diffusion term does not limit the general  $\phi$  equation to diffusion processes. Those terms which cannot be fitted into the nominal diffusion term can always be considered as a part of the source term. Except for the general differential equation in a flow problem, the continuity equation is needed as a constraint. For

incompressible fluid it is

$$\nabla \cdot (\rho \mathbf{u}) = 0 \quad (3.2)$$

Even though we have considered all the variables as dimensional quantities, equations in dimensionless variables can also be regarded as possessing the general form with  $\phi$  representing the dimensionless dependent variable and with  $\Gamma$  and  $S^*$  being the dimensionless forms of the diffusion coefficient and the source term.

"The recognition that all the relevant differential equations for heat and mass transfer, fluid flow, turbulence, and related phenomena can be thought of as particular cases of the general  $\phi$  equation is an important time-saving step. As a consequence, we need only consider the numerical solution of the general equation. We can repeatedly solve the general equation for different meanings of  $\phi$  along with appropriate expressions for  $\Gamma$  and  $S^*$ , and with appropriate initial and boundary conditions. Thus, the concept of the general  $\phi$  equation enables us to formulate a general numerical method and to prepare general purpose computer programs."

(Patankar, 1980)

## 3.2 Discretization Equation

Since both parallelogrammic and rectangular enclosures are considered, we choose the general parallelogrammic control which can be a rectangular control volume. The computational domain is discretized with a parallelogrammic control volume as a similar geometric shape to the whole domain. The parallelogrammic control volume considered is shown in Fig. 3.1, where  $\zeta_e, \zeta_n, \hat{n}_e, \hat{n}_n$  are unit vector in the non-orthogonal directions of the  $\zeta, \eta$  coordinates at faces e, n. We apply integration to the Eq. (3.1) over a control volume  $\nabla$  and over the time interval  $\Delta t$ .

$$\int_t^{t+\Delta t} \iiint_{\nabla} \left( \frac{\partial}{\partial t} (\rho \phi) + \nabla \cdot (\rho u \phi) \right) d\nabla dt = \int_t^{t+\Delta t} \iiint_{\nabla} (\nabla \cdot (\nabla \Gamma \phi) + S) d\nabla dt \quad (3.3)$$

From Gauss's divergence theorem, we can write the integrations of the convection and diffusion terms on a volume  $\nabla$  as integral on surface A which bounds the volume  $\nabla$ . Let  $\hat{n}$  be the unit normal vector on A, which assumed to be positive when drawn outward with respect to the region enclosed by A. The integrations are

$$\begin{aligned} \iiint_{\nabla} \nabla \cdot (\rho u \phi) d\nabla &= \iint_A (\rho u \phi) \cdot \hat{n} dA \\ \iiint_{\nabla} \nabla \cdot (\Gamma \nabla \phi) d\nabla &= \iint_A (\Gamma \nabla \phi) \cdot \hat{n} dA \end{aligned} \quad (3.4a, b)$$

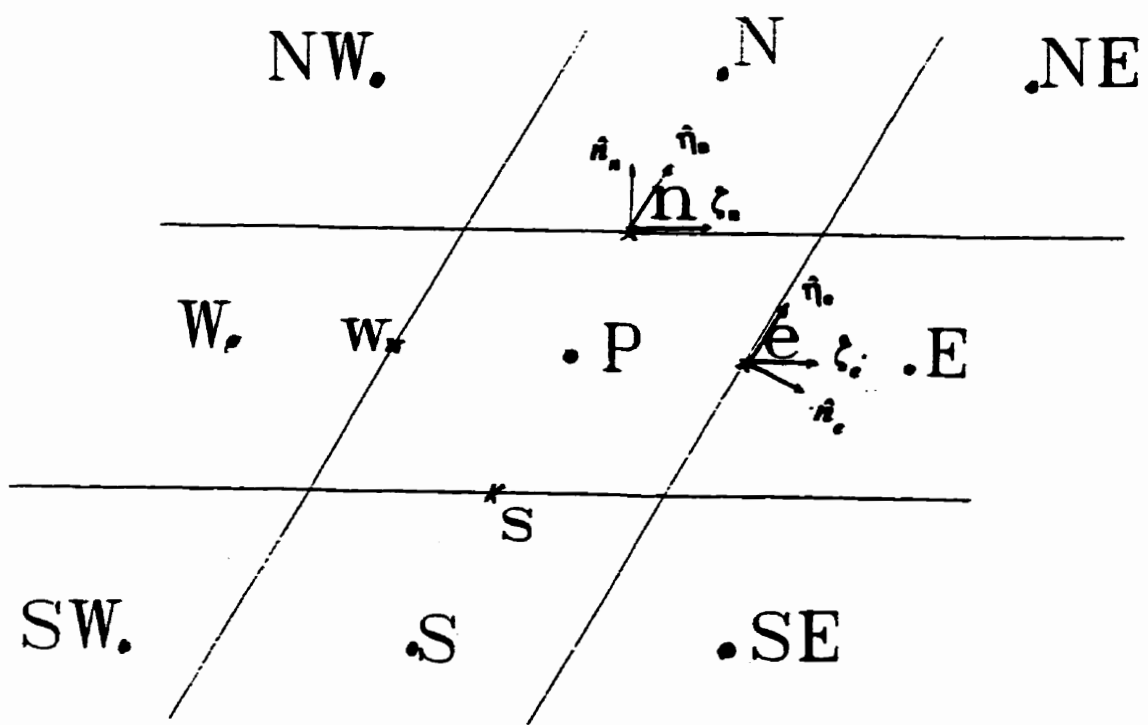


Figure 3.1 Schematic of a parallelogrammic control volume

Before we carry out integration of the general equation term by term, we first integrate the continuity equation (3.2) over the control volume by taking into account that the flow is two dimensional and obtain:

$$\begin{aligned} \iiint_V \nabla \cdot (\rho u) dV &= \iint_A \rho u \cdot \hat{n} dA = \iint_{A_e} \rho u \cdot \hat{n} dA - \iint_{A_w} \rho u \cdot \hat{n} dA \\ &\quad + \iint_{A_n} \rho u \cdot \hat{n} dA - \iint_{A_s} \rho u \cdot \hat{n} dA = F_e - F_w + F_n - F_s = 0 \end{aligned} \quad (3.5)$$

where  $F_e$ ,  $F_w$ ,  $F_n$  and  $F_s$  are mass flow rates through the faces of the control volume.

Approximating the integration by the value at midpoint, we can write

$$\begin{aligned} F_e &= \iint_{A_e} \rho u_e \cdot \hat{n}_e dA_e \approx \rho u_e \cdot \hat{n}_e A_e = \rho (\hat{u}_e \hat{n}_{xe} + \hat{v}_e \hat{n}_{ye}) A_e \\ F_w &= \iint_{A_w} \rho u_w \cdot \hat{n}_w dA_w \approx \rho u_w \cdot \hat{n}_w A_w = \rho (\hat{u}_w \hat{n}_{xw} + \hat{v}_w \hat{n}_{yw}) A_w \\ F_n &= \iint_{A_n} \rho u_n \cdot \hat{n}_n dA_n \approx \rho u_n \cdot \hat{n}_n A_n = \rho (\hat{u}_n \hat{n}_{xn} + \hat{v}_n \hat{n}_{yn}) A_n \\ F_s &= \iint_{A_s} \rho u_s \cdot \hat{n}_s dA_s \approx \rho u_s \cdot \hat{n}_s A_s = \rho (\hat{u}_s \hat{n}_{xs} + \hat{v}_s \hat{n}_{ys}) A_s \end{aligned} \quad (3.6)$$

where  $\hat{n}_e$ ,  $\hat{n}_w$ ,  $\hat{n}_n$ ,  $\hat{n}_s$  are normal unit vector at the faces,  $\hat{n}_{xe}$ ,  $\hat{n}_{xw}$ ,  $\hat{n}_{xn}$ ,  $\hat{n}_{xs}$ ,  $\hat{n}_{ye}$ ,  $\hat{n}_{yw}$ ,  $\hat{n}_{yn}$ ,  $\hat{n}_{ys}$  are projections of  $\hat{n}_e$ ,  $\hat{n}_w$ ,  $\hat{n}_n$ ,  $\hat{n}_s$  on x and y, and  $\hat{u}_e$ ,  $\hat{u}_w$ ,  $\hat{u}_n$ ,  $\hat{u}_s$ ,  $\hat{v}_e$ ,  $\hat{v}_w$ ,  $\hat{v}_n$ ,  $\hat{v}_s$  are

velocity components at faces in the x and y directions.

The Eq. (3.1) is integrated term by term over the control volume and over the time interval from  $t$  to  $t+\Delta t$  and approximations to these terms are made. The integration of the first term gives

$$\int_t^{t+\Delta t} \iiint_{V_p} \frac{\partial}{\partial t} (\rho \phi) dV dt \approx \rho \phi_p V_p - \rho \phi_p^0 V_p \quad (3.7)$$

where  $\phi_p$  represents the values at the primary point P and is assumed to be constant over the whole control volume, and  $V_p$  is the volume of the control volume which is the area of the control volume multiplied by unit thickness 1 for our two-dimensional problem. The superscript 0 denotes evaluation at the start of the time interval that starts at  $t$  and is of duration  $\Delta t$ . All other values without a superscript are to be regarded unknown at the end of the time interval  $t+\Delta t$ . The integration of the convection term generates :

$$\begin{aligned} \iint_A \rho u \phi \cdot \hat{n} dA &= \iint_{A_s} \rho u \phi \cdot \hat{n} dA - \iint_{A_e} \rho u \phi \cdot \hat{n} dA \\ &\quad + \iint_{A_n} \rho u \phi \cdot \hat{n} dA - \iint_{A_w} \rho u \phi \cdot \hat{n} dA \end{aligned} \quad (3.8)$$

Making approximation to the integration on faces, we obtain

$$\begin{aligned} & \iint_{A_e} \rho u \phi \cdot \hat{n} dA - \iint_{A_w} \rho u \phi \cdot \hat{n} dA + \iint_{A_s} \rho u \phi \cdot \hat{n} dA - \iint_{A_n} \rho u \phi \cdot \hat{n} dA \\ & \approx F_e \phi_e - F_w \phi_w + F_s \phi_s - F_n \phi_n \end{aligned} \quad (3.9)$$

To estimate the advected momentum at these faces, we express the value of  $\phi$  at the faces in terms of the value of the grid and the adjacent grid point; it follows that:

$$\begin{aligned} \phi_e &= (0.5 + sign(F_e) \alpha_e) \phi_p + (0.5 - sign(F_e) \alpha_e) \phi_E \\ \phi_w &= (0.5 + sign(F_w) \alpha_w) \phi_p + (0.5 - sign(F_w) \alpha_w) \phi_P \\ \phi_n &= (0.5 + sign(F_n) \alpha_n) \phi_p + (0.5 - sign(F_n) \alpha_n) \phi_N \\ \phi_s &= (0.5 + sign(F_s) \alpha_s) \phi_p + (0.5 - sign(F_s) \alpha_s) \phi_P \end{aligned} \quad (3.10)$$

where  $\alpha_e, \alpha_w, \alpha_n, \alpha_s$  are weighting factors,  $sign(F) = 1$ , or  $-1$  for positive and negative  $F$ . The weighting factors will be given later after we discretize the diffusion term. The diffusion term can be approximated as:

$$\begin{aligned} \iint_A \nabla \Gamma \phi dA &= \iint_{A_e} \Gamma \nabla \phi \cdot \hat{n}_e + \iint_{A_w} \Gamma \nabla \phi \cdot \hat{n}_w + \iint_{A_s} \Gamma \nabla \phi \cdot \hat{n}_s + \iint_{A_n} \Gamma \nabla \phi \cdot \hat{n}_n \\ &\approx \Gamma A_e \frac{\partial \phi}{\partial \hat{n}}|_e - \Gamma A_w \frac{\partial \phi}{\partial \hat{n}}|_w + \Gamma A_n \frac{\partial \phi}{\partial \hat{n}}|_n - \Gamma A_s \frac{\partial \phi}{\partial \hat{n}}|_s \end{aligned} \quad (3.11)$$

where  $\Gamma$  is assumed constant for every control volume.

Considering the vector relationships, these diffusion flux at faces can be expressed as

$$\begin{aligned}
 \frac{\partial \phi}{\partial n}|_e &= (\frac{\partial \phi}{\partial \zeta}|_e - \zeta_e \cdot \eta_e \frac{\partial \phi}{\partial \eta}|_e) / \zeta_e \cdot \hat{n}_e \\
 \frac{\partial \phi}{\partial n}|_w &= (\frac{\partial \phi}{\partial \zeta}|_w - \zeta_w \cdot \eta_w \frac{\partial \phi}{\partial \eta}|_w) / \zeta_w \cdot \hat{n}_w \\
 \frac{\partial \phi}{\partial n}|_n &= (\frac{\partial \phi}{\partial \eta}|_n - \zeta_n \cdot \eta_n \frac{\partial \phi}{\partial \zeta}|_n) / \hat{n}_n \cdot \eta_n \\
 \frac{\partial \phi}{\partial n}|_s &= (\frac{\partial \phi}{\partial \eta}|_s - \zeta_s \cdot \eta_s \frac{\partial \phi}{\partial \zeta}|_s) / \hat{n}_s \cdot \eta_s
 \end{aligned} \tag{3.12}$$

where  $\zeta, \eta$  are coordinates in non-orthogonal directions,  $\zeta_e, \zeta_w, \zeta_n, \zeta_s, \eta_e, \eta_w, \eta_n, \eta_s$

are unit vector in the  $\zeta, \eta$  directions at faces e, w, n, s. The  $\partial \phi / \partial \zeta|_e, \partial \phi / \partial \zeta|_w, \partial \phi / \partial \zeta|_n, \partial \phi / \partial \zeta|_s, \partial \phi / \partial \eta|_e, \partial \phi / \partial \eta|_w, \partial \phi / \partial \eta|_n, \partial \phi / \partial \eta|_s$  are approximated as follows:

$$\begin{aligned}
 \frac{\partial \phi}{\partial \zeta}|_e &= \beta_e \frac{(\phi_E - \phi_P)}{\Delta \zeta}, & \frac{\partial \phi}{\partial \eta}|_e &= \beta_e \frac{(\phi_{ne} - \phi_{se})}{\Delta \eta} \\
 \frac{\partial \phi}{\partial \zeta}|_w &= \beta_w \frac{(\phi_P - \phi_W)}{\Delta \zeta}, & \frac{\partial \phi}{\partial \eta}|_w &= \beta_w \frac{(\phi_{nw} - \phi_{sw})}{\Delta \eta} \\
 \frac{\partial \phi}{\partial \eta}|_n &= \beta_n \frac{(\phi_N - \phi_P)}{\Delta \eta}, & \frac{\partial \phi}{\partial \zeta}|_n &= \beta_n \frac{(\phi_{ne} - \phi_{nw})}{\Delta \zeta} \\
 \frac{\partial \phi}{\partial \eta}|_s &= \beta_s \frac{(\phi_P - \phi_S)}{\Delta \eta}, & \frac{\partial \phi}{\partial \zeta}|_s &= \beta_s \frac{(\phi_{se} - \phi_{sw})}{\Delta \zeta}
 \end{aligned} \tag{3.13}$$

where  $\beta$  is weighting factor, and  $\phi_{ne}, \phi_{se}, \phi_{nw}, \phi_{sw}$  are approximated as follows:

$$\begin{aligned}
 \phi_{ne} &= (\phi_N + \phi_{NE} + \phi_P + \phi_E)/4 \\
 \phi_{se} &= (\phi_P + \phi_E + \phi_S + \phi_{SE})/4 \\
 \phi_{nw} &= (\phi_N + \phi_{NW} + \phi_P + \phi_W)/4 \\
 \phi_{sw} &= (\phi_P + \phi_W + \phi_S + \phi_{SW})/4
 \end{aligned} \tag{3.14}$$

The source term integration over a control volume is

$$\iiint_{V_p} S \cdot d\mathbf{v} = S \cdot \nabla_p \tag{3.15}$$

We collect all these terms into Eq. 3.3 and rearrange to get the discretized equation as:

$$a_p \phi_p = a_E \phi_E + a_W \phi_W + a_N \phi_N + a_S \phi_S + b \tag{3.16}$$

where

$$\begin{aligned}
a_E &= F_e(0.5 - sign(F_e)\alpha_e) + \frac{\Gamma A_e \beta_e}{\Delta \zeta} \frac{1}{\zeta_e \cdot \hat{n}_e} \\
a_W &= -F_w(0.5 + sign(F_w)\alpha_w) + \frac{\Gamma A_w \beta_w}{\Delta \zeta} \frac{1}{\zeta_w \cdot \hat{n}_w} \\
a_N &= F_n(0.5 - sign(F_n)\alpha_n) + \frac{\Gamma A_n \beta_n}{\Delta \eta} \frac{1}{\hat{n}_n \cdot \hat{\eta}_n} \\
a_S &= -F_s(0.5 + sign(F_s)\alpha_s) + \frac{\Gamma A_s \beta_s}{\Delta \eta} \frac{1}{\hat{n}_s \cdot \hat{\eta}_s} \\
a_P &= \frac{\rho \nabla_p}{\Delta t} + a_E + a_W + a_N + a_S + F_e - F_w + F_n - F_s \\
&= \frac{\rho \phi_p \nabla_p}{\Delta t} + a_E + a_W + a_N + a_S \\
b &= \frac{\rho \phi_p^0 \nabla}{\Delta t} - \Gamma A_e \beta_e \frac{\zeta_e \cdot \hat{\eta}_e \partial \phi}{\zeta_e \cdot \hat{n}_e \partial \eta} \Big|_e + \Gamma A_w \beta_w \frac{\zeta_w \cdot \hat{\eta}_w \partial \phi}{\zeta_w \cdot \hat{n}_w \partial \eta} \Big|_w \\
&\quad - \Gamma A_n \beta_n \frac{\zeta_n \cdot \hat{\eta}_n \partial \phi}{\zeta_n \cdot \hat{n}_n \partial \eta} \Big|_n + \Gamma A_s \beta_s \frac{\zeta_s \cdot \hat{\eta}_s \partial \phi}{\zeta_s \cdot \hat{n}_s \partial \eta} \Big|_s + S \cdot \Delta \nabla_p
\end{aligned} \tag{3.17}$$

The weighting factors  $\alpha$  and  $\beta$  are defined here as:

$$\begin{aligned}
\alpha &= \frac{Pe^2}{10 + 2 * Pe^2} \\
\beta &= \frac{1 + 0.005 * Pe^2}{1 + 0.05 * Pe^2}
\end{aligned} \tag{3.18}$$

where  $Pe$  is Peclet number defined by  $Pe = \rho u L / \Gamma$ . It is seen that  $Pe$  is the ratio of the strength of convection and diffusion. The weighting factors have no real physical

meaning but serve as coefficients to make the discretization more accurate (Patankar 1980). Such choice is based on the power law scheme proposed by Raithby et al. (1986) and is used to achieve computing efficiency (Patankar(1980), Burmeister(1993)).

In this section, we have completed the construction of the general discretization equation for the dependent variable  $\phi$ . Although other approximations to the convective term are possible, our formulation should ensure physically realistic behaviour and thus holds the key to successful computation of fluid flow. The flow field must now be calculated and in what follows we will formulate the procedures for calculation of this field.

### **3.3 Calculation of the Flow Field**

In the last section, we formulated the procedure for solving the general differential equation for  $\phi$  in the presence of a given flow field. However, in most circumstances, we must calculate the local velocity components from the appropriate governing equations. The velocity components are governed by the momentum equations, which are particular cases of the general differential equations for  $\phi$  (with

$\phi=u,v$ ,  $\Gamma=\mu$ , and so on). Thus, we already have developed the method for solving the momentum equations to get the velocity field.

There are however, a few difficulties found when we come to solve the momentum equations. The nonlinearity of the momentum equations is one difficulty which can be handled by iteration. The convection coefficient  $\rho u$ ,  $\rho v$  being a function of the dependent variable  $u$  and  $v$  of the momentum equation can be treated by initially guessing, and then iterating to arrive at the converged values. Another difficulty is the unknown pressure field. Although the pressure gradient is a part of the source term in the momentum equation, we don't have an obvious equation for computing pressure. If we know the pressure field, we can solve the momentum equations without particular difficulty. It seems rather difficult to get the pressure field. Patankar(1980) described the nature of pressure in this problem. "The pressure field is indirectly specified via the continuity equation. When the correct pressure field is substituted in to the momentum equations, the resulting velocity field satisfies the continuity equation. This indirect specification, however, is not very useful for our purpose unless we attempt a direct solution of the whole set of the discretization equations resulting from the momentum and continuity equations. Since we have preferred iterative methods of solving the discretization equation even for a single

dependent variable, the direct solution for the entire set of velocity components and pressure seems out of the question."

There are several methods which can overcome the above difficulty by eliminating pressure from the governing equations. The pressure in two momentum equations can be eliminated by cross differentiation to get a vorticity transport in two dimensions. In consideration with the definition of a stream function for steady two-dimensional situations, we can obtain the well-known stream function-vorticity method. The stream function-vorticity method has some attractive features. We don't worry about the difficulty in the determination of the pressure. The three governing equations have been transformed into two equations in the stream function-vorticity form. We can simply define some boundary conditions for vorticity to vanish when an external irrotational flow condition is adjacent to the calculation domain. But some disadvantages exist as mentioned by Patankar(1980). "The value of vorticity at a wall is difficult to specify and is often the cause of trouble in getting a converged solution. The pressure, which is often desired and is as an intermediate outcome required for the calculation of density and other fluid properties, has been eliminated. Then, the effort of extracting pressure from vorticity offsets the computational savings obtained otherwise. But the major shortcoming of the method is that it

cannot easily be extended to three-dimensional situations, for which a stream function does not exist." Thus the method to solve the equations directly with primitive variables, namely the velocity components and pressure, has been sought, developed and improved. The next procedures present the conversion of the indirect information in the continuity equation into a direct algorithm for calculation of pressure and some difficulties which arise will be discussed.

### **3.3.1 Discretization of the Momentum Equations**

In the momentum equation,  $\phi$  stands for the relevant velocity component, and  $\Gamma$  and  $S^*$  are to be given their appropriate meanings. The adoption of the staggered grid does make the discretized momentum equations somewhat different from the discretization equations for the other  $\phi$ 's that are calculated for the main grid points. But this difference is one of detail and not of essence. It arises from the use of staggered control volumes for the momentum equations. The use of the staggered grid prevents the oscillatory solutions, particularly for  $p$ , that can occur when centred differences are used to discretize derivatives on a non-staggered grid. Harlow and Welch (1965) and Arakawa (1966) first proposed and used such a scheme to prevent nonlinear instability. The conservative property is the main feature for the difference

representation.

Since we have obtained the discretization for the general equation, the only term which we need to consider here is pressure gradient:

$$\begin{aligned}\iiint_V -\frac{\partial p}{\partial x} dV &\approx \frac{\partial p}{\partial x}|_P V_P \\ \iiint_V -\frac{\partial p}{\partial y} dV &\approx \frac{\partial p}{\partial y}|_P V_P\end{aligned}\quad (3.19)$$

By considering the relationship:

$$\begin{aligned}\nabla p &= \frac{\partial p}{\partial x} \hat{i} + \frac{\partial p}{\partial y} \hat{j} \\ \frac{\partial p}{\partial \zeta} &= \nabla p \cdot \hat{\zeta} = \frac{\partial p}{\partial x} \hat{i} \cdot \hat{\zeta} + \frac{\partial p}{\partial y} \hat{j} \cdot \hat{\zeta} \\ \frac{\partial p}{\partial \eta} &= \nabla p \cdot \hat{\eta} = \frac{\partial p}{\partial x} \hat{i} \cdot \hat{\eta} + \frac{\partial p}{\partial y} \hat{j} \cdot \hat{\eta}\end{aligned}\quad (3.20)$$

We can obtain:

$$\begin{aligned}\hat{\zeta} &= \zeta_x \hat{i} + \zeta_y \hat{j} \\ \hat{\eta} &= \eta_x \hat{i} + \eta_y \hat{j} \\ \frac{\partial p}{\partial x} &= \frac{\frac{\partial p}{\partial \zeta} \eta_y - \frac{\partial p}{\partial \eta} \zeta_y}{\zeta_x \eta_y - \eta_x \zeta_y} \\ \frac{\partial p}{\partial y} &= \frac{\frac{\partial p}{\partial \eta} \zeta_x - \frac{\partial p}{\partial \zeta} \eta_x}{\zeta_x \eta_y - \eta_x \zeta_y}\end{aligned}\quad (3.21)$$

We can also write them as:

$$\frac{\partial p}{\partial x} \Big|_P = \frac{\frac{p_e - p_w}{\Delta \zeta} \eta_y - \frac{p_n - p_s}{\Delta \eta} \zeta_y}{\zeta_x \eta_y - \eta_x \zeta_y} \quad (3.22)$$

$$\frac{\partial p}{\partial y} \Big|_P = \frac{\frac{p_n - p_s}{\Delta \eta} \zeta_x - \frac{p_e - p_w}{\Delta \zeta} \eta_x}{\zeta_x \eta_y - \eta_x \zeta_y}$$

The  $p_e$ ,  $p_w$ ,  $p_n$  and  $p_s$  are estimated as:

$$p_e = \frac{1}{2} p_E + \frac{1}{2} p_P$$

$$p_w = \frac{1}{2} p_W + \frac{1}{2} p_P \quad (3.23)$$

$$p_n = \frac{1}{2} p_N + \frac{1}{2} p_P$$

$$p_s = \frac{1}{2} p_S + \frac{1}{2} p_P$$

We can write the discretization momentum equations for P-control volume as:

$$\begin{aligned}
\alpha_P^u u_P &= \alpha_E^u u_E + \alpha_W^u u_W + \alpha_N^u u_N + \alpha_S^u u_S + b_P^u - \nabla_P \frac{\partial p}{\partial x} \Big|_P \\
\alpha_P^v v_P &= \alpha_E^v v_E + \alpha_W^v v_W + \alpha_N^v v_N + \alpha_S^v v_S + b_P^v - \nabla_P \frac{\partial p}{\partial y} \Big|_P
\end{aligned} \tag{3.24}$$

to estimate convecting velocities

$$\begin{aligned}
\hat{u}_e &= \frac{u_P + u_E}{2} - \hat{d}_e^u \left( \frac{\partial p}{\partial x} \Big|_e - \frac{1}{2} \left( \frac{\partial p}{\partial x} \Big|_P + \frac{\partial p}{\partial x} \Big|_E \right) \right) + \frac{\rho \hat{d}_e^u}{\Delta t} \left( \hat{u}_e^0 - \frac{1}{2} (u_P^0 + u_E^0) \right) \\
\hat{u}_n &= \frac{u_P + u_N}{2} - \hat{d}_n^u \left( \frac{\partial p}{\partial x} \Big|_n - \frac{1}{2} \left( \frac{\partial p}{\partial x} \Big|_P + \frac{\partial p}{\partial x} \Big|_N \right) \right) + \frac{\rho \hat{d}_n^u}{\Delta t} \left( \hat{u}_n^0 - \frac{1}{2} (u_P^0 + u_N^0) \right) \\
\hat{v}_e &= \frac{v_P + v_E}{2} - \hat{d}_e^v \left( \frac{\partial p}{\partial y} \Big|_e - \frac{1}{2} \left( \frac{\partial p}{\partial y} \Big|_P + \frac{\partial p}{\partial y} \Big|_E \right) \right) + \frac{\rho \hat{d}_e^v}{\Delta t} \left( \hat{v}_e^0 - \frac{1}{2} (v_P^0 + v_E^0) \right) \\
\hat{v}_n &= \frac{v_P + v_N}{2} - \hat{d}_n^v \left( \frac{\partial p}{\partial y} \Big|_n - \frac{1}{2} \left( \frac{\partial p}{\partial y} \Big|_P + \frac{\partial p}{\partial y} \Big|_N \right) \right) + \frac{\rho \hat{d}_n^v}{\Delta t} \left( \hat{v}_n^0 - \frac{1}{2} (v_P^0 + v_N^0) \right)
\end{aligned} \tag{3.25}$$

where  $d_e^u, d_n^u, d_e^v, d_n^v$  are

$$\begin{aligned}
 \hat{d}_e^u &= \frac{0.5\left(\frac{\nabla}{\Sigma a_{nb}^u}\right)|_P + 0.5\left(\frac{\nabla}{\Sigma a_{nb}^u}\right)|_E}{1 + 0.5\frac{\rho}{\Delta t}\left(\frac{\nabla}{\Sigma a_{nb}^u}\right)|_P + 0.5\frac{\rho}{\Delta t}\left(\frac{\nabla}{\Sigma a_{nb}^u}\right)|_E} \\
 \hat{d}_e^v &= \frac{0.5\left(\frac{\nabla}{\Sigma a_{nb}^v}\right)|_P + 0.5\left(\frac{\nabla}{\Sigma a_{nb}^v}\right)|_E}{1 + 0.5\frac{\rho}{\Delta t}\left(\frac{\nabla}{\Sigma a_{nb}^v}\right)|_P + 0.5\frac{\rho}{\Delta t}\left(\frac{\nabla}{\Sigma a_{nb}^v}\right)|_E} \\
 \hat{d}_n^u &= \frac{0.5\left(\frac{\nabla}{\Sigma a_{nb}^u}\right)|_P + 0.5\left(\frac{\nabla}{\Sigma a_{nb}^u}\right)|_N}{1 + 0.5\frac{\rho}{\Delta t}\left(\frac{\nabla}{\Sigma a_{nb}^u}\right)|_P + 0.5\frac{\rho}{\Delta t}\left(\frac{\nabla}{\Sigma a_{nb}^u}\right)|_N} \\
 \hat{d}_n^v &= \frac{0.5\left(\frac{\nabla}{\Sigma a_{nb}^v}\right)|_P + 0.5\left(\frac{\nabla}{\Sigma a_{nb}^v}\right)|_N}{1 + 0.5\frac{\rho}{\Delta t}\left(\frac{\nabla}{\Sigma a_{nb}^v}\right)|_P + 0.5\frac{\rho}{\Delta t}\left(\frac{\nabla}{\Sigma a_{nb}^v}\right)|_N}
 \end{aligned} \tag{3.26}$$

### 3.3.2 The Pressure-Correction Equation

If we know or can estimate the pressure, we can solve the momentum equations. If an estimated pressure field is used, the resulting velocity field will not satisfy the continuity equation. The velocity field based on the estimated pressure

field  $p^*$  are represented by  $u^*, v^*$ . Patankar(1980) described the issue. "This starred velocity field will result from the solution of the following discretization equations:

$$\begin{aligned}\alpha_e u_e^* &= \sum \alpha_{nb} u_{nb}^* + b^* + (p_p^* - p_E^*) A_e \\ \alpha_n v_n^* &= \sum \alpha_{nb} v_{nb}^* + b^* + (p_p^* - p_N^*) A_n\end{aligned}\quad (3.27)$$

where  $A_e, A_n$  are general representations derived from Equations. 3.13-3.14 and 3.20-3.24. The guessed pressure  $p^*$  should be improved such that the resulting starred velocity field will progressively get closer to satisfying the continuity equation. Let us propose that the correct pressure  $p$  is obtained from

$$p = p^* + p' \quad (3.28)$$

where  $p'$  will be called the pressure correction. Next, we need to know how the velocity components respond to this change in pressure. The corresponding velocity corrections  $u', v'$  can be introduced in a similar manner: "

$$u = u^* + u' \quad v = v^* + v' \quad (3.29)$$

The corresponding equations for variables  $u', v'$  are :

$$\begin{aligned} \alpha_p^u u'_p &= \sum \alpha_{nb} u'_{nb} - \nabla \frac{\partial p'}{\partial x} \Big|_p \\ \alpha_p^v v'_p &= \sum \alpha_{nb} v'_{nb} - \nabla \frac{\partial p'}{\partial y} \Big|_p \end{aligned} \quad (3.30)$$

However to make the link between  $u'$ ,  $v'$  and  $p'$  as explicit as possible , the  $u'$ ,  $v'$  approximate as

$$\begin{aligned} \hat{u}'_e &= \frac{u'_p + u'_E}{2} - \hat{d}_e^u \left( \frac{\partial p'}{\partial x} \Big|_e - \frac{1}{2} \left( \frac{\partial p'}{\partial x} \Big|_p + \frac{\partial p'}{\partial x} \Big|_E \right) \right) \\ \hat{u}'_n &= \frac{u'_p + u'_N}{2} - \hat{d}_n^u \left( \frac{\partial p'}{\partial x} \Big|_n - \frac{1}{2} \left( \frac{\partial p'}{\partial x} \Big|_p + \frac{\partial p'}{\partial x} \Big|_N \right) \right) \\ \hat{v}'_e &= \frac{v'_p + v'_E}{2} - \hat{d}_e^v \left( \frac{\partial p'}{\partial y} \Big|_e - \frac{1}{2} \left( \frac{\partial p'}{\partial y} \Big|_p + \frac{\partial p'}{\partial y} \Big|_E \right) \right) \\ \hat{v}'_n &= \frac{v'_p + v'_N}{2} - \hat{d}_n^v \left( \frac{\partial p'}{\partial y} \Big|_n - \frac{1}{2} \left( \frac{\partial p'}{\partial y} \Big|_p + \frac{\partial p'}{\partial y} \Big|_N \right) \right) \end{aligned} \quad (3.31)$$

The SIMPLEC algorithm provides the estimation as

$$\begin{aligned}
\hat{u}' &= -\hat{c}_e^u (P_E - P_P') \\
\hat{u}'_n &= -\hat{c}_n^u (P_N - P_P') \\
\hat{v}' &= -\hat{c}_e^v (P_E - P_P') \\
\hat{v}'_n &= -\hat{c}_n^v (P_N - P_P')
\end{aligned} \tag{3.32}$$

where  $\hat{c}_e^u, \hat{c}_n^u, \hat{c}_e^v, \hat{c}_n^v$  are

$$\begin{aligned}
\hat{c}_e^u &= 0.5 \left[ \left( \frac{\nabla}{a_p - \sum a_{nb}} \right) \Big|_P + \left( \frac{\nabla}{a_p - \sum a_{nb}} \right) \Big|_E \right] \frac{\eta y}{(\zeta x \eta y - \eta x \zeta y) \Delta \zeta} \\
\hat{c}_e^v &= 0.5 \left[ \left( \frac{\nabla}{a_p - \sum a_{nb}} \right) \Big|_P + \left( \frac{\nabla}{a_p - \sum a_{nb}} \right) \Big|_E \right] \frac{\eta x}{(\zeta x \eta y - \eta x \zeta y) \Delta \zeta} \\
\hat{c}_n^u &= 0.5 \left[ \left( \frac{\nabla}{a_p - \sum a_{nb}} \right) \Big|_P + \left( \frac{\nabla}{a_p - \sum a_{nb}} \right) \Big|_N \right] \frac{\zeta y}{(\zeta x \eta y - \eta x \zeta y) \Delta \eta} \\
\hat{c}_n^v &= 0.5 \left[ \left( \frac{\nabla}{a_p - \sum a_{nb}} \right) \Big|_P + \left( \frac{\nabla}{a_p - \sum a_{nb}} \right) \Big|_N \right] \frac{\zeta x}{(\zeta x \eta y - \eta x \zeta y) \Delta \eta}
\end{aligned} \tag{3.33}$$

Substituting them into continuity equation, we obtain explicit algorithm for  $p'$ :

$$a_p^p p'_p = a_w^p p'_w + a_E^p p'_E + a_S^p p'_S + a_N^p p'_N + b_p^p \tag{3.34}$$

where the  $a_p^p, a_w^p, a_E^p, a_S^p, a_N^p$ , are

$$\begin{aligned}
a_w^P &= a_w^{cu} \hat{c}_w^u + a_w^{cv} \hat{c}_w^v \\
a_e^P &= a_e^{cu} \hat{c}_e^u - a_e^{cv} \hat{c}_e^v \\
a_s^P &= a_s^{cu} \hat{c}_s^u + a_s^{cv} \hat{c}_s^v \\
a_n^P &= a_n^{cu} \hat{c}_n^u - a_n^{cv} \hat{c}_n^v \\
a_P^P &= a_w^P + a_e^P + a_s^P + a_n^P
\end{aligned} \tag{3.35}$$

and  $a_w^{cu}$ ,  $a_w^{cv}$ ,  $a_e^{cu}$ ,  $a_e^{cv}$ ,  $a_s^{cu}$ ,  $a_s^{cv}$ ,  $a_n^{cu}$ ,  $a_n^{cv}$  are defined as:

$$\begin{aligned}
a_w^{cu} &= \rho A_w \hat{n}_{xw} \\
a_w^{cv} &= \rho A_w \hat{n}_{yw} \\
a_e^{cu} &= -\rho A_e \hat{n}_{xe} \\
a_e^{cv} &= -\rho A_e \hat{n}_{ye} \\
a_s^{cu} &= \rho A_s \hat{n}_{xs} \\
a_s^{cv} &= \rho A_s \hat{n}_{ys} \\
a_n^{cu} &= -\rho A_n \hat{n}_{xn} \\
a_n^{cv} &= -\rho A_n \hat{n}_{yn}
\end{aligned} \tag{3.36}$$

and

$$b_P^P = a_w^{cu} u_w^* + a_w^{cv} v_w^* + a_e^{cu} u_e^* + a_e^{cv} v_e^* + a_s^{cu} u_s^* + a_s^{cv} v_s^* + a_n^{cu} u_n^* + a_n^{cv} v_n^* \tag{3.37}$$

where  $b_P^P$  is called the mass source which is evaluated in terms of the starred velocities. If  $b_P^P$  is zero, the starred velocities do satisfy the continuity equation so that no pressure correction is needed.

### **3.3.3 Algorithm**

At this point, we have all the discretization equations needed to obtain the velocity components and pressure. Now we describe SIMPLE algorithm due to Patankar (1980).

#### **3.3.3.1 Steps of Operations**

The important steps, in the order of their execution, are:

1. Estimate the pressure  $p^*$ .
2. Solve the momentum equations Eqs. (3.27) to obtain the  $u^*$ ,  $v^*$ .
3. Solve the  $p'$  equation (3.34).
4. Correct  $p$  from Eq. (3.28).
5. Correct  $u$ ,  $v$  from their initial, started values using the Eqs. (3.29).
6. Solve the equation for scalar  $\phi$  (temperature here).
7. Used the corrected pressure  $p$  distribution as an initial one, and go back to step 2 and repeat these procedures until a converged solution is obtained by setting the convergence criteria as that the difference of the values between current iteration and previous iteration is less than  $10^{-5}$ .

### **3.3.3.2 Boundary conditions for the Pressure-Correction Equation**

"The momentum equations are special cases of the general  $\phi$  equation, and therefore our general boundary-condition treatment applies to them as well. Since the  $p'$  equation is not one of the basic equations however, some special handling of its boundary conditions are appropriate. Normally, there are two kinds of conditions at a boundary. Either the pressure at the boundary is given (and the velocity unknown) or the velocity component normal to the boundary is specified." (Patankar 1980)

Suppose we are given pressure at the boundary. "If the guessed pressure field  $p^*$  is arranged such that at a boundary  $p^* = p_{\text{given}}$ , then the value of  $p'$  at the boundary will be zero. This is then akin to the given-temperature boundary condition in a heat-conduction problem." (Patankar 1980)

Alternatively, suppose we are given normal velocity at the boundary. If the grid is designed such that the boundary coincides with a control-volume face, the velocity  $u_e$  is given. Since  $u_e$  is defined, the  $u'_e = 0$  from Eq. 3.32 and then  $p_p' = p_e'$ .

### **3.3.3.3 The Relative Nature of Pressure**

“In many problems, the value of the absolute pressure is much larger than the local differences in pressure that are encountered. If the absolute values of pressure were used for  $p$ , round off errors would arise in calculating difference. It is, therefore , best to set  $p=0$  as a reference value at a grid point and to calculate all other values of  $p$  as pressure relative to the reference value. Similarly, before the  $p'$  equation is solved during each iteration, it is useful to start from  $p'=0$  as the guess for all points, so that the solution for  $p'$  does not acquire a large absolute value.” (Patankar 1980)

### **3.4 Solver for the Algebraic Equations**

A line-by-line method has been employed. We choose a grid line in one direction, assume that the variables along the neighbouring lines are known from their immediately updated values and solve for the variables along the chosen line by the tridiagonal-matrix algorithm (TDMA). The procedure is done by processing all lines in one direction and repeated for the lines in the other direction. The iterative method combines with the relaxation to speed up the convergence.

## **Chapter 4**

# **Experimental Instrumentation and Setup**

Digital Particle Image Velocimetry (DPIV) is employed in the current studies to measure the velocity field. Interpretation of flow fields is easier if a flow visualization technique is used in conjunction with the flow field measurements. Such a technique can offer higher temporal and spatial resolution of the instantaneous flow fields. The DPIV technique provides the instantaneous visualization of the two-dimensional velocity pattern in unsteady flows. In this chapter, we describe the assembly of the instrumentation and experimental procedures.

### **4.1 Techniques and Instrumentation of DPIV**

DPIV emphasizes the use of digitally recorded video images which are readily adaptable to machine processing and thus superior to the image acquisition and processing aspects of an analogue system. A digitized video image may be

considered to be a two-dimensional signal field analogous to a digital time series in one dimension.

In DPIV two sequential digital images are subsampled at one particular area via an interrogation window. Within these image samples an average spatial shift of particles may be observed from one sample to its counterpart in the other image, provided a flow is present in the illuminated plane. This spatial shift may be described quite simply with a linear digital signal processing model. The corresponding sections of two successive images may be cross-correlated. The position at which this matching process achieves a maximum indicates the average particle shift of all the particles within the sample. Performing this match-up between image samples over all the image pair results in a field of displacement vectors.

DPIV is used to make instantaneous measurement of the velocity field in an XY plane. Since the finite volume method used in this thesis yields velocity field itself, comparison of experimental and numerical results can be made directly. It is important to note, however, that measurement of the fluid's velocity at a point or along a line in the fluid can be obtained from the XY plane and these values can be compared with calculation. The limits of precision for the DPIV method will be

tested in this way.

The DPIV method is based on the comparison of two successively illuminated images of suspended particles in the fluid. By determining the displacement of individual particles between the two images and knowing the time interval between the images, the velocity of the particles in each of the X and Y directions in the plane of illumination is calculated. The velocity field determined in this way will only be the true velocity field if there is no component of flow through the plane. Thus the validity of the results reported here depend on the assumption that the flow is two dimensional, which appears to be the case as described below.

Illumination was provided by Argon-Ion Laser (Coherent, water cooled 10 watt) and its output at 1-2 watt is sent by optical fibre through a cylindrical lens to form a thin sheet of light. The duration of the light pulse and the interval between pulses is controlled by a timer while the geometry of the beam is determined by the orientation of the cylindrical lens. The finite width of the beam determines the extent in the Z direction of the region of measurement, but the two-dimensionality of the flow decreases the importance of the beam width.

The choice of particles to act as markers of the flow and reflect the laser light was made based on several criteria. First, the particles had to be small enough so that they would follow the flow rather than slip relative to it. But they had to be sufficiently large to reflect the laser light and be visible using a CCD camera. Finally they needed to be almost neutrally buoyant so that they would not collect on either the top or bottom boundaries. A choice of the seeding particles which satisfied these criteria were metal coated,hollow clay spheres, 10 microns in diameter.

The image acquisition system consisted of a CCD camera, and SONY video monitor. The image was stored on a flow grabber board in a PC (Compaq 486/66). Fig. 4.1 shows the flow chart of the DPIV system. The CCD camera used in these experiments had a field composed of 512 by 480 pixels with X, Y direction respectively. Images were taken over 33 milliseconds and at such an interval as determined by the velocity field. For low velocities a longer interval was chosen so that significant movement of the illuminated particles could take place between pairs of images, while at higher speeds a shorter time interval was chosen. Determination of particle displacements was

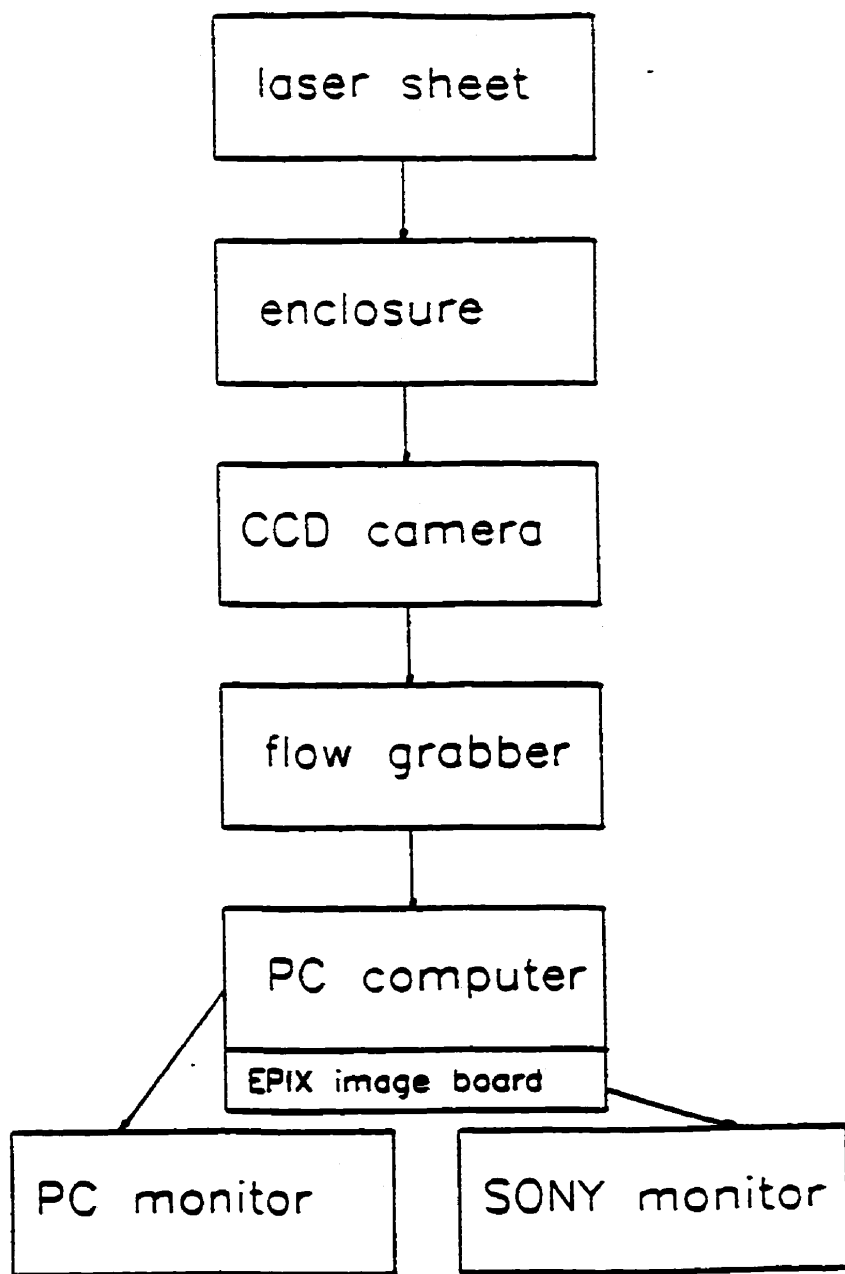


Figure 4.1 Flow chart of the DPLV system

found through cross-correlation between the two images over smaller subregions, usually 32 by 32 pixels. Each of these 32 by 32 pixel regions was overlapped by 16 pixels so that up to 32 pairs would be processed over one row of 512 pixels. Successive rows were then cross-correlated until the whole region was completed. Approximately 250,000 cross-correlations were computed for each CCD image pair that was processed and this took several minutes on the 486 computer that was used for the computation. Ultimately, however, the precision of the DPIV system is determined by the number of pixels in the field of view; this will be discussed later in relation to analysis of error.

## **4.2 Experimental Setup**

The experiments described here were conducted in conjunction with the numerical calculations using the finite volume method. Although confirmation of the validity of these numerical results was a primary goal, departures in the experiments were expected and these are discussed in the results section. In addition to confirmation of calculation, the experiments were used to determine the range of application of Digital Particle Imaging Velocimetry which was planned for use in

future experiments on elliptical instability in a rotating spherical shell.

The experiments reported here correspond to the theoretical problem of convection in a two dimensional parallelogrammic enclosure with angle of inclination 30 degrees to the vertical as already shown schematically in Figure 2.5 and reproduced here as Figure 4.2 for convenience. The left hand inclined wall is heated and maintained at temperature  $T_h$ . The opposite side wall is cooled and held at temperature  $T_c$ . The top and bottom horizontal walls are adiabatic. Gravity is in the Y direction and the Z axis is out of the page to complete a right-handed system. These idealized conditions at the boundaries were closely achieved in the actual enclosure as described below.

Fig. 4.2 shows the schematic of the parallelogrammic enclosure and dimensions. While the shape of the enclosure was determined by the need to study convection with sloping boundaries, the size of the enclosure was determined by two factors: it had to be big enough to allow close-up observations in sub regions of the cell, but small enough to allow the images being captured by CCD camera in clear quality. Following these considerations, the enclosure was constructed with 5cm by 5cm sidewalls. The enclosure needed to be long enough on the Z direction so that

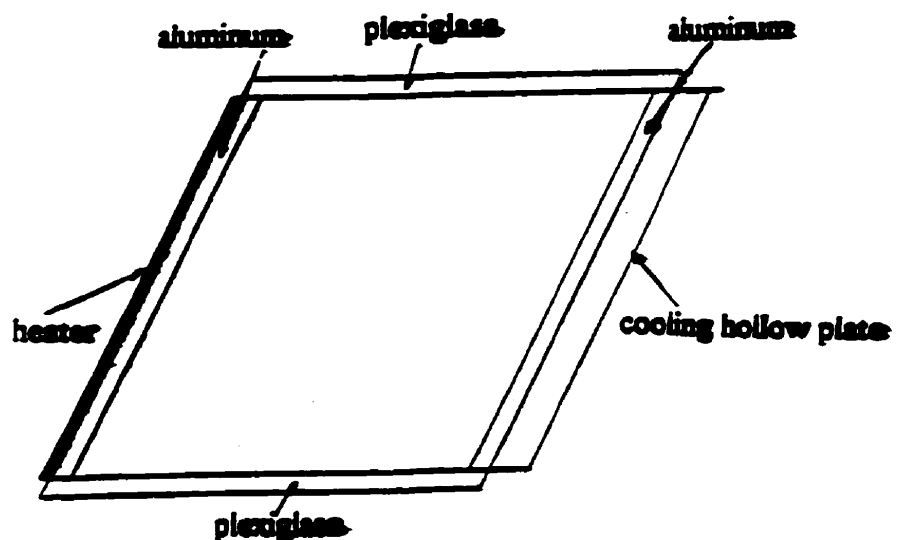
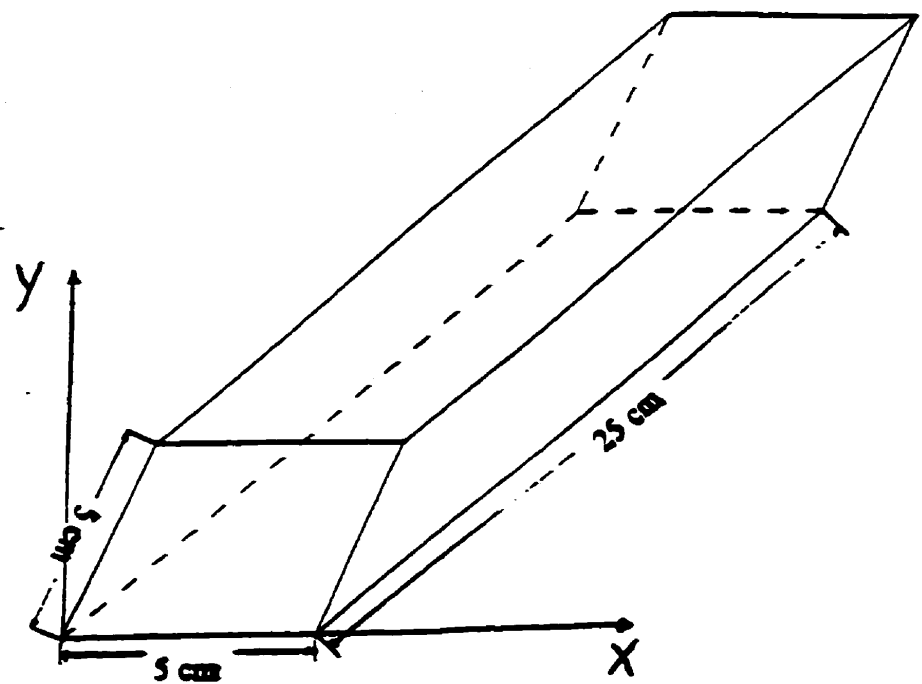


Figure 4.2 Schematic of the parallelogrammic enclosure and dimensions

the flow could be considered two dimensional in the XY plane and with this in mind the length was chosen to be 25 cm. In the course of our experiments the flow was measured along the length and found the end walls to have less than a 1% effect in the central region. The two horizontal walls, designed to be adiabatic, were constructed of plexiglass 9 mm thick. Plexiglass was chosen for these walls because it is a good insulator and is transparent as required for the passage of a light sheet from above, needed for illumination of the fluid. The end walls were also made from plexiglass to allow for images to be recorded with a CCD camera. The sloping sidewalls, on the other hand, needed to be good conductors of heat so were made of aluminum. Both plexiglass and aluminum are easy to machine and bond together, thus producing a precise, durable fluid-tight cell.

Maintenance of a constant temperature on the left inclined heating wall of the cell was achieved through a sheet of flexible silicone rubber fibreglass containing a resistance heater bonded to the aluminum face. A thin, smooth layer of Room Temperature Volcanization(RTV) cement is applied to the heater before mounting it on the inclined surface in order to minimize thermal resistance between the heater and the aluminum surface. The resistance had a maximum power density of 1.5

watts/ cm<sup>2</sup> over an area of 5cm x 25 cm. Control of the current in the resistance heater was maintained by a PID (Proportional, Integral and Derivative) temperature controller and SSR (Solid state Relay) driver. [The model numbers of the PID and SSR were CN382 and SSR240DC10 respectively, manufactured by Omega, Inc.] The PID controller combined proportional control with two additional adjustments, which help the unit automatically compensate changes in the system. These adjustments, integral and derivative, are expressed in time-based units; they are also referred to by their reciprocals, RESET and RATE, respectively. The detector for controlling temperature was a platinum Resistance Temperature Detector (RTD) probe with a 0.32cm sheath diameter and 15.24cm length which was inserted in the heated wall. A RTD operates on the principle of change in electrical resistance in platinum wire as a function of temperature and can operate in the temperature range 0 to 50°C. Since the hole in the wall occupied by the probe was very close to the fluid in the chamber, the temperature of the fluid was very well known, as the change in temperature between the probe and the fluid was estimated to be less than .001 of the temperature difference across the cell. The temperature of the heated side was maintained to within approximately 0.1 degrees C of the desired temperature.

The right hand wall was cooled by chilled type water flowing through an

attached hollow brass plate bonded to the aluminum side wall. The temperature of chilled water is observed by a temperature indicator. Achieving a good thermal contact at this interface proved difficult with the result that the temperature of the fluid in the cell was significantly different from that of the circulating chilled water. The actual temperature of the cool wall was also measured with the RTD probe, however, so that it was possible to determine the temperature of the cool wall very precisely. The cool was also maintained to within 0.1 degrees C of the specified setting.

The end walls, upper and lower walls were covered with insulating material during experiments. To limit loss of heat through the top, bottom and end walls 5 cm of high density styrofoam was added to these boundaries. Experiments conducted with and without this extra insulation showed a dramatic reduction in heat loss when the insulation was in place. A small incision in the top layer of insulation was necessary to allow the light sheet into the region to allow for flow visualization measurements (described above). The insulation was maintained on the end wall until observation with the CCD camera took place which took only a few minutes after approximately one hour during which steady state of the convection had been achieved.

## **Chapter 5**

### **Results and Discussions**

This chapter includes results obtained, mainly in steady state, from several different projects as well as discussions of these results. The first three projects listed below have been investigated in a certain range of physical parameters by other numerical methods. Part of the motivation to use the finite volume method to investigate these problems was that this technique has been rarely found in previous studies. The currently formulated numerical procedures provide a detailed description of the finite volume method. This numerical tool could be used to conduct research on natural convection with varied physical parameters which are beyond the range reported previously. For example this work provides results for side wall heating with  $\text{Ra} > 10^7$  while previous work (de Vahl Davis, 1983) stops at  $\text{Ra} = 10^6$ . Furthermore the finite volume method is readily adapted to temperature dependent parameters (eg. viscosity, thermal conductivity). The fact that there are extensive results in the literature on these problems, however, allows for a significant

evaluation of the finite volume method as developed here. The results for the last two projects are not found in previous studies. The features of natural convection for the last project may offer some implications and understanding in not only engineering applications but also in simulation of some geophysical processes such as the regions near sea bed and a subducting slab. In section 1, we first introduce the scale analysis in order to provide the basis for a physical discussion of our results. In section 2, thermal convection in an enclosure heated from below and cooled top with two vertical sides with symmetrical boundary condition is studied. In section 3, natural convection in a rectangular enclosure partly heated from the bottom wall and cooled along the right vertical sidewall is investigated. In section 4, the results for natural convection in a rectangular enclosure with two vertical walls heated and cooled are presented. This is a typical well studied problem. The results are comparable with previous results obtained by other researchers using the finite element method. Section 5 displays the results for natural convection in a parallelogrammic enclosure with one vertical wall heated and another vertical wall cooled and the two inclined walls insulated. Isotherms and heat transfer rate are presented. Some characteristics of the heat transfer are discussed. In section 6, the results for temperature and Nusselt numbers for the natural convection in a parallelogrammic enclosure with two inclined walls heated and cooled and two horizontal walls adiabatic are presented.

Subsequently these results are compared to our experimental observations.

## 5.1 Scale Analysis

In this section, we introduce some fundamental physical concepts and theoretical analysis of natural convection in an enclosure. Natural convection in an enclosure is an internal flow problem different from the external flow problem where only one solid wall boundary is often considered with the fluid body essentially infinite. Here we consider the interaction of one fluid within all of its solid boundaries.

Natural convection in an enclosure can generally be classified into two types : heating from below and heating from a sidewall. The current study includes both types of the problem. We use scale analysis to elucidate the problems of heating from below and from the sides. The finite volume numerical method and experimental observations are applied to study the sidewall heating problem with different orientations of the sidewalls confined in a parallelogrammic enclosure.

In order to provide the basis for physical explanation in later discussion of our

results, we describe the scale analysis applied to current problem which can bring physical arguments into the present analysis. Our discussion of the scale analysis is based on studies of Patterson and Imberger (1980) and Bejan (1995) for the case of natural convection in a rectangular enclosure and by Lloyd and Sparrow (1970) and Bejan (1995) for external flow with an inclined wall.

Here we introduce the scale arguments for an enclosure heated from one side as shown in figure 2.5. We begin by considering the fluid at the time the boundary conditions are applied. The fluid adjacent to the heating wall is stagnant. The energy equation (2.12) representing balance between thermal inertia and conduction can be expressed as

$$\frac{\Delta T}{t} \sim \kappa \frac{\Delta T}{\delta_T^2} \quad (5.1)$$

$$\delta_T \sim (\kappa t)^{1/2} \quad (5.2)$$

where  $\Delta T$ ,  $t$  and  $\delta_T$  are the scales of changes in  $T$ ,  $t$  and  $x$ . This expression means that the layer near the wall is a conduction layer and its thickness increase with time as  $t^{1/2}$ . Before we continue our analysis for the velocity scale, we combine the two

momentum equations (2.10) and (2.11) into one by eliminating the pressure terms and obtain:

$$\frac{\partial}{\partial x} \left( \frac{\partial v}{\partial t} + u \frac{\partial v}{\partial x} + v \frac{\partial v}{\partial y} \right) - \frac{\partial}{\partial y} \left( \frac{\partial u}{\partial t} + u \frac{\partial u}{\partial x} + v \frac{\partial u}{\partial y} \right) = \frac{\mu}{\rho} \left[ \frac{\partial}{\partial x} \left( \frac{\partial^2 v}{\partial x^2} + \frac{\partial^2 v}{\partial y^2} \right) - \frac{\partial}{\partial y} \left( \frac{\partial^2 u}{\partial x^2} + \frac{\partial^2 u}{\partial y^2} \right) \right] + g\beta \frac{\partial T}{\partial x} \quad (5.3)$$

This equation has three basic terms: inertia term, viscous diffusion term and the buoyancy term. The three terms in this equation can be rewritten as

$$\frac{\partial^2 v}{\partial x \partial t}, \quad \frac{\mu}{\rho} \frac{\partial^3 v}{\partial x^3}, \quad g\beta \frac{\partial T}{\partial x} \quad (5.4)$$

In terms of the scales, this momentum balance is inertia, or friction with buoyancy

$$\frac{v}{\delta_T}, \quad \frac{\mu}{\rho} \frac{v}{\delta_T^3} \sim \frac{g\beta \Delta T}{\delta_T} \quad (5.5)$$

Dividing by the friction term and recalling the conducting layer thickness, and considering that  $\delta_T^2 \sim kT$  we obtain

$$\frac{1}{Pr}, \quad 1 \sim \frac{g\rho\beta\Delta T\delta_T^2}{\mu v} \quad (5.6)$$

Therefore, for Pr number of order one and greater, the balance between buoyancy and friction is

$$1 \sim \frac{g\rho\beta\Delta T\delta_T^2}{\mu\nu} \quad (5.7)$$

Then the velocity scale can be written as

$$v \sim \frac{g\rho\beta\Delta T\delta_T^2}{\mu} \quad (5.8)$$

As pointed out by Bejan (1995), this scale is valid for  $\text{Pr}>1$ , and just marginally valid for gases ( $\text{Pr}\sim 1$ ).

As  $t$  increases, part of the heat conducted into the fluid from the side wall is carried away by convection. Thus, we need to consider the three effects of inertia, convection and conduction in the energy equation 2.12.

$$\frac{\Delta T}{t}, \quad v \frac{\Delta T}{L} - \kappa \frac{\Delta T}{\delta_T^2} \quad (5.9)$$

As  $t$  further increases, the convection effect becomes more important than the effect

of inertia. At a certain point in time, the balance between convection and conduction is expressed by the energy equation ,

$$v \frac{\Delta T}{L} - \kappa \frac{\Delta T}{\delta_T^2} \quad (5.10)$$

By considering the effect of convection, we may obtain an expression for the time taken to reach a balance between the heat conducted away from the wall and heat convected away by the buoyant layer; It follows from Eq. 5.8 and 5.9 that

$$t_f = \left( \frac{\mu L}{g \rho \beta \Delta T \kappa} \right)^{1/2} \quad (5.11)$$

and the layer thickness is

$$\delta_T = (kt)^{1/2} = L \left( \frac{g \rho \beta \Delta T L^3}{\kappa \mu} \right)^{-1/4} = L Ra^{-1/4} \quad (5.12)$$

Thus we expect the thermal boundary layer to scale as  $Ra^{-1/4}$  , a relationship which we will later verify in the numerical and experimental results.

In addition to the development of the thermal layer, a viscous layer is formed. We also can consider a balance between inertia and viscous diffusion in the

momentum equation. We have

$$\frac{v}{\delta_v t} \sim \frac{\mu}{\rho} \frac{v}{\delta_v^3} \quad (5.13)$$

Then we have

$$\delta_v \sim \left( \frac{\mu}{\rho} t \right)^{1/2} \sim Pr^{1/2} \delta_T \sim Pr^{1/2} L Ra^{-1/4} \quad (5.14)$$

We should realize that the analysis above is for Pr number greater or roughly order of one. In a similar analysis for external natural convection, Bejan (1995) obtained the boundary layer scales for  $Pr < 1$ . The expressions for these scales are as follows:

$$\begin{aligned} \delta_T &\sim L (Ra Pr)^{-1/4} \\ v &\sim \frac{\kappa}{L} (Ra Pr)^{1/2} \\ \delta_v &\sim L Ra^{-1/4} Pr^{1/4} \end{aligned} \quad (5.15)$$

We know that the current studies are characterized by the component of gravity acceleration along the inclined walls. When we apply the scale analysis we must,

therefore, substitute g with  $g \cdot \cos(\text{IA})$ . Thus taking into account a sloping boundary heated and cooled with inclination angle (IA), we obtain for  $\text{Pr} < 1$

$$\begin{aligned}\delta_r &\sim L(\cos(\text{IA})RaPr)^{-1/4} \\ v &\sim \frac{\kappa}{L}(\cos(\text{IA})RaPr)^{1/2} \\ \delta_v &\sim L(\cos(\text{IA})Ra)^{-1/4}Pr^{1/4}\end{aligned}\tag{5.16}$$

and for  $\text{Pr} > 1$ , we write

$$\frac{\delta_r}{L} \sim (\cos(\text{IA})Ra)^{-1/4}, \quad \frac{\delta_v}{L} \sim Pr^{1/2}(\cos(\text{IA})Ra)^{-1/4}\tag{5.17}$$

From the expression, we know that

- (1) The velocity boundary layer is thicker for the fluid with  $\text{Pr} > 1$ , like water and thinner for the fluid with  $\text{Pr} < 1$ , like air.
- (2) Boundary layers will be thicker for containers with greater sloping walls, but at most less than 20% as listed below for  $(\cos(\text{IA}))^{-1/4}$ .

IA	$\cos(\text{IA})$	$(\cos(\text{IA}))^{-1/4}$
15°	0.966	1.008
30°	0.866	1.037
45°	0.707	1.091
60°	0.5	1.189

In further discussion, two criteria for distinct vertical layers and horizontal jets are provided by Bejan (1995). Since the two boundary layer thicknesses are smaller than the length scale of enclosure, we can write the two criteria for vertical thermal and velocity boundary layers by considering Eq. 5.14 as

$$\frac{H}{L} < Ra_H^{1/4} \quad \text{and} \quad \frac{H}{L} < Ra_H^{1/4} Pr^{-1/2} \quad (5.18)$$

where H is the height of enclosure.

We also write the criterion for horizontal jets.

$$\frac{H}{L} > Ra_H^{-1/4} \quad (5.19)$$

Based on such criteria, several regimes including conduction, boundary layer , tall enclosure and shallow enclosure limits have been identified. In the conduction regime, the temperature varies linearly across the enclosure. The horizontal

temperature gradient initiates a slow circulation but the heat transfer due to this circulation is insignificant. In the boundary layer regime, thermal boundary layers along the heated and cooled side walls are distinctive. There is a core where the fluid is relatively stagnant and thermally stratified.

In the numerical results presented below for inclined sidewall heating in an enclosure, it will be shown that the scale analysis given Eq. 5.17 is consistent with the observations. Thus the physical processes described by the scale analysis provide an interpretation for the precise numerical results.

## 5.2 Rayleigh-Bénard Convection

Rayleigh-Bénard convection is common in geophysical and astrophysical systems. This problem fundamentally belongs to the category of natural convection. In the geophysical community, people used to call it Rayleigh-Bénard thermal convection. In this section, several numerical test cases are presented and results for Nusselt numbers are compared with those previously obtained by Schneck and Veronis (1967). The graphical presentations of temperature and velocity fields given here provide more explicit insight into such flow structure.

The computation domain is chosen to be a square box. The top and bottom of the box are cooled and heated respectively while symmetric boundary conditions are applied to the two side walls. A series of computations for Rayleigh number from 4000 to 50000 at Prandtl number of 6.8 corresponding to water were carried out. The range of the Rayleigh number chosen guarantees the problem is stable to two dimensional rolls as indicated by Schneck and Veronis (1967).

As we have mentioned that our code was developed for transient problem, we obtain steady results by marching with time. The initial conditions for velocity and

temperature are zero. From a physical perspective, no flow will be present and develop due to the absence of a perturbation. Numerical noise in the computation, however, will initiate the flow in the early period and flow patterns will develop randomly. With continuous marching, a convection process is built up and evolves fully to a dynamic balance. Eventually the steady state solution is approached as a developed flow pattern.

Figures 5.1 to 5.8 show velocity vectors for the cases of Rayleigh number 4000, 5000, 6000, 8000, 10000, 12000, 15000 and 20000. We observe that all flow patterns consist of one roll and are clockwise with increasing Rayleigh number. Such formation of a clockwise roll could be due to the numerical computation with initial random values decided by the computer or due to computation sweeping from left to right resulted in breaking the initial physical balance. The roll is circular in shape gradually transforms to an elliptical shape due to thinner boundary layers and speed reduction at corners while convection strengthens.

Figures 5.9 to 5.16 show the isotherms for the cases with Rayleigh number of 4000, 5000, 6000, 8000, 10000, 12000, 15000 and 20000. In Fig. 5.9, the isotherms are relatively dense in the lower right corner and upper left corner. The

clockwise circulation tends to lift warmer fluid away from the bottom heated surface and into the upper portion of the domain. This causes a spreading of the isotherms in the lower left region and compression in the upper left region. The fluid flows along the upper surface where it is cooled and reaches the right boundary flowing downward in the upper right region where the isotherms are sparsely spread. In the downward flow, isotherms are compressed again in the lower right region. The isotherms in central region are nearly vertical.

In Fig 5.10 for the case of Rayleigh number as 5000, the same characteristics prevail in corner regions but the isotherms in the central region are slightly distorted. In Fig. 5.11 for the case of Rayleigh number of 6000, the isotherms in upper left and lower right corners are denser. In the central region, isotherms are further distorted. The horizontal temperature gradient is negative everywhere to support the flow circulation. Since a weak circulation exists, the heat is transferred by conduction which is limited in the upper and lower horizontal boundaries and by convection along vertical direction. The warm vertical uprising stream takes heat away to upper wall, whereas the cold vertical descending stream brings the chilled fluid back to the lower hot wall. The isotherms are either expanded or compressed in the region of vertical streams.

For the all other cases in Figs. 5.12 to 5.16 with higher Rayleigh numbers, we observe a similar presentation of the contours of the temperature in the upper left and lower right corners where isotherms are compressed. It is noted that when the Rayleigh number increases, the isotherms at the upper left and lower right corners are more strongly compressed to form thermal boundary layers and these thermal boundary layers adjacent to the horizontal walls get thinner. In the layers, the vertical temperature gradients are increased and the conduction plays more important role. However, the vertical velocity is increasing and convection strengthens so that the total heat transfer is increased. In the central region, isotherms are distorted to form a jet shape due to the strengthening convection.

It is well known that the modes of heat transfer in this problem include both conduction and convection within a closed domain and the relative importance of these two modes presents differently in the different region of the domain. In the region near the two side vertical boundaries where there is large vertical velocity, the thermal energy is transported by convection. Near the horizontal boundaries where vertical velocity is very small, the thermal energy transport is mainly due to conduction. In these regions, the thermal gradient is performing a leading role in the thermal transport process.

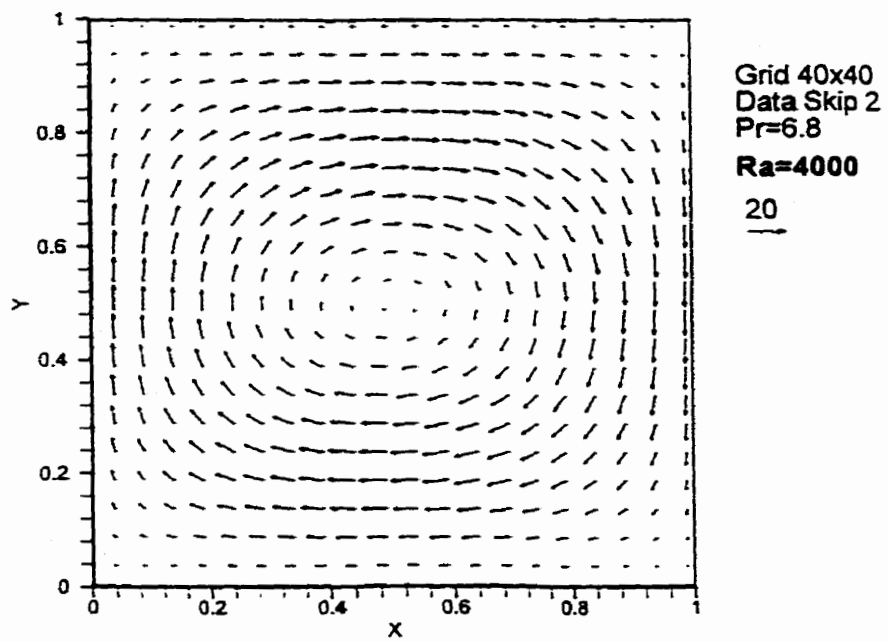


Figure 5.1 Velocity vectors for  $\text{Ra}=4000$ ,  $\text{Pr}=6.8$

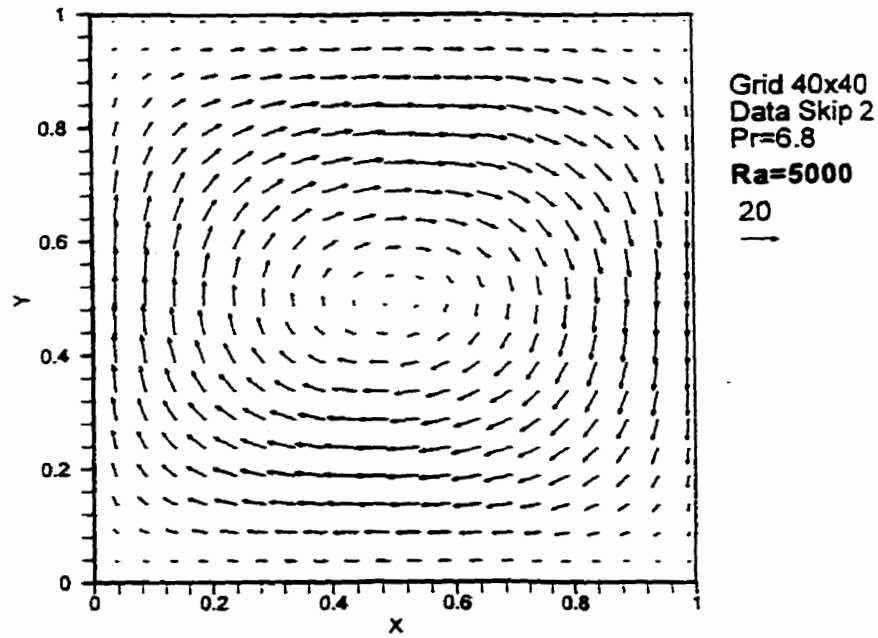


Figure 5.2 Velocity vectors for  $\text{Ra}=5000$ ,  $\text{Pr}=6.8$

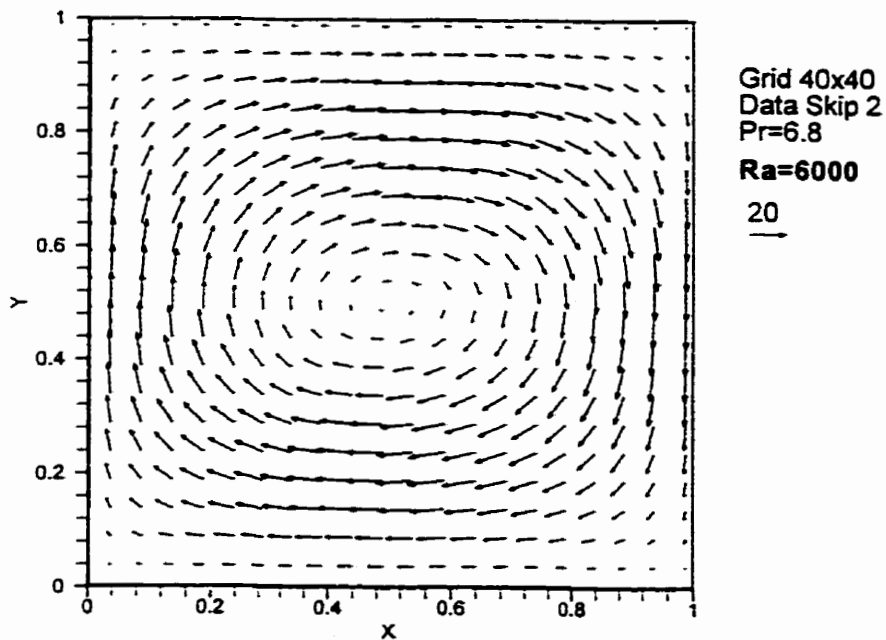


Figure 5.3 Velocity vectors for  $\text{Ra}=6000$ ,  $\text{Pr}=6.8$

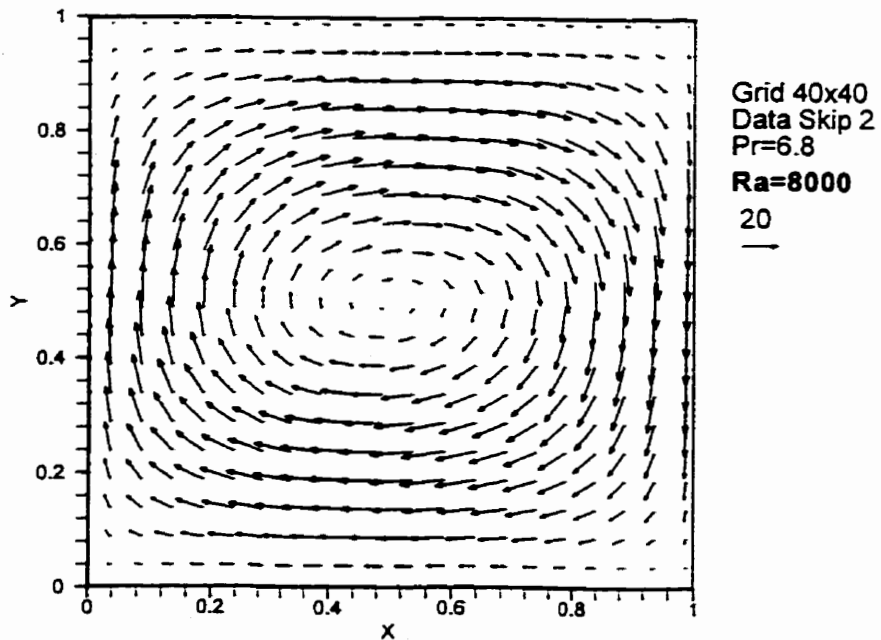


Figure 5.4 Velocity vectors for  $\text{Ra}=8000$ ,  $\text{Pr}=6.8$

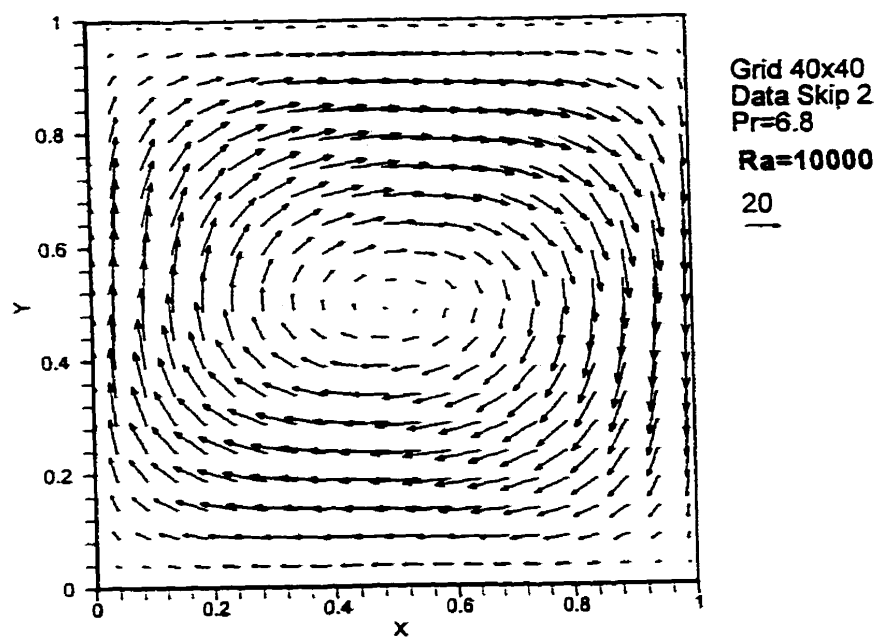


Figure 5.5 Velocity vectors for  $\text{Ra}=10000$ ,  $\text{Pr}=6.8$

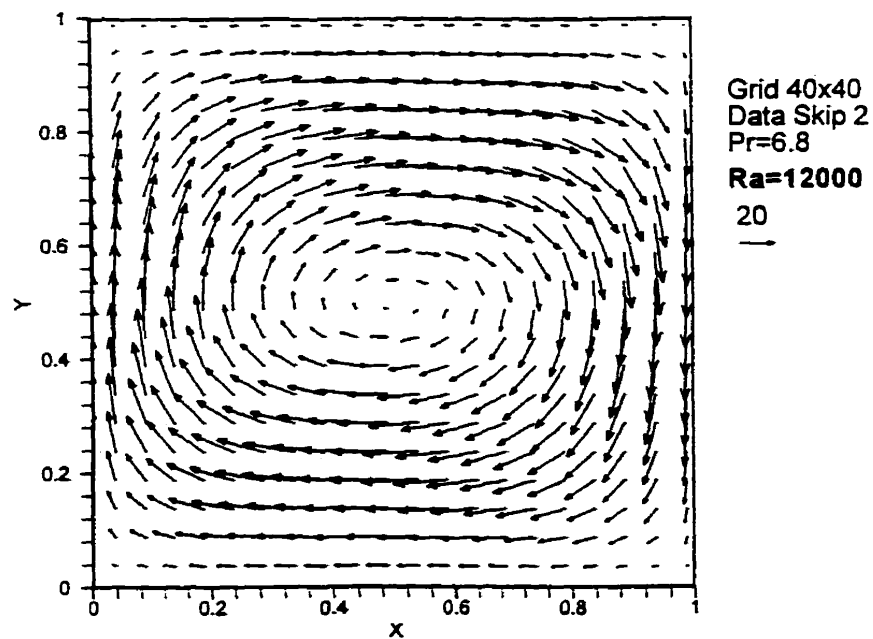


Figure 5.6 Velocity vectors for  $\text{Ra}=12000$ ,  $\text{Pr}=6.8$

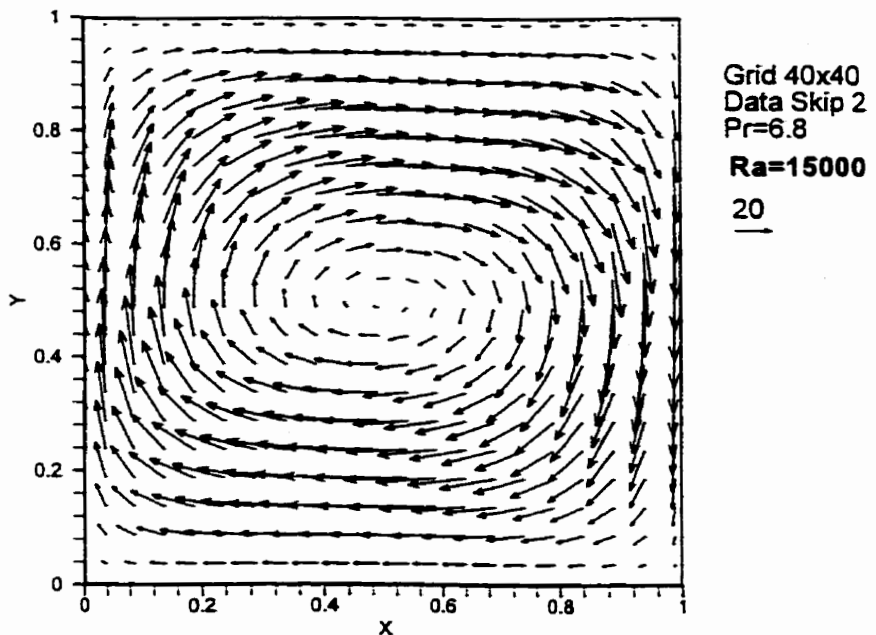


Figure 5.7 Velocity vectors for  $\text{Ra}=15000$ ,  $\text{Pr}=6.8$

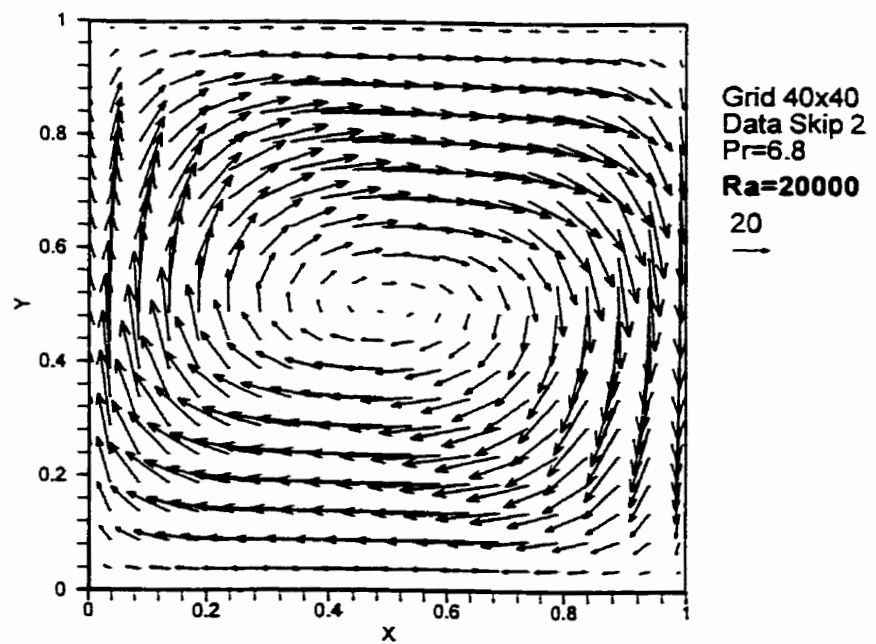


Figure 5.8 Velocity vectors for  $\text{Ra}=20000$ ,  $\text{Pr}=6.8$

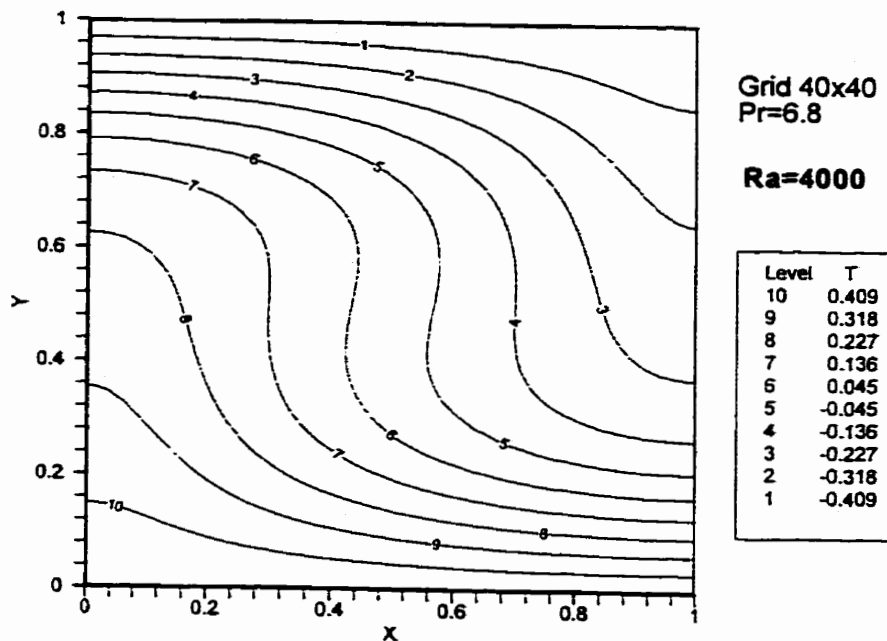


Figure 5.9 Isotherms for Ra=4000, Pr=6.8

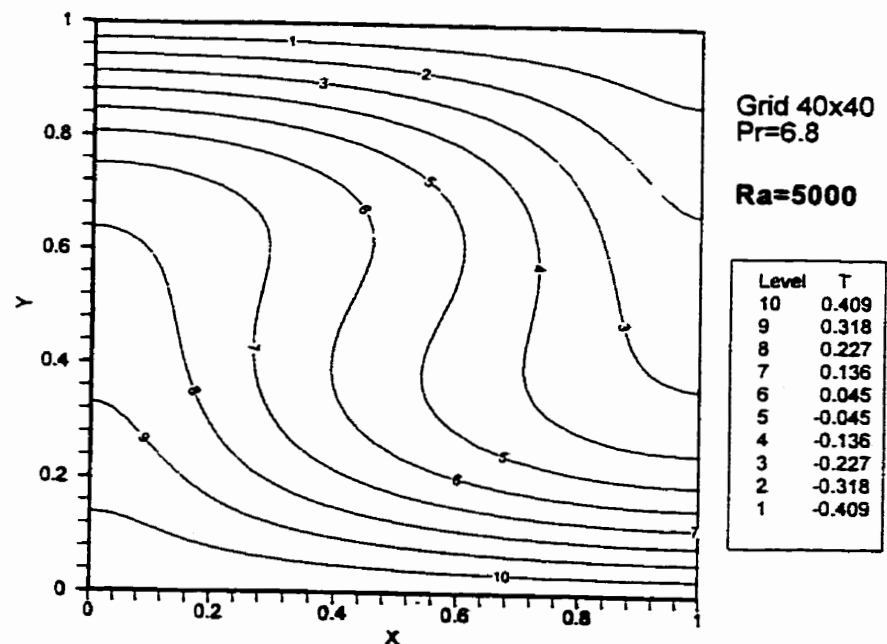


Figure 5.10 Isotherms for Ra=5000, Pr=6.8

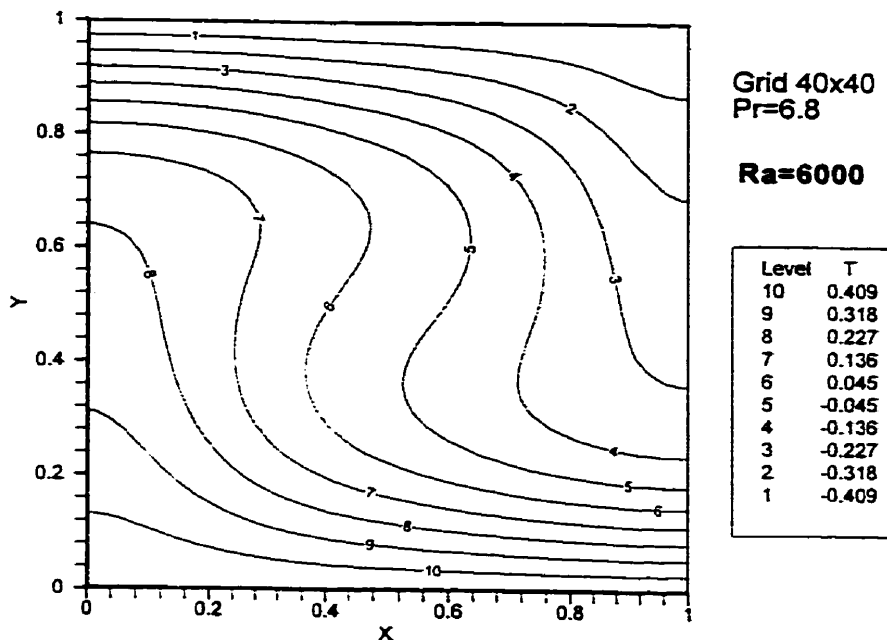


Figure 5.11 Isotherms for Ra=6000, Pr=6.8

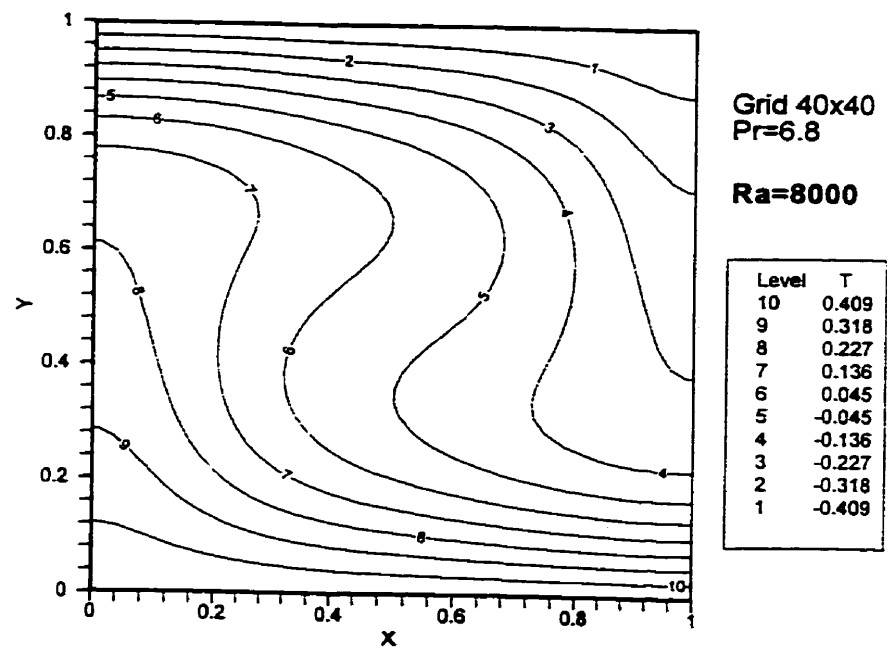


Figure 5.12 Isotherms for Ra=8000, Pr=6.8

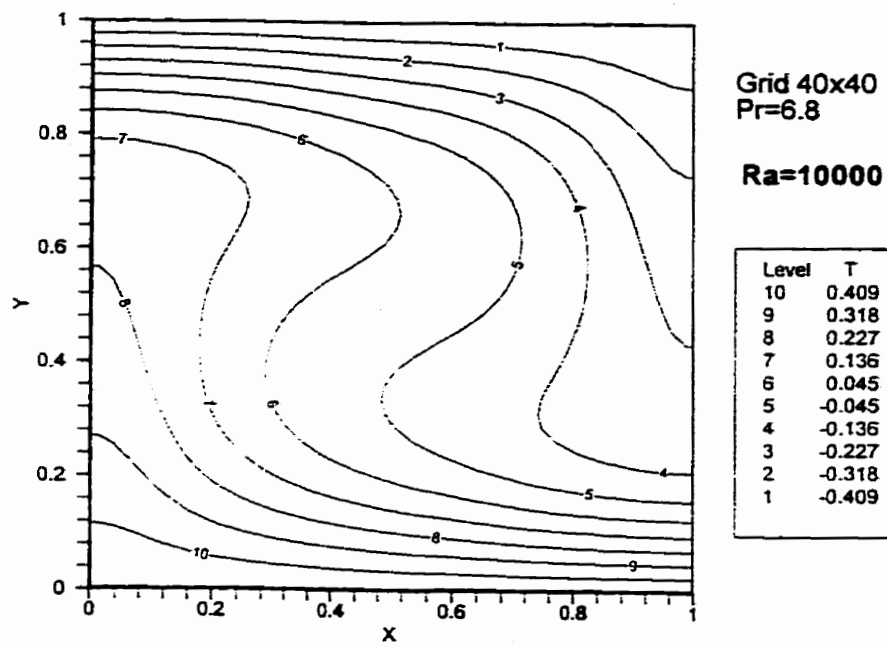


Figure 5.13 Isotherms for  $\text{Ra}=10000$ ,  $\text{Pr}=6.8$

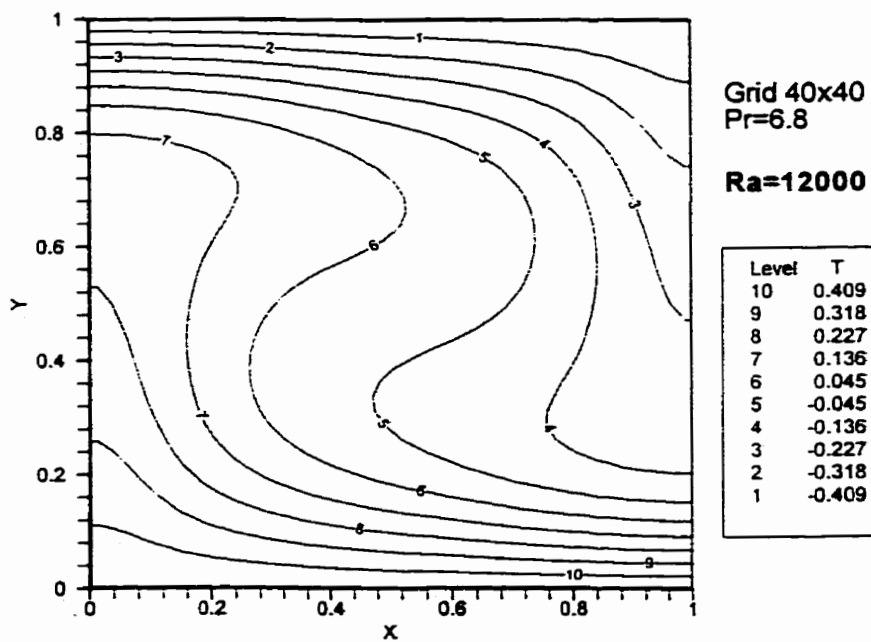


Figure 5.14 Isotherms for  $\text{Ra}=12000$ ,  $\text{Pr}=6.8$

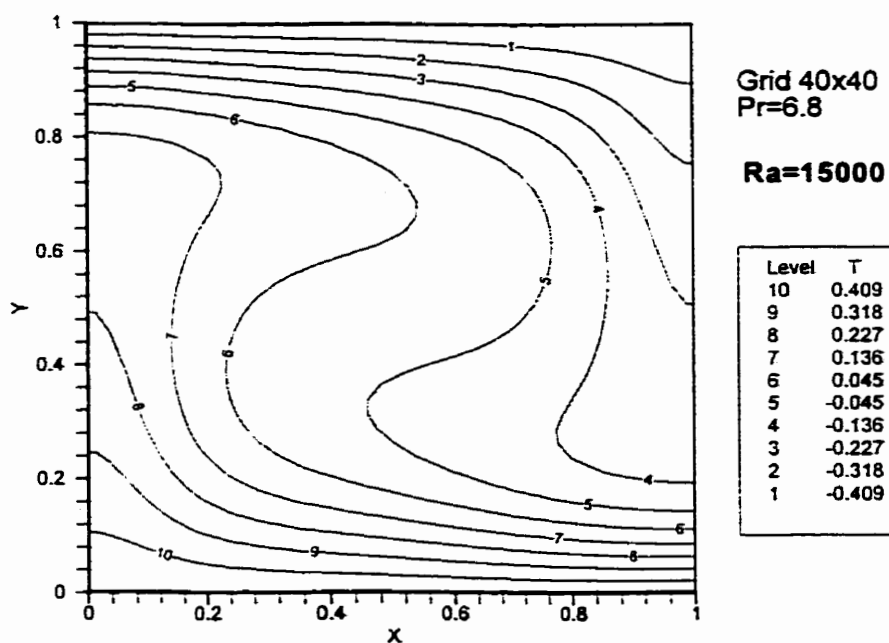


Figure 5.15 Isotherms for Ra=15000, Pr=6.8

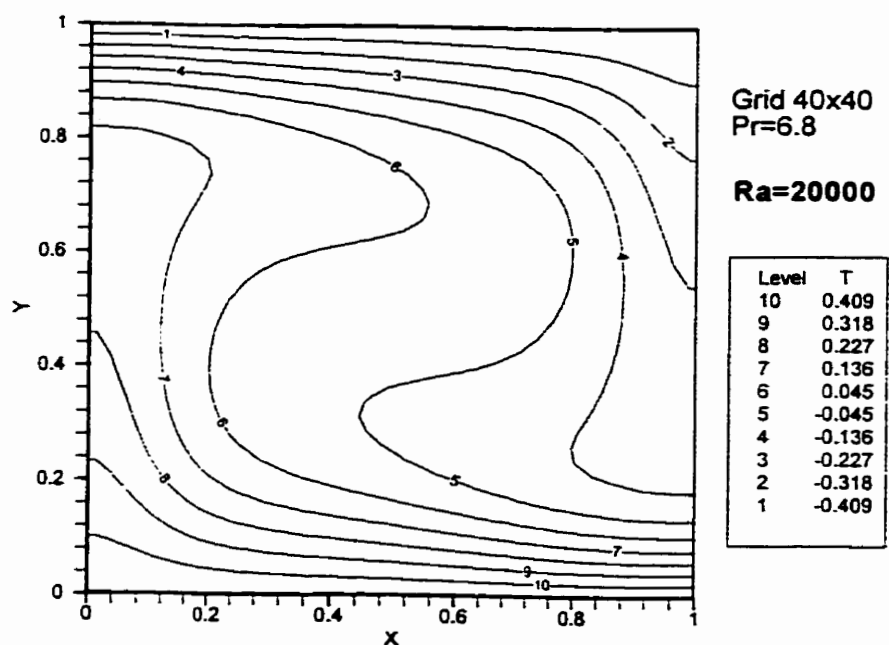


Figure 5.16 Isotherms for Ra=20000, Pr=6.8

In Table 5.1, the Nusselt numbers for these cases are listed and compared with those obtained by Schneck and Veronis (1967) for  $\text{Pr}=6.8$  and Mitrovica and Jarvis (1987) for  $\text{Pr}=\infty$  using the finite difference method. As expected the Nusselt number increases with Rayleigh number. Comparison indicates that for all cases the differences between the two studies fall in the range of 2% for  $\text{Pr}=6.8$ . The resolutions employed by Schneck and Veronis were  $30\times 30$  grids for all Rayleigh numbers 4000 to 12000 and  $40\times 40$  grids for Rayleigh number 20000. In the current study, we used  $40\times 40$  grids to discretize the computational domain for all cases. It was found that all Nusselt numbers obtained by current study were lower than that

Ra	Current $\text{Pr}=6.8$	Schneck/Veronis $\text{Pr}=6.8$	Difference %	Mitrovica/Jarvis
4000	1.928	1.941	0.67	
5000	2.109	2.116	0.33	2.102
6000	2.248	2.269	0.93	2.238
8000	2.458	2.487	1.17	2.441
10000	2.617	2.650	1.24	2.609
12000	2.746	2.780	1.22	
15000	2.907			
20000	3.120	3.147	0.86	3.107

Table 5.1 Comparison of Nusselt numbers

obtained by Schneck and Veronis (1967). Comparison reveals the better agreement between current results and results by Mitrovica and Jarvis (1987).

Theoretically speaking, the current results for Rayleigh number 4000 to 12000 are more accurate due to finer resolution. As is well known, in representing a continuum, greater accuracy comes with finer resolution in space and the error associated with coarse resolution is the discretization error caused by replacing the continuous problem by a discrete one. In order to reduce the error associated with discretization, adequate spatial resolution is necessary. Flow structures that are not resolved well enough are being represented by false features in computation. Another type of error is caused by rounding to a finite number of digits in the arithmetic operations. This called round-off error is important and we should be aware of its existence in obtaining solutions because of the large number of repetitive operations. We can hardly compare this kind of errors generated by the two studies due to the unknown numerical procedures. Schneck and Veronis (1967) mentioned, however, that the system required a longer time for convergence when a crude grid network was used. As the grid network becomes much coarser than the one required to describe the system accurately, time-oscillatory motions can be occur which are characteristic of the crude approximation but not of the actual physical system which

is being analysed. From the foregoing, the results of the current study are likely obtained more accurately.

Further computations were also carried out for Rayleigh number 50000. The present computation for this case was carried out by marching in time. In every time step, 6 iterations were applied and the number of total time steps was 10000. The dimensionless time at steady state was about 1.39, while the computation was stopped at dimensionless time 6.89. Based on a referenced dimensionless speed of 50, length of enclosure and the time, the fluid has overturned about 50 cycles in the final flow field. When the same uniform initial condition as for the low Rayleigh numbers was used, the flow structure of the steady state solution changed from a flow pattern with one roll for low Rayleigh number to flow pattern with two rolls asymmetric about the vertical centerline of the cell. Figure 5.17 and 5.18 show the velocity vectors and isotherms for this case. The asymmetry of the velocity field is also readily evident in the isotherm plot.

Mitrovica and Jarvis (1987) reported a series of computations for Rayleigh-Bénard convection. They obtained steady solutions for Rayleigh number range from 5125.5 to 512550 and infinite Prandtl number. They found the upper bound for

Rayleigh number to be 512550 which can lead to convection being time dependent. The flow patterns presented in the steady state were all one cell. In the current study, the two cell patterns could be due to the role played by the convection term in momentum equations.

After this two roll feature was observed, the question arose as to whether a one roll flow pattern could be obtained by applying different initial conditions through a small perturbation with a cosine function. Would the steady state solutions be affected by initial conditions? The investigation into such a question was then conducted through using initial conditions  $\theta_0=0.5-Y+0.01\cos(K\pi X)$  with  $K = 1, 2, 3, 4, 5$  and  $6$ .

The velocity vectors for these cases are shown in Fig. 5.19 - 5.24 which reveal the different flow patterns. The flow patterns are one clockwise roll for wavenumber  $K=1$ , two rolls with left one clockwise and right anticlockwise for  $K=2$ , two rolls with left one anticlockwise and right one clockwise for  $K=3$ , one anticlockwise roll for  $K=4$ , two rolls with left one anticlockwise and right one clockwise for  $K=5$  and one anticlockwise roll for  $K=6$ .

Moore and Weiss (1973), Goldhirsch, Pelz and Oszag (1989) and Arroyo and Saviron (1992) all mentioned that asymmetric roll patterns exist for high Rayleigh number. While a physical argument to explain this feature might be possible, several possibilities could account for the asymmetry. Alternatively the observed asymmetric feature for  $\text{Ra}=50000$  could be decided by the initial conditions. The initial values deviating from zero can break the balance to initiate a flow and end up with asymmetric roll patterns. Finally the asymmetry could be due to the natural statistical selection process which starts from random initial condition and reaches certain patterns. When more computations were carried out by changing the time steps and iterations for every step, it was found that the flow patterns can change with change of these numerical parameters. When we applied same time step which is 0.00689 and more iterations (28), the flow patterns for initial condition of zero and  $K=2$  were one cell. For the cases with other  $K$ 's, the flow patterns remained unchanged. When we adjusted the time step to be slightly larger (0.01) and 28 iterations, all patterns for these cases were one cell. It seems that such features can be attributed to the random selection process and also depend on the numerical method and schemes.

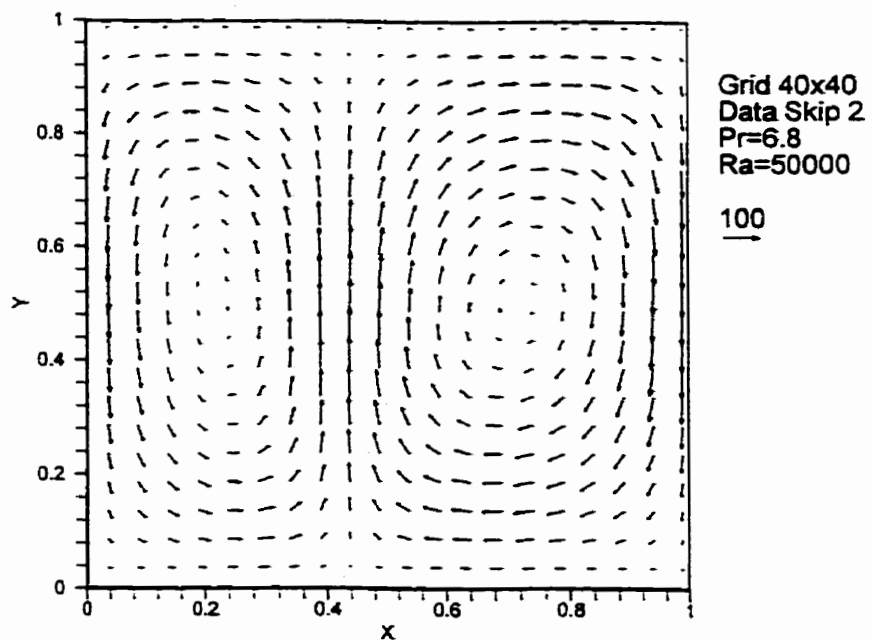


Figure 5.17 Velocity vectors for  $\text{Ra}=50000$ ,  $\text{Pr}=6.8$ , zero initial condition

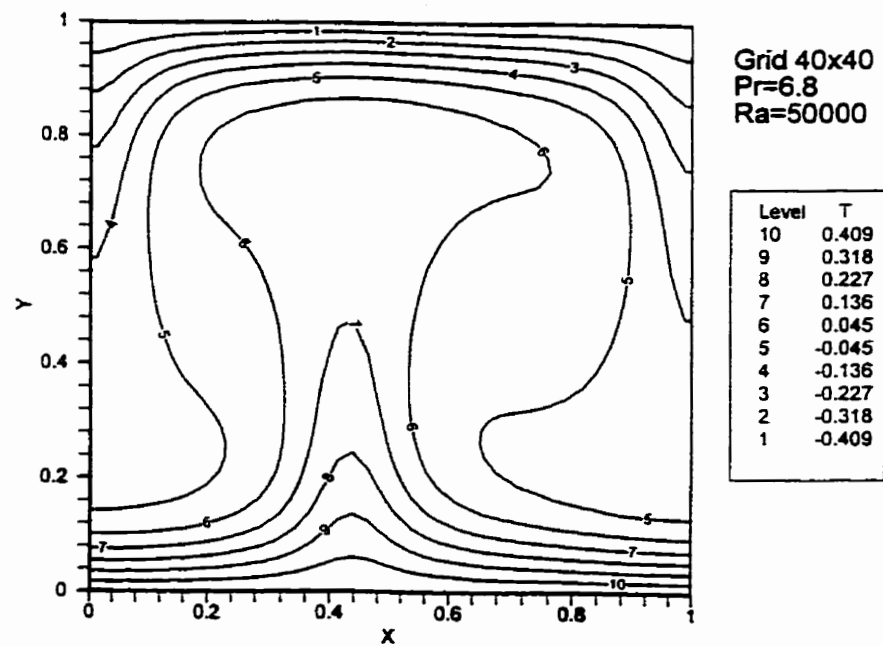


Figure 5.18 Isotherms for  $\text{Ra}=50000$ ,  $\text{Pr}=6.8$ , zero initial condition

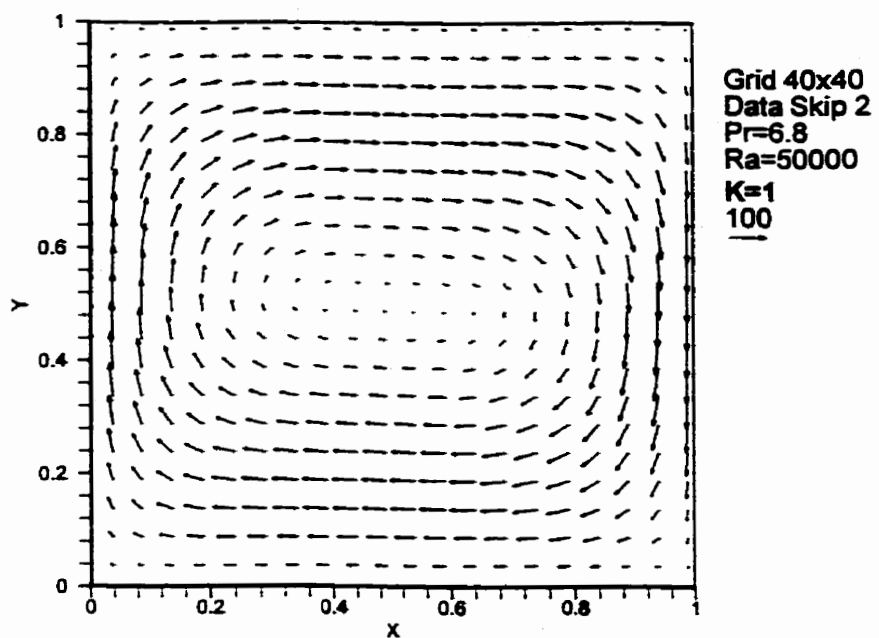


Figure 5.19 Velocity vectors for  $\text{Ra}=50000$ ,  $\text{Pr}=6.8$ ,  $K=1$

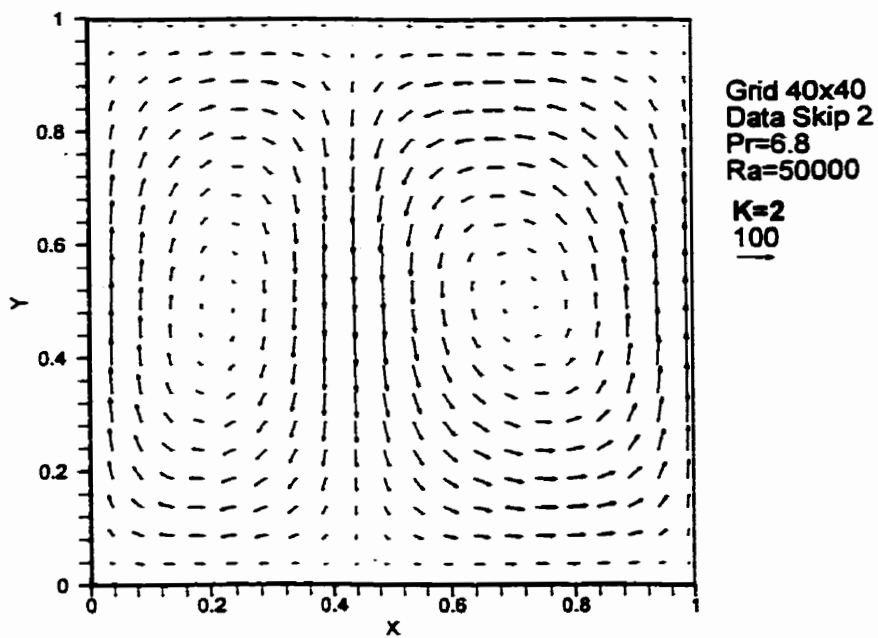


Figure 5.20 Velocity vectors for  $\text{Ra}=50000$ ,  $\text{Pr}=6.8$ ,  $K=2$

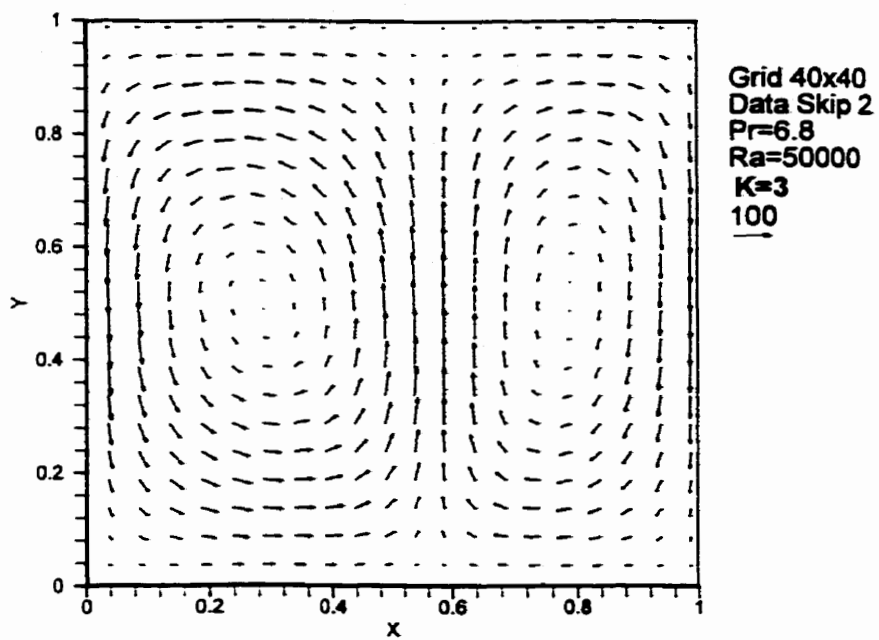


Figure 5.21 Velocity vectors for  $\text{Ra}=50000$ ,  $\text{Pr}=6.8$ ,  $K=3$

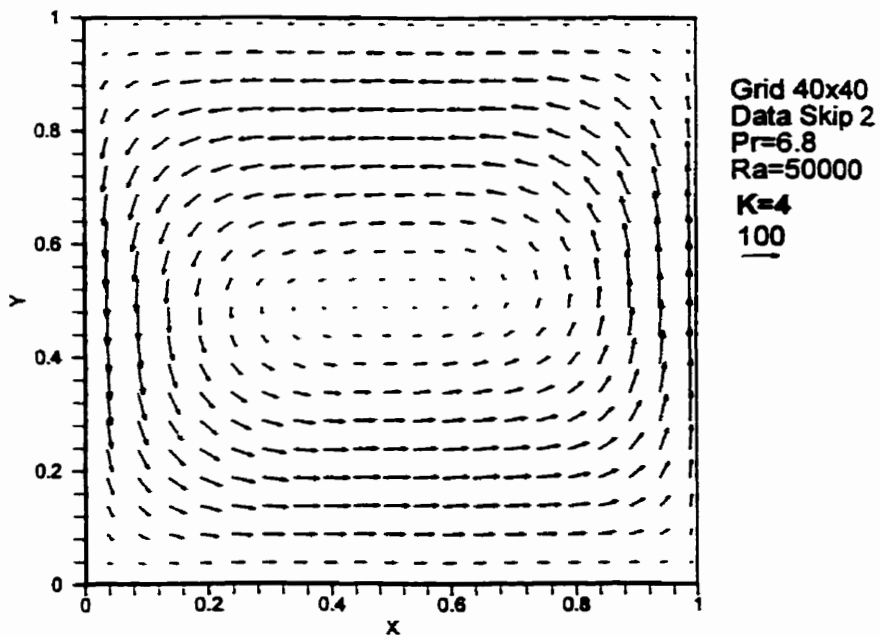


Figure 5.22 Velocity vectors for  $\text{Ra}=50000$ ,  $\text{Pr}=6.8$ ,  $K=4$

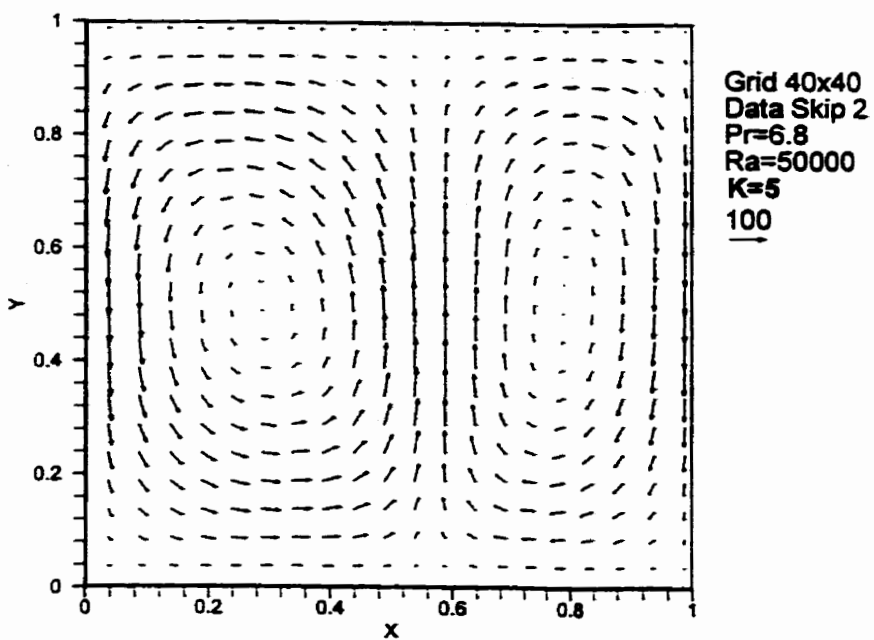


Figure 5.23 Velocity vectors for  $\text{Ra}=50000$ ,  $\text{Pr}=6.8$ ,  $K=5$

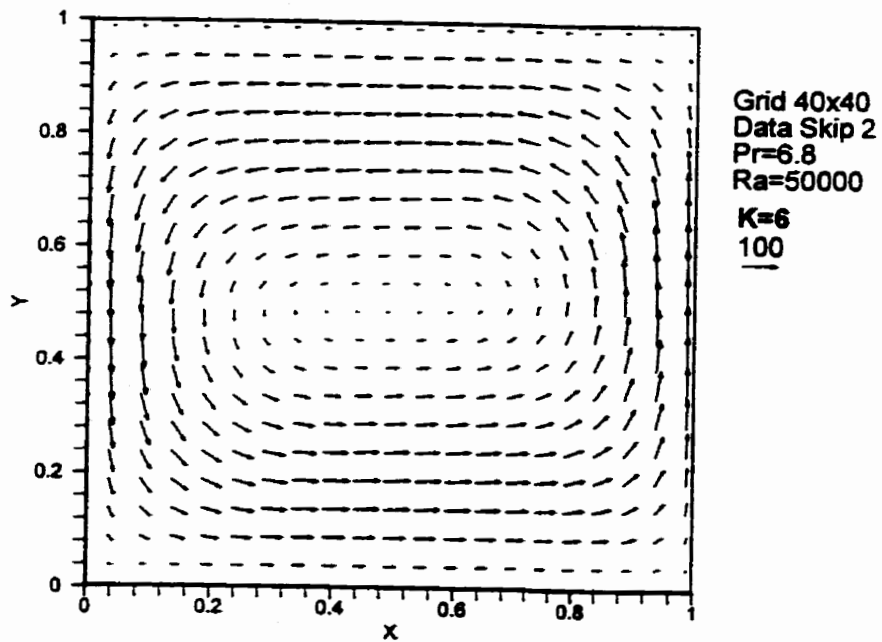


Figure 5.24 Velocity vectors for  $\text{Ra}=50000$ ,  $\text{Pr}=6.8$ , with  $K=6$

Table 5.2 lists the Nusselt numbers for different K. The Nusselt numbers are associated with the flow patterns and have same values for the pattern with one roll and same values for the pattern with two rolls. The heat transfer for the flow pattern with two rolls structure is greater by about 2.3% than that for the flow pattern with one roll structure. In two rolls structure, the more flow channels result in more heat carried by convection from bottom to top. It should be mentioned that the computations were carried out using the code for transient process. How the flow structures vary with time can be investigated so that the final steady state results can be explained with the development over time.

Initial conditions for $\theta$	Rolls	Nusselt number
=0	2	3.966
=0.5-Y+0.01cos( $\pi X$ )	1	3.876
=0.5-Y+0.01cos(2 $\pi X$ )	2	3.966
=0.5-Y+0.01cos(3 $\pi X$ )	2	3.966
=0.5-Y+0.01cos(4 $\pi X$ )	1	3.876
=0.5-Y+0.01cos(5 $\pi X$ )	2	3.966
=0.5-Y+0.01cos(6 $\pi X$ )	1	3.876

Table 5.2 Nusselt numbers in the steady state for different initial conditions

## **5.3 Natural Convection in Rectangular Enclosures Partly Heated from the Bottom and Cooled along a Side Wall**

In this section, a computational investigation of natural convection in a square enclosure heated partly from below and cooled on one vertical side is described. We consider an enclosure which has the left and top wall insulated, the bottom wall partly isothermally heated and partly insulated, and the right vertical wall isothermally cooled.

The problem of natural convection in an enclosure with obliquely applied temperature gradients also has been investigated by a few researchers. For example, Kimura and Bejan (1985) conducted a fundamental study of the natural convection in a rectangular enclosure with one vertical wall heated and the bottom wall cooled. They applied scale analysis and numerical simulations to carry out the study. Their analysis revealed that a single cell flow pattern existed in the corner region where temperature is discontinuous, regardless of Rayleigh number, while the flow rate and the net heat transfer rate varied as  $\text{Ra}^{1/7}$ . In a combined numerical and experimental study on natural convection in an inclined box, Chao et al. (1983) considered the

case of the lower wall half-heated and half-insulated while the upper wall was cooled. They found a single pair of rolls with this arrangement and that convective motion existed at all Rayleigh numbers greater than zero. In an analytical and numerical study November and Nansteel (1987) considered natural convection in a square, water-filled enclosure partly heated from below and cooled on one vertical side. Expansions for small Rayleigh number were developed to order  $\text{Ra}^2$ . Asymptotic expressions were found for temperature and heat transfer near a flux singularity on the enclosure floor. Finite difference numerical simulations indicated that the flow structure for heating from below differed dramatically from the behaviour reported by Kimuar and Bejan (1985) where heating and cooling roles were reversed. The Nusselt number was shown to reach a maximum when the insulation spanned slightly more than half of the lower surface.

In the present study, computational results are obtained for  $\text{Pr}=6.8$  (water) and  $\text{Ra} = 10^4$ ,  $10^5$ , and  $10^6$ . The heating sections of the lower wall are 0.3, 0.4, 0.5, 0.6, 0.7 and 0.8 of the whole length of the wall. The aspect ratio of the enclosure is 1. The steady state temperature and velocity are obtained and presented. The isotherms for Rayleigh number  $10^4$ ,  $10^5$ ,  $10^6$  are presented and isotherm patterns for the different amounts of bottom wall heating are revealed. The thermal boundary

layer phenomenon is readily observed for high Rayleigh number.

Figures 5.25 to 5.27 show contours of temperature for the enclosure with 0.3, 0.5 and 0.7 of the lower surface heated, and  $\text{Ra}=10^4$ ,  $10^5$ , and  $10^6$ . It is observed that isotherms become very dense at the connecting point of the heating section and adiabatic section near the flux singularity mentioned above. These isotherms are dilated along left side and pinched along right side due to the circulating motion of fluid. When the Rayleigh number increases, the thermal boundary layer becomes more distinct. Fluid flows upward near the left adiabatic wall as the heat propagates from the heating section. Warm fluid then moves across toward the upper section of the cold wall. The fluid cools and flows vertically downward along this wall. It is also observed that the isotherms are nearly horizontal in the centre, preventing any vertical motion there as  $\text{Ra}$  increases. The isotherms are compressed at the upper right corner due to flow to that region. In Fig. 5.28, the isotherm plot for Rayleigh number  $10^6$  and heating section of 0.5 is compared with a previous numerical study by November and Nansteel (1987) using the finite difference method to solve the equations for vorticity and stream function. Very good agreement between the two sets of temperature contours is found as shown thus providing further good evidence of the success of the present formulation and application of the finite volume method.

Grid 40x40, Pr=6.8, Heating Section 0.3

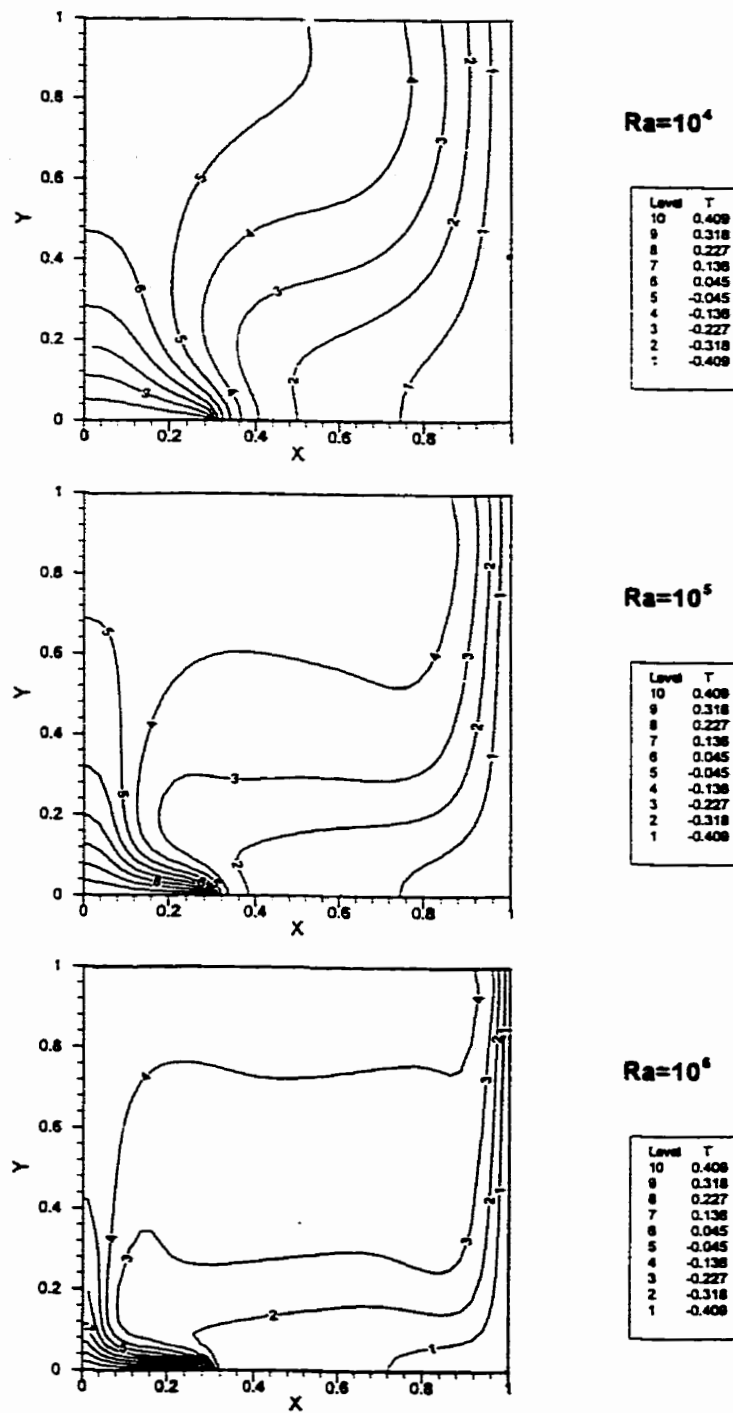


Figure 5.25 Temperature contours for heating section of 0.3,  $Ra=10^4, 10^5, 10^6$

Grid 40x40, Pr=6.8, Heat Section 0.5

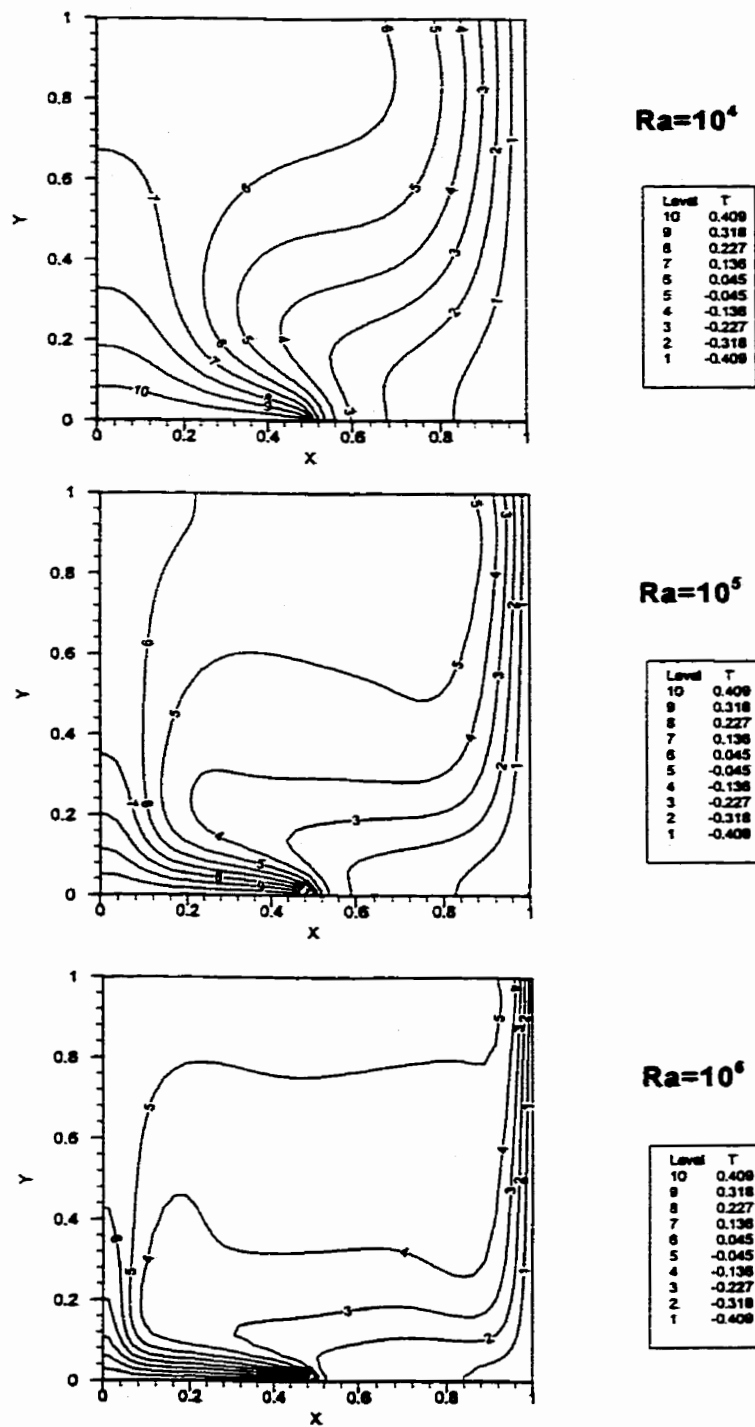


Figure 5.26 Temperature contours for heating section of 0.5, Ra=10<sup>4</sup>, 10<sup>5</sup>, 10<sup>6</sup>

Grid 40x40, Pr=6.8, Heating Section 0.7

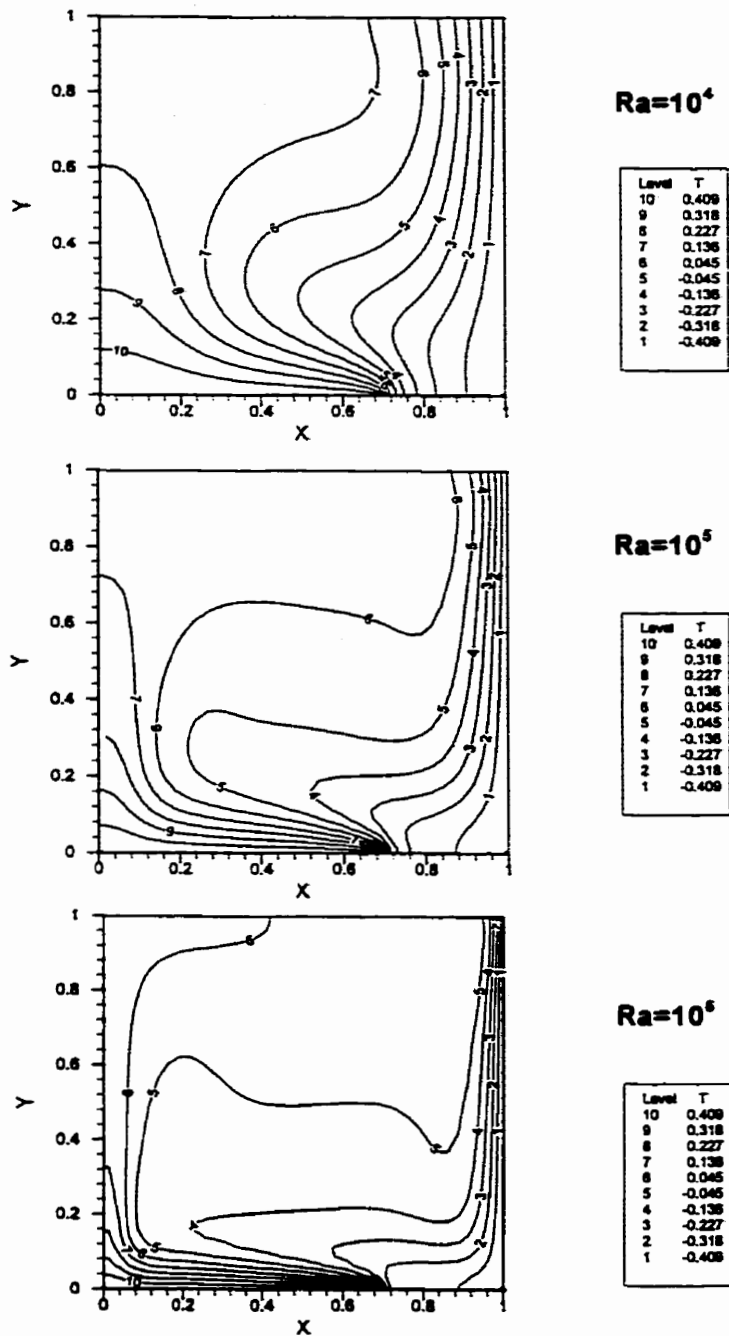
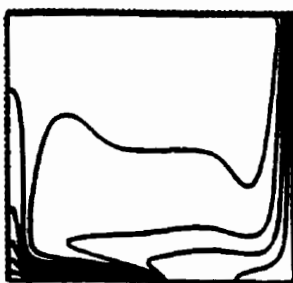
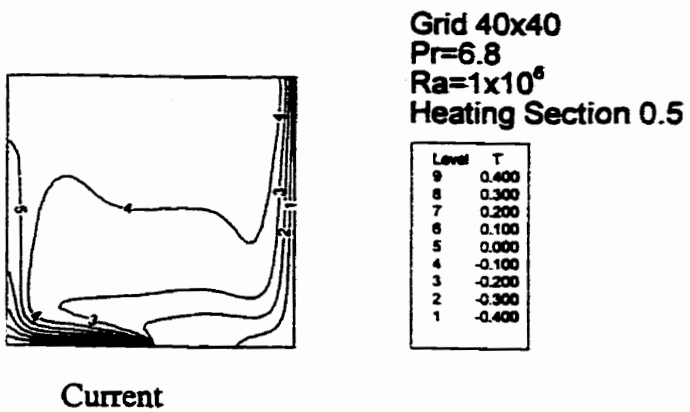


Figure 5.27 Temperature contours for heating section of 0.7,  $Ra=10^4, 10^5, 10^6$



**November and Nansteel**

**Figure 5.28 Comparison of temperature contours between the current work and November and Nansteel's study for  $Ra=10^6$  and heating section of 0.5**

From the isotherms, we see that the thermal boundary layers are getting thinner when heating sections vary from 0.3 to 0.7 for same Rayleigh number. By observing the isotherms marked 4 and 5, we see the trend of migration of these isotherms. For Rayleigh number of  $10^6$ , the upper end of isotherm 5 is attached to the left wall for heating section of 0.3, but migrates to the upper wall for heating section of 0.5 and 0.7. If we observe the migration of isotherm 4, we estimate the thermal boundary layer thicknesses are roughly about 0.08, 0.05 and 0.03 for Rayleigh number  $10^6$ . For the same heating section, as Rayleigh number increases, the thermal boundary layer becomes thinner. In the case of the heating section of 0.5, the isotherm 5 migrates from 0.78, to 0.88 and to 0.92 in X position. If we consider isotherm 5 as boundary of the thermal boundary layer, the thicknesses would be 0.22, 0.12 and 0.08. The migration of the isotherms demonstrates the convection strengthening with increasing Rayleigh number and heating section.

Fig. 5.29 to 5.31 show velocity vectors for the enclosure with 0.3, 0.5 and 0.7 of the lower surface heated, and Rayleigh number,  $Ra=10^4$ ,  $10^5$ , and  $10^6$ . Due to the high temperature and strong buoyancy near the heating section, the velocity boundary layers are thinner along the two vertical walls and lower wall with fast flow

and thicker along the upper walls with slow flow in order to satisfy mass conservation. The boundary layers get thinner as the Rayleigh number increases which is expected due to the relationship between boundary layer thickness and Rayleigh number given by scale analysis. From the velocity vectors it is seen that the maximum velocity occurs near the two vertical walls. In table 5.3, the maximum vertical velocity components and their locations are listed for different heating section (HS in table) and Rayleigh number. It is seen that when convection strengthens with increasing Rayleigh number, the maximum vertical velocity moves to close to the sidewall ( $X=0$ ) with indication of a thinner velocity boundary layer.

Ra	HS	X	Y	$V_{max}$
$10^4$	0.3	0.1625	0.4125	17.72
$10^5$	0.3	0.0875	0.3375	76.82
$10^6$	0.3	0.0375	0.2375	257.32
$10^4$	0.5	0.1625	0.4125	19.63
$10^5$	0.5	0.0875	0.3625	85.28
$10^6$	0.5	0.0625	0.3125	283.21
$10^4$	0.7	0.1875	0.4375	19.73
$10^5$	0.7	0.0875	0.3625	87.54
$10^6$	07	0.0625	0.3375	300.35

Table 5.3 Maximum vertical velocities and their locations for different cases

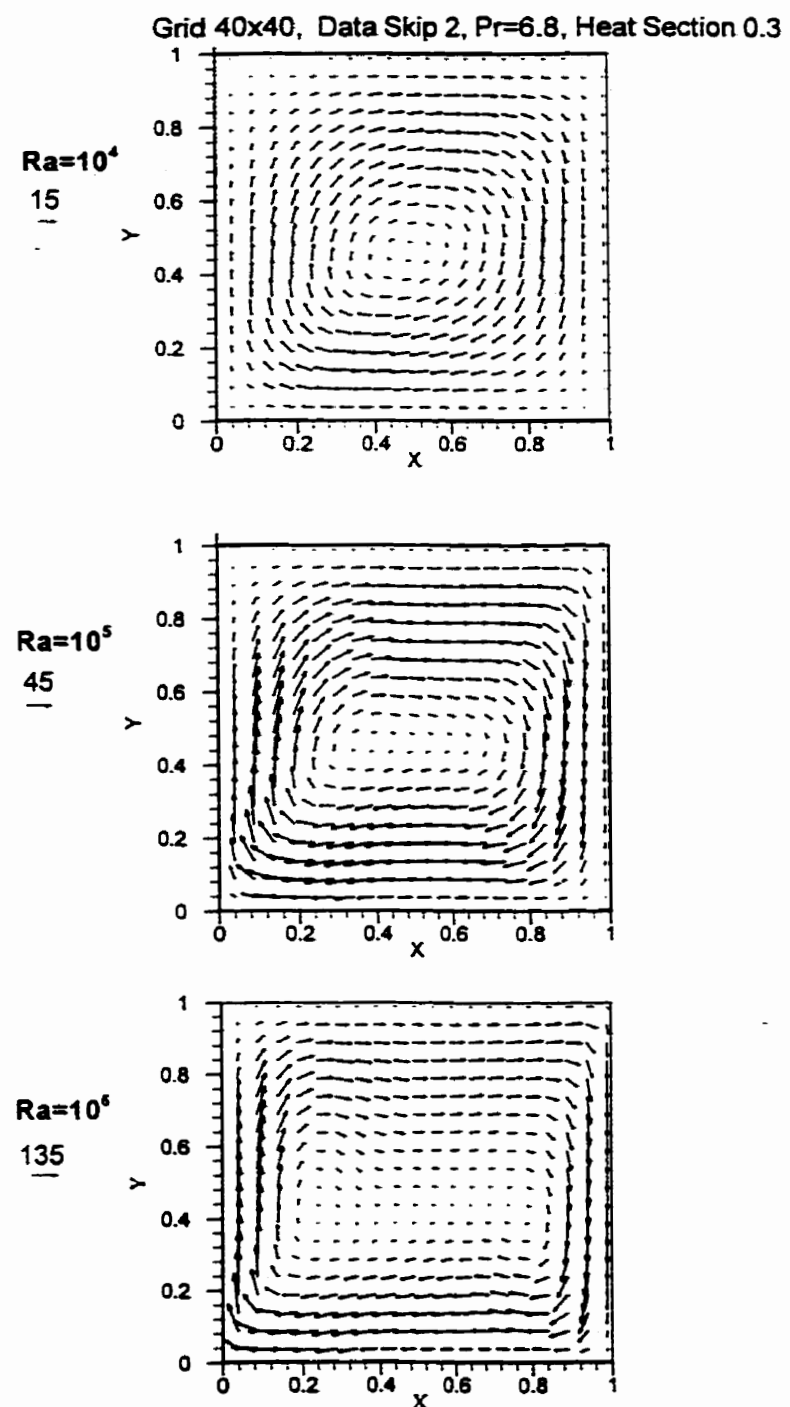


Figure 5.29 Velocity vectors for heating section of 0.3,  $\text{Ra}=10^4, 10^5, 10^6$

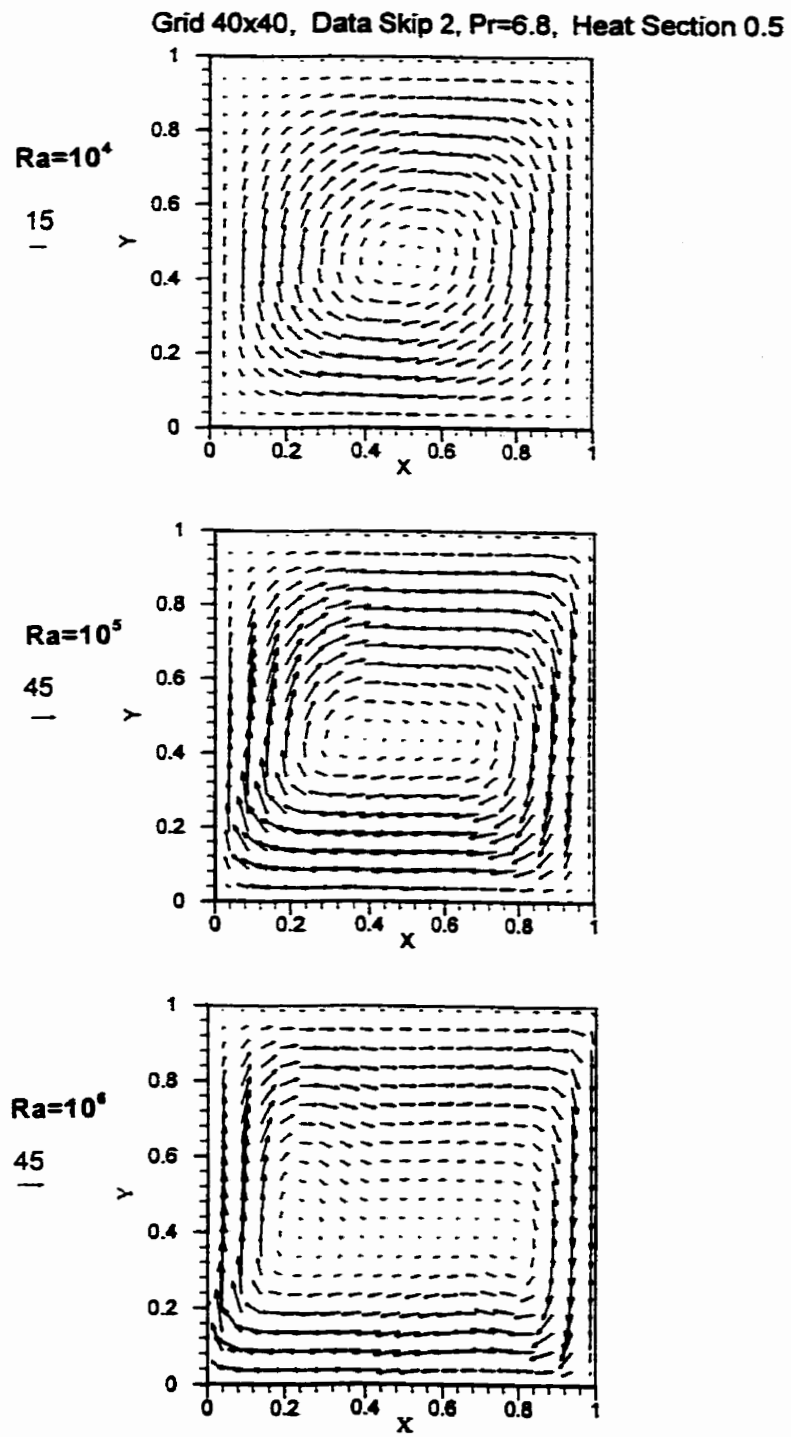


Figure 5.30 Velocity vectors for heating section of 0.5,  $Ra=10^4, 10^5, 10^6$

Grid 40x40, Data Skip 2, Pr=6.8, Heat Section 0.7

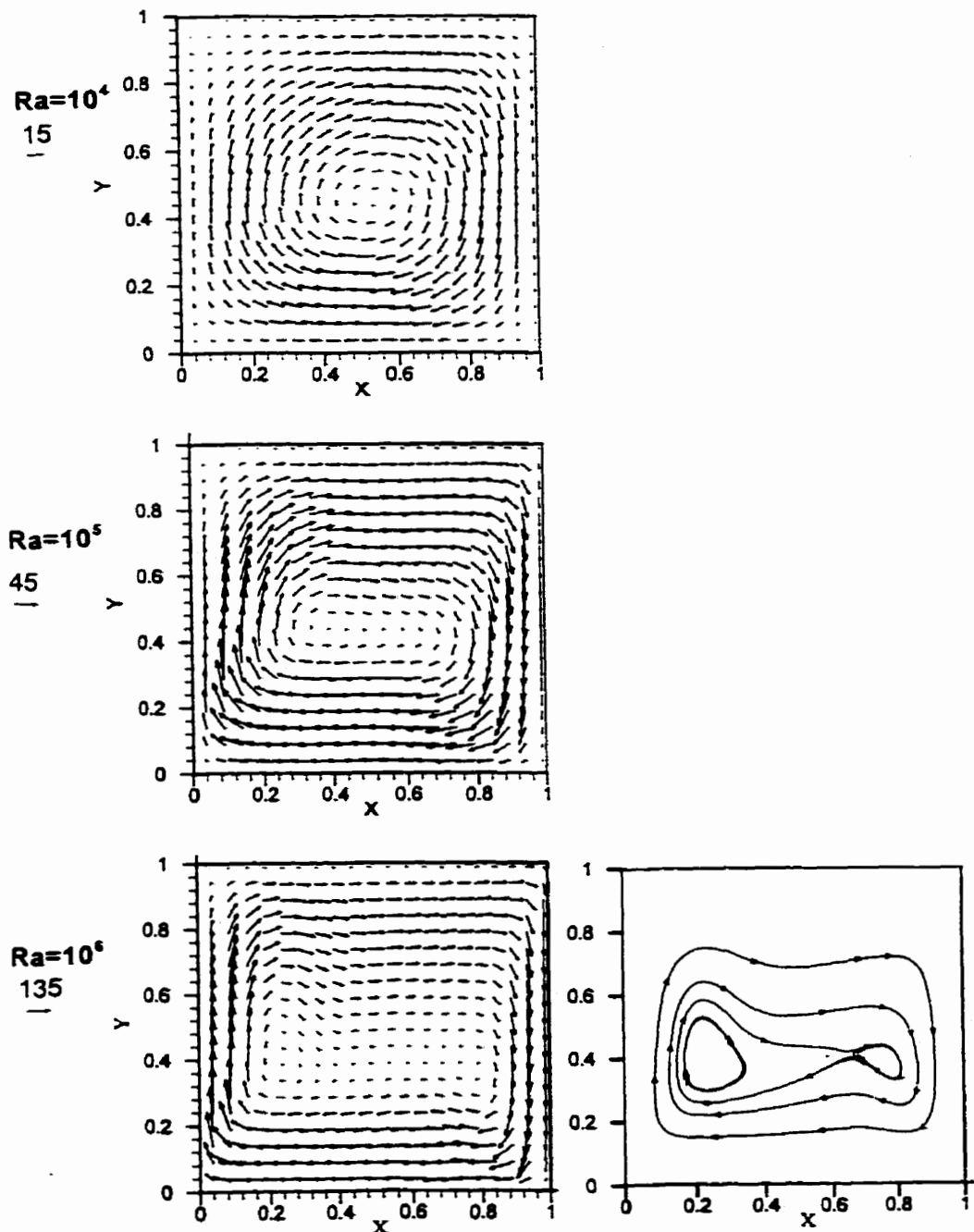


Figure 5.31 Velocity vectors for heating section of 0.7,  $\text{Ra}=10^4, 10^5, 10^6$  and streamtraces for  $\text{Ra}=10^6$

The one cell flow pattern for lower Rayleigh number has developed to two co-rotating cells as the Rayleigh number reaches  $10^6$ . For increasing heating section, it is noted that the amplitude of the velocity has increased and the temperature field is more distorted. Strong convection occurs for the large heating section. The high velocity vectors move to the left and right walls and boundary layers get thinner when the Rayleigh number increases. This is consistent with the scale analysis for the relationship of boundary layer thickness proportional to the quarter power of the Rayleigh number.

In Fig. 5.32, Nusselt numbers from current study (solid line) plotted against the heating section for Rayleigh number  $10^4$ ,  $10^5$ , and  $10^6$  are compared with that obtained by November and Nansteel (1987)(symbols). The Nusselt numbers obtained by November and Nansteel are measured by a ruler from their graph. The Nusselt number increases when the heating section increases. It also shows that the difference between the two studies is small. It is important to note that they used a finer mesh size  $61 \times 61$ , than the one employed in current study of  $40 \times 40$ . The results found here are consistent with those of November and Nansteel thus further supporting the current formulation of the finite volume method for a problem of mixed horizontal and vertical, heating and cooling.

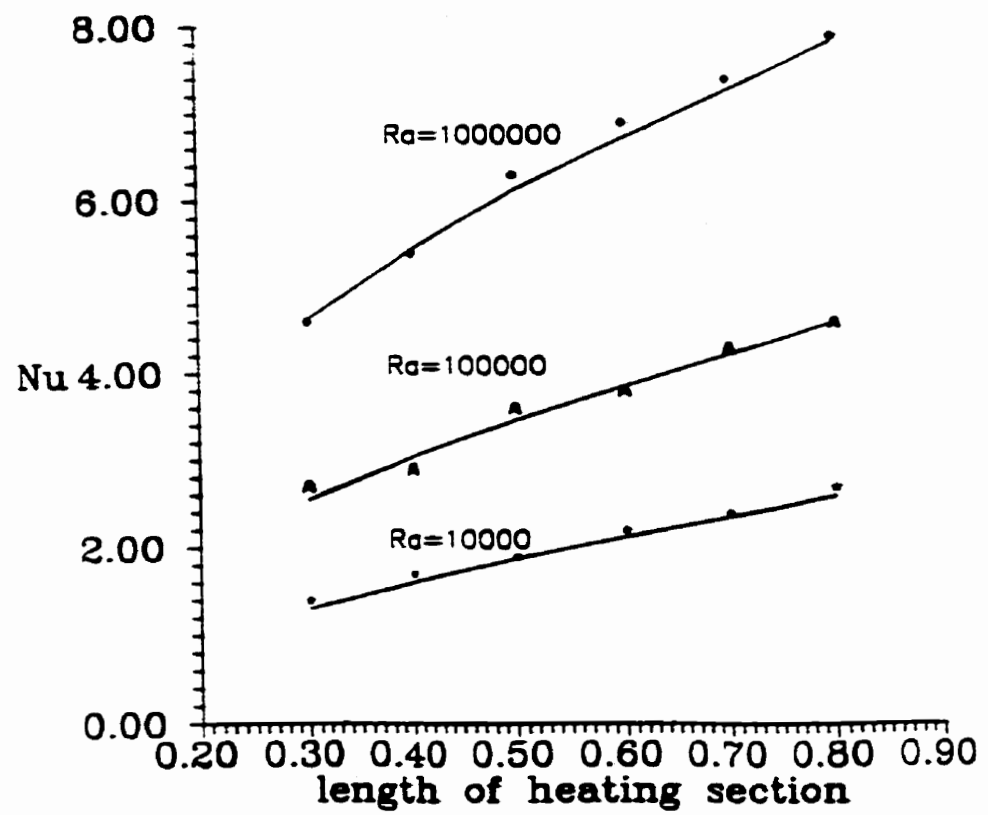


Figure 5.32 Nusselt number versus heating section for  $Ra=10^4, 10^5, 10^6$

## **5.4 Results for Natural Convection in a Rectangular Enclosure**

Studies on natural convection in a rectangular enclosure have been extensively conducted by many researchers using the finite difference method, the finite element method and experimental methods. The features of heat transfer and flow in such a problem have been well expounded. Among these studies, de Vahl Davis's (1983) numerical solution on such problems using the finite difference method has been cited as a classical reference for other researchers. Hortmann, Perić and Scheuerer (1990) presented a finite volume multigrid procedure for study on laminar natural convection. Their studies were conducted by numerically solving steady state natural convection problem. The current study is conducted by numerically solving the unsteady natural convection problem to obtain steady solutions. In order to test the current method and perform a comparison with the results of others, numerical solutions for several examples in the present study are presented in this section.

The enclosure considered here is with left wall heated, right wall cooled, top

and bottom walls adiabatic, and non-slip velocity boundary conditions as shown in Figure 2.3. These examples provided here are for Rayleigh number of  $10^4$ ,  $10^5$ ,  $10^6$  and Prandtl number of 0.71, representing air as the working fluid. The grids used are 40x40 for Rayleigh number of  $10^4$ ,  $10^5$ , and 40x40 and 80x80 for Rayleigh number of  $10^6$ . The time step is 0.011 with 6 iterations in its interval for the cases with 40x40 grids and 0.0005 with 35 iterations in its interval for the case with 80x80 grids to guarantee the stable solution. It is common that a criterion for judging a steady state solution achieved is by considering the Nusselt number. We observe both variations of the Nusselt number and a velocity component and define convergence by a change of 0.0001 over 10 to 100 steps in time.

Figure 5.33 shows the velocity vectors at steady state for Rayleigh number of  $10^4$ ,  $10^5$ , and  $10^6$  and streamtraces for rayleigh number of  $10^6$  at the central region. For Rayleigh number of  $10^4$ , the flow pattern is identified as a one vortex. Due to heating of the left wall, the rotation is clockwise. The fluid at the hot side flows up to the top wall then toward the cold wall flowing down to complete the circulation. For Rayleigh number of  $10^5$ , the flow is characterized by two secondary vortices. Such a feature of the flow has been noted by all previous researchers. The secondary vortices in the enclosure are apparently caused by convective distortion

of the temperature field. Heat transfer due to convection in the viscous boundary layers makes the temperature gradients near zero in central region and contributes to the development of secondary vortices in the region. When the Ra increases to  $10^6$ , the secondary vortices move closer to the walls and a small third vortex rotating clockwise develops in the central region. This could be attributed to the small positive temperature gradient in the centre. The viscous boundary layers at the two vertical side walls are thinner and flow faster. Heat transfer is mostly due to convection by jets near the side walls. Taking consideration of the scale analysis for boundary layer thicknesses  $\delta_v \sim (\text{Pr}/\text{Ra})^{1/4}$ , we note that boundary layer thickness decreases with increasing Rayleigh number. From the plots we estimate the ratio of two thicknesses for two Rayleigh numbers to be roughly 1.8, whereas the ratio of two thicknesses for two Rayleigh numbers is  $(10)^{1/4} = 1.778$  from the scale analysis presented in section 5.1. Therefore, the trend of variation of the boundary layer thickness can be estimated based on the dependence of Rayleigh number.

Fig. 5.34 presents isotherms for Rayleigh number of  $10^4$ ,  $10^5$ ,  $10^6$ . We note that when the Rayleigh number increases, the thermal boundary layer gets intensive and thinner. From the scale analysis, the thermal boundary layer thickness expressed as  $\delta_T \sim (\text{PrRa})^{-1/4}$  has same trend of variation as velocity boundary layer thickness. It

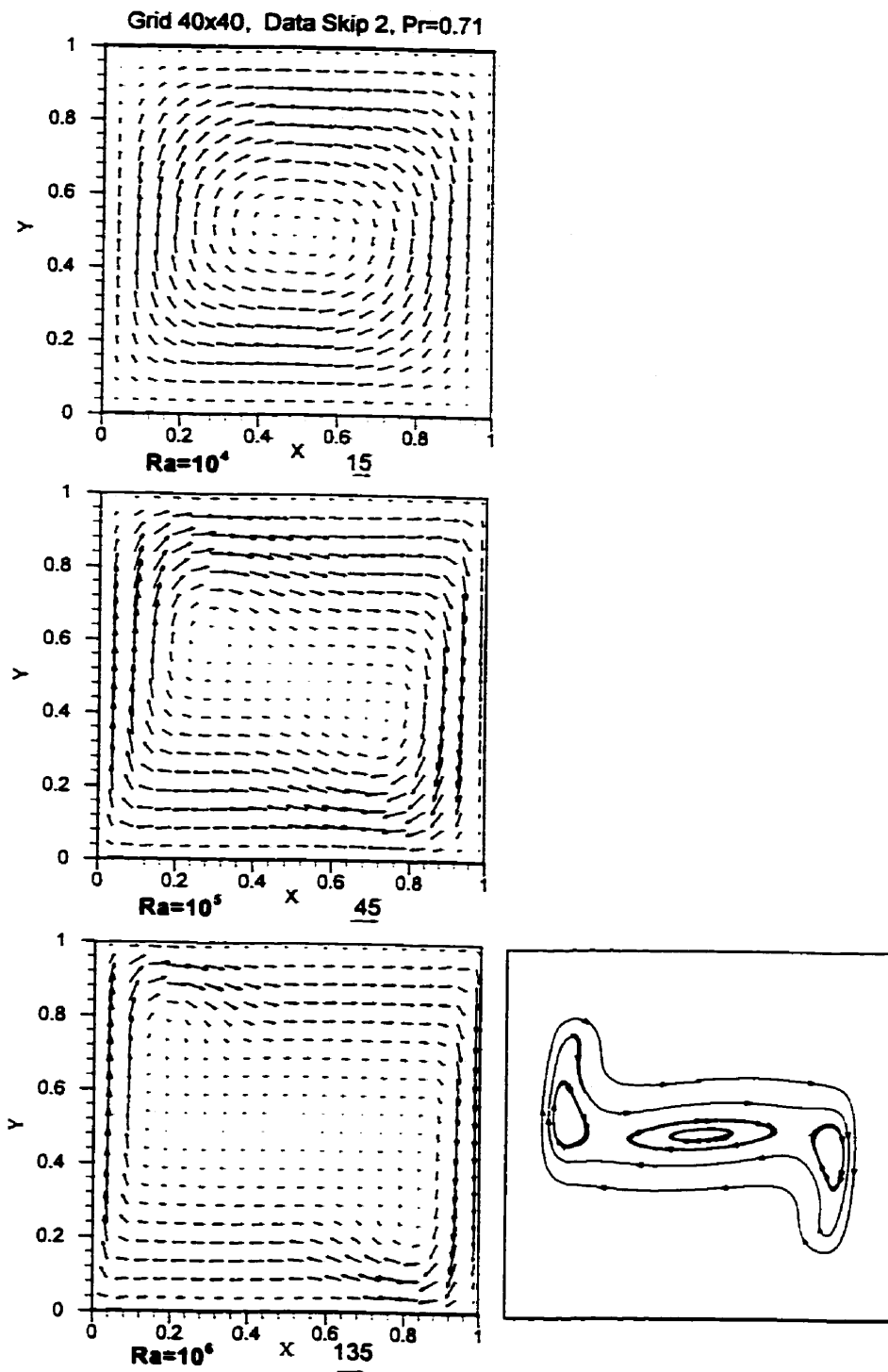


Figure 5.33 Velocity vectors for  $\text{Ra}=10^4, 10^5, 10^6$ , streamtraces for  $\text{Ra}=10^6$ ,  $\text{Pr}=0.71$

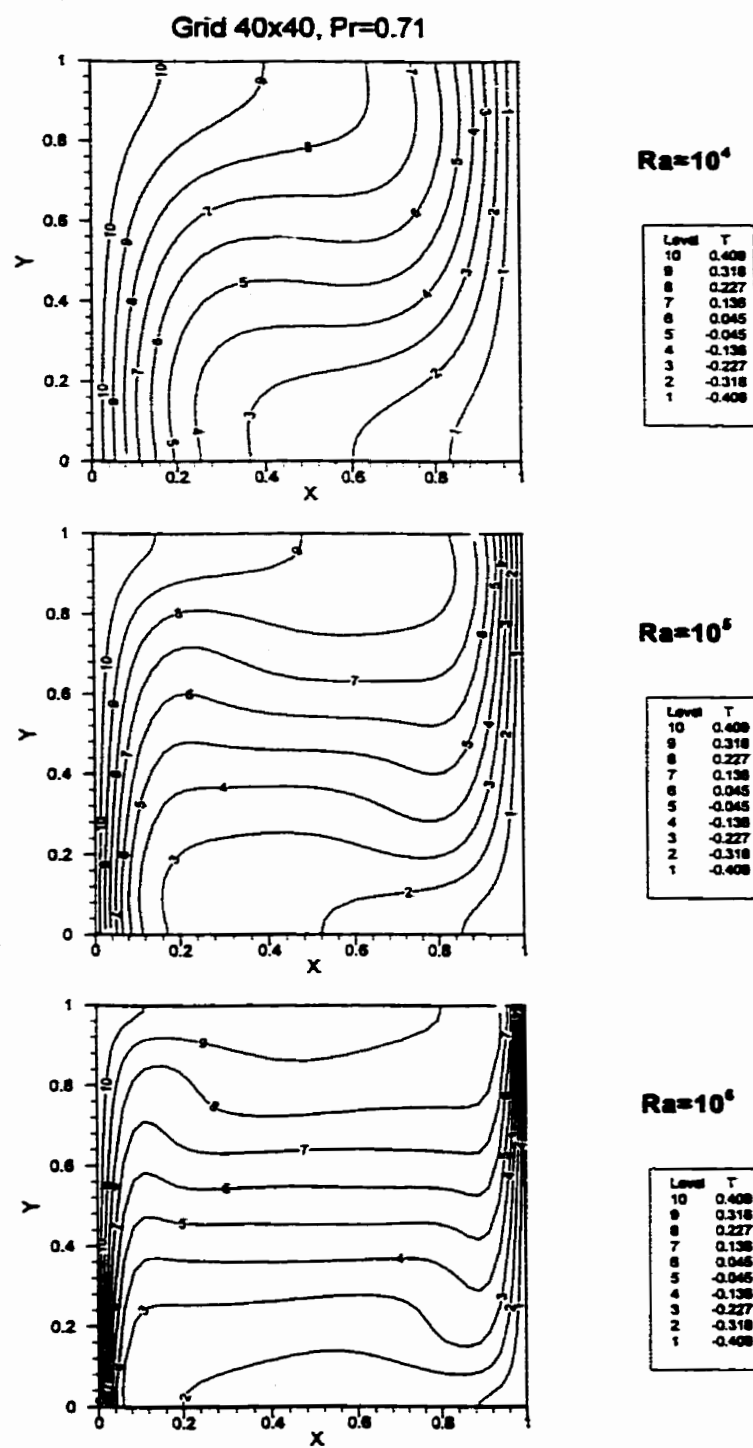


Figure 5.34 Isotherms for  $\text{Ra}=10^4, 10^5, 10^6$ ,  $\text{Pr}=0.71$

should be noted that such expression can be only used as rough estimation of the trend of the thicknesses variation. Because convection strengthens and secondary vortices appear, isotherms become horizontal in the centre. At a Rayleigh number  $10^6$ , the temperature distribution is vertically stratified in the central region and temperature increases from bottom to top of the enclosure thus preventing vertical motion. In the central region, velocity is much smaller than that in the boundary layer. For decreasing Rayleigh number the thicknesses of thermal boundary layer are about 0.04, 0.09 and 0.2 if we trace the upper end of the isotherm of 6. However, the values for these thicknesses by scale analysis are about 0.034, 0.061 and 0.109 so that while we can only use the expression for boundary layer thickness by scale analysis as an estimation of the actual thickness, the trend of thickness change is consistent with the scaling of  $\text{Ra}^{-1/4}$ .

De Vahl Davis (1983) carried out the computations using different meshes. Table 5.4 lists the average Nusselt numbers obtained by current study (2) and by de Vahl Davis (1)(1983). The values listed here are for meshes  $40 \times 40$ . We also applied  $80 \times 80$  grids to the case of Rayleigh number of  $10^6$  and obtained the Nusselt number of 8.9693. As expected the Nusselt number increases when the Rayleigh number increases. Agreement between the two methods improves to 1% at  $\text{Ra}=10^4$ .

Ra	$10^4$		$10^5$		$10^6$	
	1	2	1	2	1	2
Nu	2.242	2.243	4.564	4.519	9.270	9.386

Table 5.4 Comparison of Nusselt numbers between current(2) and de Vahl Davis(1)

In table 5.5, we list the results for Nusselt numbers on uniform grids 40x40(3) and non-uniform grids 40x40(4) obtained by Hortmann et al. (1990) who solved the steady problem using the finite volume method.

Ra	$10^4$		$10^5$		$10^6$	
	4	3	4	3	4	
Nu		2.2436	4.6165	4.5373	9.4217	8.9313

Table 5.5 Nusselt numbers from Hortmann et al.

What we found is that the current results listed in table 5.4 for Nusselt numbers are lower than those for uniform grid (3) from Hortmann et al. (1990). It appears that the current results are more accurate ones than (3). According to the

arguments by Hortmann et al. (1990), the results on a non-uniform grid are more accurate than those on a uniform grid. As already noted, the current results are more accurate than the results on a uniform grid by Hortmann et al. (1990) but even slightly more accurate than the results on non-uniform grid of Hortmann et al. (1990) for Rayleigh number of  $10^4$  and  $10^5$ , as shown as comparing case (2) from table 5.4 with case (4) from table 5.5

The results from de Vahl Davis were obtained by solving steady state governing equations for stream function and vorticity. The present results are obtained by solving unsteady state governing equations for primitive variables. In order to gain an understanding of transient features, the horizontal velocities at the mid-vertical line for three points at various vertical positions are presented in Fig. 5.35- 5.37. The oscillatory behaviour during the early period has been displayed. We see that as time reaches a certain point, the results remain constant and reflect a steady state solution. Further investigation on features of transient flow structure and heat transfer can be done by outputting the intermediate results.

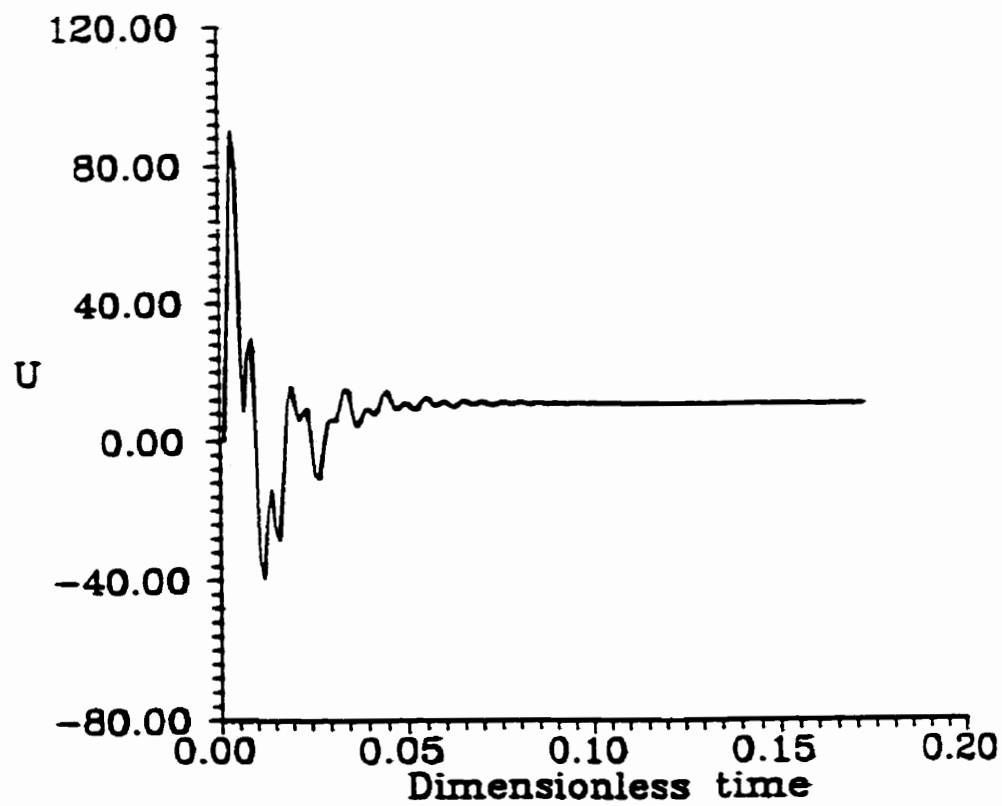


Figure 5.35 Horizontal velocity  $U$  at  $X=0.4875$ ,  $Y=0.6375$ , for  $Ra=10^6$ ,  $Pr=0.71$   
versus dimensionless time

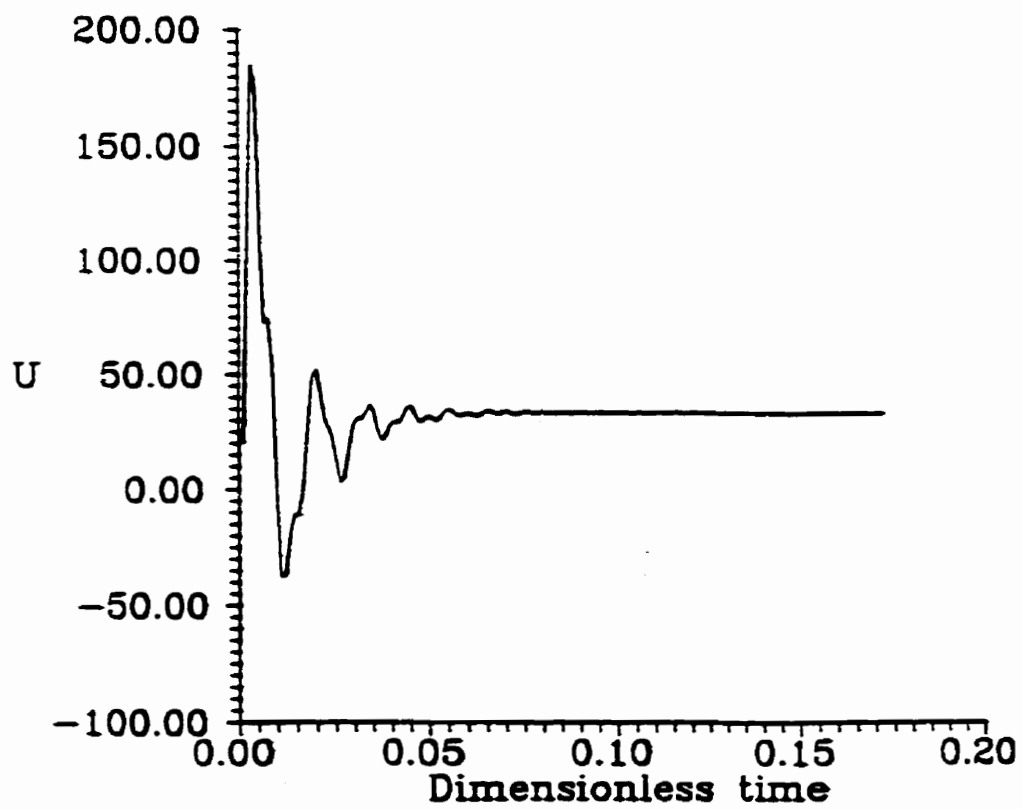


Figure 5.36 Horizontal velocity  $U$  at  $X=0.4875$ ,  $Y=0.7625$ , for  $Ra=10^6$ ,  $Pr=0.71$  versus dimensionless time

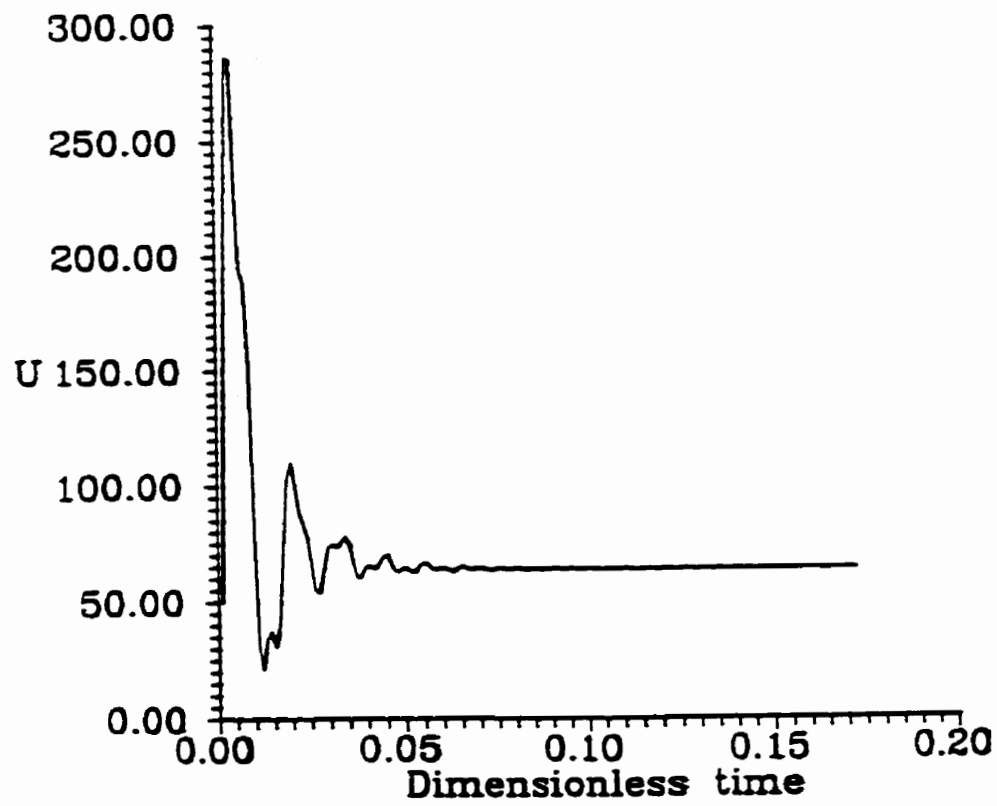


Figure 5.37 Horizontal velocity  $U$  at  $X=0.4875$ ,  $Y=0.8875$ , for  $Ra=10^6$ ,  $Pr=0.71$   
versus dimensionless time

## **5.5 Natural Convection in a Parallelogrammic Enclosure with Two Vertical Walls and Two Inclined Walls**

This section presents the numerical results for natural convection in a two-dimensional parallelogrammic enclosure. The enclosure considered has the left vertical wall isothermally heated, right vertical wall cooled, and two inclined parallel upper and lower walls insulated. In such a geometric shape, the enclosure is discretized with a non-orthogonal, parallelogrammic control volume. As mentioned in chapter 3, the finite volume method can be directly applied to solving mass, heat and momentum transport problems with a complex computational domain. Using a non-orthogonal grid in solving such a problem, complex mathematical transformation is not needed.

Computations were carried out for Rayleigh numbers of  $10^4$ ,  $10^5$ , and  $10^6$  and Prandtl number of 0.71. The enclosures have equal length of sidewalls. The inclination angles of the upper and lower walls of the parallelogrammic enclosure are chosen as  $15^\circ$ ,  $30^\circ$ ,  $45^\circ$ , and  $60^\circ$  relative to the horizontal direction. Results for temperature, velocity and Nusselt numbers at steady state are presented.

Figures 5.38 and 5.39 show the velocity vectors and isotherms for the case of inclination angle  $15^\circ$ . At the lowest  $\text{Ra}=10^4$ , the flow pattern is observed to be one cell. The vectors are plotted at every other point (data skip 2) of the  $40 \times 40$  grid. In this case, conduction plays a dominant role so that the velocity boundary layers almost extend to the centre of the enclosure. Convection does exist, however, and in the steady state there is approximate balance between the rate at which heat is conducted into fluid and the rate at which heat is convected away. Accordingly, a slow steady circulation is generated, with flow upward along the hot wall and downward along the cold wall. From Figure 5.39, we observe that the isotherms are distorted due to the weak circulation. The temperature gradient in the horizontal direction is negative almost everywhere in the whole interior of the enclosure. The isotherms starting at the lower wall near the heating side are nearly parallel to the sidewall and spread out about half way up the wall. Since there is a slight tilt of the bottom wall, fluid does not flow into the corner so that the isotherms are not quite parallel to the wall. As the hot fluid circulates towards to the cooling sidewall, isotherms are compressed at the upper right corner. These dense isotherms diverge from the lower half of cooling side because the fluid cools down at this side and circulates to form a cool jet. These isotherms finally are compressed again to the lower left corner. The higher temperature gradients in horizontal direction are at the

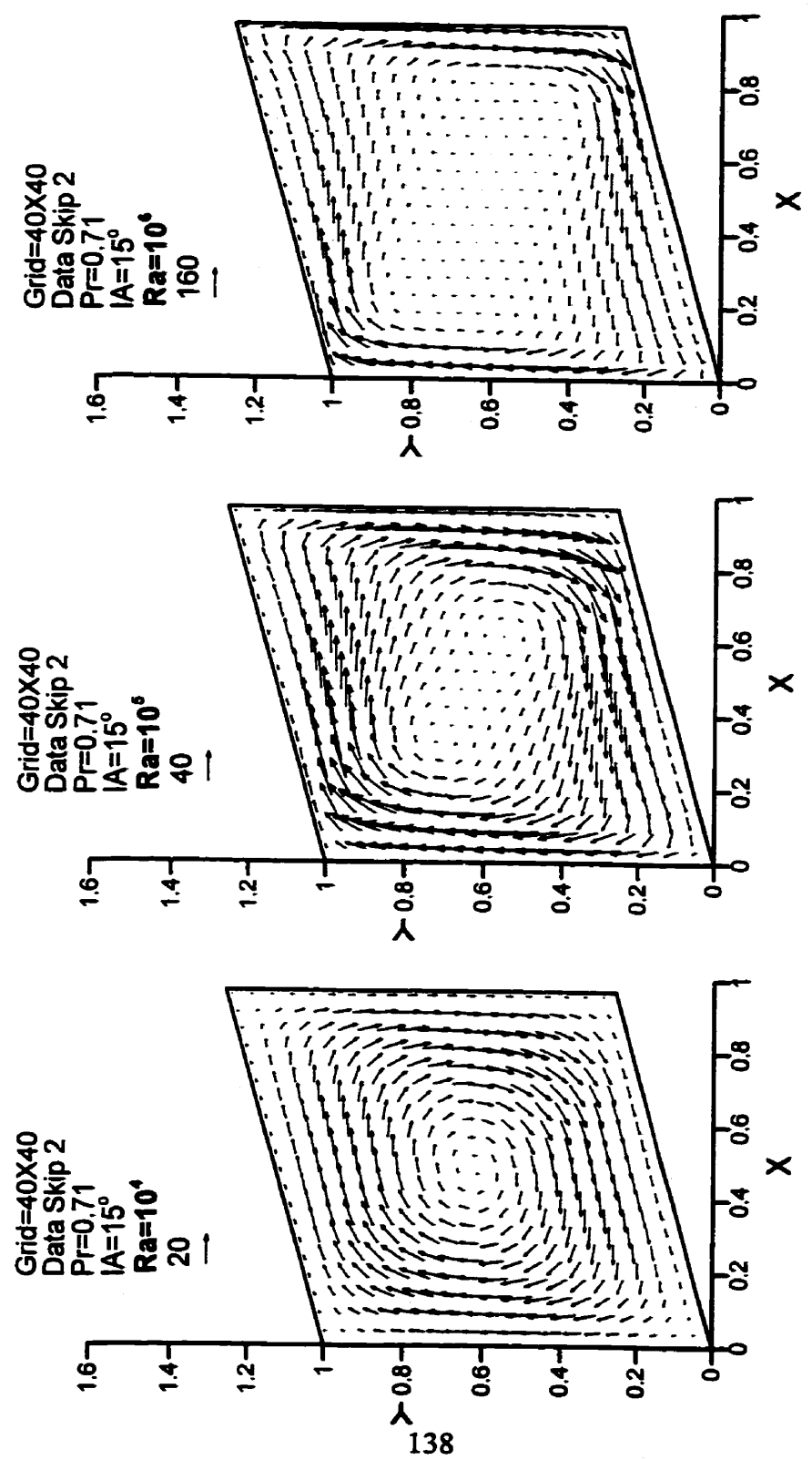


Figure 5.38 Velocity vectors for  $IA=15^\circ$ ,  $Ra=10^4, 10^5, 10^6$

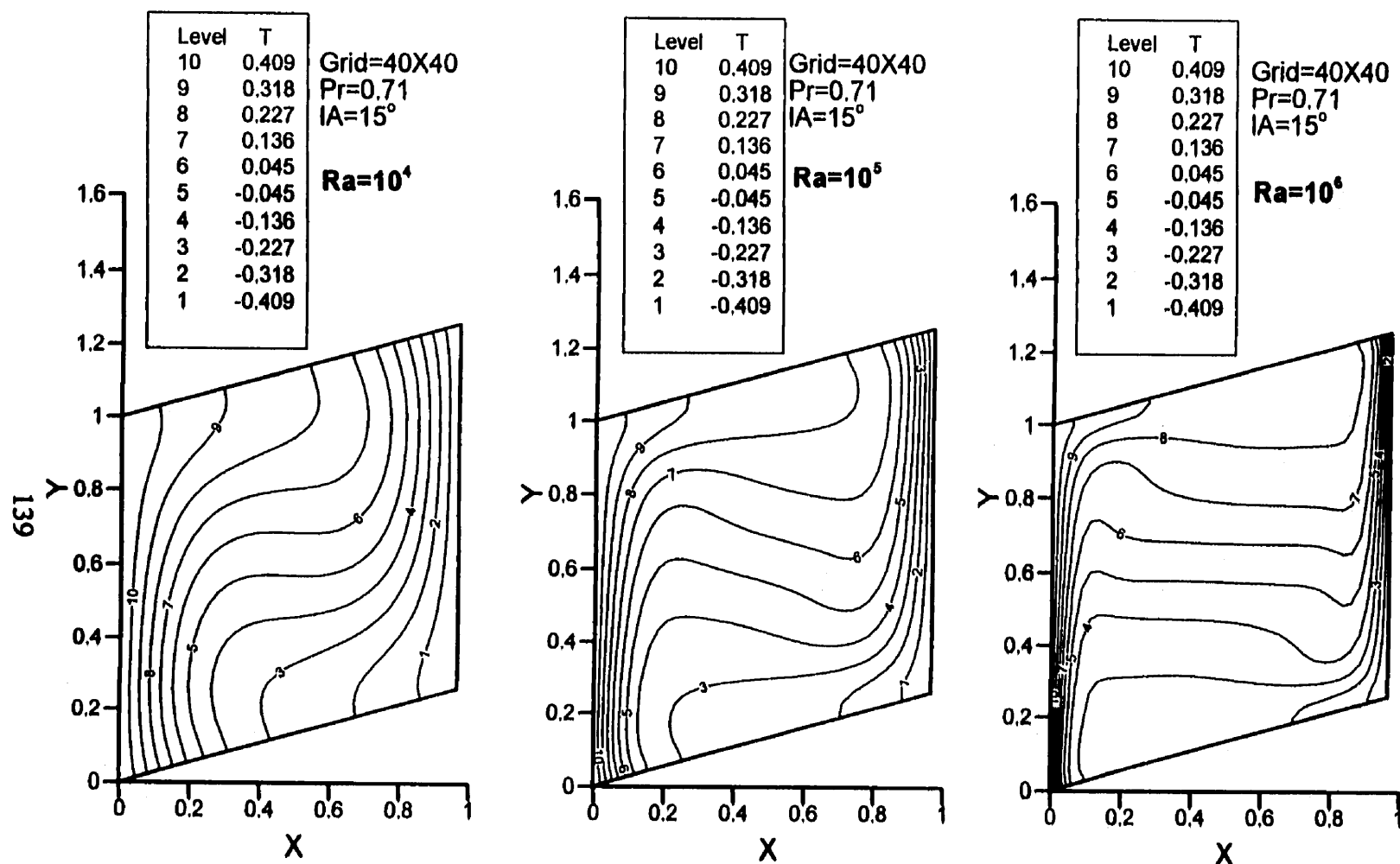


Figure 5.39 Isotherms for  $\text{IA}=15^\circ$ ,  $\text{Ra}=10^4, 10^5, 10^6$

upper right and low left corners, while the lower temperature gradients are seen at the upper left side and lower right side. As the Rayleigh number increases to  $10^5$ , larger temperature gradients are created along the walls. Convection is stronger and the flow has concentrated near the walls to form the boundary layers. While the same balance as discussed above exists, the heat transfer is increased and is accompanied by a strengthened convection mode. At this  $\text{Ra}=10^5$ , the flow pattern becomes two secondary vortices in the central region, with the main circulation confined to boundary layers. The formation of the secondary vortices was attributed to a sign change of the temperature gradient in the central region as previously argued by Mallinson and de Vahl Davis (1984) . In this case, the isotherms are further distorted due to the stronger convection. Compressed isotherms extend longer along the side wall due to the stronger convection. This defines the thermal boundary layer which is thinner than in the previous case. A negative horizontal temperature gradient is generated. The isotherms are more densely compressed at the upper right and lower left corners with appearance of the thermal boundary layer. At  $\text{Ra}=10^6$  , the convection continues to strengthen with the creation of thinner boundary layers and the two secondary vortices are stretched towards to the side walls and convected further downstream. At this high Rayleigh number, the boundary layer flow is so well established that the strong vorticity near the walls is able to sustain a weak

Grid 80X80  
Data Skip 2  
 $\text{Ra}=10^6$   
 $\text{Pr}=0.71$   
 $\text{IA}=15^\circ$   
 $10^-$

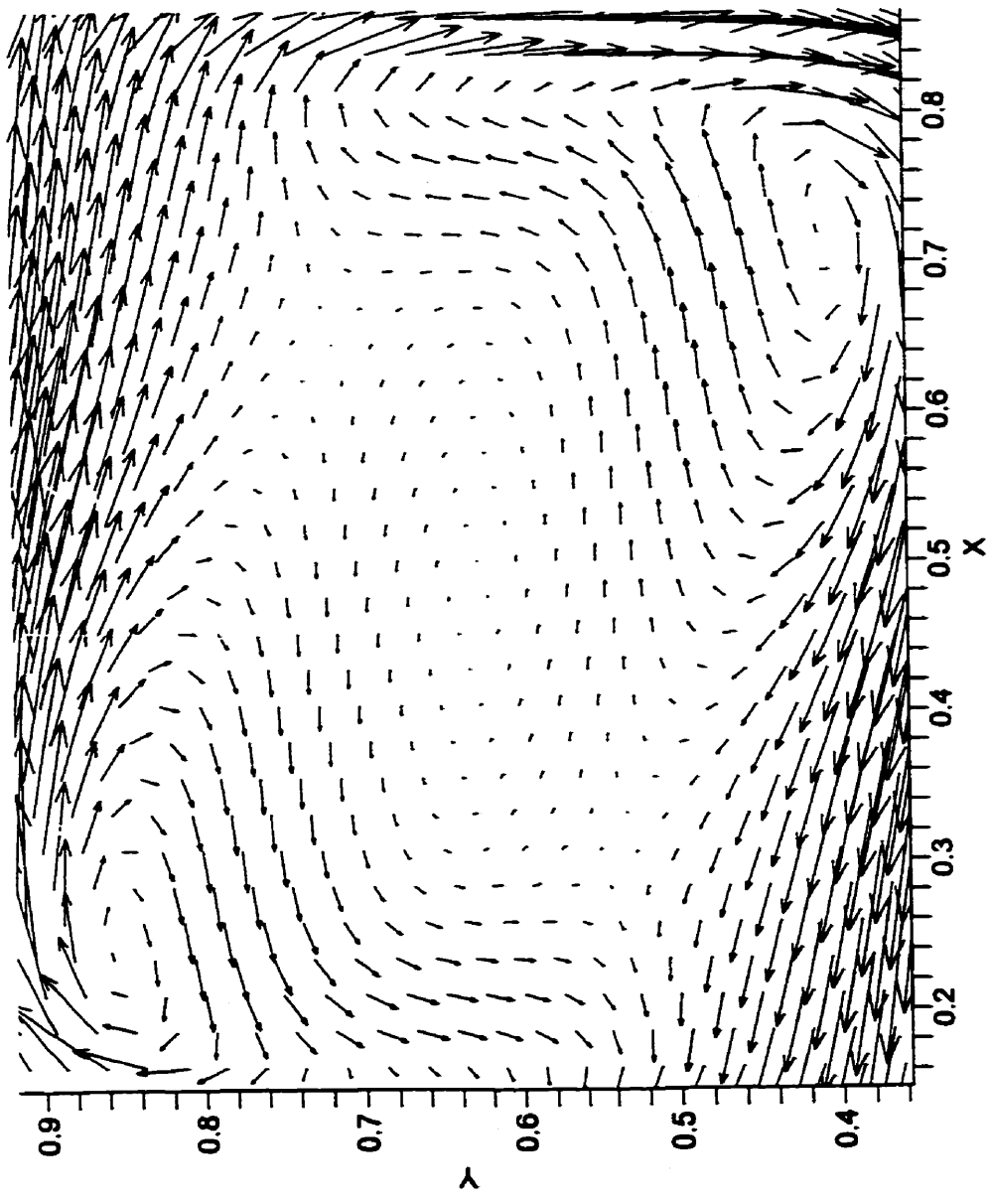


Figure 5.40 Velocity vectors in central region of the enclosure for  $\text{IA}=15^\circ$ ,  $\text{Ra}=10^6$

return motion “counterclockwise roll” possibly through viscous force coupling in this region of return flow as shown in Figure 5.40. The isotherms are further compressed along the two sidewalls and layered in the low velocity central region. The temperature gradient in the horizontal direction near the walls is increased and the central region has horizontal contours. The thermal boundary is thinner and heat transfer increases due to stronger convection.

Figure 5.41 and 5.42 show the velocity vectors and temperature contour for the inclination angle of  $30^\circ$  and for  $\text{Ra}=10^4, 10^5, 10^6$ . Here we observe flow patterns for the Rayleigh number  $10^4$  and  $10^5$  as one vortex. The boundary layers for the latter case are distinctive while for the former case the boundary layers extended into the centre of the box. This boundary layer development is characteristic of slow viscous flow with solid boundaries. At  $\text{Ra}=10^6$ , the boundary layers are thinner and flow is confined to these narrow layers. The core region of low velocity becomes larger. The isotherms are slightly less compressed compared to the case for inclination angle of  $15^\circ$ . The development of the thinner thermal boundary is observed with increasing Rayleigh number. For  $\text{Ra}=10^4$ , the convection allows convection of heat away so that the isotherms are distorted slightly with positive temperature gradient. For  $\text{Ra}=10^5$ , the convection is stronger, however the isotherms are more distorted with

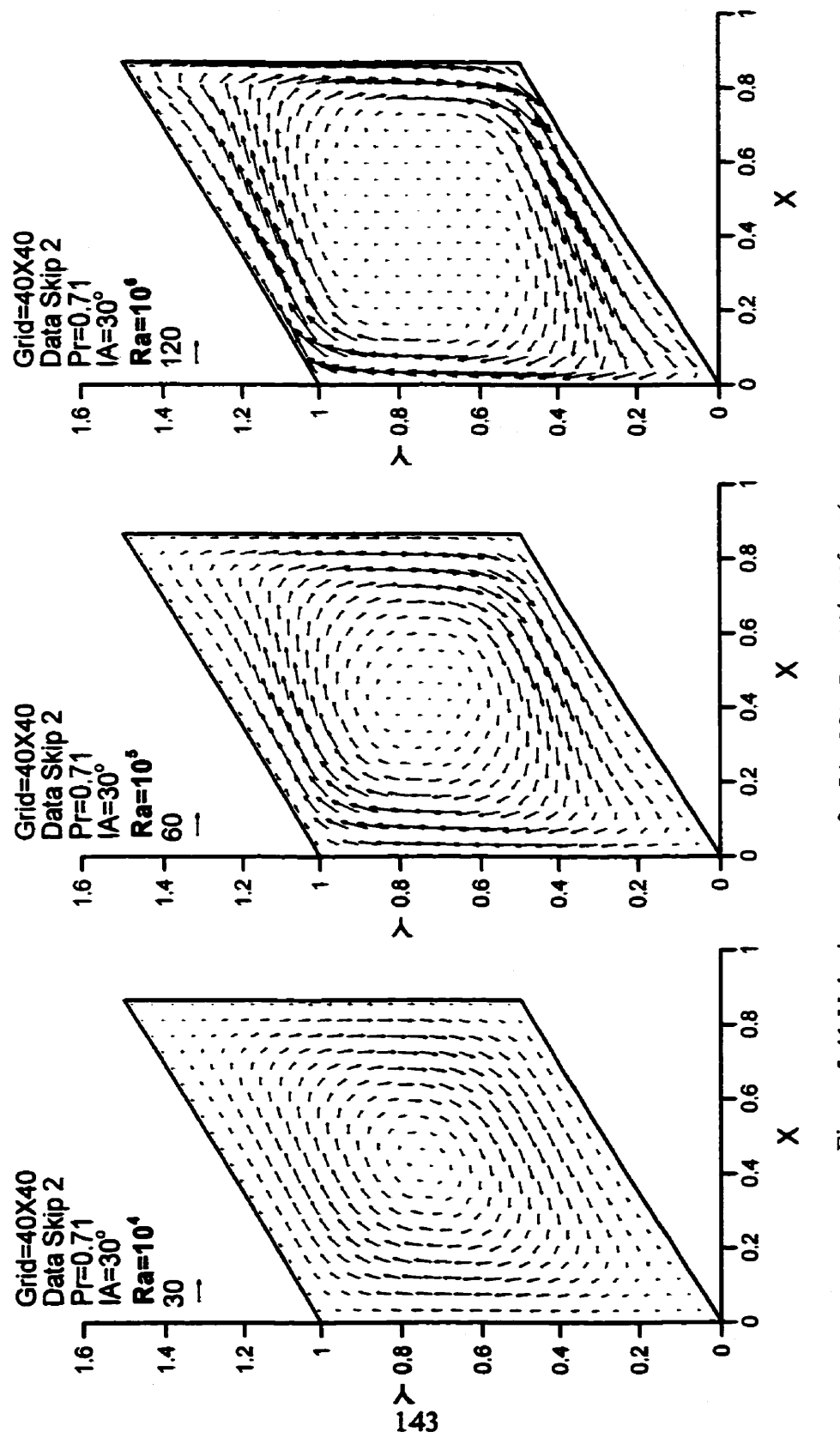


Figure 5.41 Velocity vectors for  $\text{IA}=30^\circ$ ,  $\text{Ra}=10^4, 10^5, 10^6$

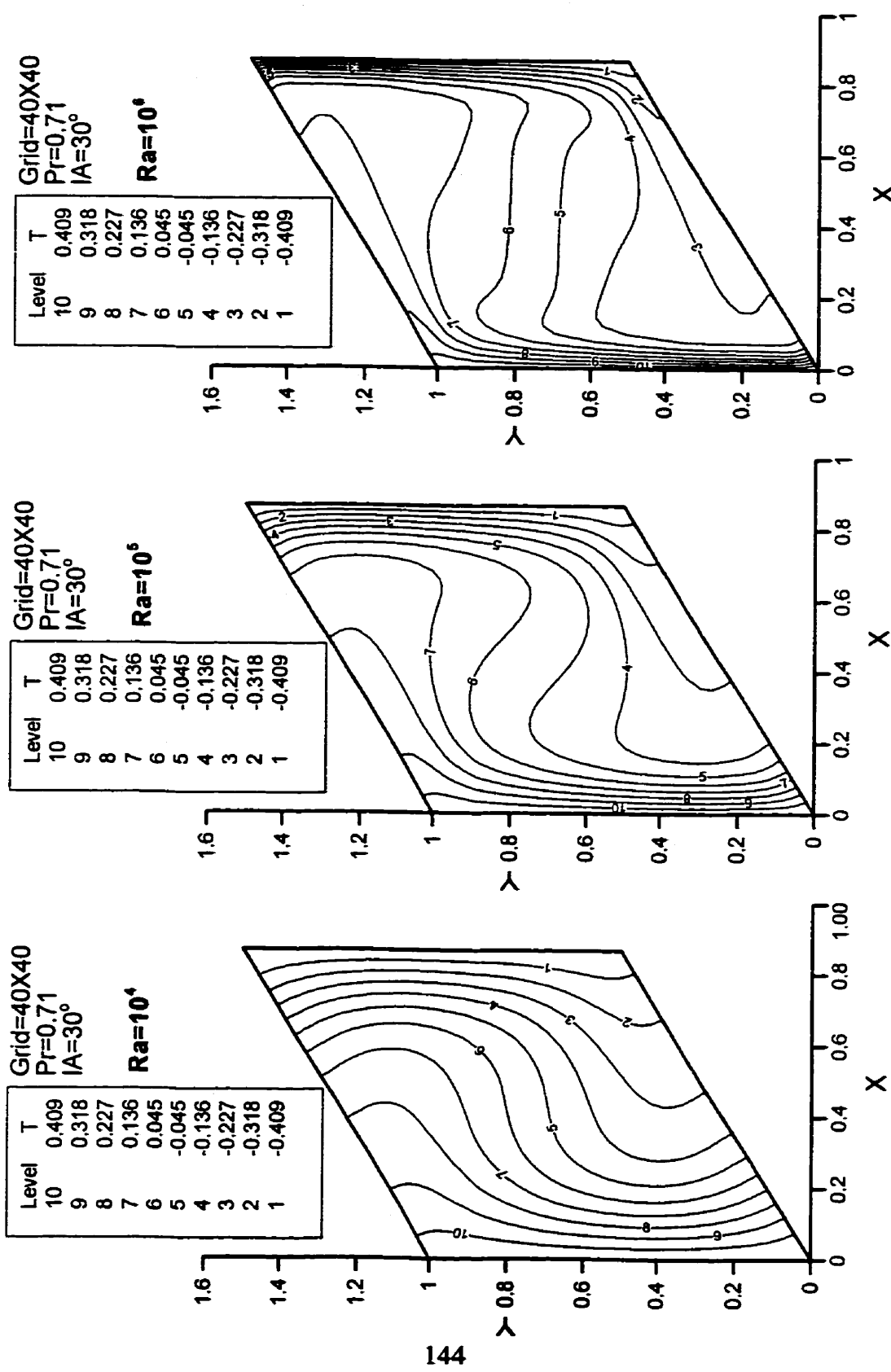


Figure 5.42 Isotherms for  $IA=30^\circ$ ,  $\text{Ra}=10^4, 10^5, 10^6$

a smaller region of negative horizontal temperature gradient compared to the case of inclination angle  $15^\circ$ . For  $\text{Ra}=10^6$ , the isotherms are compressed tightly on both side walls. Temperature jet-like profiles are formed near the two side while the small central region has stratified layers.

Figure 5.43 and 5.44 show the velocity vectors and isotherms for the inclination angle of  $45^\circ$  and for  $\text{Ra}=10^4, 10^5, 10^6$ . For this angle, the flow patterns are almost same as for the case of inclination angle of  $30^\circ$ , with the main flows marked as one vortex but with slightly thicker boundary layers. The regime in the centre continues as a slow motion region. At  $\text{Ra}=10^6$ , the boundary layers are still thinner and the flow is transported in these narrow layers. The core region of lower velocity occupies a small fraction of the cell compared to the case for  $\text{IA}=30^\circ$ . At this inclination angle, the isotherms are less distorted than the case of inclination angle of  $15^\circ$ . Heat transfer increases with increasing Rayleigh number and bounder layers are thinner as expected.

Figure 5.45 and 5.46 show the velocity vectors and isotherms for the inclination angle of  $60^\circ$  and for  $\text{Ra}=10^4, 10^5, 10^6$ . While the main flow patterns are not significantly changed compared to the case of inclination angle of  $45^\circ$ , boundary

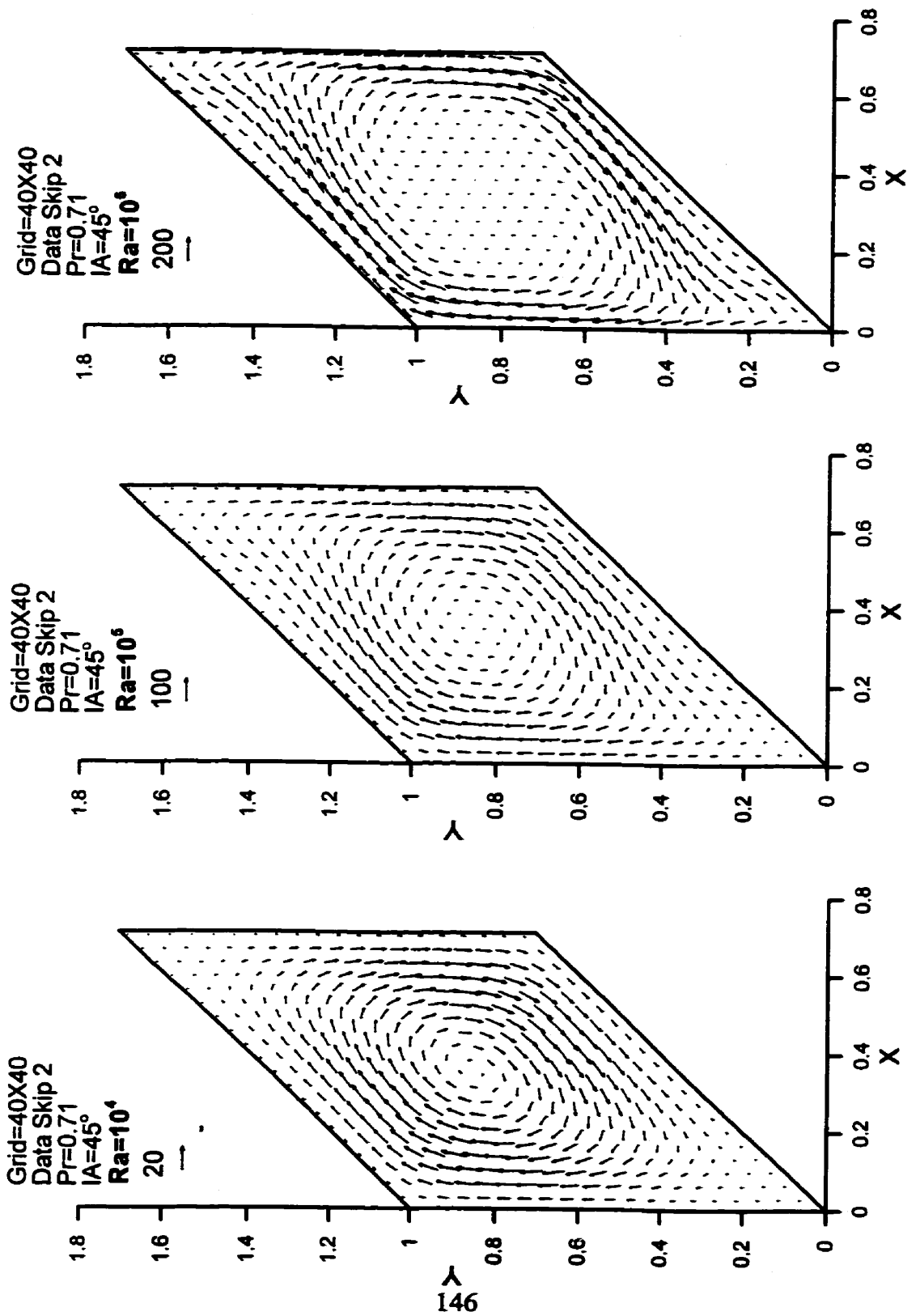


Figure 5.43 Velocity vectors for  $IA=45^\circ$ ,  $Ra=10^4, 10^5, 10^6$

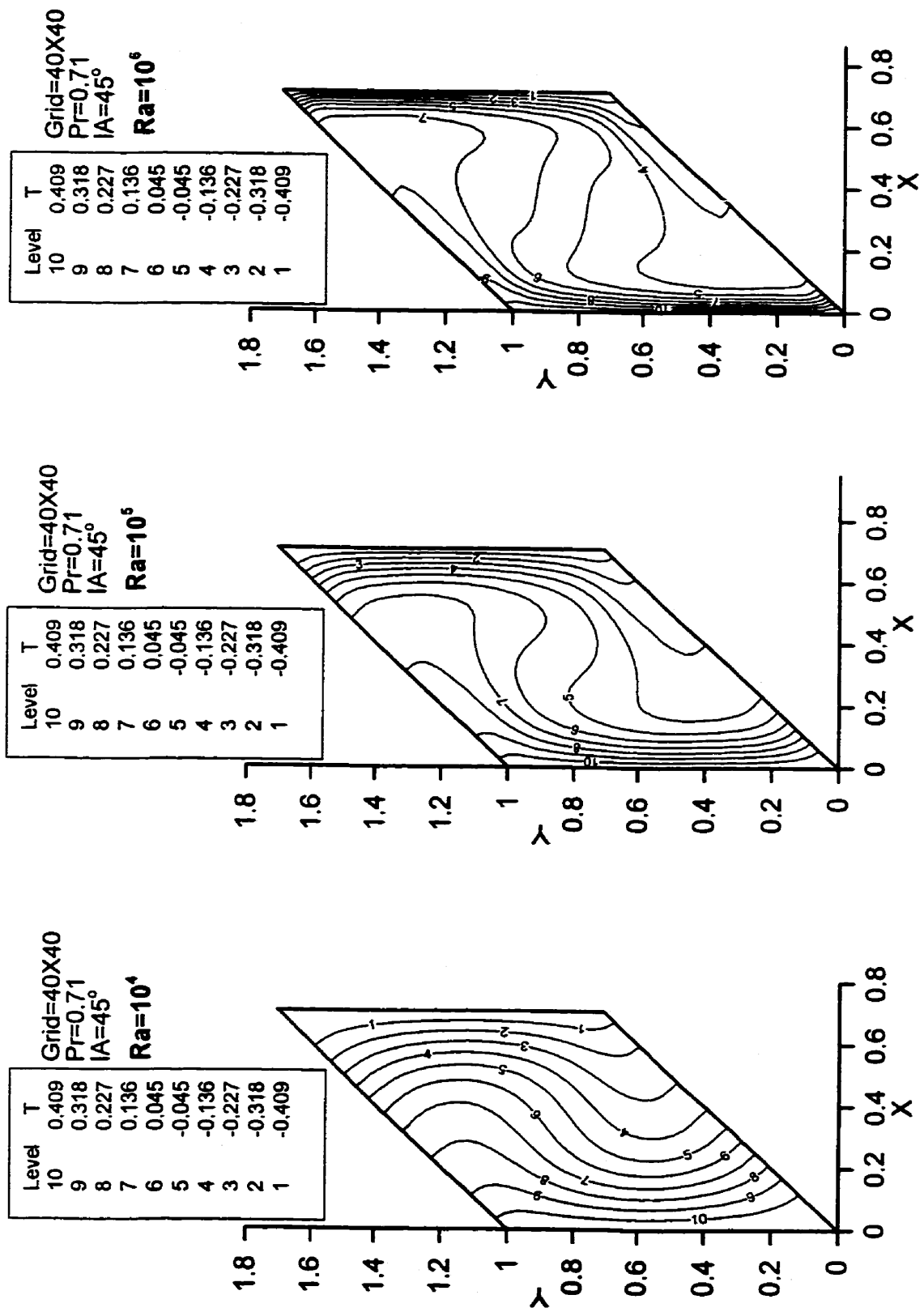


Figure 5.44 Isotherms for  $\text{IA}=45^\circ$ ,  $\text{Ra}=10^4, 10^5, 10^6$

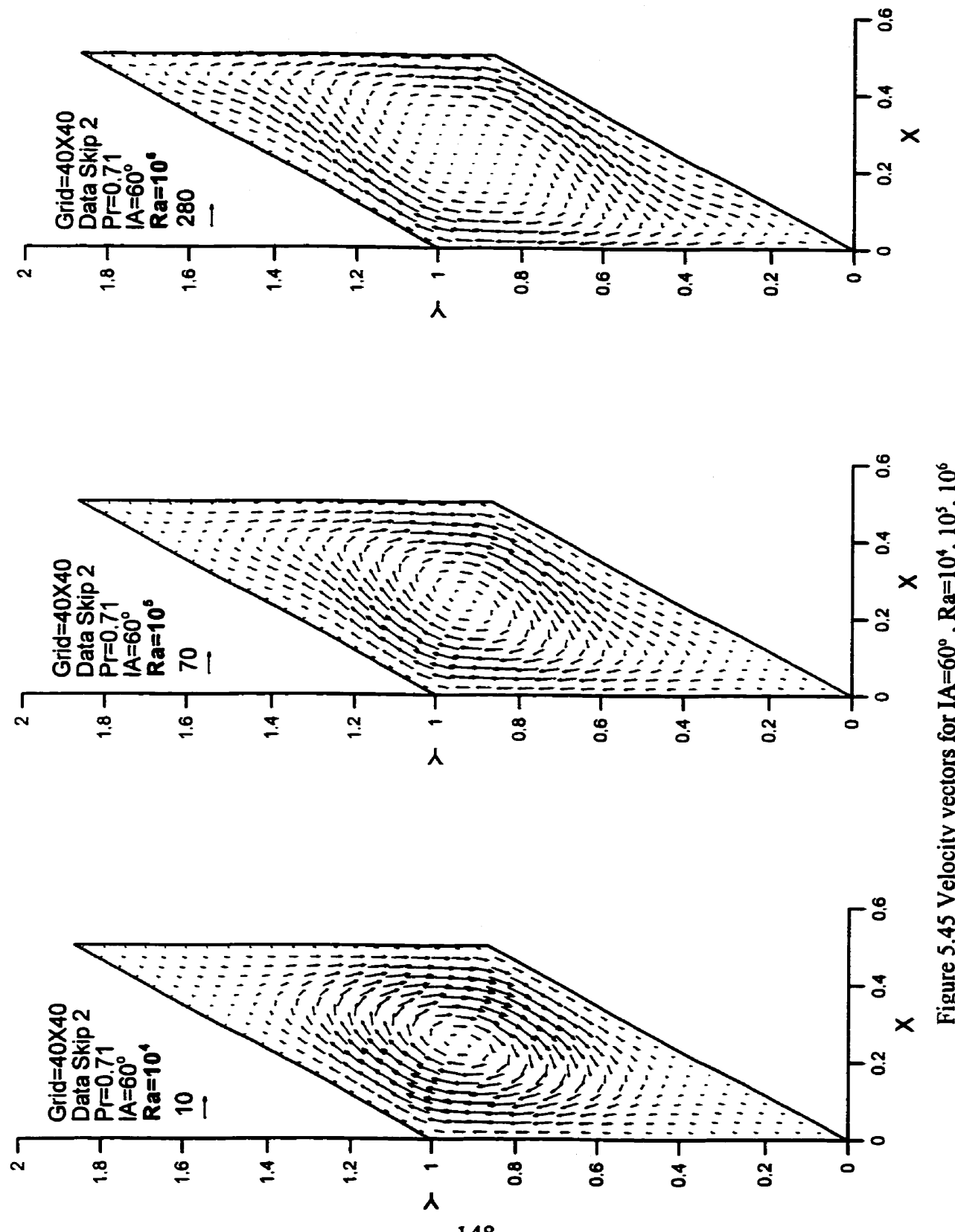


Figure 5.45 Velocity vectors for  $\text{IA}=60^\circ$ ,  $\text{Ra}=10^4, 10^5, 10^6$

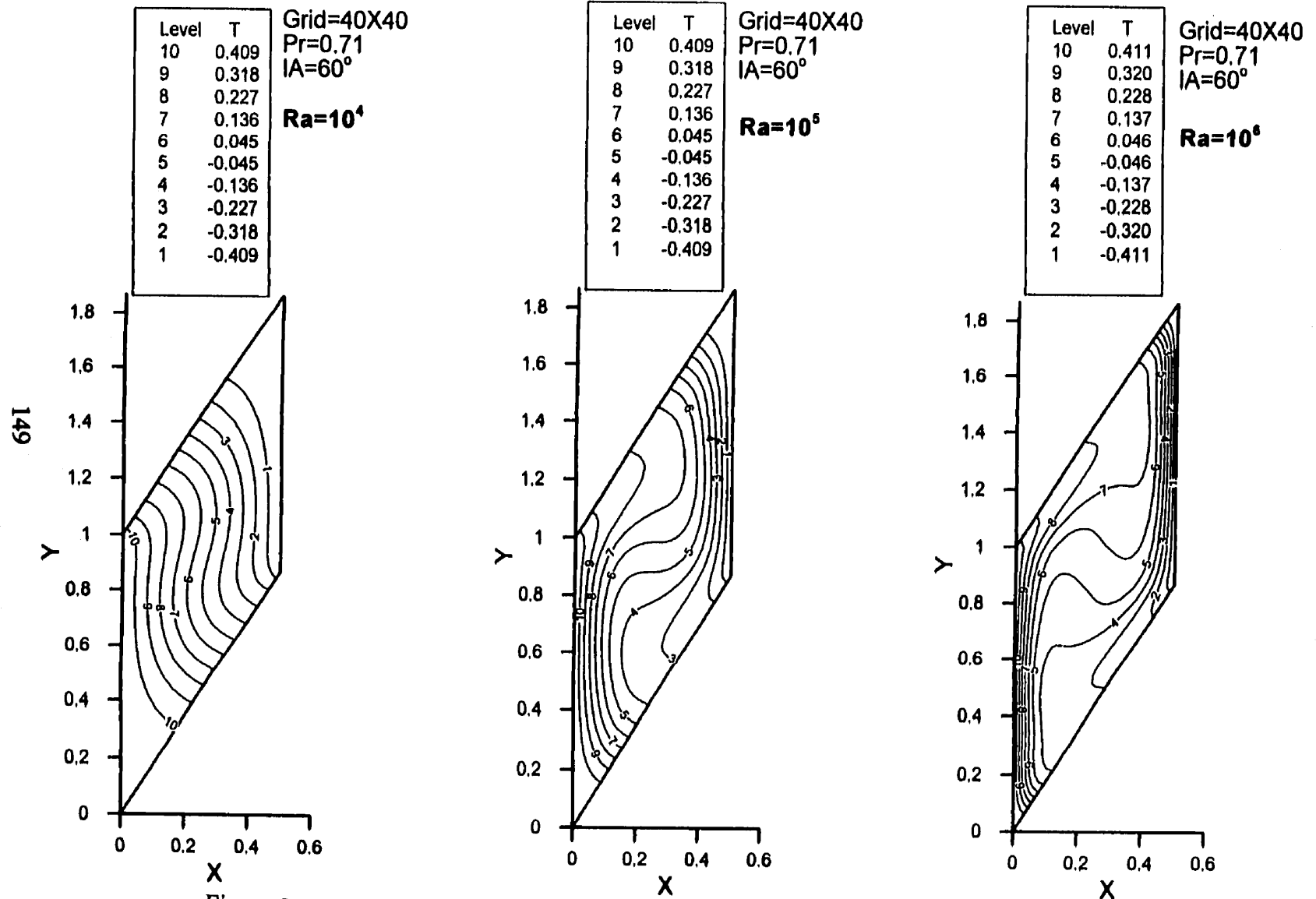


Figure 5.46 Isotherms for IA=60°, Ra=10<sup>4</sup>, 10<sup>5</sup>, 10<sup>6</sup>

layers are again slightly thicker. Most noticeable at  $\text{Ra}=10^6$  is a narrow band of lower velocity vectors along a diagonal between the two sharper corners and the central region. The heated flow rises from the narrower boundary layer along the hot wall and turns around at the upper inclined walls until it reaches the cold wall to lose energy within the narrower layer. At  $\text{Ra}=10^6$ , even though the velocity jet is noticeably greater than for the previous inclination angle, the flow has difficulty penetrating into the sharp corner. Close inspection reveals there is a small component of velocity developed normal to the upper and lower boundaries thus providing a low velocity region there. Furthermore it appears that there is a net flux into from the upper and lower corners, implying a nonphysical flow. This phenomenon is discussed later. For the  $\text{Ra}=10^4$ , we notice much less distortion of the isotherms compared to the case for other inclination angles. The isotherms have approximate equal distance between them which means a linear temperature across the enclosure. The region with lower temperature in the sharp upper right corner gets bigger with increasing inclination angle. Since the temperature is increased along a vertical line from upper wall to central of the enclosure, this represents a heating process which may be caused by the main circulation path away from the upper right corner where the temperature is lower. Hot fluid seems to be deflected by the essential stagnant region of cold fluid in the sharp corner.

Overall, with increasing inclination angle we notice that for fixed Rayleigh number, the ends of isotherms at the upper wall migrate toward the hot side wall signifying a weakening of convection. This migration can be seen by the isotherm labelled 8 for  $\text{Ra}=10^4$  over different inclination angles. We observe that the end of it migrates to the side wall from more than half of the enclosure's width to about less than one fourth of the width as the inclination angle varies from  $15^\circ$  to  $60^\circ$ . The larger the ratio of the height to the width, the more the flow regime approaches the conduction regime. Taller or narrower enclosures limit the growth of convection mode. Furthermore, the geometry with sharper corners also resists the convection strengthening. Thus, in the current studies, we have found boundary layer and conduction regimes with similar features as described by Bachelor (1954) and Bejan (1995).

While the previous figures show the main flow patterns, smaller vectors in the two sharper corners, however, are hard to see in the numerical results. Since in these two corners, the magnitude of the velocity is only about 10% of the maximum velocity, we have zoomed into this region. As shown in Figure 5.47, the velocity vectors at the corners falsely represent the physical solutions. Here we see that the corner flow violates the regional conservation of mass, with these velocity vectors

behaving as though some sources were at the corners. The problem was investigated by the following different approaches. We first examined the mass flux at every control volume, but found the mass residual to be zero meaning the mass is conserved for each control volume. Subsequently, we looked at the mass flux at each of the interfaces for every control volume and we found the sum of the mass flow in and out of the control volume is zero, supporting the results of the first output for zero mass residual. Some numerical data for the flux at interfaces are presented in the appendix. Following that, we printed out the velocities at the interfaces of the control volume and found that these velocities are almost parallel to the interfaces. Figure 5.48 shows the velocity vectors at interfaces in the corner. We conclude that since the non-physical velocities there are parallel to the control volume interfaces they do violate mass conservation in the control volume.

The source of the non-physical velocities vectors appears to be the numerical method, compounded by a coarse resolutions. Accordingly, more computations were carried out using more refined grids of 60x60, 100x100 and 200x200 for this special case of  $\text{IA}=60^\circ$ . This work showed that the values of non-physical velocity near the regions of the two sharp corners decreased and the regions themselves retreated close

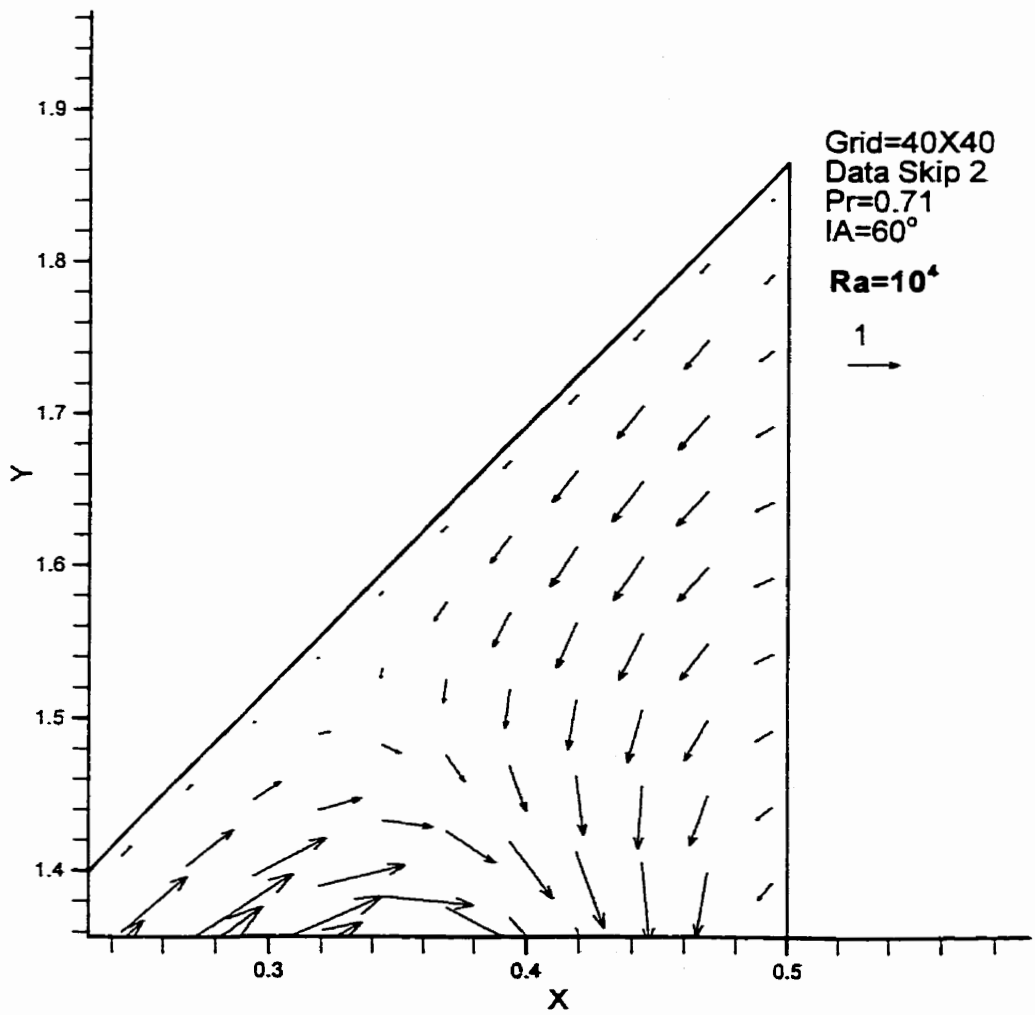


Figure 5.47 Velocity vectors in the upper right corner

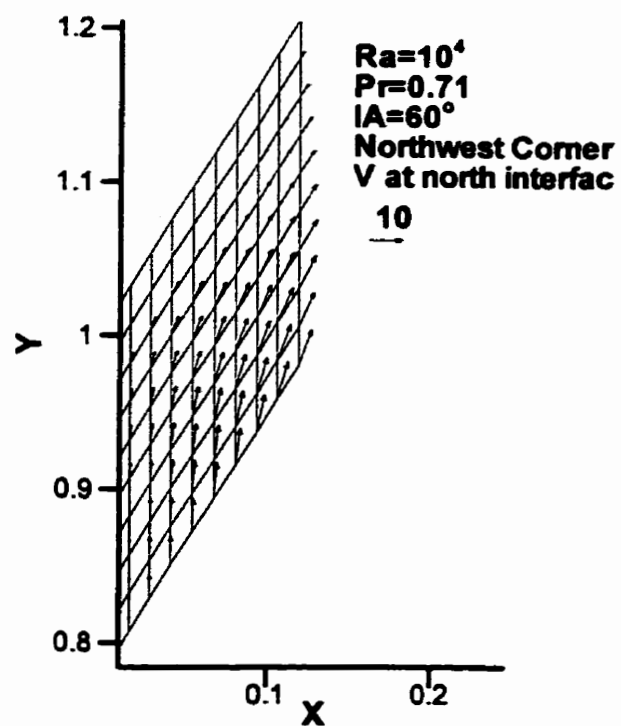
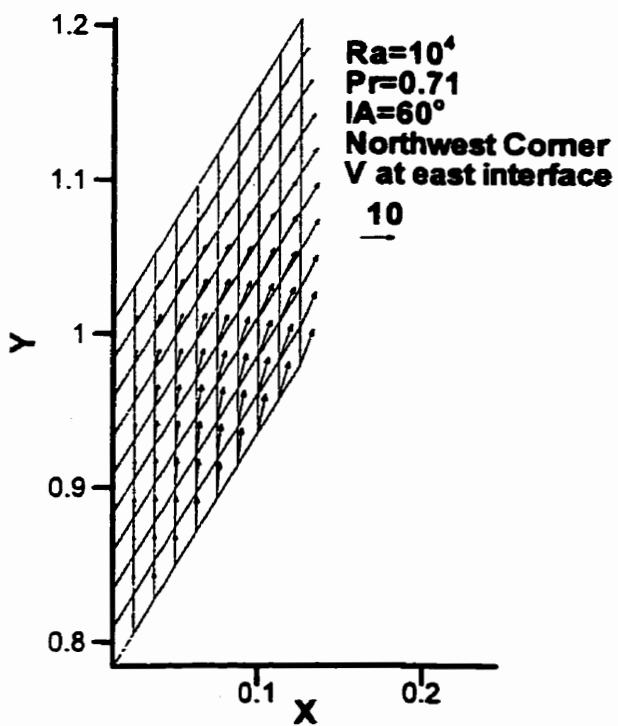
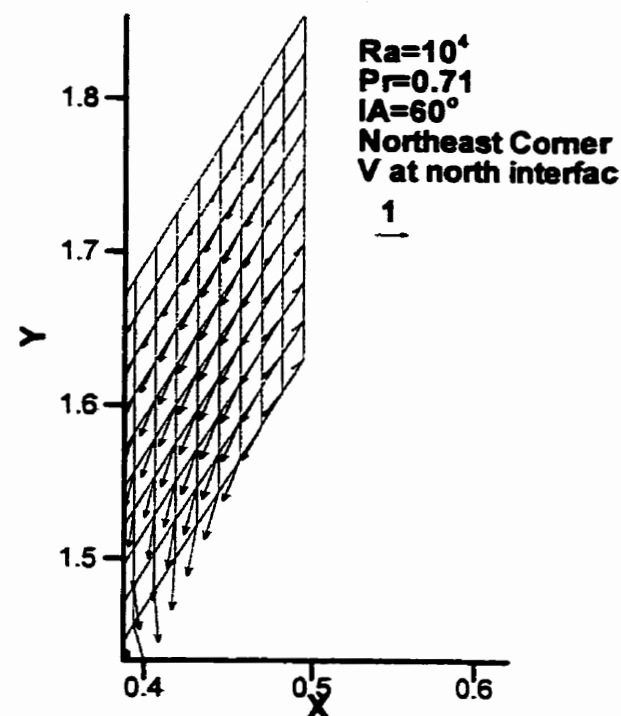
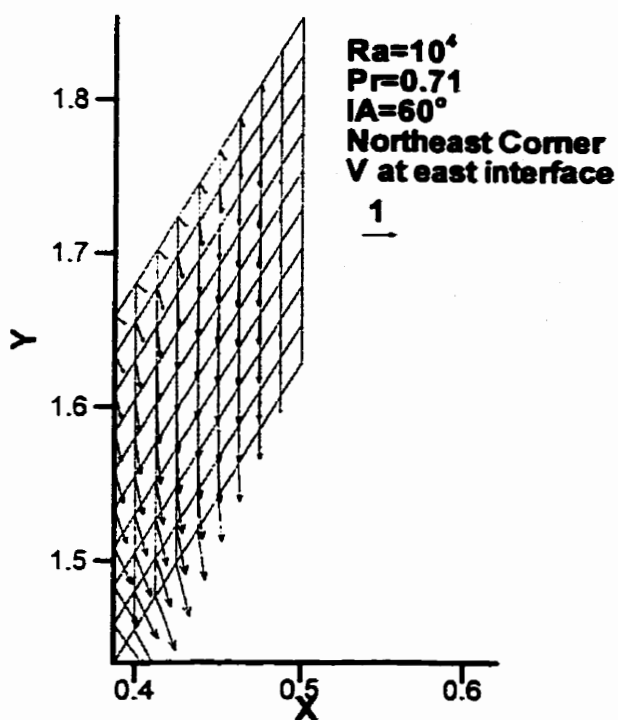
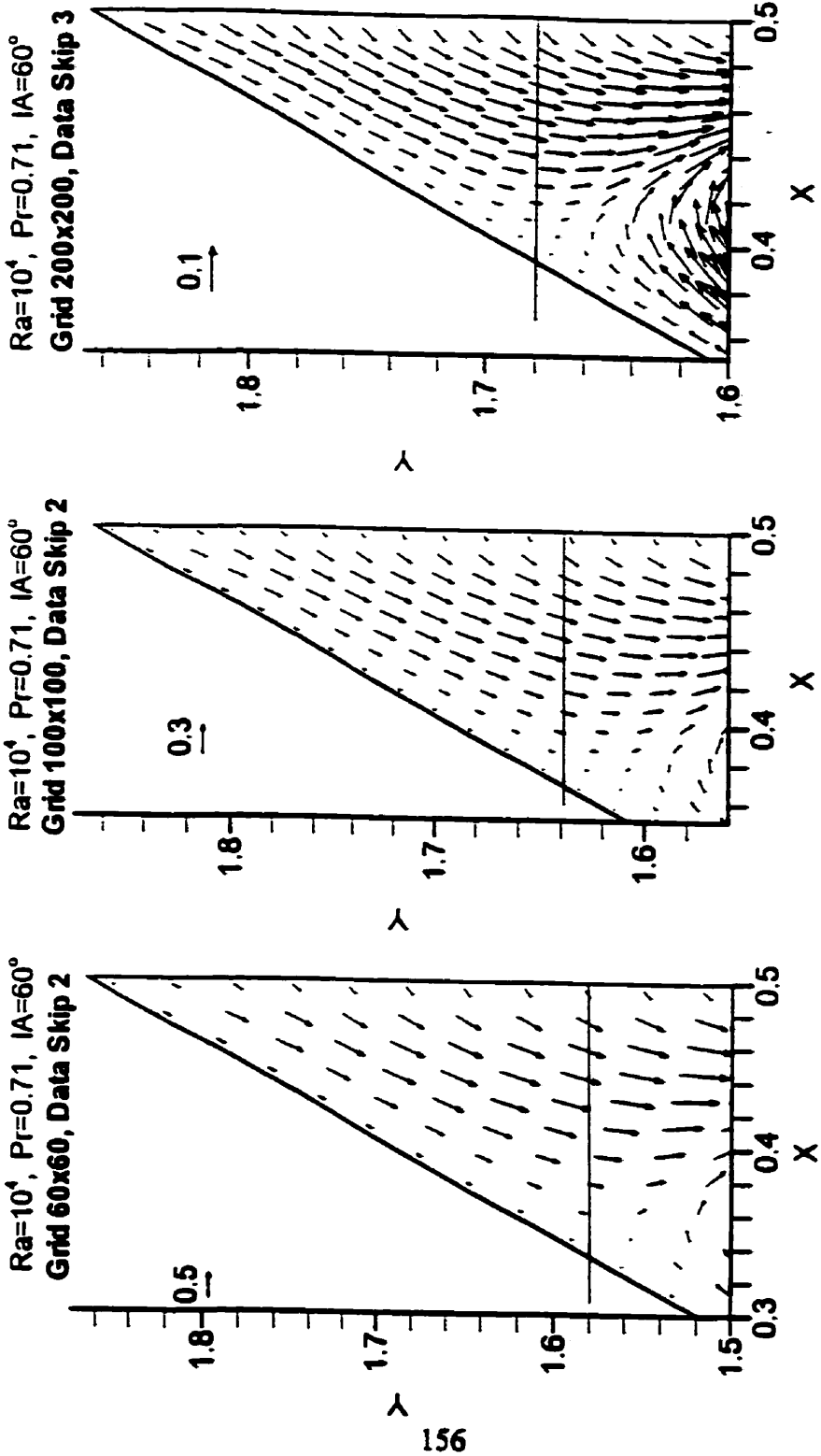


Figure 5.48 Velocity vectors at interfaces in the upper right corner for  $\text{IA}=60^\circ$ ,  $\text{Ra}=10^4$

to the apex. This is demonstrated in the panels of Fig. 5.49 showing the velocity vectors in the upper right corner with marking lines to separate the region of non-physical and physical flows. As the result of such investigations, we can conclude that the grid resolution strongly affects the numerical results in the cases of severe non-orthogonality. Such a breakdown could lead to regional unphysical solutions or numerical noise which falsely represent the physical results. Finer resolution applied in the computation will give better performance and a physically more realistic solution. Figure 5.50 shows the upper right corner with  $Y>1.7$  that the ratio of the averaged kinetic energy to the averaged kinetic energy in the whole enclosure plotted against the logarithm of the number of control volumes. The averaged kinetic energy in the upper right corner is represented by ‘avcke’ which is the sum of kinetic energy divided by the number of control volumes. The averaged kinetic energy in whole enclosure is represented by ‘avtke’ which is sum of the kinetic energy divided by the total number of control volumes. The kinetic energy is substantially decreased when the 200x200 grid is applied. In fact, the ratio of the average kinetic energy at the corner to the average kinetic energy in the whole enclosure is less than about 1% for the 40x40 grid to less than about 0.01% for 200x200 grid. Thus, the numerical error due to the effect



**Figure 5.49** Velocity vectors in the upper right corner region for  $\text{IA}=60^\circ$ ,  $\text{Ra}=10^4$   
**Horizontal line separates the regions of non-physical and physical flows.**

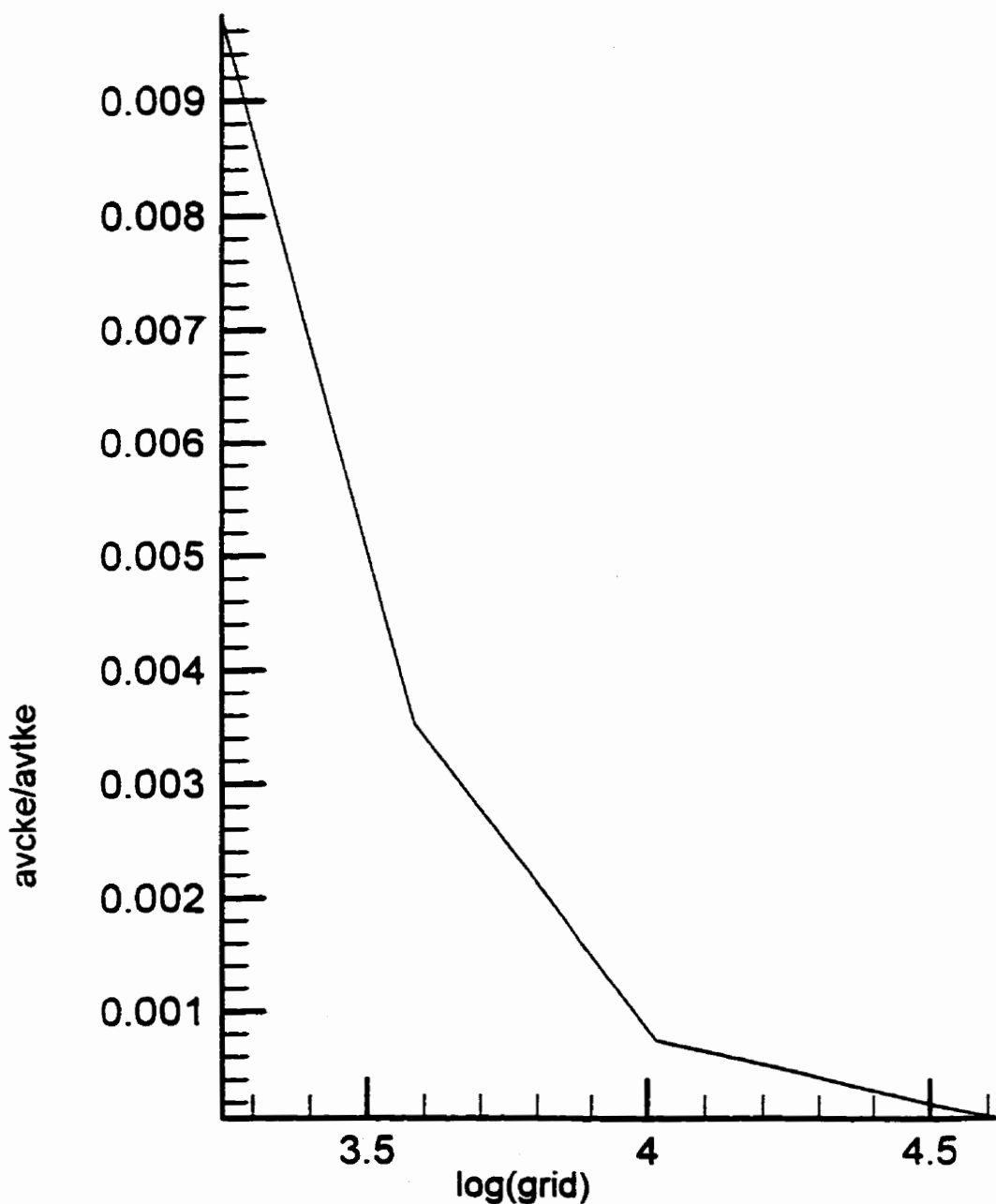


Figure 5.50 The ratio of average kinetic energy verses log(grid)

of meshes is reduced dramatically by applying finer mesh.

There appears to be very little discussion in the literature on severe non-orthogonality. Possibly better performance could be achieved by improving the interpolation schemes as well integration with higher order. Another source of the problem could be attributed to the discretization of the derivatives which would be alleviated by adding correction terms, thus further improving the approximation to the derivatives as discussed by Dick(1996).

It is apparent from these calculation that convection in parallelogrammic enclosure with two vertical and two inclined walls is physically different from the convection in a parallelogrammic enclosure with two inclined and two horizontal walls which is discussed in a later section. We know that near the four walls the boundary layers and wall jets are formed. For the first case, however, the gravity force plays a role along all walls but not for the second case where the gravity force is perpendicular to the horizontal walls thus producing no contribution to the buoyancy force along the horizontal walls. The buoyancy force along a inclined wall is different from that along a vertical wall with a cosine of the inclined angle.

Fig. 5.51 shows the effect of inclination angle and Rayleigh number on Nusselt number. As expected, Nusselt number increases with more vigorous flow due to increasing Rayleigh number. But the Nusselt number increases at first with increasing inclination angle, attains a maximum, then decreases. Apparently for a given Rayleigh number convection becomes more vigorous as the upper and lower walls attain a small tilt and corresponding buoyancy along these walls. But as the tilt increases the effect of the sharper corner appears to limit the convection as flow is trapped in this corner. The effects of inclination angle on heat transfer are most apparent for Rayleigh number of  $10^4$ . The Nusselt number for inclination angle of  $15^\circ$  is about 2 times that for inclination angle of  $60^\circ$  at  $\text{Ra}=10^4$ . Nusselt number for inclination angle of  $15^\circ$  and  $60^\circ$  reduces to 10% at Rayleigh number of  $10^5$  and 5% for Rayleigh number of  $10^6$ .

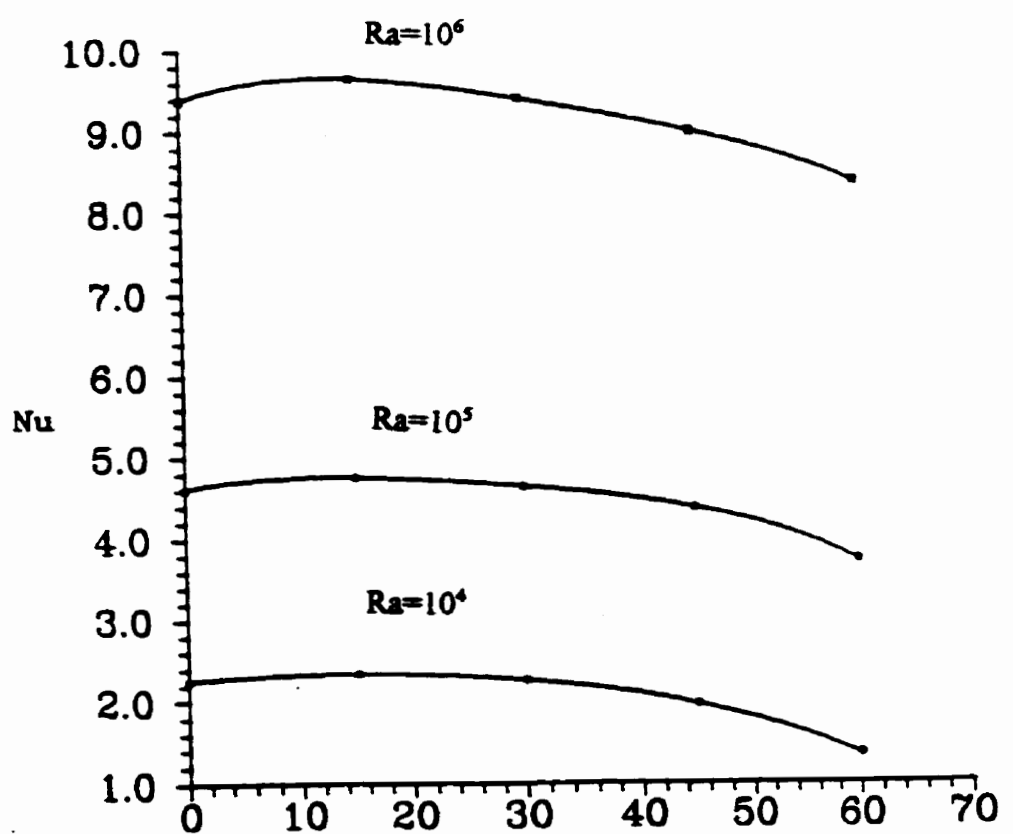


Figure 5.51 Nusselt number versus IA and Ra for  $Pr=0.71$

## **5.6 Natural Convection in a Parallelogrammic Enclosure with Two Horizontal Walls and Two Inclined Walls**

Natural convection in a two-dimensional parallelogrammic enclosure with two horizontal walls insulated and two inclined walls isothermally heated and cooled has been studied numerically using the finite volume method. Results reported here provide a basic understanding of this physical phenomenon. Although the results reported in these simulations correspond to enclosures, they could be interpreted for an external geophysical problem. For example an inclined isothermal side boundary could represent a region near the sea bed and near a subducting slab in the Earth's mantle. Another application is to obtain the numerically simulated heat transfer and flow data for air flow in a building's inclined double windows.

In addition to the numerical method, this problem has been studied experimentally. The decision to choose this problem for experimental work was made for two reasons. First, there appear to be more practical applications which would make observations unanticipated by calculation a good basis for future work. Second, we considered that the code had been sufficiently tested on several classical

problems that it could be trusted in the interpretation of a new problem. We also noted that construction of a cell for this problem could allow for future work using the same cell tilted so that its heated and cooled walls were vertical. The flow field was observed using DPIV with the results for the experimentally obtained flow field compared with those found numerically.

### **5.6.1 Numerical Results for Prandtl Number of 0.71**

The two-dimensional parallelogrammic enclosure has the left inclined wall heated isothermally and the right inclined wall cooled isothermally, while the upper and lower horizontal walls are insulated. The computations were conducted for Rayleigh number of  $10^4$ ,  $10^5$ ,  $10^6$  and Prandtl number of 0.71. The inclination angles to the vertical were varied through  $15^\circ$ ,  $30^\circ$ ,  $45^\circ$ , and  $60^\circ$ . Temperature, velocity and Nusselt number were obtained and presented.

Figure 5.52 and 5.53 show the velocity vectors computed on a 40x40 grid and isotherms for inclination angle of  $15^\circ$  and Rayleigh numbers  $10^4$ ,  $10^5$ ,  $10^6$ . In this figure every other computed vector is plotted and this is termed data skip 2. In the top panel for  $\text{Ra}=10^4$ , the flow pattern is one cell. Buoyant fluid rises at the heating side

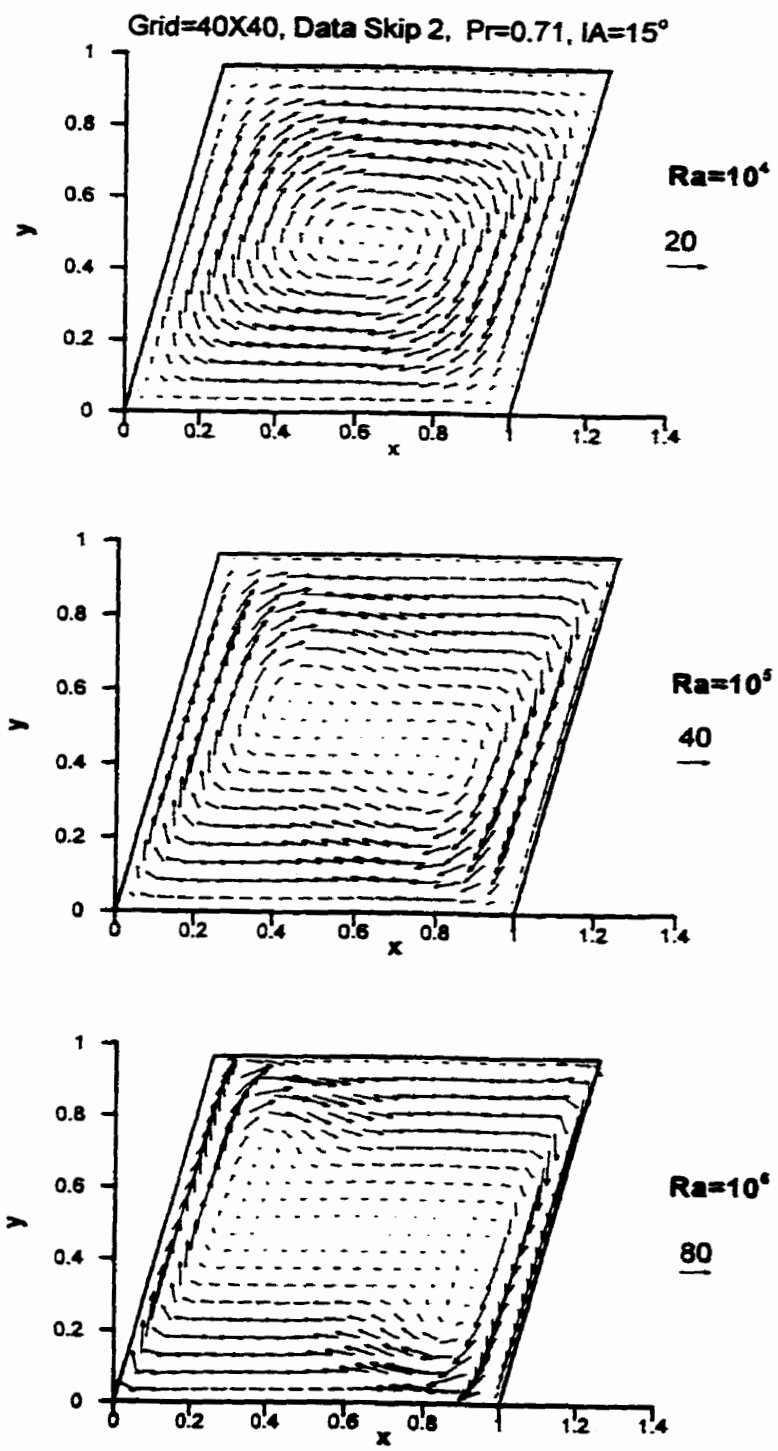


Figure 5.52 Velocity vectors for IA=15° and Ra=10<sup>4</sup>, 10<sup>5</sup>, 10<sup>6</sup>

Grid=40X40, Pr=0.71, IA=15°

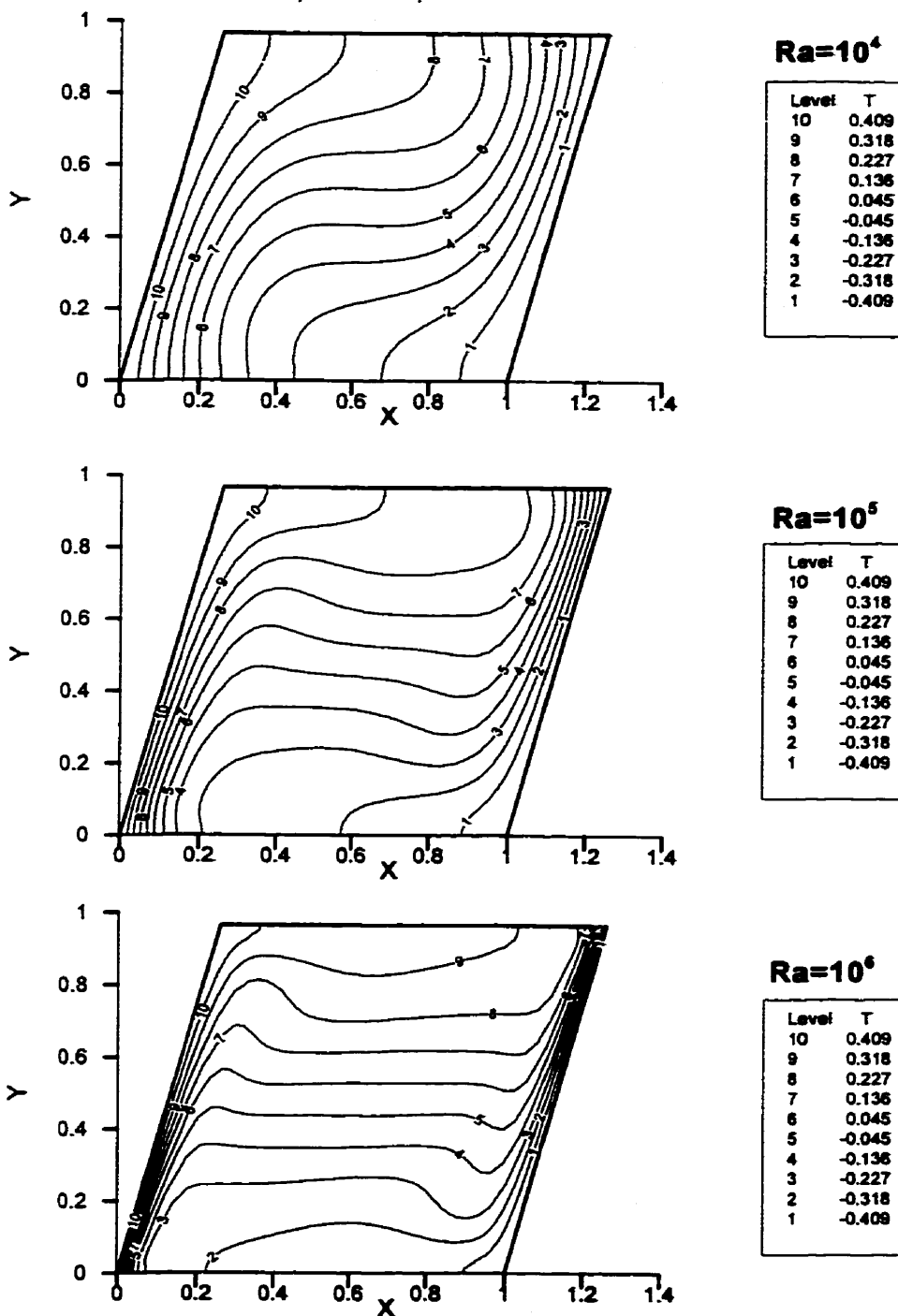


Figure 5.53 Isotherms for  $\text{IA}=15^\circ$  and  $\text{Ra}=10^4, 10^5, 10^6$

towards to the top, horizontal wall then turning to continue flowing along the top wall. While flowing into the upper right corner, the fluid develops a downward component as it turns and then to flow down along the cold wall. To complete the circulation the fluid flows along the bottom horizontal wall to reach the heating wall. In this case, we see only a broad boundary layers near the walls with a low velocity region near the centre.

For  $\text{Ra}=10^5$ , the overall flow pattern is still one cell but rather small, weak, secondary cells develop in the interior. These are probably viscously driven coupled to the strong corner vorticity as the flow spreads out from the horizontal wall. Two secondary vortices are created due to the hot fast flow impinging on the top impervious boundary and turning right. This flow moving along upper wall is decelerated due to viscous shear. Mass conservation leads to the top and bottom boundary layers thicker than the sidewall boundary layers.

For  $\text{Ra}=10^6$ , greater conduction of heat from the wall leads to still stronger convection. The two secondary vortices move close to the inclined walls and are convected further down stream. For this case, a streamtrace and stream function integrated from velocity fields on 80x80 grids are plotted in figure 5.54. At the centre

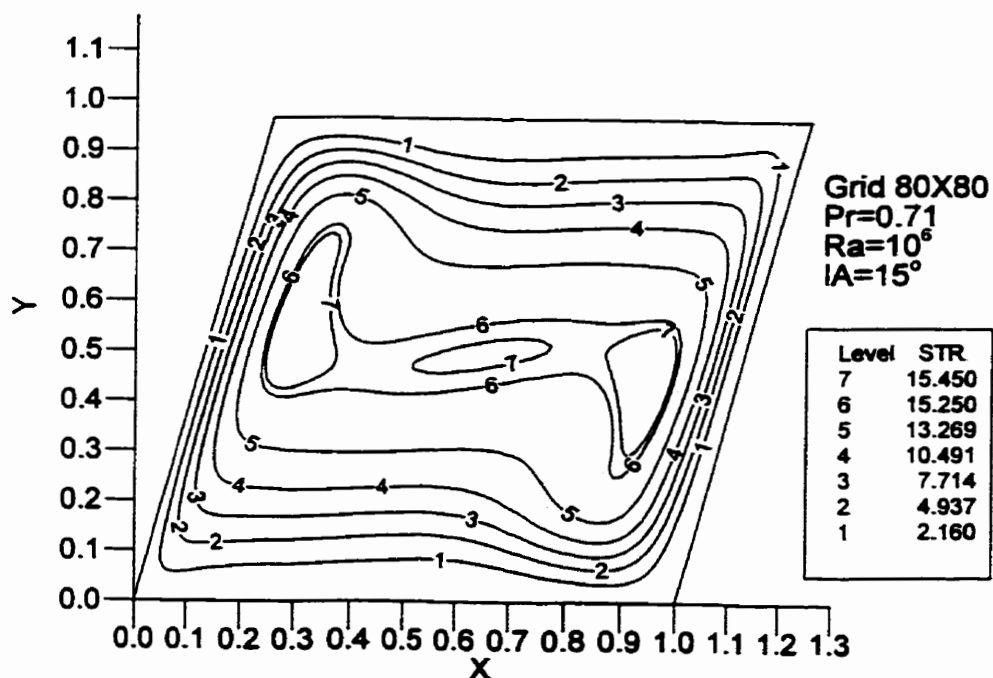
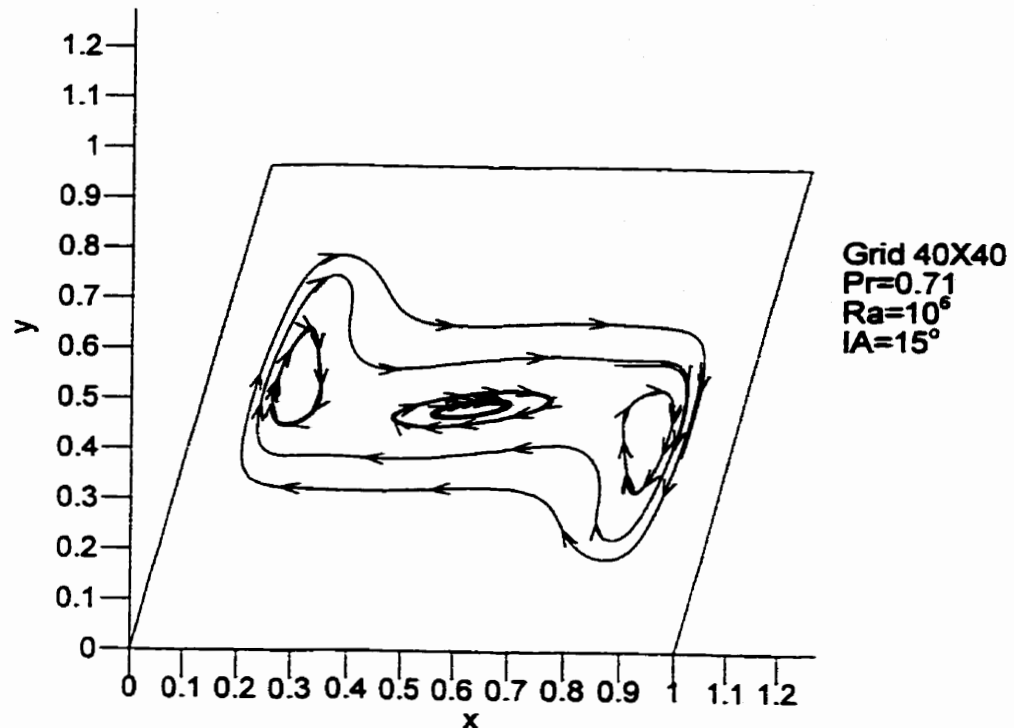


Figure 5.54 Streamtrace and stream function for  $\text{IA}=15^\circ$  and  $\text{Ra}=10^6$

region, a small vortex appears. This has been attributed to the presence of a small temperature gradient in the centre in the same sense as mentioned by Mallionson and de Vahl davis (1977) for natural convection in a rectangular enclosure. With increasing Ra number, the boundary layers become thinner and more obvious. The flow fans out from the corner into the interior thus leading to a wider boundary layer at the top wall in order to satisfy mass conservation. At this high Ra number the boundary jet is so strong that heat transfer is mostly due to the convection mode in the boundary layers.

From the isotherm plot for  $\text{Ra}=10^4$ , we can see that the isotherms are approximately parallel to the left hot wall and are dense at the lower left side and upper right corner . Due to the effect of convection, the isotherms are propagated from the hot wall to the cold wall leading to distortion of the isotherms in the upper and lower half region. In the centre the temperature change across the cell is small with isotherms parallel to the horizontal direction.

As the Ra increases to  $10^5$  , the temperature gradients in the X direction in the central region are close to zero and change sign, thus promoting negative vorticity leading to the formation of secondary vortices in the core . In the situation of natural

convection in a rectangular enclosure, Markatos and Pericleous (1984) have discussed that as Rayleigh number increases, the development of thermal boundary layers intensifies temperature gradients in the X direction in the region of vicinity of the walls, and the convection within each boundary layer leads to a reversed temperature gradient in the X direction approaching the centre. This reversed flow and reversed temperature gradient can be seen in Fig. 5.55 and 5.56 for velocity and temperature at fixed Y. The reversed flow for  $Ra=10^6$  occurs near  $X=0.32$  which is near the maximum reversed temperature gradient as seen in Fig. 5.56. A vorticity sink thus separates the regions of concentrated vorticity generation and two secondary vortices are formed. For  $Ra = 10^4$ , the convection is weak and viscous diffusion prohibits the development of these vortices. But for  $Ra=10^5$ , stronger convection of the temperature fields leads to isotherms that are nearly horizontal in the centre when the region with horizontally parallel isotherms is bigger than for  $Ra=10^4$ . The thermal boundary layers become thinner and consequently more obvious .

For the case  $Ra=10^6$ , the convection strengthens further. The thermal and momentum boundary layers are thinner than for  $Ra = 10^5$ ,  $10^4$  and fluid speed increases in the boundary layers. As shown in figures 5.55 for vertical velocity and in figure 5.56 for the temperature near the central line, the thickness of the thermal

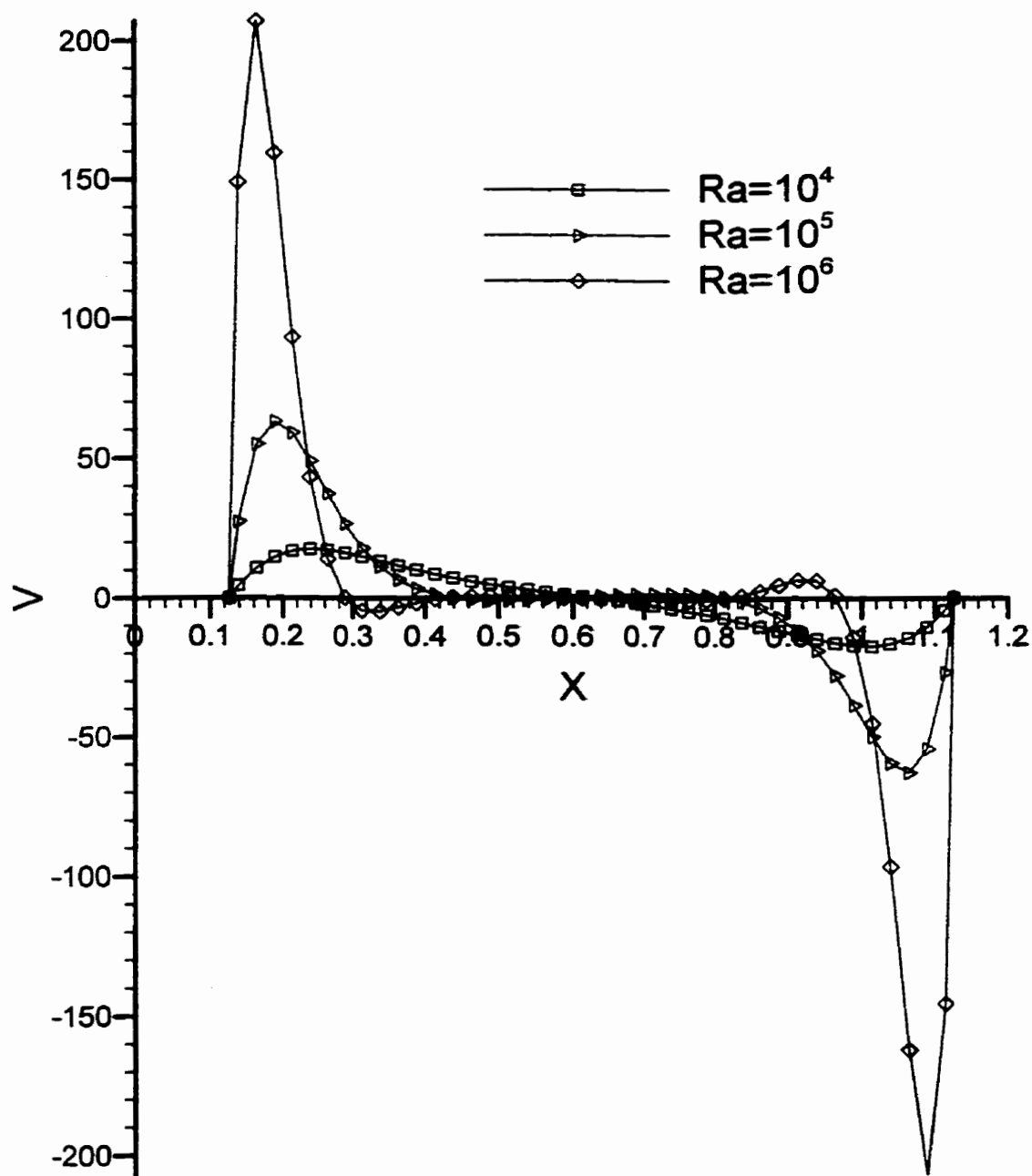


Figure 5.55 Vertical velocity at  $Y=0.4709$  for  $IA=15^\circ$

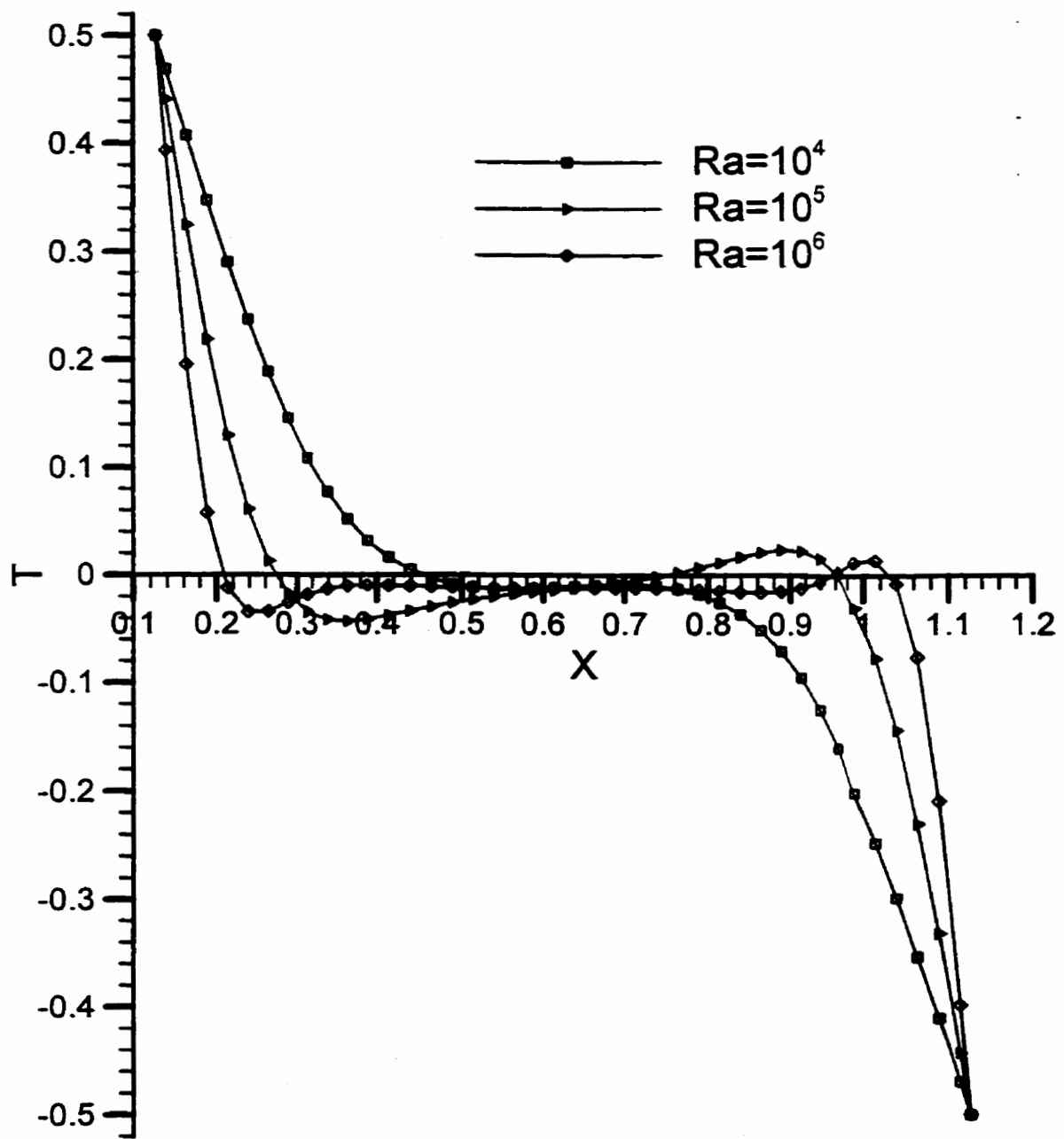


Figure 5.56 Temperature at  $Y=0.4709$  for  $IA=15^\circ$

boundary layer along the X direction is about 0.09 compared to the thickness of 0.15 and 0.33 for  $\text{Ra} = 10^4$ ,  $10^5$ . The thickness of the velocity boundary layer is about 0.16 compared to the thickness of 0.3 and 0.5 for  $\text{Ra} = 10^5$ ,  $10^4$ . From the scale analysis discussed in section 5.1, we have an approximate expression for the thickness of thermal and velocity boundary layers. Since the expression is only an approximate relationship, we can only use it as a rough estimation. In order to reconcile the expression derived by scale analysis with the numerical calculation, we compare the ratio of the theoretical and numerical layer thicknesses. Table 5.6 lists the ratios of the two layer thicknesses. From the values shown in the table, we can say that the expression for boundary layer thickness derived from scale analysis reasonably represents the relationship between the thickness and Ra number thus showing that the theoretical analysis based on physical arguments is approximately confirmed by the calculation.

The temperature distribution in the central region is vertically stratified with the values of temperature increasing from bottom to top. The gradient of temperature in the X direction is very small but negative in the central region of the cross-section thus leading to the creation of a clockwise vortex in this region. This vortex could be explained by frictional coupling with the top and bottom boundary layers.

Ra	ratio of $\delta_T$ observed (numerical)	ratio $\delta_T$ expected (scaling)	ratio of $\delta_v$ observed (numerical)	ratio of $\delta v_v$ expected (scaling)
$10^4$	1.77	1.78	1.67	1.78
$10^5$				
$10^5$	1.60	1.78	1.85	1.78
$10^6$				

Table 5.6 Ratios of the layer thickness

Figure 5.57 and 5.58 show the velocity vectors and isotherms for the case of inclination angle of  $30^\circ$ . In the case  $Ra=10^4$ , the flow patterns and temperature contours are not much different from those in the case of inclination angle  $15^\circ$ . The convection is weaker however and the magnitudes of velocity are smaller. For the cases of  $Ra=10^4, 10^5, 10^6$ , it can be seen that the secondary vortices are not convected downstream as much as for the case of inclination angle of  $15^\circ$ .

Figure 5.59 and 5.60 present the velocity vectors and isotherms for the case of inclination angle of  $45^\circ$ . In these cases, it is further demonstrated that the convection is still weaker, with thicker boundary layers and decreased heat transfer. The flow patterns change between  $Ra=10^5$  and  $10^6$ , with one central vortex and two

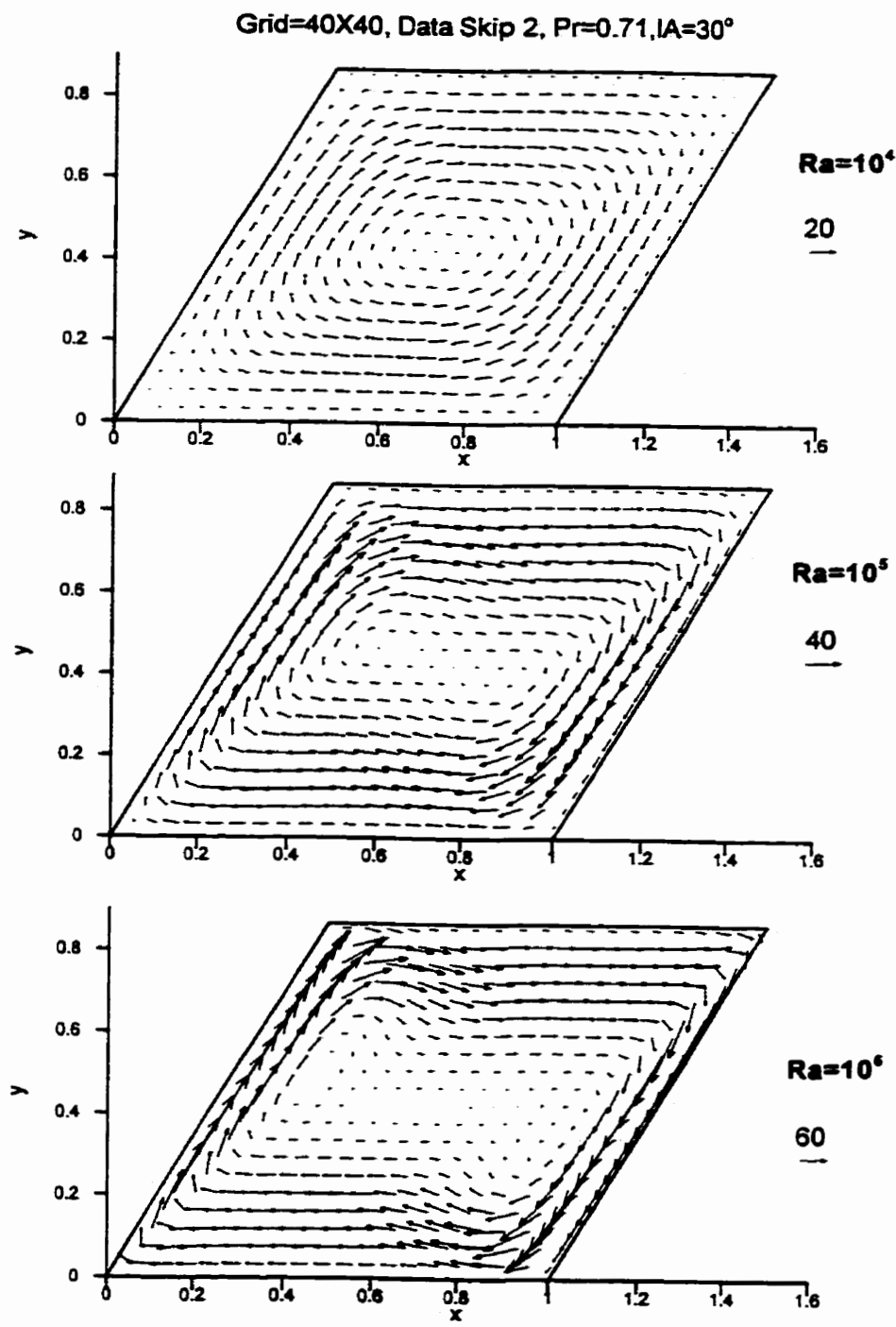
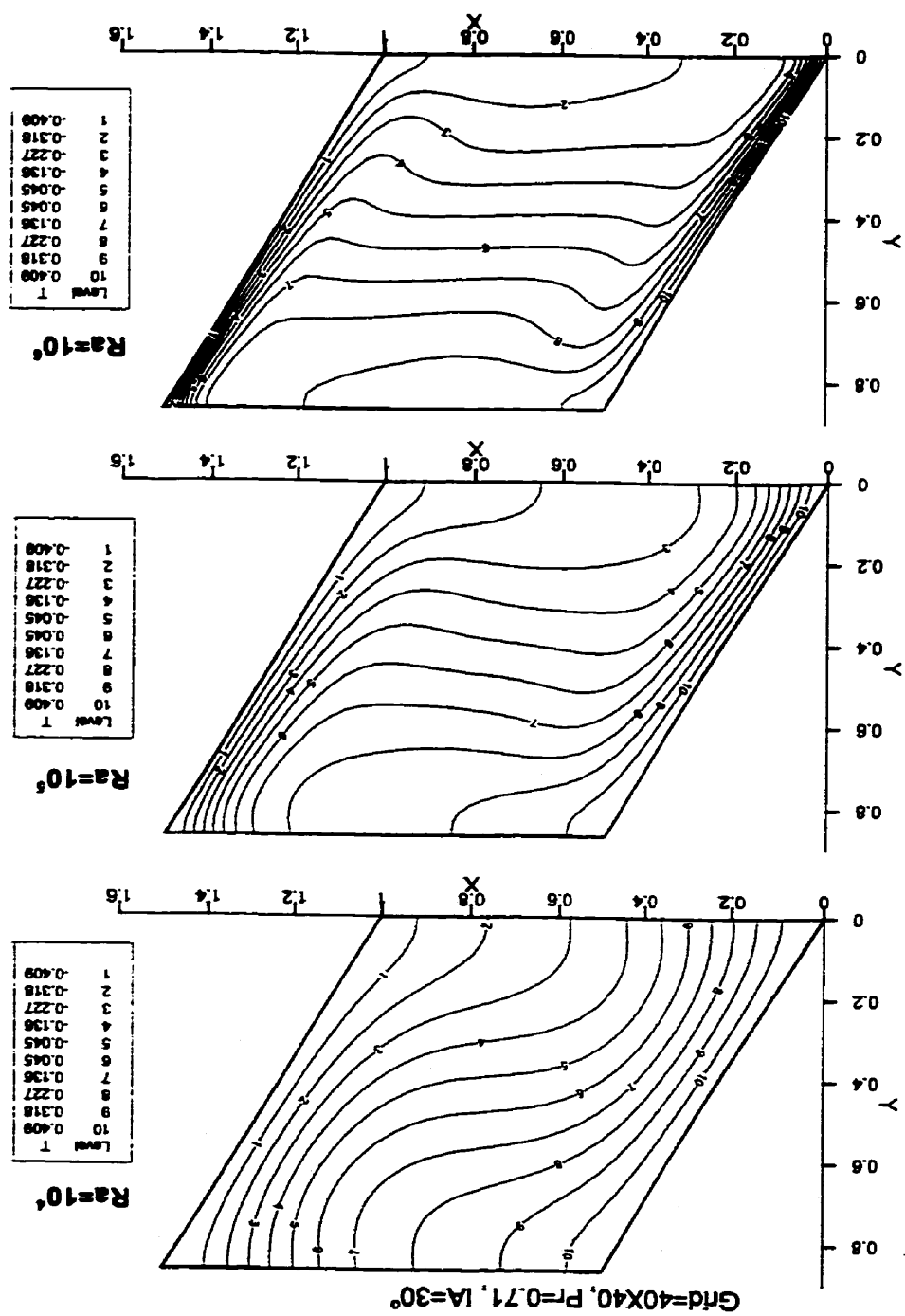


Figure 5.57 Velocity vectors for  $\text{IA}=30^\circ$  and  $\text{Ra}=10^4, 10^5, 10^6$

Figure 5.58 Isotherms for  $\text{LA}=30^\circ$  and  $\text{Ra}=10^4, 10^5, 10^6$ 

Grid=40X40, Data Skip 2, Pr=0.71, IA=45°

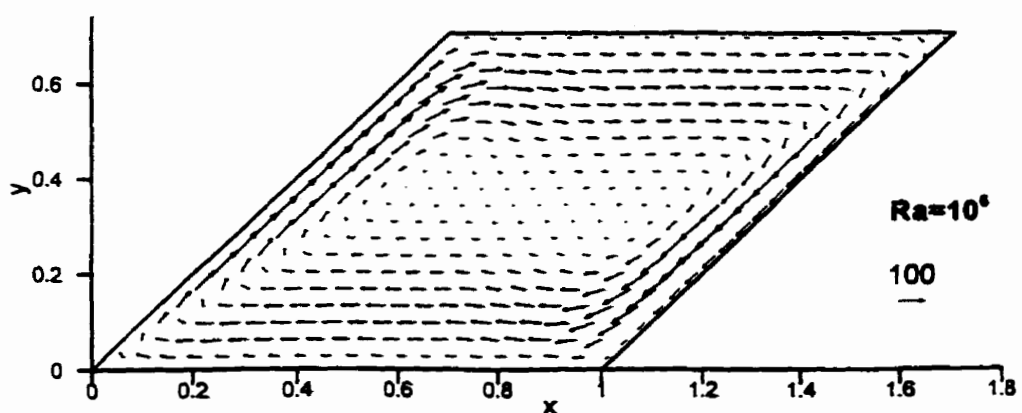
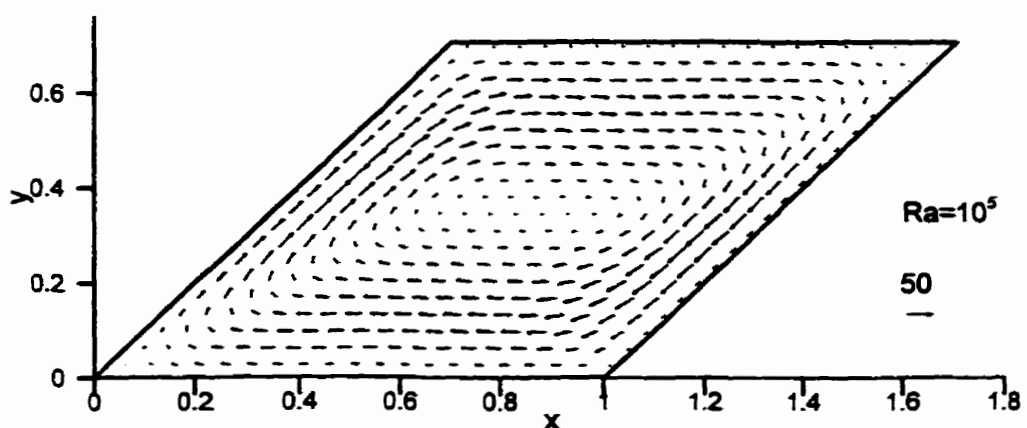
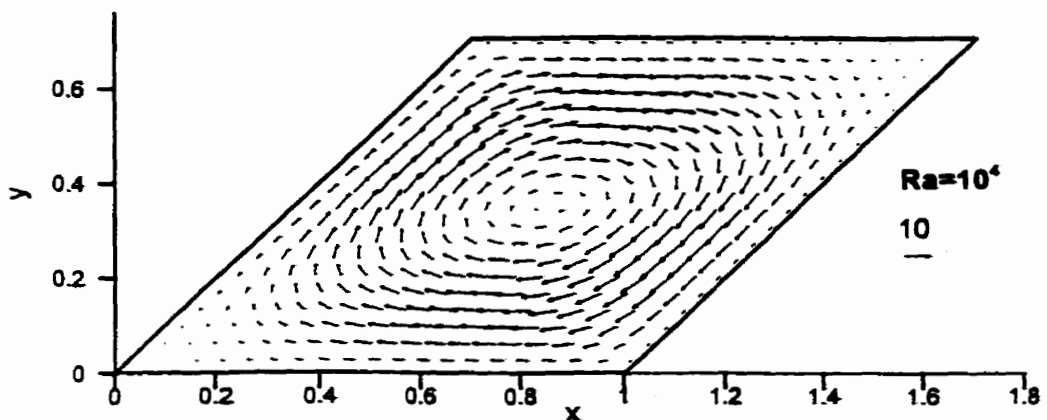


Figure 5.59 Velocity vectors for IA=45° and Ra=10<sup>4</sup>, 10<sup>5</sup>, 10<sup>6</sup>

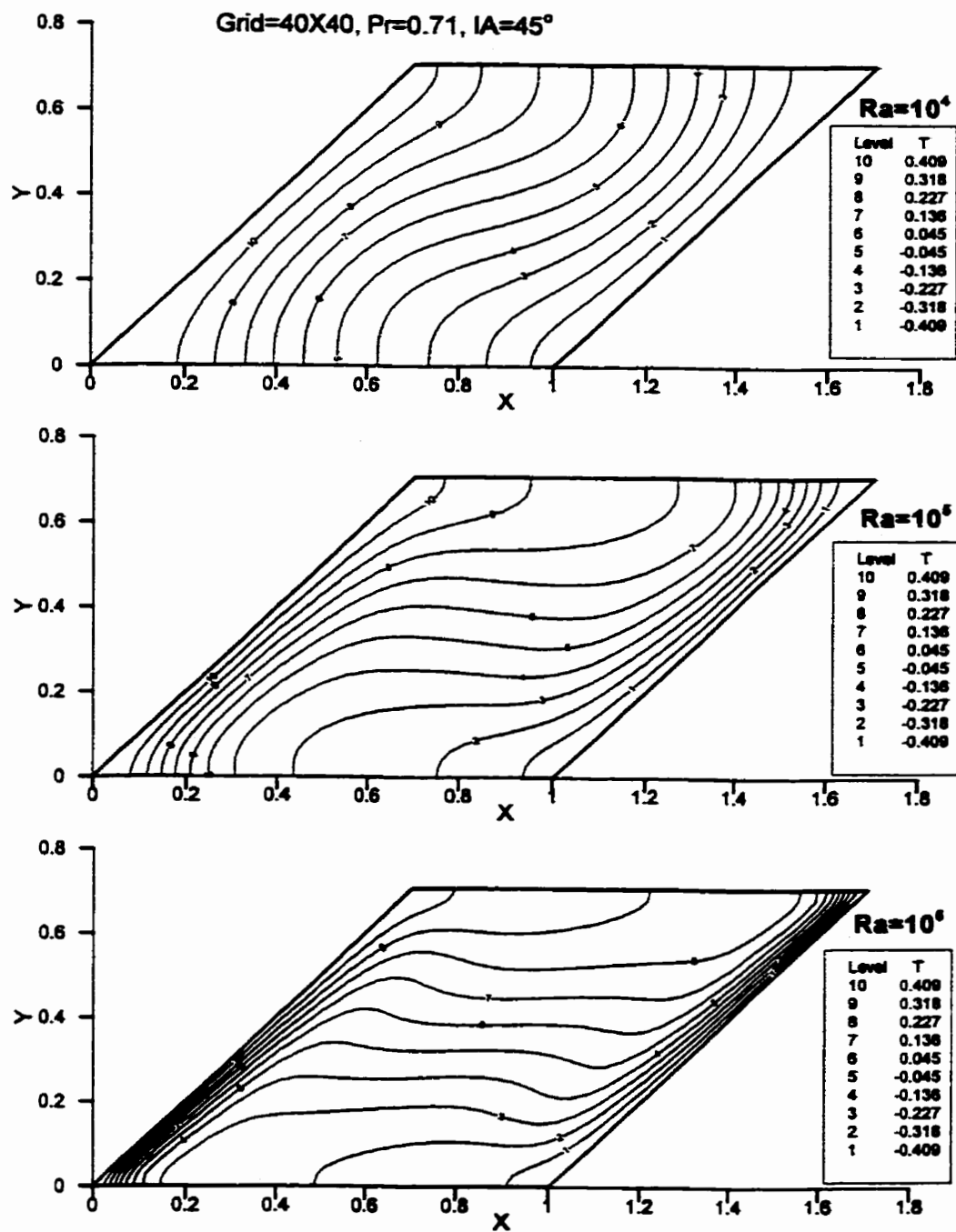


Figure 5.60 Isotherms for  $IA=45^\circ$  and  $Ra=10^4, 10^5, 10^6$

secondary vortices for the two cases respectively. We also note that in comparison with the previous inclination angle of  $30^\circ$ , the flow in the upper right and lower left corner is retarded, presumably due to difficulty turning the sharper corner.

Figure 5.61 and 5.62 present the velocity vectors and isotherms for the case of  $\text{Ra}=10^4, 10^5, 10^6$  with inclination angle of  $60^\circ$ . The effect of the convection in these cases is still weaker again compared to smaller inclination angles with magnitudes of the velocity decreased. Here the flow patterns for all three Ra numbers have only one vortex. Even though for the case  $\text{Ra}=10^6$ , the convection is not strong enough to generate the secondary vortices. In all these cases because of the weakened convection, the heat transfer is decreased compared to smaller inclination angles as expected. From these flow fields, we observe that no unphysical results were found in such orientation of the enclosures with two horizontal and two inclined walls. In the present case the flow along the upper horizontal wall will not be affected by buoyancy force which exists in flow along the inclined upper wall for the cases in the previous section.

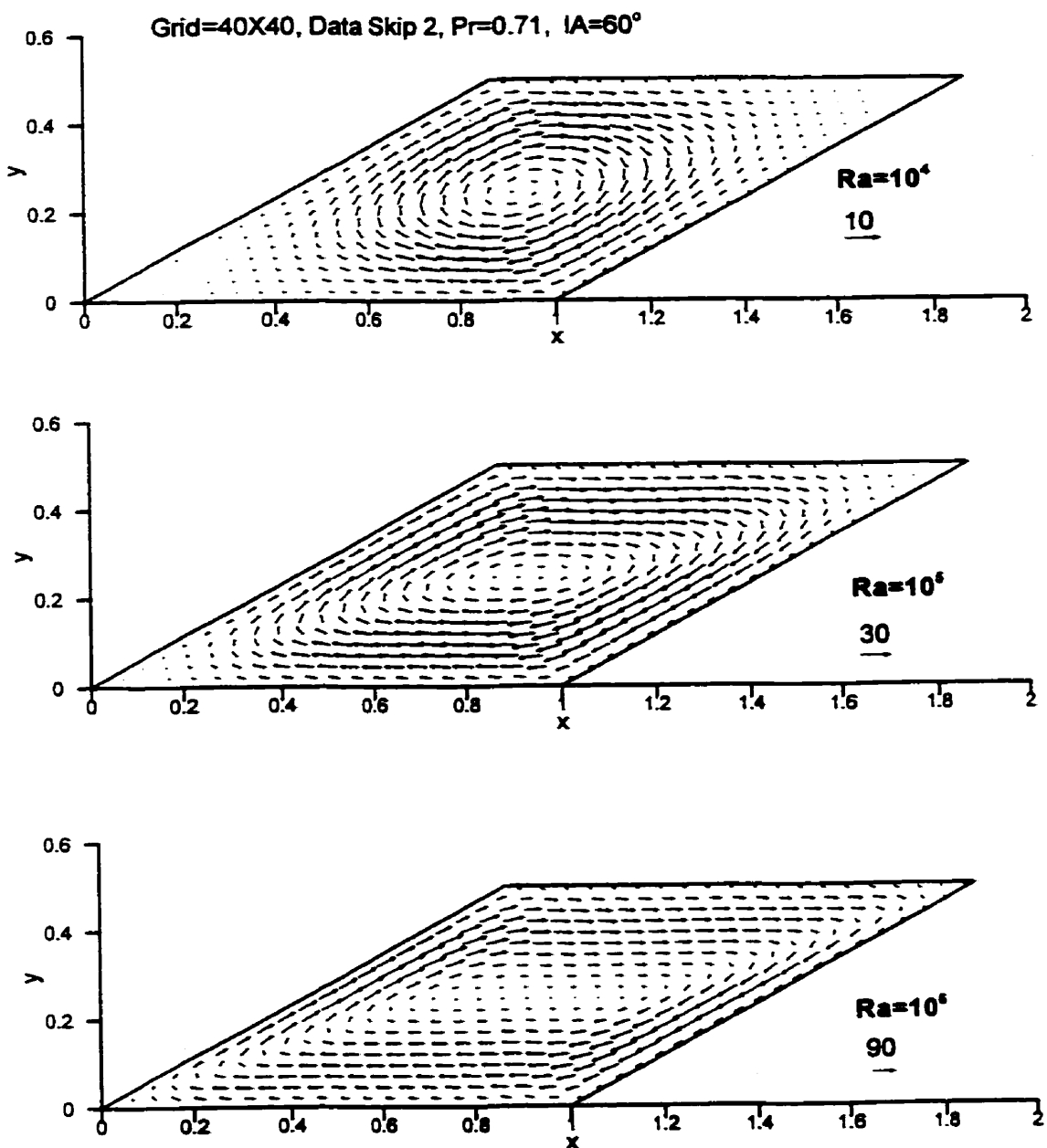


Figure 5.61 Velocity vectors for IA=60° and Ra=10<sup>4</sup>, 10<sup>5</sup>, 10<sup>6</sup>

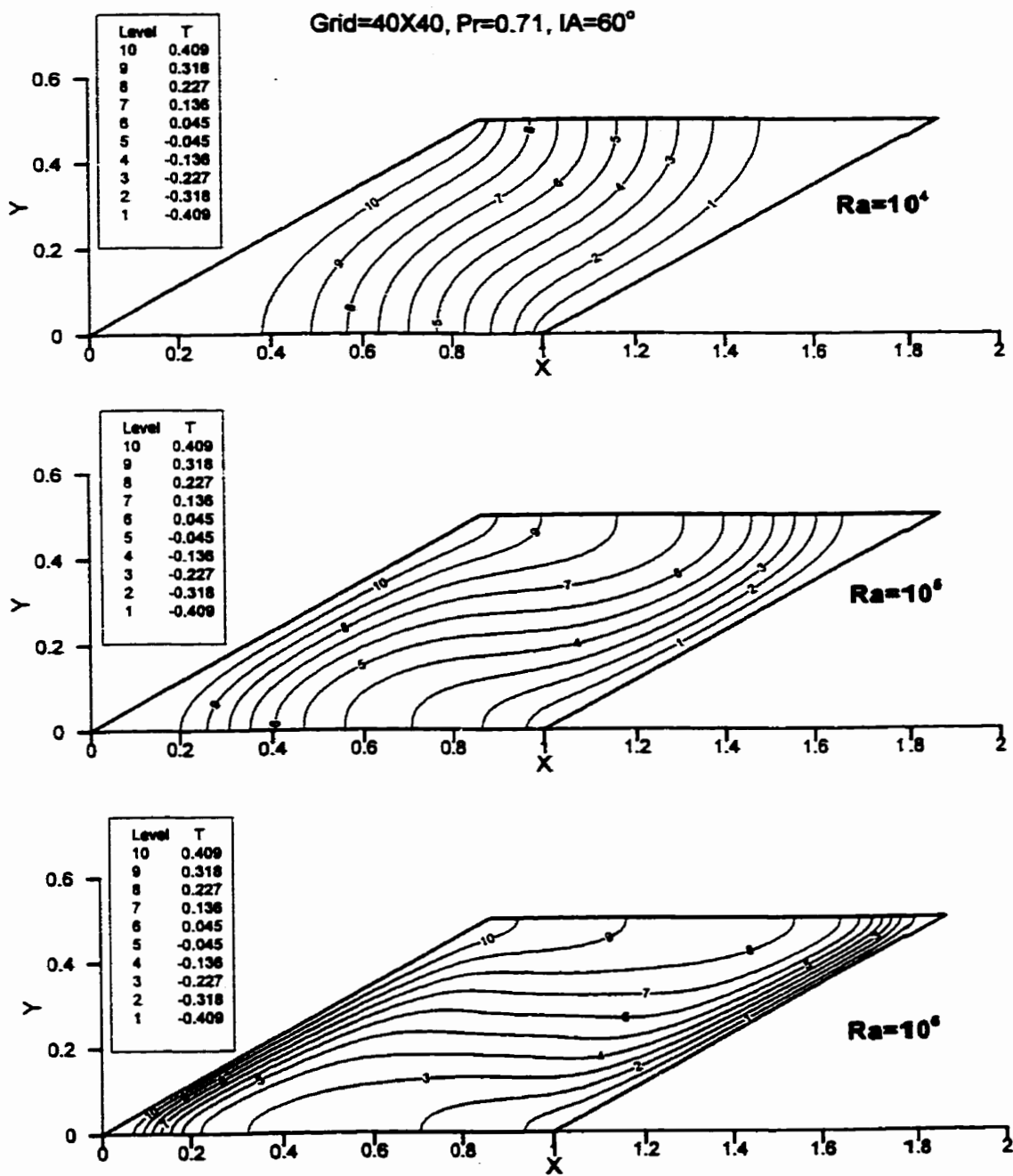


Figure 5.62 Isotherms for IA=60° and Ra= $10^4$ ,  $10^5$ ,  $10^6$

Gill(1966) has discussed the boundary layers in a rectangular enclosure theoretically and given some physical insight for this convection problem. "In a rectangular enclosure, there are two layers competing for fluid, so one would expect the layer on the warmer wall to entrain fluid from the lower half of the enclosure, and the layer on the cooler wall to entrain fluid from the upper half. This influx of cooler fluid maintains a strong horizontal temperature gradient across the layer, and this gradient maintains the upward flow in the layer and the entrainment into the layer. The flow across the core brings cooler fluid into the lower half and warmer fluid into the upper half, leading to a stable vertical temperature gradient in the core. This vertical gradient is very important as it is the main factor in determining the structure of the boundary layers on the vertical wall. Its existence allows the boundary layers to eject as well as to entrain fluid. The flow in the core is weaker than in the boundary layers on the vertical walls and is not strong enough to maintain a horizontal temperature gradient as a result of horizontal isotherms in the core. The viscous and thermal diffusion in the adjacent to the horizontal boundaries tend to limit the velocity and temperature gradients there." A similar physical phenomenon is found in the current research for natural convection in a parallelogrammic enclosure. In the current study, however, the inclination angle has an additional influence on the boundary layers. As we noted from scale analysis, the thickness of

boundary layer is varied with  $(\cos(\text{IA}))^{-1/4}$  so that the thickness of boundary layer increases with increasing inclination angle. Higher inclination angle weakens the convection and results in the reduction of heat transfer.

Table 5.7 lists the Nusselt numbers and the ratio of two Nusselt numbers between  $15^\circ$  to  $60^\circ$ , showing heat transfer increases with increasing Rayleigh number and decreases with increasing inclination angle. For an inclination angle of  $60^\circ$ , the heat transfer decreases by about 50% to 30% for  $\text{Ra}=10^4$  to  $10^6$  compared to the inclination angle of  $15^\circ$ .

$\text{Ra}\backslash \text{IA}$	$15^\circ$	$30^\circ$	$45^\circ$	$60^\circ$	$\text{Nu}_{60}/\text{Nu}_{15}$
$10^4$	2.151	1.911	1.544	1.169	0.54
$10^5$	4.503	4.190	3.584	2.538	0.56
$10^6$	9.281	8.915	8.149	6.556	0.71

Table 5.7 Nusselt numbers for different Rayleigh numbers and inclination angles

### **5.6.2 Results for High Prandtl Numbers**

Numerical results for natural convection for high Prandtl number fluid and the same geometry, with an inclination angle of  $45^\circ$ , are obtained. The Prandtl numbers are 6.8, 20, 100 and 1000, while Rayleigh numbers are still taken as  $10^4$ ,  $10^5$  and  $10^6$ . Fig. 5.63 to 5.66 show the isotherms for these cases. If we trace the position of the ends of one isotherm, we find that the temperature fields are not influenced by varying the fluids which have higher viscosity than water. The density of isotherms near the walls is strongly influenced by Rayleigh number. The isotherm patterns for the four cases with different Prandtl numbers are almost identical for a given Rayleigh number. Clearly the Prandtl number has reached a limit, where the temperature distribution does not change so that the flow field and temperature will not be affected by Prandtl number. This implies that the dominant balance in such a physical process of natural convection is between viscous and buoyancy forces so that the flow is entirely determined by the Rayleigh number. The dependence of the flow field and heat transfer on only the Rayleigh number, at high Prandtl numbers, was an important condition for our experiments. In order to increase the range of Rayleigh number for experiments, it is necessary to use fluids which also have a high Prandtl number. The lack of dependence of Prandtl number permits a relatively large

range of Rayleigh number to test the numerical code as well as to expand the range of experimental observations. The thermal boundary layer thickness decreases as Rayleigh number increases. In particular, this thermal boundary layer extends to centre of the enclosure for Rayleigh number of  $10^4$ , and shrinks to one tenth of the width of the enclosure for Rayleigh number of  $10^6$ . The thicknesses of thermal boundary layer comply with the arguments from scale analysis. The layer thickness only depends on the Rayleigh number ( $(Ra)^{-1/4}$ ). Let us take a look at the ratio of the layer thicknesses from scale analysis. The ratios of  $(10^4)^{-1/4} / (10^5)^{-1/4}$  and  $(10^5)^{-1/4} / (10^6)^{-1/4}$  are 1.778. If we trace the isotherm labelled 5 from the plots of isotherms, we observe that the ratios of the layer thickness are 2.4 and 2.1, similar to the results of scale analysis. This demonstrates the layer thickness can be obtained using scale analysis derived from a simple physical argument.

Figure 5.67 shows the velocity vectors for Rayleigh number of  $10^6$  and Prandtl number of 6.8, 20, 100, 1000. From the velocity vectors, we further observe that the effect of Prandtl number on the flow field is very small at these large Prandtl numbers. One way to understand this is to recall that the flow is caused by buoyancy force and the temperature is coupled with velocity so that the temperature and velocity fields are identically influenced by Prandtl number. While the velocity

boundary layers still exist, it seems that the numerical results are not consistent with the expression for velocity boundary layer thickness as a function of both Rayleigh number and Prandtl number (Eq. 5.14) which is limited in its validity to Prandtl number up to order of 10 from scale analysis.

Table 5.8 lists the Nusselt numbers. The Nusselt number is essentially unchanged with the change of Prandtl number at the same Rayleigh number. Such lack of effect was reported numerically by de Vahl Davis (1983) for flow in a rectangular enclosure as well as experimentally by Krishnamurti (1970) for the transition from two to three dimensional flows in a fluid layer. At large  $\text{Pr}$ , the inertia term is small compared to the viscous force term, and is of the same order when the Prandtl number is greater than 6.8 so that the effect of Prandtl number on the flow and heat transfer is small.

$\text{Pr} \setminus \text{Ra}$	$10^4$	$10^5$	$10^6$
6.8	1.540	3.663	8.554
20	1.541	3.663	8.559
100	1.543	3.664	8.560
1000	1.542	3.664	8.560

Table 5.8 Nusselt numbers for different Prandtl and Rayleigh numbers, for  $\text{IA}=45^\circ$

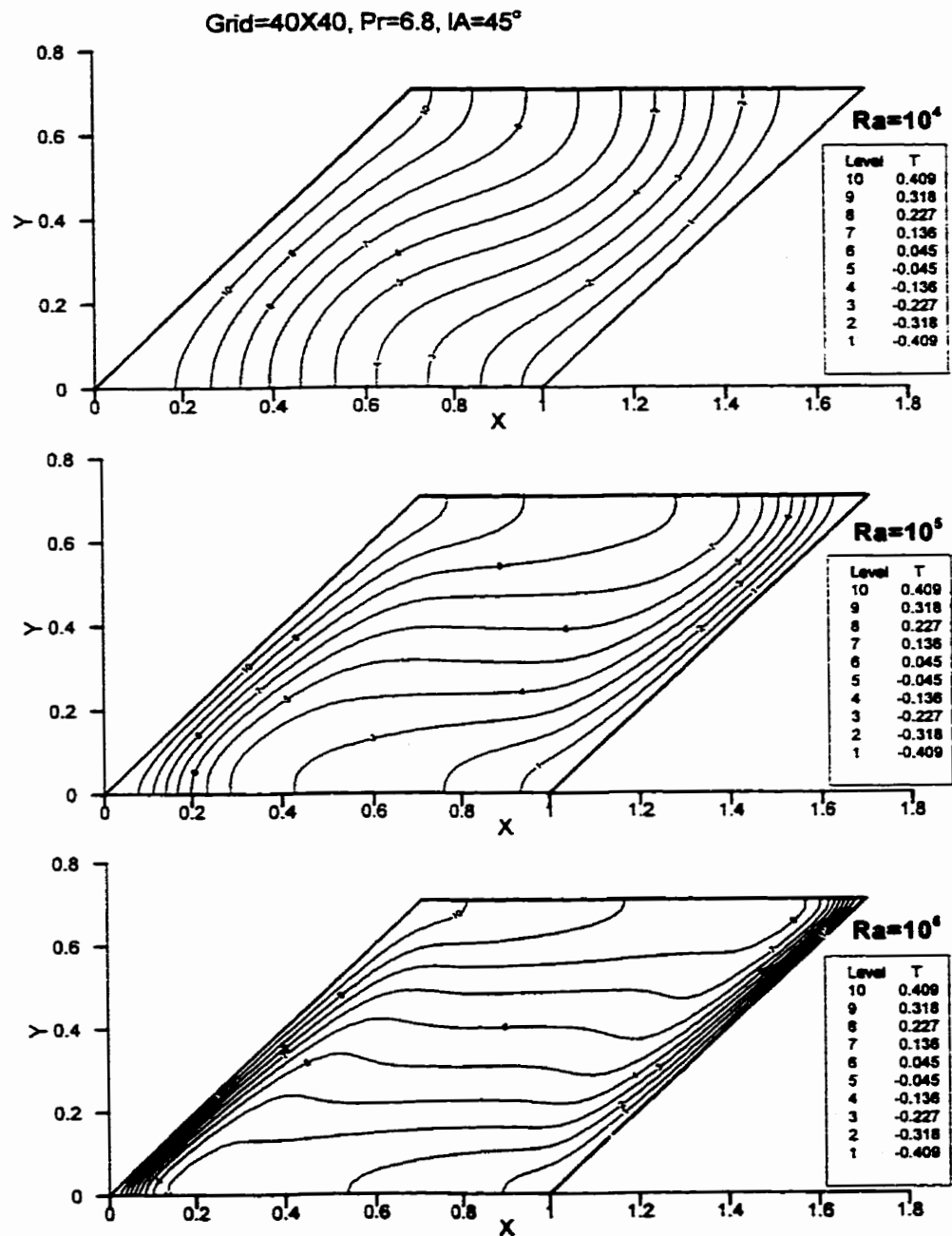


Figure 5.63 Isotherms for inclination angle (IA)=45°, Pr=6.8, Ra=10<sup>4</sup>, 10<sup>5</sup>, 10<sup>6</sup>

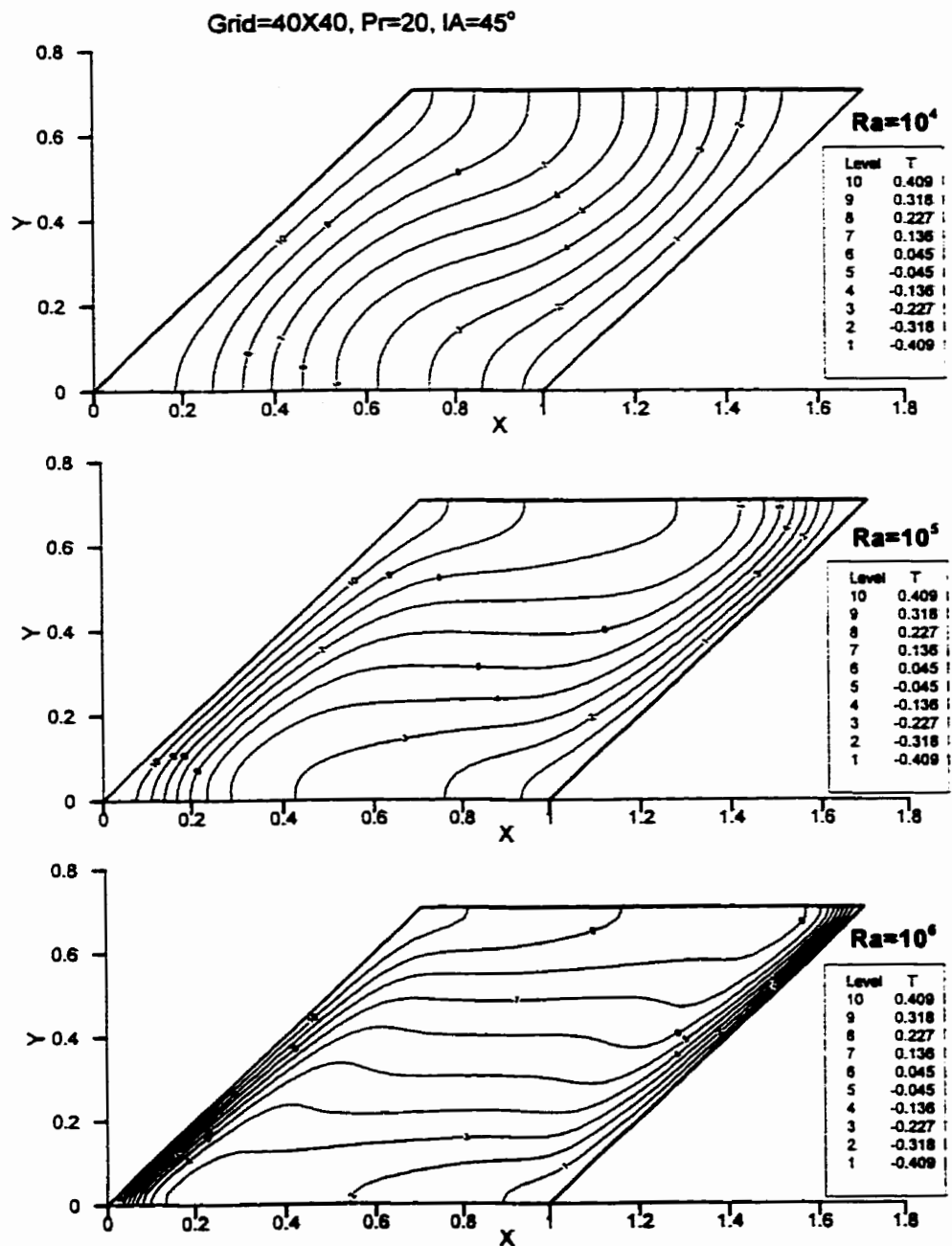


Figure 5.64 Isotherms for inclination angle(IA)=45°, Pr=20, Ra=10<sup>4</sup>, 10<sup>5</sup>, 10<sup>6</sup>

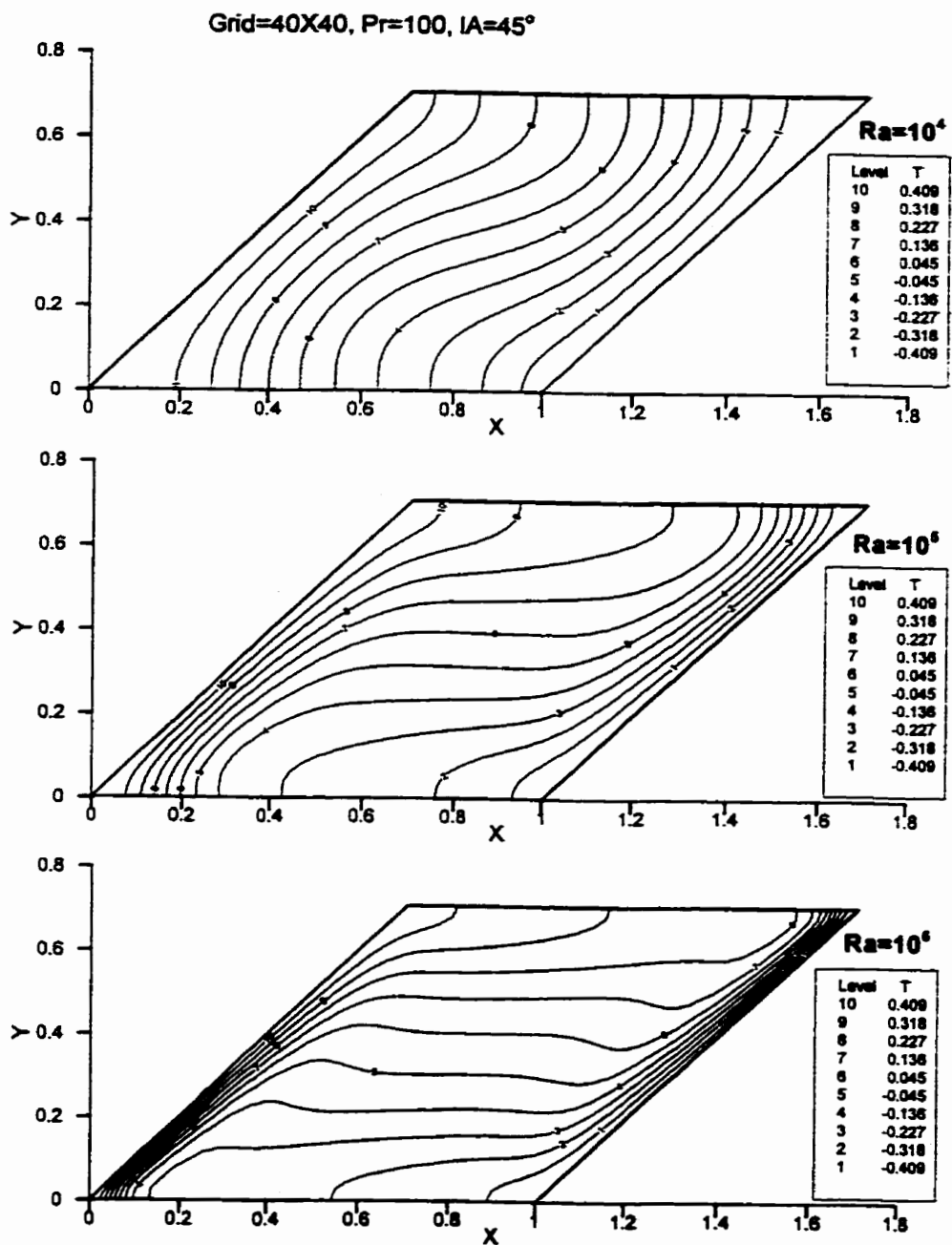


Figure 5.65 Isotherms for inclination angle (IA)=45°, Pr=100, Ra=10<sup>4</sup>, 10<sup>5</sup>, 10<sup>6</sup>

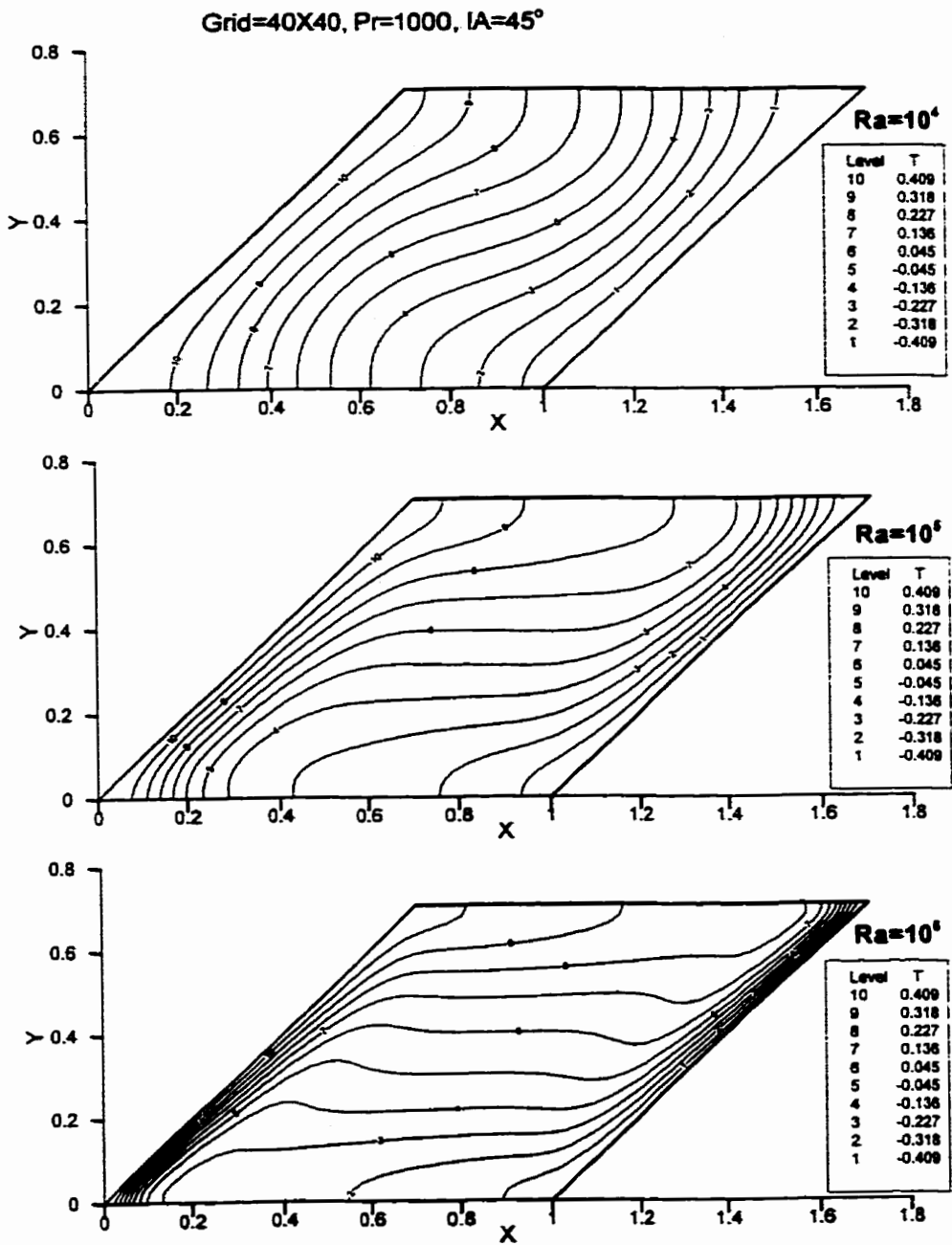


Figure 5.66 Isotherms for inclination angle(IA)=45°, Pr=1000, Ra= $10^4$ ,  $10^5$ ,  $10^6$

Grid=40X40, Data Skip 2, Ra=10<sup>6</sup>, IA=45°

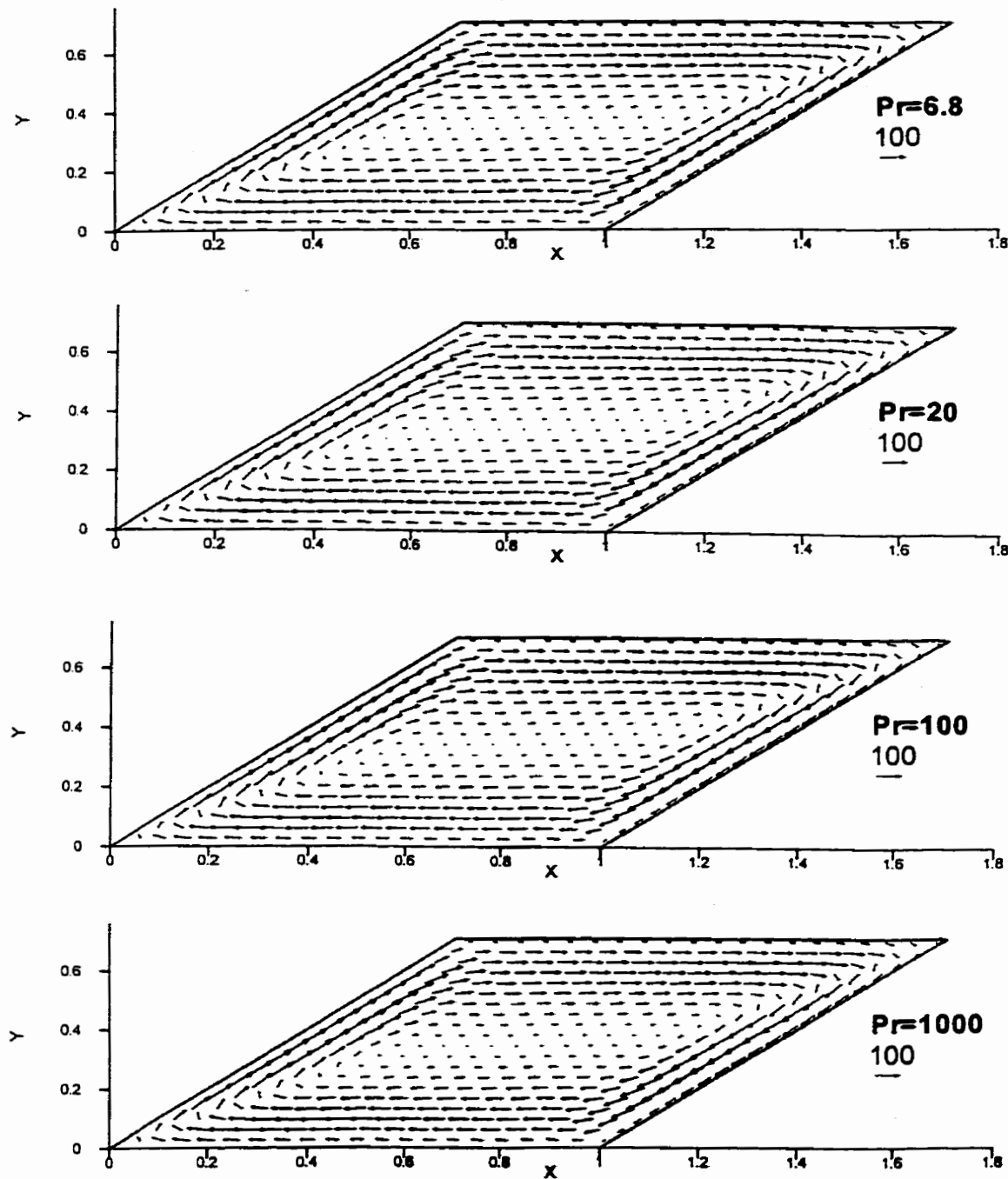


Figure 5.67 Velocity vectors for  $\text{Ra}=10^6$ ,  $\text{Pr}=6.8, 20, 100, 1000$

### **5.6.3 Comparison of Numerical and Experimental Results for Velocity**

Experiments were conducted to observe the flow field using DPIV as described in chapter 4. The experiments described here were conducted in conjunction with the numerical calculations using the finite volume method. Although confirmation of the validity of these numerical results was a primary goal, departures in the experiments from numerical predictions were expected and these are discussed. The velocities obtained for four cases with water and silicon oil as working fluid are compared with the results of computation.

It has been established that the two dimensionless parameters,  $Ra = g\rho\alpha\Delta T d^3/\kappa\mu$ , the Rayleigh number, and  $Pr = \mu/\rho\kappa$ , the Prandtl number, determine the response of the fluid in the cell when the initial and boundary conditions are set. It is desirable to adjust these parameters over as large a range as possible in order to test the validity of the calculations as well as observe phenomena which go beyond the range of the numerical work. In the experiments described here, the dimension  $L$ , of the enclosure with  $30^\circ$  inclination angle, is fixed for the duration of the experiments while the fluid can be changed from one experiment to

the next. Thus,  $\kappa$ ,  $\alpha$  and  $v$  were fixed with the choice of water or silicone oil. What can be changed most readily are the two applied temperatures through the heating element and cooling bath. While it was impractical to vary the temperature difference across the enclosure by more than a factor of 10, use of water and a viscous silicone oil made it possible to significantly increase the range of Rayleigh number. We report four cases in the experiments. With temperature differences for water ( $Pr=6.58$ ) at  $1.3^{\circ}\text{C}$  and  $15^{\circ}\text{C}$ , Rayleigh numbers were  $2.55 \times 10^6$  and  $2.92 \times 10^7$  respectively. For silicone oil ( $Pr=3300$ ) and temperature differences of  $1.3^{\circ}\text{C}$  and  $10.3^{\circ}\text{C}$ , Rayleigh numbers were  $4.3 \times 10^4$  and  $3.2 \times 10^5$  respectively. Thus, the experiments cover a range of almost 3 orders of magnitude in both Rayleigh number and Prandtl number providing a good test of the numerical work. We have already seen from the numerical results for high Prandtl number in the previous section that our observations should be essentially independent of Prandtl number so that we are really testing the fluid's response over a wide range of Rayleigh numbers.

The numerical results for the purpose of comparison were obtained using  $40 \times 40$ ,  $60 \times 60$  and  $80 \times 80$  grids for water. In Figures 5.68 and 5.69, the vertical velocities across the left boundary layer near the central line are presented for grids  $40 \times 40$ ,  $60 \times 60$  and  $80 \times 80$ , and Rayleigh number of  $2.55 \times 10^6$  and  $2.92 \times 10^7$ . From the

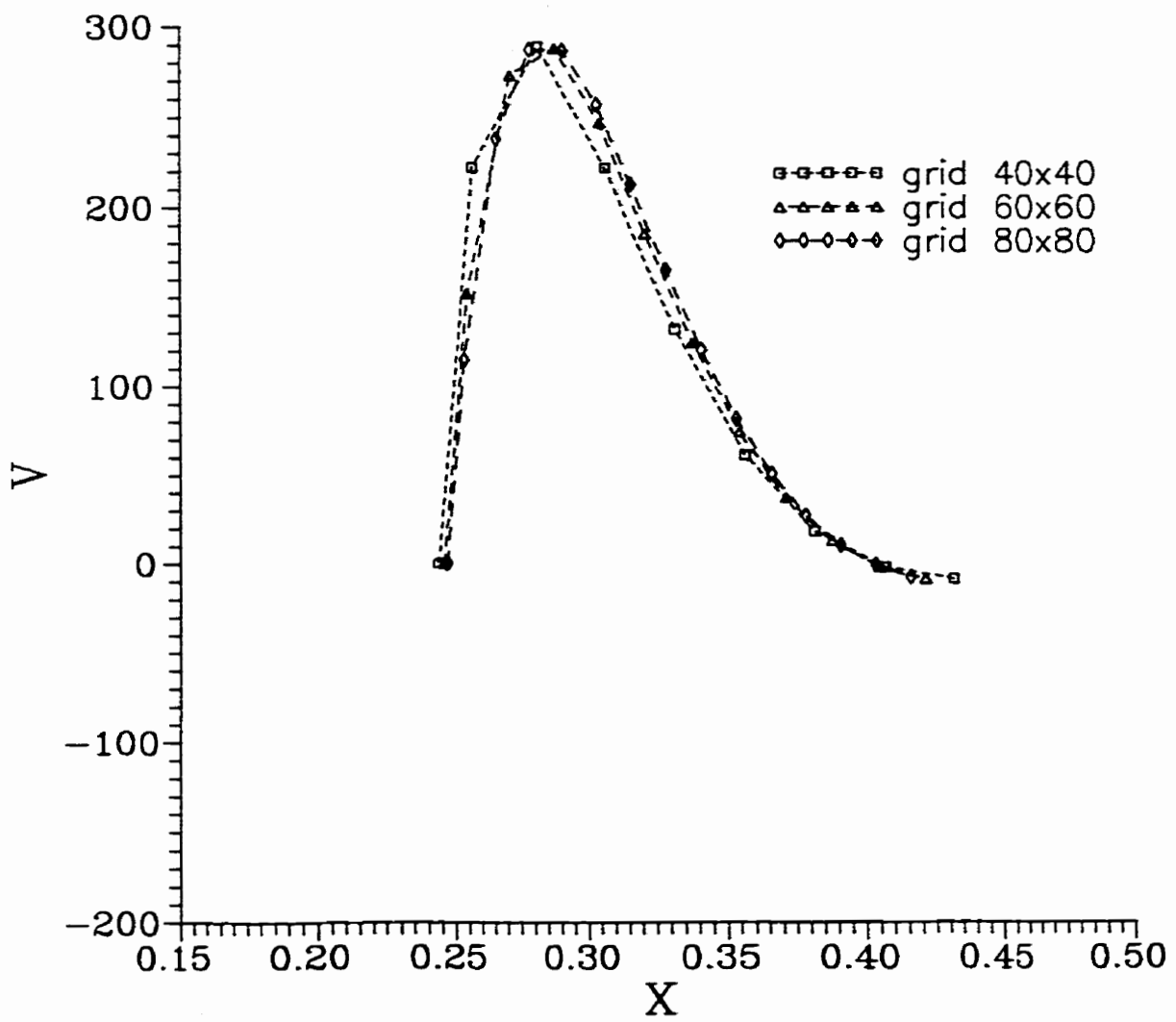


Figure 5.68 Dimensionless vertical velocity profiles near central line along Y for different grids and  $\text{Ra}=2.55 \times 10^6$  and  $\text{Pr}=6.58$

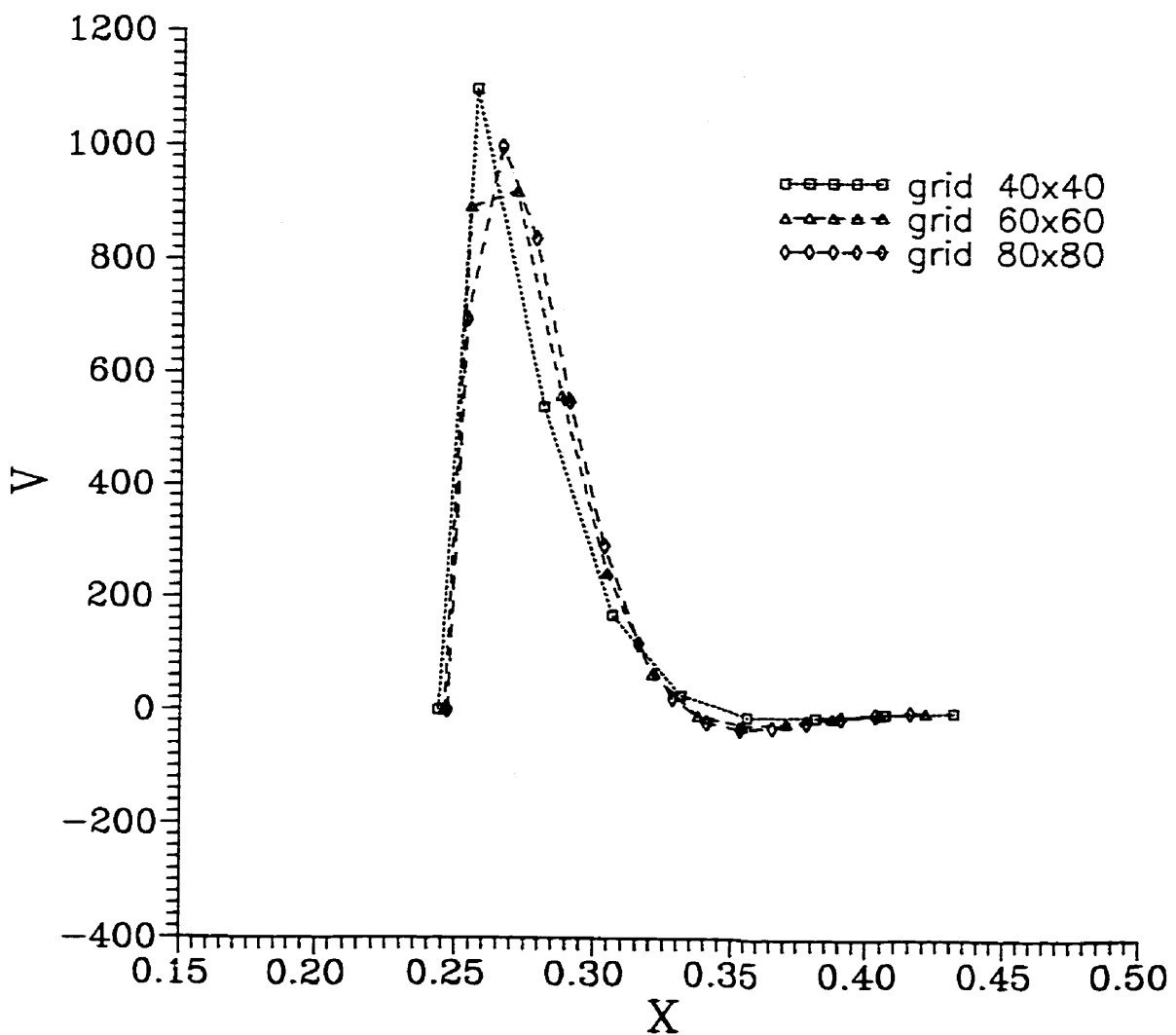


Figure 5.69 Dimensionless vertical velocity profiles near central line along Y for different grids and  $\text{Ra}=2.92 \times 10^7$  and  $\text{Pr}=6.58$

plots, we see that there is a small deviation of the velocity profiles among the three cases with different grids. Even with 40x40 grids, the boundary layer profile still can be seen. For the case of  $Ra=2.55*10^6$ , we observe that the effect of grids with 40x40 to 80x80 on the profile is very small. For  $Ra= 2.92*10^7$ , we observe about 10 to 15 % difference of the maximums of the vertical velocity for the three different grids so that using 40x40 grids we can still obtain relatively accurate solution.

Experimental vertical velocity, in dimensionless form, near the central line of the cell in the Y direction is presented in Figures 5.70, 5.71, 5.72 and 5.73 along with the computational results. The random error from DPIV observations is about 10% and this is represented by the error bars shown on the plots. The experimental observations were obtained in two parts and combined together to obtain a complete plot over all X. The inset in Fig. 5.71 shows the effect of the fixed wall on DPIV due to the averaging process which will be discussed later under error analysis.

The overall features of the computational results are reproduced experimentally. The boundary jets at the heating and cooling walls have widths commensurate with calculational ones and the velocity amplitude at maximum is close to agreement with the calculation for the three higher Rayleigh numbers, while

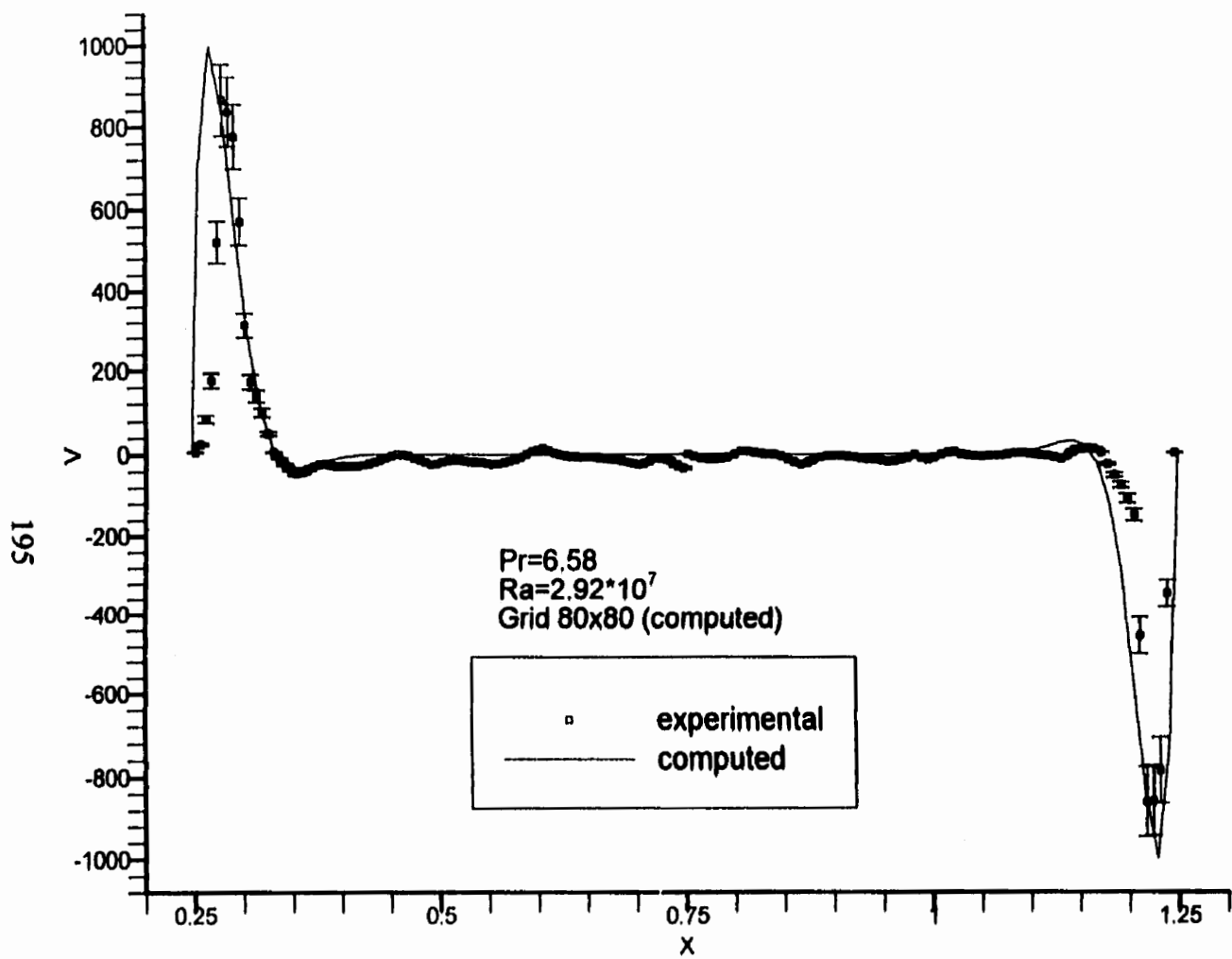


Figure 5.70 Comparison of dimensionless vertical velocity profiles between numerical and experimental results near central line along Y direction for water

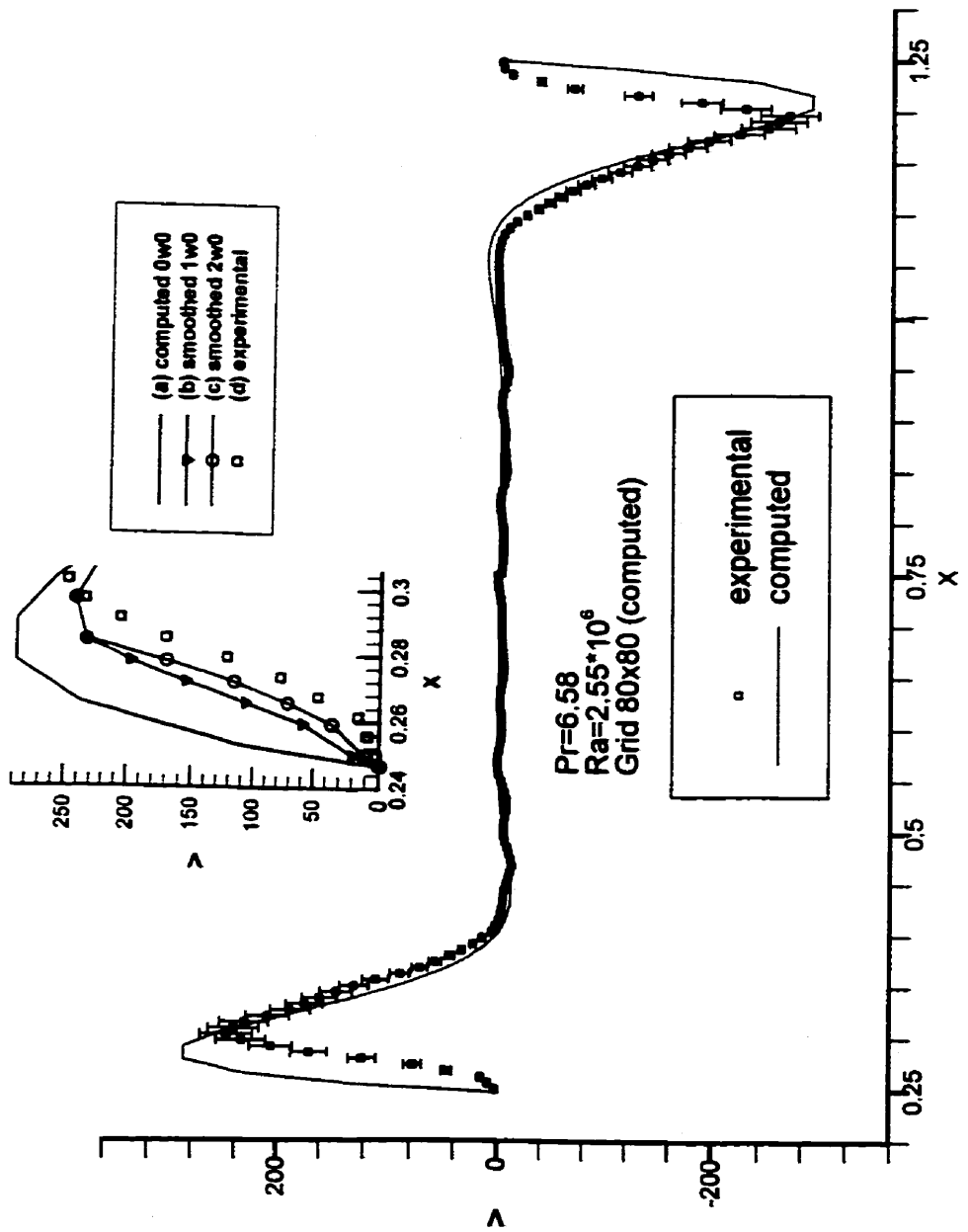


Figure 5.71 Comparison of dimensionless vertical velocity profiles between numerical and experimental results near central line along Y direction for water

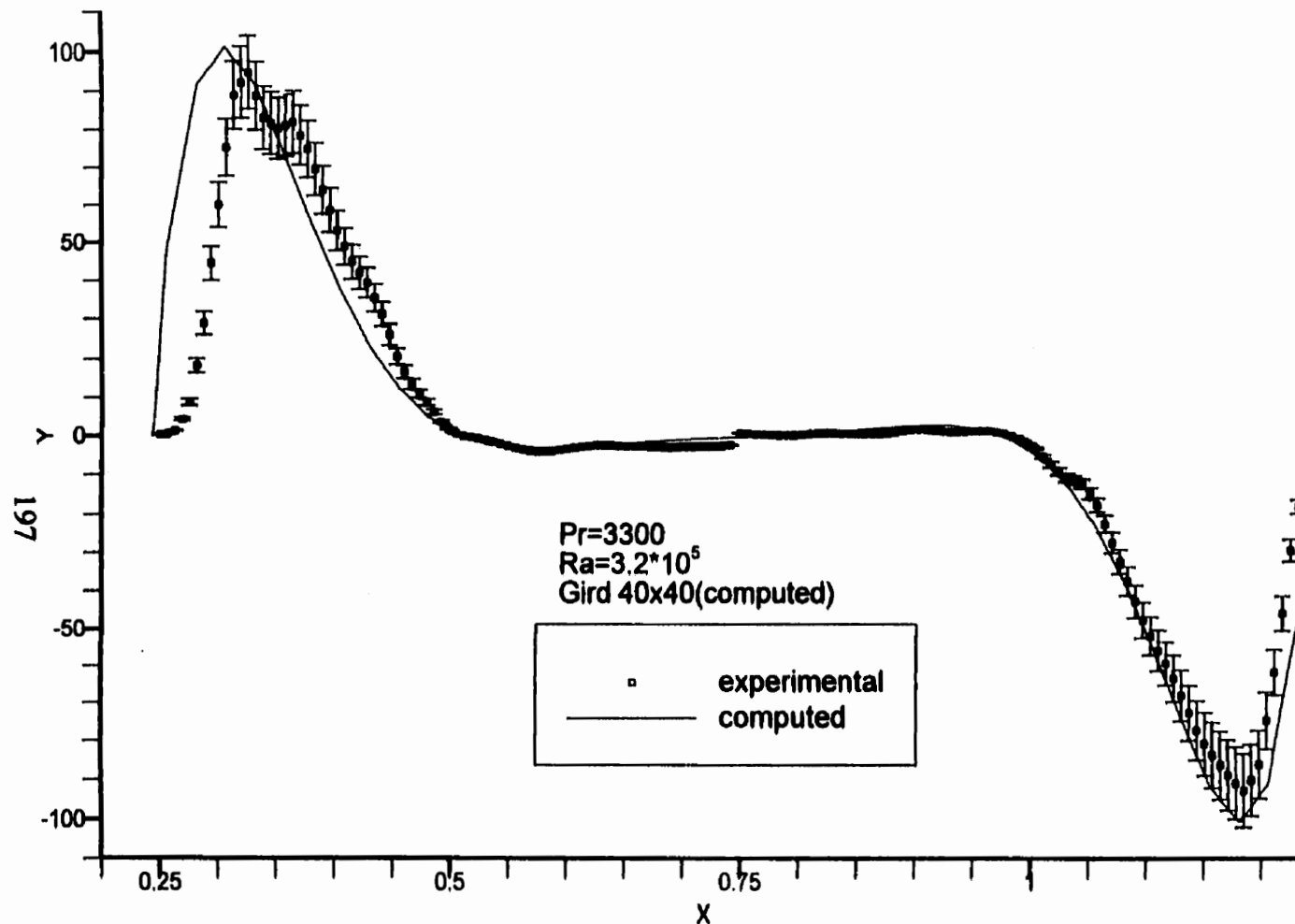


Figure 5.72 Comparison of dimensionless vertical velocity component profiles between numerical and experimental results near central line along Y direction for silicone oil

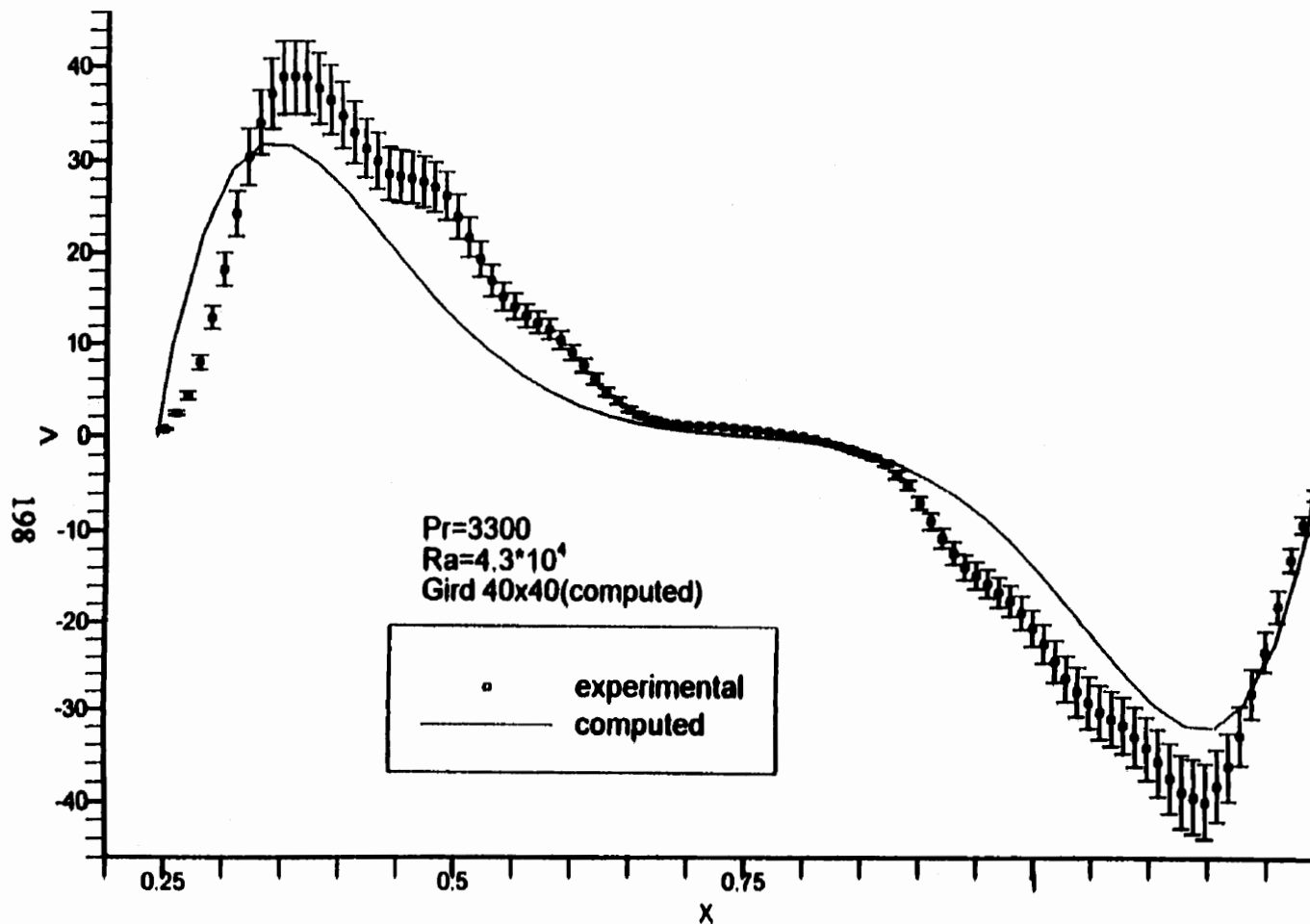


Figure 5.73 Comparison of dimensionless vertical velocity profiles between numerical and experimental results near central line along Y direction for silicone oil

significant amplitude differences arise at the lowest Rayleigh number. In this case errors due to positioning the data points in X were high partly due to the optical distortion caused by refraction in the silicone oil. Furthermore, at the lowest Rayleigh number control of the temperature was the least precise. Errors in horizontal positioning, most noticeable in Fig. 5.72, are seen as a shift of the data points to the right relative to the calculated points. Thus, the agreement between the observations and the calculations at the cool wall is an artifact. The smallest error in horizontal positioning is seen in Fig. 5.71 where the data points are symmetric in X relative to the calculated results. In this case we can see clearly that there is excellent agreement between theory and measurement in the interior side of the wall jets but very poor agreement next to the walls. This phenomenon is apparent in all four cases and can be understood as a systematic error in measurement of the DPIV system near a boundary and explained in detail in the following discussion of systematic error, under point 4. Since the velocity from DPIV is obtained by applying the averaging and correlating in image processing, large errors can result in regions of steep velocity gradients.

As the Rayleigh number increased over almost 3 orders of magnitude in the experiments, a significant reversed flow was found between the sidewall boundary

layers and the otherwise stagnant interior. The velocity field shown in figure 5.70 for  $\text{Ra} = 2.92 \times 10^7$  clearly illustrates this observation: a wall jet consisting of rapidly rising fluid next to the heated boundary is separated from the almost stagnant interior by a downward flow. (A similar phenomenon is also observed near the cooled wall, but with all signs reversed, as expected). This reversal, already described earlier as found in the numerical calculations for Rayleigh numbers greater than  $10^5$ , is a consequence of the overpowering convective forces at high Rayleigh numbers. Experimentally it has been observed that the boundary layer gets thinner and the velocity jet increases with increasing Rayleigh number. The strength of this convection is due to the steepening of the temperature gradient near the wall. The sign change of temperature gradient can lead to a convective reverse flow. Indeed, it is this reverse flow which accounts for the inability of the sidewall boundary layer to frictionally couple with the interior. Hence at higher Rayleigh numbers a stagnant interior remains while at lower Rayleigh numbers this reverse flow, does not exist, so much of the interior remains in motion.

Figures 5.74 to 5.77 show the observed and computed velocity fields with scales between the two fields about 2, 5, 2, and 2 for the four cases described above. There are three main features of the flow patterns obvious in the velocity field.

First, at low Rayleigh numbers the flow is as expected, with convection throughout the cell but at higher Rayleigh numbers there is a clear demarcation between a boundary layer jet and a relatively stagnant region occupying the entire central area. This pattern from experimental results is consistent with the calculations, but it is noteworthy that there appears to be no frictional coupling between the inner stagnant region and the outer boundary jet at higher Rayleigh numbers. This indicates that very high shears exist along the two side boundary layers.

Second, it is noteworthy that at larger Rayleigh numbers the boundary layers near the top and bottom of the cell on the insulated walls are noticeably thicker than the previously mentioned sidewall boundary layers. This too is expected from the numerical calculations as seen in these figures.

Third, while there is overall symmetry in the flow pattern through the midpoint in Y with 180° rotation, significant departures from symmetry are found in some regions. These departures are not expected from the calculations and are largely due to departures of the actual experiment from the idealized model of the calculations. Included in the discussion of errors below are these effects and other

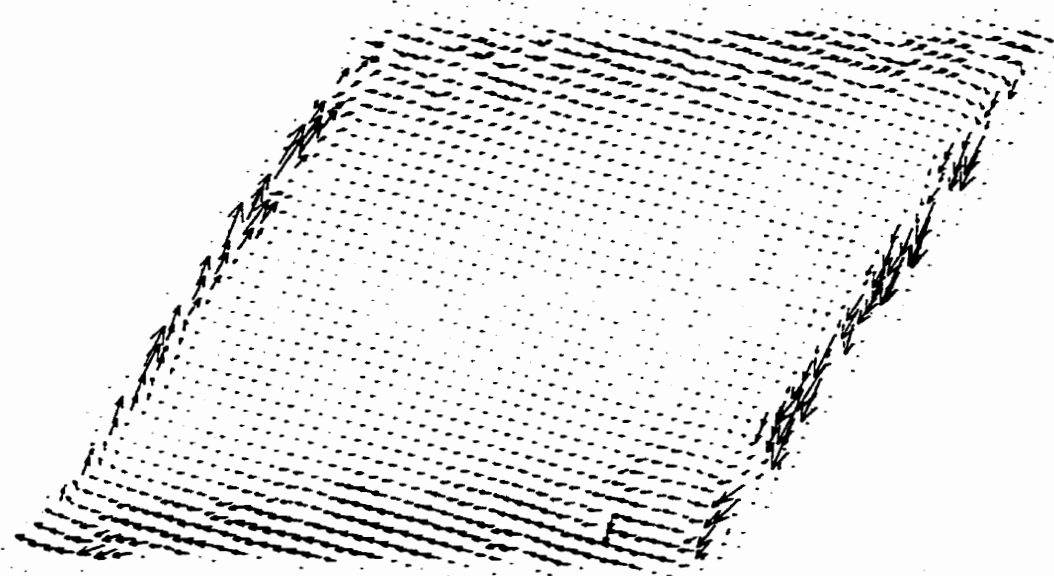
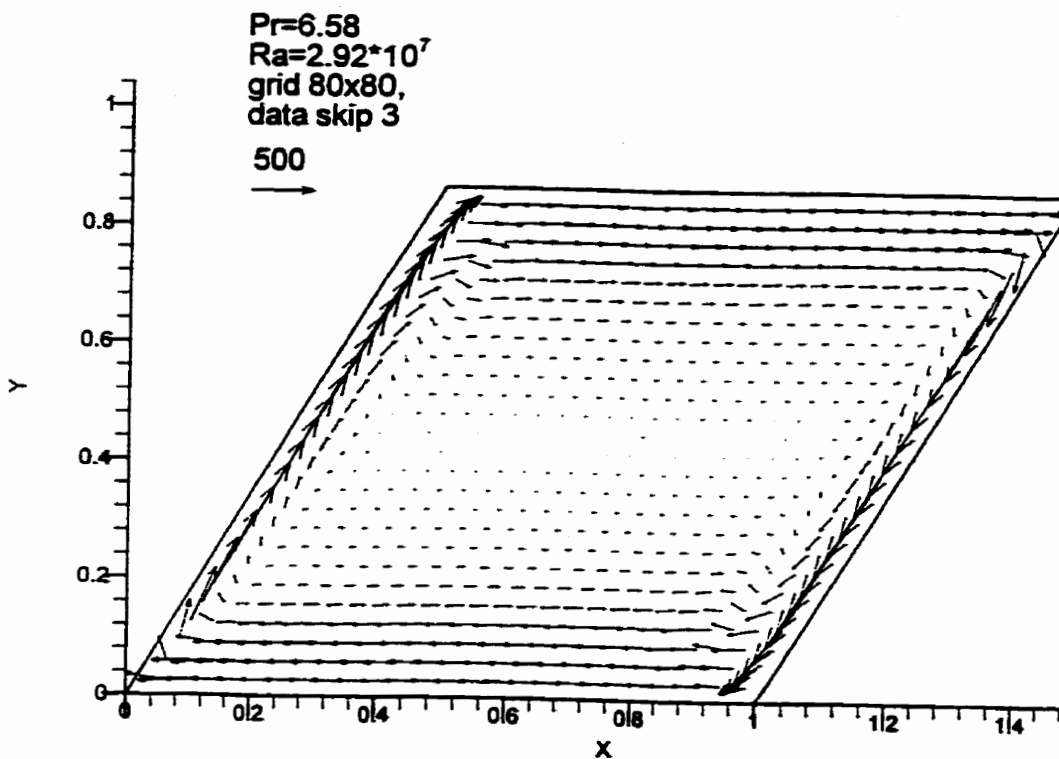


Figure 5.74 Velocity fields from experimental (lower) and numerical (upper) results

$\text{Ra}=2.92 \times 10^7$ ,  $\text{Pr}=6.58$

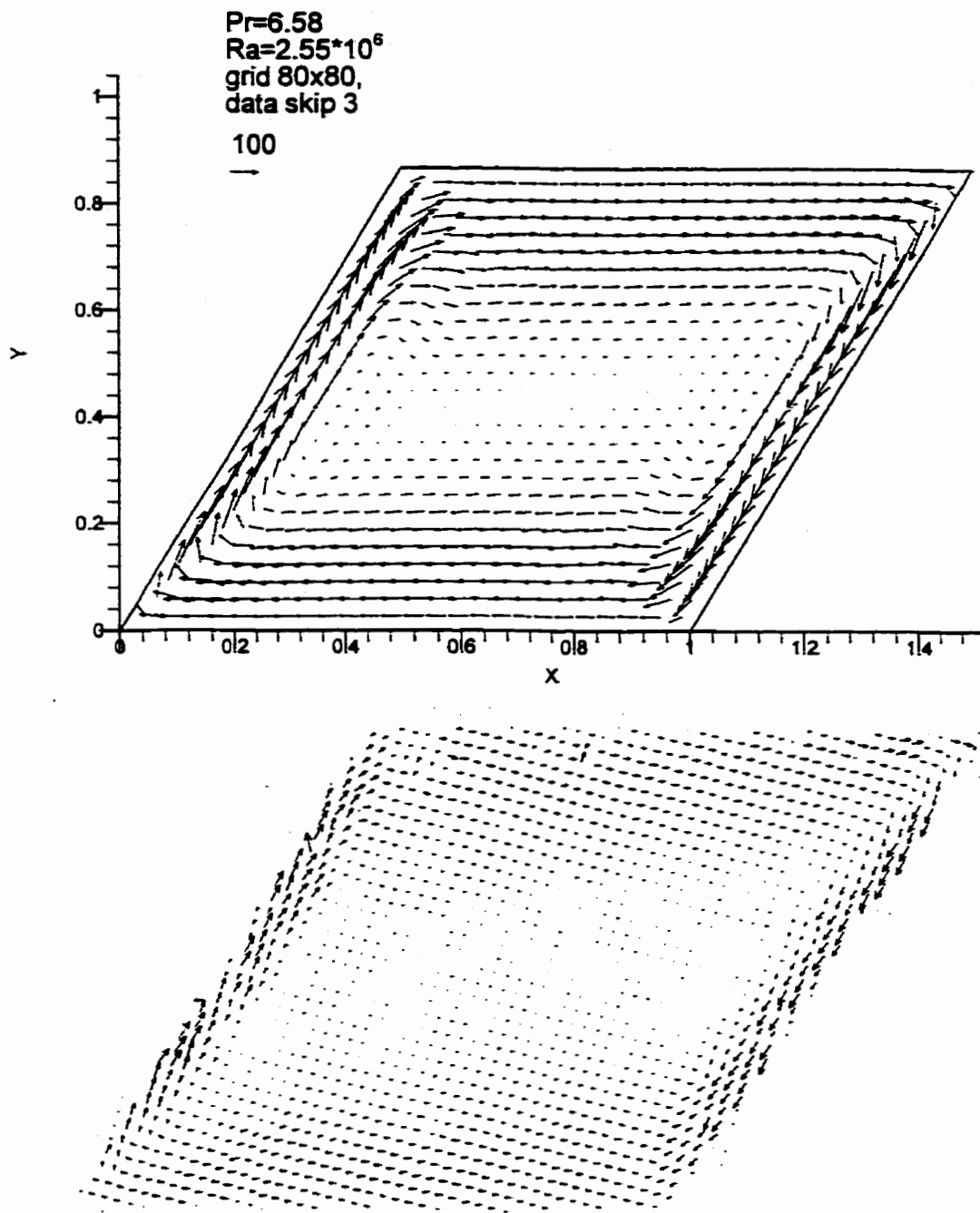


Figure 5.75 Velocity fields from experimental (lower) and numerical (upper) results

$\text{Ra}=2.55 \times 10^6$ ,  $\text{Pr}=6.58$

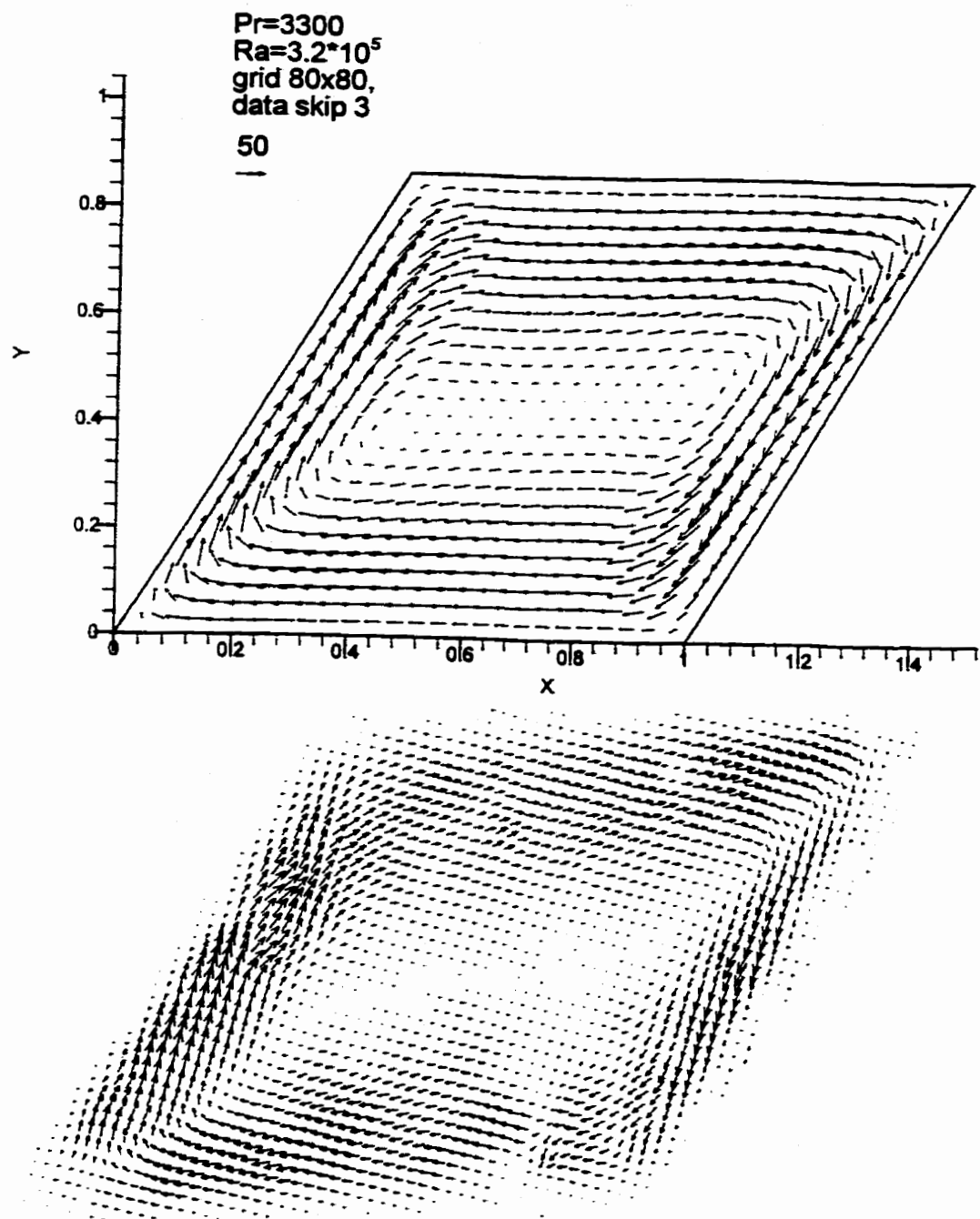


Figure 5.76 Velocity fields from experimental (lower) and numerical (upper) results

Ra= $3.2 \times 10^5$ , Pr=3300

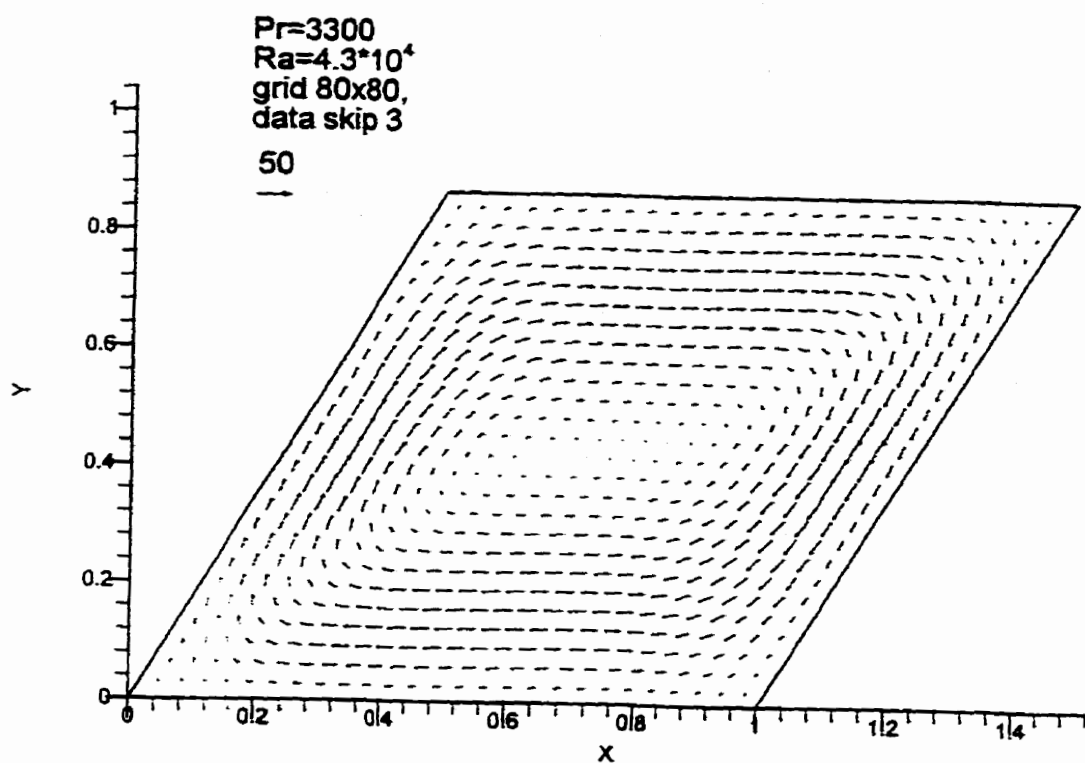


Figure 5.77 Velocity fields from experimental (lower) and numerical (upper) results

$\text{Ra} = 4.3 \times 10^4$ ,  $\Pr = 3300$

measurement errors.

Also, noted in the numerical calculations is the increasing thickness of the horizontal boundary layers compared to the sidewall boundary layers as the Rayleigh number increases. This phenomenon has been observed experimentally as shown in figures 5.74 to 5.77. The physics of this phenomenon is simply the conservation of mass: as the boundary layer jet on the sidewall, already confined to a very thin region and at high speed when the Rayleigh number is high, hits the top corner it is slowed since there is no buoyancy force along the horizontal wall to overcome friction. At lower Rayleigh numbers the jet is less intense and so slows down less when it hits the corner thus accounting for the smaller difference between sidewall and endwall boundary layer thicknesses.

At the highest Rayleigh number in Fig. 5.74, spatial oscillations were observed experimentally in the horizontal boundary layer, well after steady state conditions had been achieved. Apparently the limits of laminar flow were being approached so that for larger temperature differences across the cell, we already see what appears to be the beginning of the regime of turbulent flow. This phenomenon was not observed in the computation, since the ideal condition assumed there did not

prevail in the experiments.

Systematic errors in the experimental observations can be due to several factors which are discussed below.

1. Insulation. There are small areas where heat is escaping on the top, bottom and end walls due to imperfect insulation.
2. Shaded regions due to corners blocking the light. This leads to erroneous velocity fields near the boundary.
3. Mislocation of reflected images due to gradients of index of refraction associated with thermal gradients. This is most noticeable for the silicone oil as seen in figures 5.74, 5.75.
4. Poor correlations in region of high velocity gradients. If the velocity changes over the region of observation (32 by 32 pixels) the DPIV can only give the mean value. One place where an extreme gradient occurs is near the sidewall. The DPIV method can only give a mean value over the region of observation. Near the walls reflected light from the stationary wall will give zero velocity while the light reflected from the moving particles will give their velocity. But when averaged together these values will drastically underestimate the true velocity near the wall. This explains the significant underestimate of the reported experimental values near the walls while

the values on the interior side of the wall jet match quite well with the values expected from the calculations. The inset in figure 5.71 shows a simulation of the effect of the stationary wall on the DPIV measurements. Since the window used for DPIV sees particles on the wall as fixed, a zero velocity is averaged in with the observed velocities. In addition to the original computed ( a ) and observed ( d ) near the left wall from the figure below, the values of the calculation averaged over a moving window of width approximately the same as the DPIV window are shown by ( b ). In order to simulate the enhanced effect of the brightness of particles on the wall, a second averaging with the fixed particles weighted twice as much as the moving ones is shown by curve ( c ). It is clear that the averaging ( b ) and even more so with ( c ) that this simulation corroborates the difficulty in obtaining DPIV results near a fixed wall when the velocities vanish.

5. Insufficient control of temperature at the heated and cooled walls. Control of the temperature to  $0.1^\circ \text{ C}$  leads to the most significant errors when the temperature difference across the cell is smallest at  $1.3^\circ \text{ C}$ . Thus at lower Rayleigh number it is expected that temperature control is poorer so that it is not surprising to see significant departure between experimental and numerical results.

All of the above will contribute to systematic departures of the expected velocity distribution from that predicted by computation.

## **Chapter 6**

### **Summary and Conclusions**

The research work reported in this thesis includes several projects completed primarily through numerical methods with some experimental studies. In the numerical work, we have employed the finite volume method which is gaining popularity in the computational fluid dynamics (cfd) society. The application of conservation of physical quantities in the finite volume method is a primary reason for the increasing use of this method. Also, through the finite volume method, we can more readily obtain pressure directly as well as velocity and temperature rather than stream function and vorticity as usually obtained by the finite difference method.

In the comparison of computational results with laboratory observation which is essential, the finite volume method is ideal since the primitive variable of velocity is directly measurable through the DPIV system. Furthermore, the sloping boundaries used in the convection problem reported here are readily modelled using the finite

volume method. It is important to note that, in general, irregular boundaries can be accommodated by the finite volume method with numerical stability achieved through the inherent physical conservation in the control volume. In general, irregular geometries are important in many physical applications, so that the finite volume method is appropriate for modelling convection in these areas. For example, multiple pane windows could be tilted to reduce heat transfer, since Table 5.7 indicates that the heat transfer can be reduced up to 50% as inclination angle increases from  $15^\circ$  to  $60^\circ$ , thus saving energy. Although computation forms the basis of a design for heat transfer in many applications, obvious consideration must be made beyond heat transfer determined by the computation here. For example, practically an optimal angle for a multiple pane window with respect to heat transfer may not be acceptable for reasons of aesthetics.

Through this study, the feasibility of the finite volume method has been demonstrated by performing comparison with previous several studies. The formulated procedures and computer programs provide a potential tool to investigate thermal fluid problems occurring in geophysical applications with irregular geometries. For example, the flow field in the Earth's asthenosphere near a subducting plate evolves time. In the finite volume method, the steady solutions are

reached through a set of the transient process, so that a finite volume method could be used to model this application.

Numerical results have been found for five natural convection projects: heating the bottom wall and cooling the top wall of a square domain; cooling and heating sidewalls of a square enclosure; partly heating the bottom wall and cooling one sidewall of a square enclosure; heating and cooling vertical sidewalls of a parallelogrammic enclosure; heating and cooling inclined sidewalls of a parallelogrammic enclosure. A wide range of Rayleigh numbers and Prandtl numbers, as readily allowed by the finite volume method, are chosen to conduct these studies. In the experimental project, we designed the experimental cell and procedures for the last configuration. The DPIV technique was adapted to this geometry and used to capture the flow fields. Flow velocities using this method were compared with those from numerical computation. Although the results presented in the thesis are mainly steady state solutions, the transient results can readily be obtained. A further study of the intermediate features of such a physical process of natural convection can be done as future work.

For applications to cooling in computer chips, this research shows that

consideration should be given to mounting the chips at an optimum angle to the horizontal in order achieve maximum cooling, a result which is derived from Figure 5.51 showing heat transfer as a function of inclination angle. Fins on heat exchangers could be mounted to achieve maximum heat transfer by taking into account the angle of orientation of the fin. Specifically, with the base as hot side and the surrounding boundary as the cold side, fins would mounted on the base at an angle of 10° to 15° to optimize heat transfer as determined from Figure 5.51. At present, apparently due to tradition, such fins are mounted on supports at right angles.

In the first project, we conducted research on Rayleigh-Bénard convection. A two-dimensional square computational domain with top and bottom rigid boundaries and symmetric conditions at the sides was modelled with water as the working fluid. We obtained the steady results and determined the Nusselt numbers for Rayleigh numbers from 4,000 to 20,000 and Prandtl number of 6.8, corresponding to water. Comparison of Nusselt numbers was made between the current work and the early work by Schneck and Veronis (1967) and Mitrovica and Jarvis (1987). By performing such a comparison, we can conclude that the finite volume method is a suitable means to be used for investigating geophysical problems and instability. Agreement between the two studies was obtained with the

discrepancy in Nusselt number at about 2%. This agreement is as much a compliment to the early work when only limited computation was available as it is to verification of the finite volume method. Flow patterns were found with the features of one roll for these parameters under uniform initial conditions. The steady solutions reported with one roll flow pattern for different physical parameters were reached by evolution after starting with uniform initial conditions. As expected, the heat transport achieves maximum at the highest Rayleigh numbers with the main heat transfer basically located in the regions near the two side walls. By extending the studies to higher Rayleigh number of 50000, we found that the convection flow pattern could change from one roll to two rolls. Busse and Or (1986) derived a new class of solutions with asymmetric convection rolls. Also when we added a small perturbation of the form  $\theta=0.5-Y+0.01*\cos(K\pi X)$  to the initial conditions, the flow patterns and heat transfer for steady state changed with the changing wave number K from 1 to 6. It is found that the heat transfer is associated with the flow patterns, such that the heat transfer rates are the same for the flows with one roll pattern and the same for the flows with two rolls. In recent numerical experiments for this case, we found that the flow patterns depend on the numerical schemes. The time step and iterations for every time step do affect the steady solution of this problem in numerical computations. To explain these results requires a much more extensive

study. The insight and mechanism of these phenomena could be further investigated by looking into the transient results. Mitrovica and Jarvis (1987) conducted a numerical study for infinite Prandtl number and found the upper bound for Rayleigh number beyond which the solution is time-dependent. Applying the current computer code, it is practical to test the upper bound for which the flow becomes time-dependent.

In the second project, we numerically investigated the natural convection in a square enclosure with partly heated bottom and cooled one sidewall. The effects of length of the heating portion and Rayleigh number on heat transfer were displayed. Heat transfer increased with increasing Rayleigh number and heating section, with greater dependence of heating section on heat transfer occurring at Rayleigh number  $10^6$  as seen in Figure 5.32. The flow patterns are a single cell for Rayleigh number  $10^4$ ,  $10^5$  and two cells for Rayleigh number  $10^6$ . The flow structure found here is consistent with the findings by November and Nansteel (1987) using the finite difference method. Increasing the Rayleigh number generated more complex and strong flow and in consequence the heat transfer was increased.

In the third project, we have presented the steady numerical results of natural

convection in a square enclosure with sidewalls heated and cooled for Rayleigh number of  $10^4$ ,  $10^5$ , and  $10^6$  and Prandtl number of 0.68. The flow patterns and heat transfer were found to be consistent with those reported by De Vahl Davis (1982). As a basic feature in the natural convection problem, the heat transfer increases as Rayleigh number increases. The development of boundary layer and the reverse flow near the centre of the enclosure, as Ra number increases, are clearly demonstrated and shown as previously observed by De Vahl Davis (1982). The study by DeVahl Davis is based on the finite element method and the equations for the problem are steady. Hortmann (1990) et al. reported a benchmark solution and more accurate results for natural convection using the finite volume method. Current results are obtained by applying 40x40 and 80x80 grids. Comparing our current results on 40x40 and 80x80 grids with those from Hortmann et al. (1990), we obtained more accurate results using uniform grids. By comparison with the results of Hortmann et al. (1990) who considered only steady problem, we found that the steady solution for the time dependent convective flow can be obtained by solving the transient equations accurately. We note that there are few papers reporting the transient features of such a convection problem. We also found the oscillatory behaviour of the transient solution which has previously been reported by Patterson and Armfield (1990). Although some limited results of the transient problem have been presented

here, detailed study and presentation of transient processes must be a subject of future work.

In the fourth project, in order to demonstrate the strength of the finite volume method for irregular geometry, we carried out computation for natural convection in a parallelogrammic enclosure with two vertical walls heated and cooled and inclined walls insulated. The computations were for the cases with Rayleigh numbers of  $10^4$ ,  $10^5$ , and  $10^6$  and Prandtl number of 0.71 corresponding to air as the working fluid. The inclination angles of the upper and lower walls relative horizontal were chosen at  $15^\circ$ ,  $30^\circ$ ,  $45^\circ$ , and  $60^\circ$ . We found that the heat transfer increases first, reaches a maximum at about  $15^\circ$  and then decreases with increasing inclination angle. Such heat transfer characteristics provide us information in designing fins as mentioned earlier. Figure 5.51, discussed above, shows the effect of inclination angle on heat transfer. Some non-physical results found in the corner regions, were attributed to factors of meshes and schemes. Specially it was found that when the inclination angle was larger, this problem became more noticeable, but calculations at higher grid resolution revealed that the kinetic energy was not only small but rapidly decreased with increasing grid resolution as illustrated in Figure 5.50.

In the fifth project, we investigated both numerically and experimentally the problem of natural convection in a parallelogrammic enclosure with two inclined sidewalls heated and cooled and two horizontal walls insulated. Research into such a project is the basis for the understanding needed for energy efficient design in engineering applications, for example, in windows. Furthermore research on convection with a sloping boundary provides some understanding for the flow mechanism in a region with sloping boundary in ocean and a region near a subducting slab. We can simulate the physical process in the region by using the method developed if we employ appropriate boundary conditions.

We have presented the numerical results for different inclination angles, Rayleigh numbers and Prandtl numbers. It was found that the heat transfer decreases as inclination angle increases with the heat transport about 50% less for a change in the inclination angle of  $15^\circ$  to  $60^\circ$  as shown in table 5.7 . For the fluid with larger Prandtl numbers, the heat transfer is almost unchanged. The comparison between the numerical and experimental results is made for the case of inclination angle of  $30^\circ$  and for water and silicon oil. We compared the velocity near centre line of the enclosure and good agreement was found after accounting for systematic errors. Several sources of error in measurement were identified including temperature

fluctuations during the experiment and positioning. Difficulties in this DPIV near walls were found to account for large errors in obtaining velocities next to these boundaries. Velocity profiles reveal that the boundary layer is strongly developed for large Rayleigh number where strong convection dominated the transport process. At high Rayleigh number the experiments also showed the presence of a reverse flow near the wall jet as predicted by the numerical results. The most significant phenomenon found in the experiments not predicted in the computations was the oscillatory behaviour in the wall jet at high Rayleigh number. To study this problem more carefully, improvements in the control of the heating and cooling are needed so that any observed fluctuations would not be due to the source and sink of heat.

The finite volume method developed for this dissertation has been thoroughly tested by comparison with several classical numerical studies. In the new work, convection in a parallelogrammic enclosures, an extensive set of results has been achieved. Experimental observations, which are always important in evaluating new numerical results, were particularly essential here because of the calculation of non-orthogonal grids in the numerical work. After taking into account the systematic and random errors in the experimental observations, agreement between the computations and observations was found both qualitatively over the whole field of the cell as well

as quantitatively on the individual profiles. DPIV has been shown to be an important tool on both these scales as well as an ideal experimental method for validating numerical results from the finite volume method which yields the velocity field directly.

All current research work focused on the two-dimensional geometry domain with the side length aspect ratio of 1. Although some research work describing investigations of the effects of aspect ratio on heat transfer and flow fields exists, further numerical study should be done to find the effects of aspect ratio on heat convection in rectangular, and particularly parallelogrammic, enclosures. Further experimental work can be conducted for parallelogrammic enclosures with inclination angles other than 30°. In addition, the computer program described here can be implemented to perform numerical analysis for natural convection with internal heating. In general the this program can be applied to any natural convection problem in a quadrilateral enclosure. Finally the routines developed in this thesis can be used to investigate further more detailed flow problems with nonuniform boundary conditions.

## Appendix

Numerical data for mass residuals, flux at interfaces are listed below at selected control volumes. I, J, MassRe, MassE, MassN are index of control volumes, mass residual, and mass flux at east and north interfaces. Consider the following example to examine the sum of mass flux for control volume (I=40, J=40). The mass fluxes at its east and north face are -0.000257 and -0.000823 and the mass fluxes at east face of control volume (I=39, I=40) and at north face of the control volume (I=40, 39) are -0.000174 and -0.000905. The sum of the mass flux in and out of this control volume(40,40) is  $-0.000257 - 0.000823 + 0.000174 + 0.000905 = 0.000001$  which is 0 due to rounding off the numbers as shown by mass residual.

I	J	MassRe	MassE	MassN
32	32	0.000000	0.029985	-0.034049
33	32	0.000000	0.022108	-0.029134
34	32	0.000000	0.015419	-0.024231
35	32	0.000000	0.009975	-0.019461
36	32	0.000000	0.005784	-0.014907
37	32	0.000000	0.002800	-0.010609
38	32	0.000000	0.000920	-0.006466
39	32	0.000000	-0.000006	-0.001889
40	32	0.000000	-0.000181	0.003150
41	32	0.000000	0.000000	0.003781
32	33	0.000000	0.023970	-0.026251

I	J	MassRe	MassE	MassN
33	33	0.000000	0.017221	-0.022385
34	33	0.000000	0.011587	-0.018597
35	33	0.000000	0.007095	-0.014969
36	33	0.000000	0.003728	-0.011540
37	33	0.000000	0.001425	-0.008306
38	33	0.000000	0.000080	-0.005121
39	33	0.000000	-0.000444	-0.001366
40	33	0.000000	-0.000326	0.003031
41	33	0.000000	0.000000	0.003455
32	34	0.000000	0.018529	-0.019622
33	34	0.000000	0.012876	-0.016732
34	34	0.000000	0.008237	-0.013957
35	34	0.000000	0.004613	-0.011345
36	34	0.000000	0.001974	-0.008901
37	34	0.000000	0.000252	-0.006584
38	34	0.000000	-0.000651	-0.004218
39	34	0.000000	-0.000843	-0.001174
40	34	0.000000	-0.000465	0.002653
41	34	0.000000	0.000000	0.002990
32	35	0.000000	0.013817	-0.014126
33	35	0.000000	0.009195	-0.012109
34	35	0.000000	0.005460	-0.010222
35	35	0.000000	0.002598	-0.008483
36	35	0.000000	0.000569	-0.006873
37	35	0.000000	-0.000687	-0.005328
38	35	0.000000	-0.001251	-0.003654
39	35	0.000000	-0.001191	-0.001233
40	35	0.000000	-0.000597	0.002059
41	35	0.000000	0.000000	0.002393
32	36	0.000000	0.009981	-0.009697
33	36	0.000000	0.006297	-0.008426
34	36	0.000000	0.003353	-0.007278
35	36	0.000000	0.001125	-0.006255
36	36	0.000000	-0.000425	-0.005323
37	36	0.000000	-0.001345	-0.004408
38	36	0.000000	-0.001689	-0.003310

I	J	MassRe	MassE	MassN
39	36	0.000000	-0.001470	-0.001452
40	36	0.000000	-0.000712	0.001301
41	36	0.000000	0.000000	0.001681
32	37	0.000000	0.007187	-0.006241
33	37	0.000000	0.004325	-0.005563
34	37	0.000000	0.002038	-0.004991
35	37	0.000000	0.000302	-0.004519
36	37	0.000000	-0.000914	-0.004106
37	37	0.000000	-0.001642	-0.003680
38	37	0.000000	-0.001894	-0.003058
39	37	0.000000	-0.001622	-0.001724
40	37	0.000000	-0.000782	0.000460
41	37	0.000000	0.000000	0.000899
32	38	0.000000	0.005613	-0.003646
33	38	0.000000	0.003443	-0.003393
34	38	0.000000	0.001676	-0.003224
35	38	0.000000	0.000285	-0.003128
36	38	0.000000	-0.000747	-0.003074
37	38	0.000000	-0.001428	-0.003000
38	38	0.000000	-0.001738	-0.002747
39	38	0.000000	-0.001556	-0.001907
40	38	0.000000	-0.000753	-0.000343
41	38	0.000000	0.000000	0.000147
32	39	0.000000	0.005488	-0.001793
33	39	0.000000	0.003881	-0.001786
34	39	0.000000	0.002494	-0.001837
35	39	0.000000	0.001306	-0.001940
36	39	0.000000	0.000305	-0.002074
37	39	0.000000	-0.000498	-0.002196
38	39	0.000000	-0.001049	-0.002196
39	39	0.000000	-0.001158	-0.001799
40	39	0.000000	-0.000595	-0.000905
41	39	0.000000	0.000000	-0.000449
32	40	0.000000	0.007109	-0.000568
33	40	0.000000	0.005953	-0.000630
34	40	0.000000	0.004836	-0.000719

I	J	MassRe	MassE	MassN
35	40	0.000000	0.003730	-0.000834
36	40	0.000000	0.002623	-0.000968
37	40	0.000000	0.001529	-0.001102
38	40	0.000000	0.000520	-0.001188
39	40	0.000000	-0.000174	-0.001104
40	40	0.000000	-0.000257	-0.000823
41	40	0.000000	0.000000	-0.000706
32	41	0.000000	0.008072	0.000000
33	41	0.000000	0.007441	0.000000
34	41	0.000000	0.006723	0.000000
35	41	0.000000	0.005889	0.000000
36	41	0.000000	0.004921	0.000000
37	41	0.000000	0.003819	0.000000
38	41	0.000000	0.002632	0.000000
39	41	0.000000	0.001528	0.000000
40	41	0.000000	0.000706	0.000000
41	41	0.000000	0.000000	0.000000

## **References**

- Anderson, D. A., Tannehill, J. C. And Pletcher, R. H. (1984) Computational Fluid Mechanics and Heat Transfer, Hemisphere Publishing Corporation.
- Arakawa, A., (1966) Computational design for long-term numerical integrations of the equations of atmospheric motion. *J. Comput. Phys.*, 1, pp119-143.
- Armfield, S.W. and Patterson, J. C. (1991) Direct simulation of wave interactions in unsteady natural convection in a cavity, *Int. J. Heat Mass transfer*, Vol. 34, No. 4/5, pp.929-940.
- Arroyo, M. P. and Savirón, J. M. (1992) Rayleigh-Bénard convection in a small box: spatial features and thermal dependence of the velocity field, *J. Fluid Mech.*, Vol. 235, pp. 325-348 .
- Batchelor, G. K. (1954) Heat transfer by free convection across a closed cavity between vertical boundaries at different temperature. *Q. Appl. Math.*, Vol. 12, pp. 209-233.
- Bejan A. (1995) Convection Heat Transfer, John Wiley & Sons Inc. .
- Bergé, P. and Dubois, M. (1984) Rayleigh-Bénard convection, *Contem. Phys.*, Vol.

25, No. 6, pp. 535-582.

- Burmeister, L. C. (1993) Convective Heat Transfer, John Wiley & Sons Inc. .
- Busse, F.H. (1985) Transition to Turbulence in Rayleigh-Bénard Convection, Hydrodynamic Instabilities and the Transition to Turbulence, edited by H.L. Swinney and J. P. Gollub, Springer-Verlag.
- Busse, F.H. (1989) Fundamentals of Thermal Convection, in Mantle Convection edited by W.R. Peltier, Gordon and Breach Science Publishers, pp. 23-95.
- Busse, F. H. and Clever, R. M.(1981) An asymptotic model of two-dimensional convection in the limit of low Prandtl number, J. Fluid Mech. , Vol.102 , pp. 75-83.
- Catton, I. (1978) Natural convection in enclosures, Heat Transfer 1978, Vol. 6, pp. 13-43.
- Catton, I., Ayyaswamy, P.S. and Clever, R. M (1974) Natural convection flow in a finite rectangular slot arbitrarily oriented with respect to the gravity vector, Int. J. Heat Mass Transfer, Vol. 17., pp. 173-184.
- Chandrasekhar, S. (1961) Hydrodynamic and Hydromagnetic stability, Oxford Clarendon.
- Chapman, C. J. and Proctor, M. R. E (1980) Nonlinear Rayleigh-Bénard convection between poorly conducting boundaries, J. Fluid Mech. Vol. 101, part 4, pp.

759-782.

Chen, K.S. and Ko, P.W. (1991) Natural convection in a partially divided rectangular enclosure with an opening in the partition plate and isoflux side walls, Int. J. Heat Mass Transfer, Vol. 34, No. 1, pp. 237-246.

Chung, K. C. and Trefethen, L. M. (1982) Natural convection in a vertical stack of inclined parallelogrammic cavities, Int. J. Heat Mass Transfer, Vol. 25, No. 2, pp. 277-284.

Clever, R. M. and Busse, F. H. (1981) Low-Prandtl-number convection in a layer heated from below, J. Fluid Mech. , Vol. 102, pp. 61-74.

De Vahl Davis, G. and Jones, I. P. (1983) Natural convection in a square cavity: a comparison exercise, Int. J. For Num. Methods in Fluids, Vol. 3, pp. 227-248.

De Vahl Davis, G. (1983) Natural convection of air in a square cavity: a bench mark numerical solution, Int. J. for Nuemrical Methods in Fluids, Vol. 3, pp. 249-264.

Dick E. (1996) Computational Fluid Dynamics, Edited by Wendt. J. F., Springer-Verlag.

Fletcher, C. A. (1988) Computational Techniques fro Fluid Dynamics, Vol. 1 and Vol. 2 , Springer-Verlag.

Foster, T. D. (1969) Convection in a variable viscosity fluid heated from within, J. Geophys. Res., Vol. 74, pp. 685-693.

Gill, A. E. (1966) The boundary layer regime for convection in a rectangular cavity, J. Fluid Mech., Vol. 26, pp. 515-536.

Goldhirsch, I., Pelz , R. B. and Orszag, S. A. (1989) Numerical simulation of thermal convection in two-dimensional finite box, J. Fluid Mech. Vol. 199, pp. 1-28.

Grötzbach, G. (1982) Direct numerical simulation of laminar and turbulent Bénard convection, J. Fluid Mech. Vol. 119, pp. 27-53.

Grötzbach, G. (1983) Spatial resolution requirements for direct numerical simulation of the Rayleigh-Bénard convection, J. of computational physics, Vol. 49, pp.241-264.

Han, J. T. (1979) A computational method to solve nonlinear elliptic equations for natural convection in enclosure, Numerical Heat Transfer, Vol. 2, pp. 165-175.

Hansen, U., Yuen, D. A. and Kroening, S. E. (1992) Mass and heat transport in strongly time-dependent thermal convection at infinite Prandtl number, Geophys. Astrophys. Fluid Dynamics, Vol. 63, pp. 67-89.

Harlow, F. H. And Welch, J. E. (1965) Numerical calculation of time-dependent viscous incompressible flow of fluid with free surfaces, Physics of Fluids,

Vol. 8 pp. 2182-2189.

Hart, J. (1971) Stability of the flow in a differentially heated inclined box, *J. Fluid Mech.*, Vol. 47, pp 547-576.

Hiller, W. J., Koch, A.T. Kowaleski, T.A. and Stella, F. (1993) Onset of natural convection in a cube, *Int. J. Heat Mass Transfer*, Vol.36, No. 13, pp. 3251-3263.

Hortmann M., Perić M., and Scheuerer G. (1990) Finite volume multigrid prediction of laminar natural convection: bench-mark solutions, *Int. J. For Num. Meth. In Fluids*, Vol. 11, pp. 189-207.

Hyun, J. M. and Lee, J. W. (1989) Numerical solutions for transient natural convection in a square cavity with different sidewall temperatures, *Int. J. Heat and Fluid Flow*, Vol. 10, No. 2, pp. 146-151.

Ivey, G. N. (1984) Experiments on transient natural convection in a cavity, *J. Fluid Mech.*, Vol. 144, pp. 389-401.

Jaluria, Y. (1980) *Natural Convection*, Pergamon Press.

Karayiannis, T. G. and Tarasuk, J. D. (1988) Natural convection in an inclined rectangular cavity with different thermal boundary conditions at the top plate, *J. Heat Transfer*, Vol. 110, pp. 350-357.

Kazmierczak, M. and Chinoda, Z. (1992) Buoyancy-driven flow in an enclosure with

- time periodic boundary conditions, Int. J. Heat Mass transfer, Vol. 35, No.6 , pp. 1507-1518.
- Kim, D. M. and Viskanta, R. (1985) Effect of wall heat conduction on natural convection heat transfer in a square enclosure, J. Heat Transfer, Vol. 107, pp. 139 - 152.
- Korpela, S. A. (1974) A study on the effect of Prandtl number on the stability of the conduction regime of natural convection in an inclined slot, Int. J. Heat Mass Transfer, Vol. 17, pp. 215-222.
- Koschmieder, E. L. (1993) Bénard Cells and Taylor Vortices, Cambridge, University Press.
- Krishnamurti, R. (1970) On the transition to turbulent convection. Part 1. The transition from two- to three-dimensional flow, J. Fluid Mech., Vol. 42, pp. 295-309.
- Krishnamurti, R. (1970) On the transition to turbulent convection. Part 2. The transition to time-dependent flow, J. Fluid Mech., Vol. 42, pp. 309-320.
- Kröner, D. (1997) Numerical Schemes for Conservation Laws, Wiley & Sons Ltd and Teubner.
- Kuo, C. H., Sharif, M. A. R. and Schrieber, W. C. (1992) Numerical simulation of two-dimensional Bénard convection, The American Society of Mechanical

**Engineers, HTD-Vol.198.**

Kurzweg, U. H. (1970) Stability of natural convection within an inclined channel, *J.*

**Heat Transfer**, Vol. 14, pp. 190-191.

Kvernvold, O. (1979) Rayleigh-Bénard convection with one free and one rigid boundary, *Geophys. Astrophys. Fluid Dynamics*, Vol. 12, pp. 273-294.

Lage, J. L. and Bejan, A. (1993) The resonance of natural convection in an enclosure heated periodically from the side, *Int. J. Heat Mass transfer*, Vol. 36, No.8 , pp. 2027-2038.

Lage, J. L. and Bejan, A. (1991) The Ra-Pr domain of laminar natural convection in an enclosure heated from the side, *Numerical Heat Transfer, Part A*, Vol. 19, pp. 21-41.

Liang, S. F. and Acrivos, A. (1970) Stability of buoyancy-driven convection in a tilted slot, *Int. J. Heat Mass Transfer*, Vol. 13, pp. 449-458.

Lin, D. S. and Nansteel, M. W. (1987) Natural convection heat transfer in a square enclosure containing water near its density maximum, *Int. J. Heat Mass Transfer*, Vol. 30, No. 11, pp. 2319-2329.

Maekawa, T. and Tanasawa, I. (1982) Natural convection heat transfer in parallel ogrammic enclosures, *Proc. 7th Int. Heat Tarnsfer Conference*, Vol. 2, pp. 227-232.

Markatos, N.C. and Pericleous, K.A. (1984) Laminar and turbulent natural convection in an enclosed cavity, Int. J. Heat Mass transfer, Vol. 27, No.5 , pp. 755-772.

May, H. O. (1991) A numerical study on natural convection in an inclined square enclosure containing internal heat sources, Int. J. Heat Mass Transfer, Vol. 34, pp. 919-928.

Meunier, P. (1996) Convection libre dans une cellule oblique, Report to Department of Earth and Atmospheric Science, York University.

Mitrovica, J. X. and Jarvis, G. T. (1987) A numerical study of thermal convection between rigid horizontal boundaries, Geophys. Astrophys. Fluid Dynamics, Vol. 38, pp. 193-224.

Moore, D. R. and Weiss, N. O. (1973) Two-dimensional Rayleigh-Bénard convection, J. Fluid Mech. Vol. 58, part 2, pp. 289-312.

Morrison, G. L. and Tran, V.Q. (1978) Laminar flow structure in vertical free convective cavities, Int. J. Heat Mass Transfer, Vol. 21, pp. 203-213.

Nakayama, W., Hwang, G. J. and Cheng, K. C. (1970) Thermal instability in plane Poiseuille flow, J. Heat Transfer, Vol. 92, pp. 61-68.

Nicolette, V. F., Yang, K. T. and Lloyd, J. R. (1985) Transient cooling by natural

convetcion in a two-dimensional square enclosure, Int. J. Heat Mass Transfer, Vol. 28, No. 9, pp. 1721-1732.

November, M. and Nansteel, M. W. (1987) Natural convection in rectangular Enclosures heated from below and cooled along one side, Int. J. Heat Mass Transfer, Vol. 30, pp. 2433-2440.

Ostrach, S. (1972) Natural convection in enclosures, Advances in Heat Transfer, J. P. Hartnett And T. F. Irvine Jr. , ed., Vol.8, pp.161-227.

Ostrach, S. (1982) Natural convection Heat Transfer in Cavities and cells, Heat Transfer 1982, Vol. 1, pp.365-379.

Ostrach, S. (1988) Natural convection in enclosures, J. Heat Transfer, Vol. 110, pp. 1191-1204.

Ozoe, H., Yamamoto, K., Sayama, H. and Churchill, S. W. (1974) Natural circulation in an inclined rectangular channel heated on one side and cooled on the opposing side, Int. J. Heat Mass Transfer, Vol. 17, pp. 1209-1217

Ozoe, H., Sayama, H. and Churchill, S. W. (1975) Natural convection in an inclcined rectangular channel at various aspect ratios and angles - experimental measurements, Int. J. Heat Mass Transfer, Vol. 18, pp. 1425-1431.

Ozoe, H., Yamamoto, K., Sayama, H. and Churchill, S. W. (1977) Natural convetcion patterns in a long inclcined rectangular box heated from below, Int.

J. Heat Mass Transfer, Vol. 20, pp. 131-139.

Ozoe, H., Mouri, A., Ohmuro, M., Churchill S. W and Lior, N. (1985) Numerical calculations of laminar and turbulent natural convection in water in rectangular channels heated and cooled isothermally on the opposing vertical walls, Int. J. Heat Mass Transfer, Vol. 28, pp. 125-138.

Patankar, S. V. (1980) Numerical Heat Transfer and Fluid Flow, Hemisphere Publishing Corporation.

Patterson, J. and Imberger, J. (1980) Unsteady natural convection in a rectangular cavity, J. Fluid Mech., Vol 100, part 1, pp.65-86.

Pedlosky, J. (1987) Geophysical Fluid Dynamics, Springer-Verlag .

Plows, W. H. (1968) Some numerical results for two-dimensional steady laminar Bénard convection, Physics of Fluids, Vol . 11, 1593-1599.

Raithby, G. D. , Glpin, P. F. And Van Doormaal, J. P. (1986) Prediction of heat and fluid flow in complex geometries using general orthogonal coordinates, Numerical Heat Transfer, Vol. 9, pp. 125-142.

Ruth, D. W. (1981) Finite amplitude convection in inclined and vertical slots - a power integral analysis, Int. J. Heat Mass Transfer, Vol. 24, No. 5, pp. 933-944.

Seki, N., Fukusako, S. and Yamaguchi,A. (1983) An experimental study of free

convective heat transfer in parallelogrammic enclosure, J. Heat Transfer, Vol. 105, pp. 433-439.

Stevens, W. N. R. (1982) Finite element, stream function-vorticity solution of steady laminar natural convection, Int. J. for Numerical Methods in Fluids, Vol. 2, 349-366.

Schneck, P. And Veronis, G. (1967) Comparison of some recent experimental and numerical results in Bénard convection, Physics of Fluids, Vol. 10, 927-931.

Tabarrok, B. and Lin, R. C. (1977) Finite element analysis of free convection flows, Int. J. Heat Mass transfer, Vol. 20, pp. 945-952.

Travis, B. J., Anderson, C., Baumgardner, J., Gable, C. W., Hager, B.H., O'Connell, R. J., Olson, P., Raefsky, A. and Schubert, G. (1990) A benchmark comparison of numerical methods for infinite Prandtl number thermal convection in two-dimensional cartesian geometry, Geophys. Astrophys. Fluid Dynamics, Vol. 55, pp. 137-160.

Turner, J. S. (1973) Buoyancy Effects in Fluids, Cambridge University Press .

Veronis, G. (1966) Large-amplitude Bénard convection, J. Fluid Mech. , Vol. 26, part 1, pp. 49-68.

Wendt, J. F. (1996) Computational Fluid Dynamics, Springer-Verlag.

Whitehead, J. A., Jr. and Parsons, B. (1978) Observations of convection at Rayleigh

- numbers up to 76000 in a fluid with large Prandtl number, Geophys. Astrophys. Fluid Dynamics, Vol. 9, pp. 201-217.
- Yang, H.Q., Yang, K. T. and Lloyd, J. R. (1988) Buoyant flow calculations with non-orthogonal curvilinear co-ordinates for vertical and horizontal parallelepiped enclosures, Int. J. For Numerical Methods in Enginggering, Vol. 25, 331-345.
- Yao, H., Xiao, M. And Aldridge K. (1994) Numerical study of natural convection in an inclined enclosure filled with air by finite difference method, Proceedings CFD94, pp. 75- 82.
- Yao, H., Aldridge, K. And Xiao, M. (1995) Heat transfer by natural convection in a parallelogrammic enclosure, Proceedings CFD95, Vol. 2, pp. 31-35.
- Yao, H., Xiao, M. and Aldridge, K. (1995) A numerical study of natural convection in a parallelogrammic enclosure, Numerical Methods in Thermal Problems, Vol. 9, pp.29-36.
- Yao, H. and Aldridge, K. (1996) High-Prandtl-number natural convection in a parallelogrammic enclosure, Proceedings CFD96, pp.369-373.
- Yao, H. and Aldridge, K. (1997) Natural convection in parallelogrammic enclosures partly heated from the bottom and cooled along an inclined side wall. Numerical Methods in Thermal Problems, Vol. 10.
- Yao, H. and Aldridge, K. (1997) Natural convection in rectangular enclosure partly

heated from the bottom wall and cooled along a vertical side wall.  
Proceedings CFD97, pp. 13.9-13.15.

Yin, S. H., Wung T. Y. and Chen, K.(1978) Natural convection in an air layer enclosed within rectangular cavities, Int. J. Heat Mass Transfer, Vol. 21, pp. 307-317.

Yüncü, H. and Yamac, S. (1991) Laminar natural convective heat transfer in an air-filled parallelogrammic cavity, Int. Comm. Heat Mass Transfer, Vol. 18, pp559-568.